

Investigation of Brownian Motion in Simple and Complex Fluids under Oscillatory Perturbations

Dissertation
zur Erlangung des Grades
des Doktors der Naturwissenschaften
der Naturwissenschaftlich-Technischen Fakultät II
- Physik und Mechatronik -
der Universität des Saarlandes

von

Andreas Gross

Saarbrücken

2014



| | |
|-------------------------------------|--|
| Tag des Kolloquiums: | 04.09.2014 |
| Dekan: | Univ.-Prof. Dr. rer. nat. Christian Wagner |
| Mitglieder des Prüfungsausschusses: | |
| Vorsitzender: | Univ.-Prof. Dr. rer. nat. Rolf Pelster |
| Gutacher: | Univ.-Prof. Dr. rer. nat. Christian Wagner Univ.-Prof. Dr. rer. nat. Albrecht Ott |
| Akad. Mitarbeiter: | Dr. rer. nat. Andreas Tschöpe |

Abstract

Brownian motion is present in any kind of fluid at a finite temperature and thus plays an important role in our daily life. Under normal circumstances, these stochastic forces are independent in orthonormal directions. If specific flow profiles are present, though, this situation may change. Three systems were examined in the scope of this thesis, in which Brownian motion plays a central role.

A setup of optical tweezers was utilized to confine single colloids within a microfluidic device while being subjected to a continuous shear flow. The shearing forces led to a coupling of motion in the direction parallel and perpendicular to the flow direction, and hence, gave rise to particular cross-correlation functions. Their specific features allowed the characterization of the flow.

The second system of interest is the biological fluid mucus, which covers and shields many organs in the human body. Respiratory mucus, found in the tracheal region of the body, is crucial to the transport of medical drugs and was investigated using macro- and microrheological methods. This confrontation of large and small structural scales revealed insight into the unique transport properties of the material.

In the third part of this thesis, DNA molecules of the bacteriophage λ were utilized to research the dynamic mechanical properties of these polymers in an oscillating, linear shear flow. A basic bead-spring model was successfully applied to predict the displacement of the center of mass of the molecules. However, phase shifts between driving and response oscillation, which could not be explained by the model, leave room for debates.

Kurzzusammenfassung

In Flüssigkeiten laufen bei Temperaturen oberhalb des Nullpunkts jederzeit dynamische Prozesse ab, die durch die Brownsche Molekularbewegung verursacht werden. Normalerweise ist die Bewegung in orthogonalen Richtungen statistisch unabhängig, in bestimmten Flüssigkeiten kann sich diese Situation jedoch ändern. Im Rahmen dieser Dissertation wurden drei Systeme untersucht, in denen der Brownschen Molekularbewegung eine zentrale Bedeutung zukommt.

Eine optische Pinzette wurde verwendet um einzelne Kolloide in einer Mikrofluidik zu lokalisieren, während sie gleichzeitig einem kontinuierlichen Scherfluss ausgesetzt wurden. Die Scherkräfte führten zu einer Kopplung der Auslenkungen in und senkrecht zur Flussrichtung und verursachten dadurch charakteristische Kreuzkorrelationsfunktionen. Ihr Verlauf konnte zur Analyse des Flusses eingesetzt werden.

Beim zweiten untersuchten System handelt es sich um Mukus, eine biologische Flüssigkeit, die viele Organe im menschlichen Körper bedeckt und schützt. Respiratorischer Mukus, der im Bereich der Atemwege vorkommt, hat eine große Bedeutung beim Transport von Arzneiwirkstoffen in den Körper und wurde mittels makro- und mikrorheologischer Methoden untersucht. Die Gegenüberstellung der verschiedenen Größenordnungen der Strukturen erlaubten Einblick in die einzigartigen Transporteigenschaften des Materials.

Im dritten Teil der Arbeit wurden DNA der Bakteriophage λ verwendet, um ihre dynamischen mechanischen Eigenschaften in einem oszillierenden, linearen Scherfluss zu erforschen. Ein grundlegendes Kugel-Feder-Modell wurde erfolgreich angewandt, um die Auslenkung des Masseschwerpunktes der Moleküle vorherzusagen. Allerdings lassen Phasenverschiebungen zwischen antreibender Schwingung und Antwortschwingung, die nicht vom Modell erfasst werden konnten, Raum für Diskussion.

Contents

| | |
|--|-----------|
| Introduction | 3 |
| I. Investigation of Oscillatory Perturbations of a Colloid in Linear Shear Flow | 5 |
| I.1. Introduction | 7 |
| I.2. Literature Survey | 9 |
| I.3. Optical Tweezers | 13 |
| I.3.1. Historical Development | 13 |
| I.3.2. Scattering Regimes | 14 |
| I.3.2.1. Rayleigh Regime | 14 |
| I.3.2.2. Ray Optics Regime | 15 |
| I.3.2.3. Mie Regime | 16 |
| I.3.3. Force Balance Considerations | 17 |
| I.3.4. Summary | 18 |
| I.4. Flows through Small Channels | 19 |
| I.4.1. Solution of the Navier-Stokes Equation in Rectangular Channels . . | 19 |
| I.4.2. Design of the Microfluidic Device | 23 |
| I.4.3. Colloids in Linear Shear Flow without Forced Oscillations | 25 |
| I.4.4. Colloids in Linear Shear Flow Forced by an Oscillating Optical Trap | 32 |
| I.4.5. Summary | 37 |
| I.5. Numerical Analysis | 39 |
| I.5.1. Colloids in a Quiescent Fluid | 40 |
| I.5.2. Colloids in Linear Shear Flow without Forced Oscillations | 42 |
| I.5.3. Colloids in Linear Shear Flow Forced by an Oscillating Optical Trap | 43 |
| I.5.4. Summary | 49 |

| | |
|---|------------|
| I.6. Experimental Study | 51 |
| I.6.1. Experimental Setup | 51 |
| I.6.1.1. Guidance System of the Laser Beams | 52 |
| I.6.1.2. Microscope, Visualization, & Signal-Synchronization System | 56 |
| I.6.1.3. Flow Control in the Microfluidic Device | 60 |
| I.6.2. Utilized Software | 61 |
| I.6.3. Calibration of the Setup | 63 |
| I.6.4. Results | 70 |
| I.6.4.1. Colloids in Linear Shear Flow without Forced Oscillations . | 71 |
| I.6.4.2. Colloids in Linear Shear Flow Forced by an Oscillating Op- tical Trap | 76 |
| I.6.5. Summary | 84 |
| I.7. Discussion | 87 |
| I.8. Summary | 91 |
| | |
| II. Macro- & Microrheology of Mucus | 95 |
| II.1. Introduction | 97 |
| II.2. Literature Survey | 99 |
| II.3. Rheology of Fluids | 101 |
| II.3.1. Macrorheology | 104 |
| II.3.2. Microrheology | 106 |
| II.3.3. Summary | 109 |
| II.4. Experimental Study | 111 |
| II.4.1. Experimental Setups | 111 |
| II.4.1.1. Rheometer | 111 |
| II.4.1.2. Optical Tweezers | 112 |
| II.4.2. Measurements | 113 |
| II.4.2.1. Macrorheology | 113 |
| II.4.2.2. Microrheology | 119 |
| II.4.3. Summary | 127 |
| II.5. Discussion | 129 |
| II.6. Summary | 135 |

| | |
|---|------------|
| III. Single-End-Grafted DNA-Molecules in an Oscillatory Linear Shear Flow | 137 |
| III.1. Introduction | 139 |
| III.2. Literature Survey | 141 |
| III.3. Theory | 145 |
| III.3.1. Flow Profile between Two Parallel Oscillating Surfaces | 147 |
| III.3.2. Model for a Single-End-Grafted DNA-Molecule | 150 |
| III.3.3. Summary | 154 |
| III.4. Experimental Study | 155 |
| III.4.1. Experimental Setup | 157 |
| III.4.2. Utilized Programs | 161 |
| III.4.3. Measurements | 163 |
| III.4.4. Summary | 172 |
| III.5. Discussion | 173 |
| III.6. Summary | 177 |
| Summary | 181 |
| IV. Appendix | 183 |
| A. Materials & Methods | 185 |
| A.1. Materials | 185 |
| A.2. Methods | 186 |
| A.2.1. Production of Microfluidic Devices | 186 |
| A.2.2. Preparation of Gene Frames for Microrheology Experiments | 187 |
| A.2.3. DNA preparation | 187 |
| A.2.4. Preparation of a cover slip and DNA for shear experiments | 188 |
| B. Calculations | 191 |
| B.1. Auto- and Cross-Correlation Functions of Brownian Motion in a Shear Flow | 191 |
| C. Custom written Software | 195 |
| C.1. Calculation of Auto- and Cross-Correlation Functions | 195 |

Contents

| | |
|-------------------------------------|------------|
| D. Supplementary Tables | 197 |
| Acknowledgements | 205 |
| Eidesstattliche Versicherung | 207 |
| List of Variables | 209 |
| List of Figures | 211 |
| List of Tables | 215 |
| Bibliography | 217 |

Introduction

The dynamics of Brownian suspensions are determined by the fluctuations of their microscopic constituents. Even at rest or at equilibrium, one may observe a rich phase behavior depending on properties like concentration, temperature, pressure, and many more. In this context, it hence poses a very interesting challenge to evolve an understanding of these phenomena. However, in most applications, fluids are typically not at rest but they flow in order to allow material transport. Thus, the study of fluids and the Brownian fluctuations therein is important both for applications and from a scientific point of view. Here, one of the fundamental questions is: How will external fields influence and hence change Brownian dynamics?

The kind of systems which will be in the focus of this work contain sols and gels. In case of a sol, solid particles with sizes between 1 nm and approximately $10\ \mu\text{m}$ are dispersed in a continuous liquid phase (e. g. water, glycerol, etc). A gel, on the other hand, is rather the opposite: Liquid “particles” are dispersed within a solid-like cross-linked network. In many cases, the network is built by polymers. Such materials, as they contain both liquids and solids, thus also show both the elastic properties of a solid and the viscous properties of a Newtonian fluid. This kind of a mixture of properties hence reveals rich characteristics which, due to their viscous and elastic nature, motivated the term viscoelastic or also complex fluid for such materials. This class of materials is very common and often encountered in our everyday lives. We use them to bake a cake, i. e. the dough, to brush our teeth, they are contained within our food and so forth. We are currently just beginning to build an understanding of their material properties and, as already mentioned, our grasp on Brownian dynamics within such materials is far from being complete. This is especially true as soon as external fields are involved and when we consider systems out of their thermodynamic equilibrium.

Within this thesis, the Brownian dynamic in oscillatory fields is studied for three different experimental realizations. In part I, the motion of a colloid is examined in a shear flow while it is subjected to external oscillations. This is implemented by utilizing a setup of optical tweezers of which the main element is a strongly focused laser beam. It allows to confine particles to a small volume around the focal region of the beam and thus additionally enables the visualization of the particle’s motion over a long period of time. A microfluidic device is used in combination with a gravitationally driven flow in order to create the required shear flow. Such a shear flow provides a coupling of the motion of the colloid in perpendicular directions which would not be present in a system in thermodynamic equilibrium. Thus, we expect the cross-correlation functions of the motion in these perpendicular directions to display characteristic properties which cannot be found in the equilibrium system.

Part II gives details about how external oscillatory driving of colloids can be used to study Brownian motion in complex environments like biological gels. In our case, the study was performed in mucus. The analysis of colloidal motion allows the determination

of the viscoelastic properties of the gel. In order to conduct this study, just as in case of part I, a setup of optical tweezers is utilized to confine and visualize the particles. Mucus is of specific interest in pharmaceutical research since it covers many cell surfaces within the human body and could be exploited for a more efficient drug transport. However, this is not possible without knowledge of the diffusion properties of colloids within this material. Hence, in this study, we aim at the structural exploration of mucus by active probing with oscillating colloidal particles.

In part III of this thesis, the simple case of a single particle in shear flow is extended to long-chained polymers which are grafted to a surface while being subjected to an oscillating shear flow. When considering not only a single colloid but a whole chain of particles which are interlinked by springs, this represents a simple model for a polymer. As our polymer of choice we pick deoxyribonucleic acid (DNA) for this part of the study. The oscillating shear flow is created by aligning an optical lens, which is fixed to a piezoelectric device, in a certain distance above the plain surface the DNA is attached to. Oscillations are controlled through electric signals sent to the piezo device. By varying the distance between oscillating lens and the surface at rest as well as the oscillation amplitude and frequency we aim at gaining a deeper understanding of Brownian motion of polymers in shear flow.

Part I.

Investigation of Oscillatory
Perturbations of a Colloid
in Linear Shear Flow

I.1. Introduction

This first part of the thesis deals with small particles of sizes in the micrometer range that are immersed in the bulk of a fluid. Since all experiments discussed later will take place at room temperature, among the first questions one should ask about such a system is: How exactly are the particles going to behave? What is going to happen if these particles are driven out thermodynamic equilibrium by, say, an external flow?

To our current understanding, each fluid consists of molecules that move due to their thermal energy. In doing so, since there is a great number of them, they cannot move far before encountering another molecule. When they approach each other closely enough they exchange momentum according to their angle of impact and their masses which causes their velocity and direction of propagation to change. Assuming a colloidal probe particle in the bulk of a fluid which is bigger than the fluid molecules, these impacts come in from all directions, which means that in average the colloid just remains in its original place (Fig. I.1.1). However, Einstein could show that the particle diffuses randomly in such a way that its mean squared displacements increase linearly in time. This is of course only valid if the fluid container possesses no walls.

So after long years of discussion, the riddle of Brown's molecular motion, which was discovered in 1784, was finally solved about 120 years later in 1905. But even now in the year of its 230th birthday, there are still many open questions in context with Brownian motion especially in non-equilibrium situations and it remains a much investigated topic. Colloidal suspensions like inks and paints play an important role in industrial

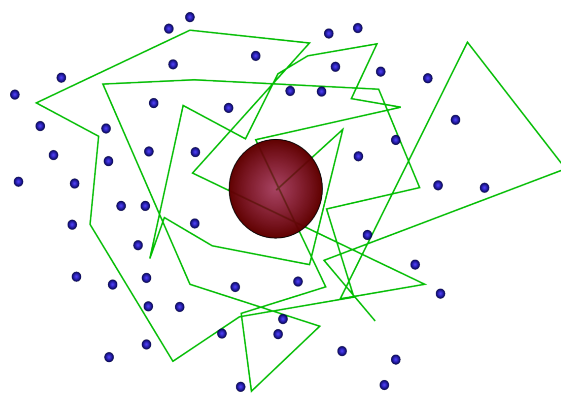


Figure I.1.1.: Arbitrary path (green) of a colloidal particle (red) in the bulk of a fluid (blue).

I.1. Introduction

applications. The equilibrium phase behavior of colloidal suspensions has been intensively studied, but still there is qualitative disagreement between theoretical predictions and experimental results, even for thermodynamic phase transitions [1]. Recently, it was found that hydrodynamic interactions between colloids have to be considered even at equilibrium [2]. However, still one does not need to consider complex systems to find fascinating open questions. Even seemingly simple questions have not been answered yet: How will two or more colloidal particles in a fluid bath behave when they approach each other? How will a confined colloid react when brought into a shear flow? Especially the experimental examination of such systems has proven a challenge. One method which enables the investigation and also the active manipulation of colloidal systems is a setup of optical tweezers. It was developed about 30 years ago by Arthur Ashkin [3] and improved further in the following years, so today it can be used efficiently in order to study colloidal systems.

Part I of the thesis will focus on single particles immersed in water, which are confined to a certain region within a microfluidic channel by optical tweezers. By choice of an optimal position close to the channel walls, the flow profile the particle interacts with is close to a linear shear profile (Ch. I.4). Oscillatory motion of the trap position along the gradient direction are used to drive the system even further out of equilibrium and by analysis of the auto- and cross-correlation functions the local shear rate can be determined. The features of these functions will be compared to earlier results gained by Andreas Ziehl [4, 5]. It is of great importance to understand how external forces like forced oscillations influence confined colloids in a flow field. Especially, if and how these forces couple to the Brownian forces intrinsic to such systems and hence cause additional contributions to the auto- and cross-correlation functions of motion is an interesting question that was not fully answered in the past. If such contributions are indeed present they might also play a role for localized DNA molecules in shear flow as discussed in part III of this thesis. Thus, they should be understood first before more complex systems can be studied. The focus of this work will be threefold: In chapter I.4 a Langevin equation will be applied as the constitutive differential equation of the system and solved analytically. Furthermore, the correlation functions of motion will be determined. Chapter I.5 deals with numerical simulations that enable the examination of the behavior of the colloids not only under experimental conditions but also under conditions that cannot be realized directly due to restrictions of the setup. The experimental study of the system is performed in chapter I.6. The results from all methods will be compared and discussed in chapter I.7.

I.2. Literature Survey

Brownian motion was in the scope of researchers since its discovery by Jan Ingenhousz in 1784 [6], who reported about coal dust moving on the surface of an alcohol droplet. These dust particles seemed to move back and forth in an irregular fashion without any clear direction. The effect was forgotten for nearly half a century until Robert Brown, a Scotch biologist, rediscovered it for pollen on a water surface [7]. He assumed the life force of the pollen as being responsible for this effect. The topic was covered in many a debate in the following years. As possible causes, heat, electricity, and light were the main suspects [8, 9].

Joseph Delsaulx was the first to suggest that the reason might be linked to fluid molecules impacting on the surface of the immersed objects, which in turn leads to the irregular tumbling motion [10]. His suggestion was quite revolutionary since it contained the idea that every fluid consists of smaller parts like molecules. It took until 1905 or respectively 1906 when Albert Einstein [11] and Marian von Smoluchowski [12], independently from each other, formulated a theory to explain and prove the atomistic nature of fluids. A quantitative proof was delivered a few years later by Jean-Baptiste Perrin [13], who managed to determine Avogadro's or respectively Boltzmann's constant experimentally. For this groundbreaking achievement, Perrin was honored with the Nobel prize in 1926.

While Brownian motion was investigated during the 20th century using different methods like light scattering [14] or the intensity analysis during fluorescence microscopy [15], experimental methods for the study of Brownian motion of colloids in active flows were scarce. When Arthur Ashkin demonstrated in 1986 how a focused laser beam could be used to confine and manipulate small particles [3], a very handy tool was developed which could be used to examine Brownian motion directly. Details about the historical evolution of this technique and its applications will be given in the following chapter I.3. This chapter however will focus on the specific use of optical tweezers and similar techniques in context with correlation functions of Brownian motion in colloidal systems that was published until today.

The first study involving optical tweezers in the examination of cross-correlation-functions of Brownian motion of more than one colloid is published in a paper by Jens-Christian Meiners and Stephen Quake [16]. To achieve this, they used a dual-beam optical tweezers setup to independently trap two particles. Each beam was visualized on a separate quadrant photo diode after transiting through the sample cell to allow for

I.2. Literature Survey

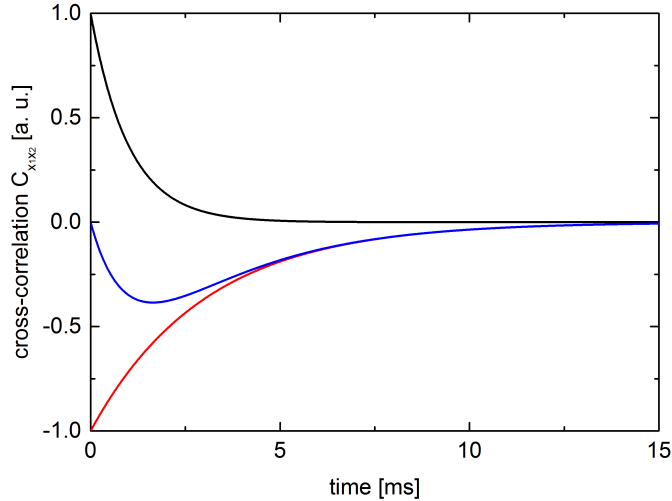


Figure I.2.1.: Contributions of correlated and anti-correlated modes of motion of two beads along the same coordinate axis. The decay time of correlated motion (black) is shorter than the decay of the anti-correlated mode (red) and thus results in a minimum when adding both contributions up (blue).

the separate tracking of each bead. In their experiments, they placed both traps in close vicinity to each other on a line parallel to one of the main axes of their diodes, i. e. the x- or the y-axis. They showed experimentally that the auto-correlation functions of the position in each direction of each bead was represented by a double exponential decay function. Much more remarkable however were their experimental results in respect to the bead-to-bead cross-correlation functions. When correlating the motion in the x-direction of the first bead (denoted by x_1) with the motion of the second bead in the same direction (denoted by x_2), they found a dip in the cross-correlation function $C_{x_1x_2}(\tau)$ close to $\tau = 0$ (compare to Fig. I.2.1). The same is true for the cross-correlations along the y-axis $C_{y_1y_2}(\tau)$ ¹. This dip originates from two superimposed exponential functions, one of which is related to the decay of correlated modes of motion (shown in black), while the second is related to the decay of anti-correlated modes of motion (shown in red).

A similar experiment was performed about 13 years later by Skryabina et al. [17] using magnetic microparticles. In comparison to the setup used by Meiners and Quake, this setup contained an electromagnet which allowed an additional magnetic manipulation of the beads. This again resulted in a shift of all the correlation functions. However, neither Meiners and Quake nor Skryabina et al. found any correlations for the motion in perpendicular directions, i. e. $C_{x_1y_1} = C_{x_2y_2} = C_{x_1y_2} = C_{x_2y_1} = 0$. Since Brownian fluctuations in isotropic systems at equilibrium occur due to collisions with surrounding molecules in an arbitrary way and hence the motion in perpendicular directions is

¹For the sake of brevity, the time-dependence of the correlation functions is omitted in the rest of this chapter although the fluctuations are still time-dependent.

completely uncorrelated this result is not surprising. However, it is possible to observe non-zero cross-correlations of Brownian motion as soon as a coupling mechanism for perpendicular directions is introduced into the system as for example a shear flow. This was observed by Ziehl et al. in experiments [5] and by Bammert et al. [18] as well as Holzer et al. [19] in theory. Instead of immersing the particles in a quiescent fluid without any kind of flow, Ziehl placed the particles in the middle of a microfluidic counter-flow device. While the particles experienced nearly no absolute flow velocity, they were at the same time positioned in the region of the strongest shear gradient. The shear flow led to the coupling of motion in perpendicular directions, so additional cross-correlations were found.

Experiments and theory agree on the results for one single and two particles in shear flow. While the auto-correlation functions remain unchanged for a single particle, the shear flow causes the cross-correlation function C_{xy} to deviate from zero (this case will be discussed in more detail in chapter I.4.3). The most interesting feature is the asymmetry of the function in respect to time which results from the bead being driven out of its thermodynamic equilibrium by the flow. In case of two beads in close vicinity to each other, this effect adds up with the hydrodynamic interaction, so even the movement of the first bead along the x-axis is coupled with the movement of the second bead along the y-axis, i.e. $C_{x_1y_2} \neq 0$. This can be explained in the following way: Both beads interact hydrodynamically causing an anti-correlation of $C_{x_1x_2}$ as discovered by Meiners and Quake. Due to the shear flow, $C_{x_iy_i}$ shows correlations for each of the beads as well. This information is carried over to the other bead through hydrodynamic interaction causing $C_{x_iy_j}$ ($i \neq j$) to be coupled. In addition to the case of both beads being placed on the same streamline, Bammert also discusses the situation when both beads are placed above and below the center streamline in the same distance from it. He furthermore takes oblique cases into account.

Apart from these five publications there have been more publications in the field of cross-correlations in context with the study of Brownian motion in flows. Many of them are only related indirectly and deal with the application of particle image velocimetry in microchannels [20, 21, 22]. There has also been a report on the usage of temperature-related broadening of correlation peaks in temperature measurements within fluid cells [23]. Correlation functions have also been used to detect the torque of particles that were confined within an optical trap [24]. In this study, we apply an additional oscillation to the base shear flow used by A. Ziehl [5]. In this manner, we introduce a further time scale into the system which may give access to fascinating dynamics of colloids away from thermodynamic equilibrium. The study of Brownian motion in an oscillatory shear flow is of great importance since it is a common situation. Consider for example the pulsating flow of blood which can be described by a continuous shear flow with an additional oscillatory contribution. Also the results will help in understanding the influence of the shear flow on DNA molecules which are grafted to one of the side walls of a flow chamber.

I.2. Literature Survey

Hence, the pre-requisites for the analysis of the dynamics of DNA molecules in oscillating shear flows in part III of this work will be achieved in this first part.

The first part of this thesis is going to focus on a special implementation of the last of these questions. Specifically, the position of the optical trap will oscillate harmonically in the direction perpendicular to the flow direction in the microchannel while a bead is confined in it. Similar to the state in the counter-flow device of Andreas Ziehl, the shear flow will cause a non-equilibrium situation for the bead which is additionally perturbed by the oscillatory motion of the trap.

I.3. Optical Tweezers

I.3.1. Historical Development

Light or electromagnetic radiation can be described as a wave and as a particle at the same time. This principle, which is well-known as wave-particle dualism, was found by Albert Einstein as the explanation for the photoelectric effect and published in one of his famous papers from 1905 [25]. It was the first quantum-physical explanation that considered light as a quasi-particle called photon that is able to interact with matter. Thus, the effect that an electric current is caused by light shining on a surface can be understood. But even hundreds of years before, when Johannes Kepler watched the passage of comet Halley, he detected that the tail of the comet was directed away from the sun. He explained this effect by the radiation pressure of the sun. Today, applications for radiation pressure exist over a wide scale of sizes. Among the largest are solar sails which are used for the propulsion of satellites, among the smallest are optical tweezers.

The first realization of a setup of optical tweezers was developed by Arthur Ashkin in 1970 [26] and used two counter-propagating laser beams to confine particles. While creating stable traps, this kind of a setup brought the disadvantage that either two lasers had to be used or the beam of a single laser had to be split and carefully aligned. Still, it presented the proof-of-principle that it is possible to confine particles by light. In the following years, Ashkin continued his work on optimizing his setup which led among others to a levitation trap [27] and finally, about 15 years later, to the typical setup as it is still used today [3]. Only a single, tightly focused beam is used, which is thus able to directly confine particles. Ashkin also worked on a theoretical model for the interaction of the laser with the particles [28, 29, 30].

Since then, a wide range of applications has been found for optical tweezers in scientific research. One of the most famous is the use for force measurements at molecular motors [31, 32, 33] and DNA molecules [34, 35]. Also in recent years, microrheology became more important, which was established by Mason in 1995 [36] and used for the examination of numerous fluids like polymers [37, 38], gels [39, 40], and especially biological materials like the filamentous bacteriophage fd [41], B lymphocyte membrane tethers [42], fibroblast cells [43], and more. The huge advantage of microrheology in this context is two-fold. On the one hand, no mechanical contact with the sample is necessary to perform measurements and manipulate particles, which reduces the probability of contamination. On the other hand, measurements can be performed in the smallest

I.3. Optical Tweezers

sample volumes, even smaller than $30 \mu\text{l}$.

The following chapter will give details on the interaction of laser light in a setup of optical tweezers with small particles by scattering. It will conclude with the derivation of a simple interaction force which will be used in the analytical examination of the system later.

I.3.2. Scattering Regimes

A setup of optical tweezers will play a central role in this part and also part II about the rheology of mucus. Thus, developing an understanding of its basic properties is important for the discussions following later. While details about the construction of such a setup will follow in chapter II.4, here, the electromagnetic interaction of the involved lasers with colloids will be explained. They will play a crucial role in the analytic description of the system and the equations of motion of the particles in the focal region of an optical trap.

When considering scattering of photons by colloids in a setup of optical tweezers, the interaction of light and colloid can be split into a force that stabilizes the trap, also called gradient force, and a second one that decreases its stability, the so-called scattering force. The models that qualify to describe their interaction depend on the relation of the wavelength of the photon to the size of the colloid $d_c = 2r_c$, where r_c is the radius of the colloidal particle. The following sections deal with three size regimes that result from this comparison.

I.3.2.1. Rayleigh Regime

The first case considered here deals with colloid sizes much smaller than the wavelength of the laser beam ($d_c \ll \lambda$). Due to their small size, colloids can be described as punctiform electric dipoles interacting with the electric field component of the light [44]. This idea results in two formulas for the scattering and gradient force [3]

$$\vec{F}_{scat} = \frac{\sigma_s n_m}{c} \langle \vec{S} \rangle, \quad (\text{I.3.1})$$

$$\vec{F}_{grad} = \frac{\alpha_p}{2} \vec{\nabla} \langle \vec{E}^2 \rangle. \quad (\text{I.3.2})$$

Here, the scattering cross-section is given as

$$\sigma_s = \frac{128\pi^5 r_c^6}{3\lambda^4} \left(\frac{m_r^2 - 1}{m_r^2 + 2} \right)^2 \quad (\text{I.3.3})$$

and α_p represents the polarizability of the colloid

$$\alpha_p = n_m^2 r_c^3 \left(\frac{m_r^2 - 1}{m_r^2 + 2} \right). \quad (\text{I.3.4})$$

In these formulas, the optical properties of the colloids and the surrounding medium are contained in the shape of the respective refractive indices n_c and n_m as well as the relative refractive index $m_r = n_c/n_m$.

I.3.2.2. Ray Optics Regime

If the particle size is big in comparison to the wavelength of the laser ($d_c \gg \lambda$), the interaction of light and matter can be described by classical ray optics. This means that the laser is divided into infinitely small partial beams that move in straight paths until they reach an interface to a material with different optical properties. Under the assumption that there is no partial reflection of the incoming beam, the rays propagate according to Snell's law [44]

$$n_m \sin(\theta_i) = n_c \sin(\theta_e). \quad (\text{I.3.5})$$

Here, n_m and n_c denote the refractive indices of medium and colloid, θ_i and θ_e represent the angle of incidence and emergence of the beam relative to the surface normal vector.

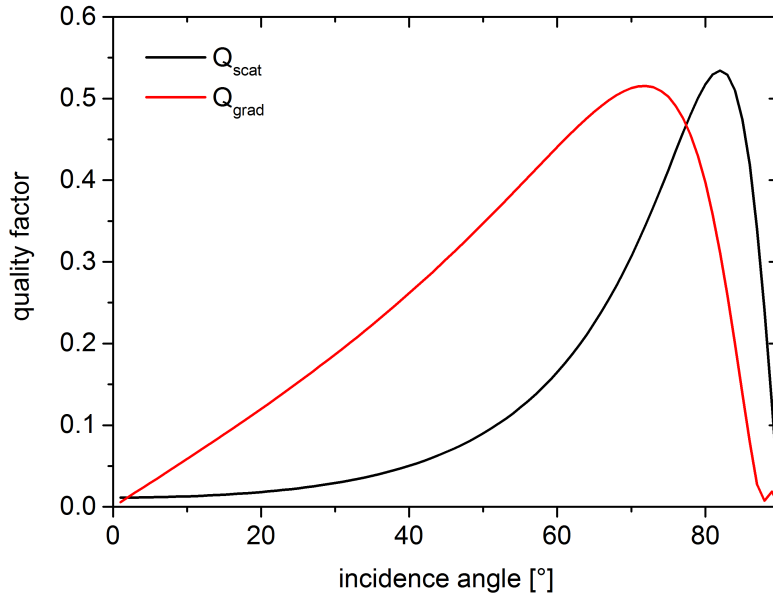


Figure I.3.1.: The quality factors for scattering (Eq. I.3.6) and gradient force (Eq. I.3.7) are plotted here for incidence angles between 0° and 90° . A combination of water as the surrounding medium ($n_m \approx 1.33$) and polymethylmethacrylate (PMMA) as the colloid material ($n_c \approx 1.49$) was assumed for the calculation.

I.3. Optical Tweezers

However, partial transmission and reflection of the beams must also be taken into account. Here, every time a ray of power P encounters an interface, only a part of it is able to transmit, while the rest is reflected at the interface. When integrating over the whole width of the incoming laser beam, one can define the total scattering and gradient forces as [30]

$$|\vec{F}_{scat}| = \frac{n_m P}{c} \underbrace{\left[1 + R_F \cos(2\theta_i) - \frac{T_F^2 (\cos(2\theta_i - 2\theta_e) + R_F \cos(2\theta_i))}{1 + R_F^2 + 2R_F \cos(2\theta_e)} \right]}_{Q_{scat}}, \quad (\text{I.3.6})$$

$$|\vec{F}_{grad}| = \frac{n_m P}{c} \underbrace{\left[R_F \sin(2\theta_i) - \frac{T_F^2 (\sin(2\theta_i - 2\theta_e) + R_F \sin(2\theta_i))}{1 + R_F^2 + 2R_F \cos(2\theta_e)} \right]}_{Q_{grad}}, \quad (\text{I.3.7})$$

where R_F and T_F are Fresnel's coefficients of reflection or, respectively, transmission. The terms in brackets are denoted as the quality factors of scattering and gradient force Q_{scat} and Q_{grad} . These allow the determination of the ideal angle of incidence for a given combination of medium and colloid materials (compare Fig. I.3.1). The graph displays the quality factors for the combination of polymethylmethacrylate (PMMA) beads in water, the most common materials used in this part of the thesis. The highest value of the gradient quality factor is reached at about 72° , while the scattering is strongest around 82° . This leads to the conclusion that the optimal angle of incidence lies around $50^\circ - 70^\circ$ where a high absolute value of Q_{grad} is reached, while the relative value Q_{grad}/Q_{scat} is as big as possible. Such high angles of incidence can only be realized by an objective of high numerical aperture. A stable confinement of a particle is possible only if the surrounding medium is of less optical density than the sphere, i. e. $n_c > n_m$. If this was the case, the sphere would always be pushed away from the focal point and stable trapping would be impossible.

I.3.2.3. Mie Regime

In this intermediate regime in which the wavelength of the light is of roughly the same order as the particle size ($d_c \approx \lambda$), additional corrections to the forces of the Rayleigh regime have to be taken into account. This can either be attempted by using an approach via the coupled-dipole method [45] or the generalized Lorenz-Mie theory (GLMT) [46, 47]. To achieve a more precise formulation of the acting forces, the plane of polarization of the laser beam itself also has to be taken into account [48]. More details on the description of scattering in the Mie regime can as well be found in a book by Bohren and Huffman on the absorption and scattering of light by small particles [44]. Due to its large complexity, this regime will not be discussed in the scope of this thesis. However, more details about it can be found by the attentive reader in the referenced literature.

I.3.3. Force Balance Considerations

As becomes apparent depending on the size of the scattering object as compared to the wavelength of light different descriptions of the interaction of light and matter are applicable. No matter which scattering regime is considered there are always two common forces (Fig. I.3.2): A scattering force \vec{F}_{scat} pushes the sphere in direction of the Poynting vector of the incident beam and a gradient force \vec{F}_{grad} pulls the sphere in direction of the strongest electric field gradient. If a focused beam is assumed at this point as indicated in figure I.3.2 the sphere moves towards the focal point of the laser. However, the scattering force results in the sphere always being pushed slightly away from the focal point so that it reaches a new equilibrium position. In total, close to the focal point of the laser beam, all acting forces can be combined to a linear law independent of the size regime

$$\vec{F}_{trap} = -k_{trap}\Delta\vec{r}, \quad (I.3.8)$$

where $\Delta\vec{r}$ denotes the displacement of the trapped object away from the focal point. The spring constant or trap stiffness k_{trap} can vary from one Cartesian direction to another, in general, the components are identical. However, equation I.3.8 only holds true close to the focal point of the laser. For bigger distances, higher order corrections have to be taken into account.

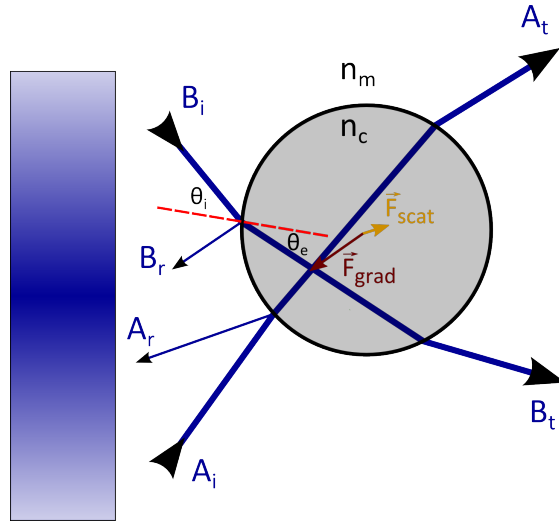


Figure I.3.2.: Total force balance of scattering and gradient force for the interaction of a focused laser beam with a sphere of refractive index n_c in a medium of index n_m . Two exemplary incident beams A_i and B_i are partially reflected (A_r and B_r) and partially transmitted through the sphere (A_t and B_t). Multiple reflections within the sphere are not depicted to keep the image clear. The colored bar on the left side of the sketch indicates the Gaussian intensity distribution of the laser beam.

I.3.4. Summary

In the past chapter, the principle of optical tweezers was discussed. The main feature is a strongly focused laser beam that interacts with objects in its beam path. The exact description of this interaction depends on the size of the object relative to the wavelength of the beam. Small objects ($d_c \ll \lambda$) act as punctiform dipoles in the electromagnetic field of the laser [3], while bigger objects ($d_c \gg \lambda$) lead to classical refraction of the beam [30]. For all regimes, acting forces can be sub-divided into a scattering force \vec{F}_{scat} and a gradient force \vec{F}_{grad} . While \vec{F}_{scat} always leads to a weakening of the trap since it is directed in the propagation direction of the laser beam, \vec{F}_{grad} stabilizes the trap if the setup of optical tweezers is constructed correctly. The total force acting on a sphere in an optical trap is described by a linear law (Eq. I.3.8) which will be helpful in the following chapters to derive a differential equation of motion for the confined particle. This force balance in context with the scattering and gradient forces will have repercussions on the actual construction of the setup utilized in this study. More details on this topic will follow in a later chapter (Sect. I.6.1).

I.4. Flows through Small Channels

In this thesis, microfluidic channels are used to create a shear flow. They are designated microfluidic devices since at least one of their dimensions is in the micrometer range. This is certainly the case here, since they have a width of $50\ \mu\text{m}$ and a height of about $40\ \mu\text{m}$. While the flow is purely gravitationally driven, which results in a Poiseuille velocity profile, these kinds of devices can be used to create quasi-linear shear flows, nonetheless. This idea will be developed over the course of the next sections.

The second topic and one of the central keypoints of this thesis is the interaction of a trapped colloid with the flowing fluid. The force balance for such a bead will be discussed without (Sect. I.4.3) and with forced oscillations (Sect. I.4.4), and the solutions of the differential equations will be employed to determine the auto- and cross-correlation functions of their motion.

I.4.1. Solution of the Navier-Stokes Equation in Rectangular Channels

When talking about microfluidic devices and flows through channels, among the first questions asked should be how the velocity profile of the fluid will look like. Central principles necessary for the solution are the conservation of mass, momentum, and energy [49]. Then, the Navier-Stokes equation can be cast in the following form

$$\rho \left(\frac{\partial}{\partial t} + \vec{v} \vec{\nabla} \right) \vec{v} = \eta \Delta \vec{v} - \vec{\nabla} p + \rho \vec{g}, \quad (\text{I.4.1})$$

where p is the pressure, ρ the density, and η the dynamic viscosity of the fluid. This equation gives the full Navier-Stokes equation with which any kind of flow in any geometry can be characterized. For steady unidirectional flows like present in a rectangular channel driven by hydrostatic pressure, this problem can be strongly simplified. Then, the flow can be considered stationary, eliminating the time-dependence, and also convection-free. The description can be reduced to the Stokes equation

$$\eta \Delta \vec{v} - \vec{\nabla} p + \rho \vec{g} = 0 \quad (\text{I.4.2})$$

I.4. Flows through Small Channels

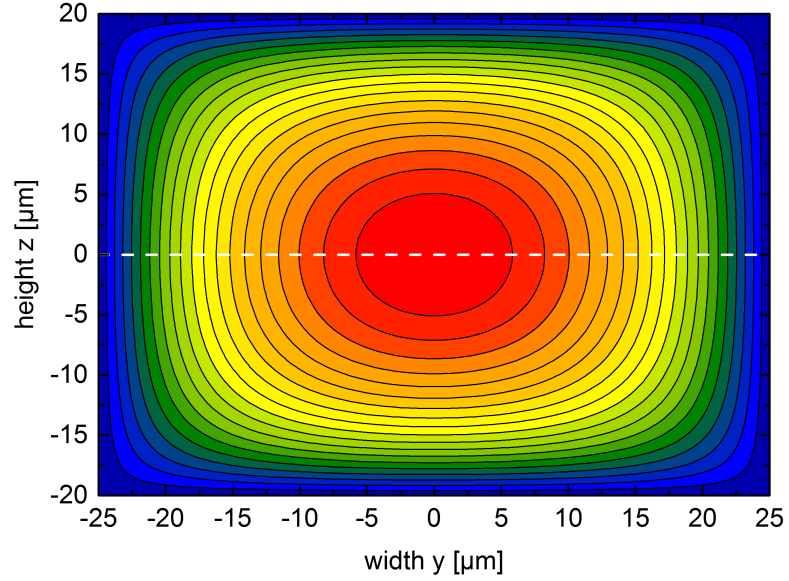


Figure I.4.1.: Color-coded plot of the normalized flow velocity in the x-direction of a rectangular channel in the y-z-plane. The velocity increases from a complete stand-still at the channel walls (dark blue) to the maximum velocity in the center of the channel (red). The white horizontal line indicates the cutting line along which the flow profile in Fig. I.4.2 is drawn.

or respectively when assuming a channel with a flow solely in the horizontal x-direction of velocity $v_x \hat{=} v$

$$\eta \left(\frac{\partial}{\partial y^2} + \frac{\partial}{\partial z^2} \right) v - \frac{\partial p}{\partial x} = 0. \quad (\text{I.4.3})$$

A solution can be computed for no-slip boundary conditions¹ by using Fourier-expansions in the z-direction, giving [50]

$$v(y, z) = \frac{3Q}{8ab^3 F\left(\frac{a}{b}\right)} \left[b^2 - z^2 + 4b^2 \sum_{n=1}^{\infty} \frac{(-1)^n \cosh\left(\alpha_n \frac{y}{b}\right)}{\alpha_n^3 \cosh\left(\alpha_n \frac{a}{b}\right)} \cos\left(\alpha_n \frac{z}{b}\right) \right], \quad (\text{I.4.4})$$

where Q is the flow rate, a is half the channel width, b is half of its height, $\alpha_n = (2n - 1)\pi/2$, and

$$F(x) = 1 - \frac{6}{x} \sum_{n=1}^{\infty} \frac{\tanh(\alpha_n x)}{\alpha_n^5}. \quad (\text{I.4.5})$$

¹When assuming no-slip boundary conditions, the velocity of the fluid at the position of the container walls equals the velocity of the walls themselves. Here, the walls do not move at all leading to the conditions $v(y = -b/2) = v(y = +b/2) = v(z = -a/2) = v(z = +a/2) = 0$.

I.4.1. Solution of the Navier-Stokes Equation in Rectangular Channels

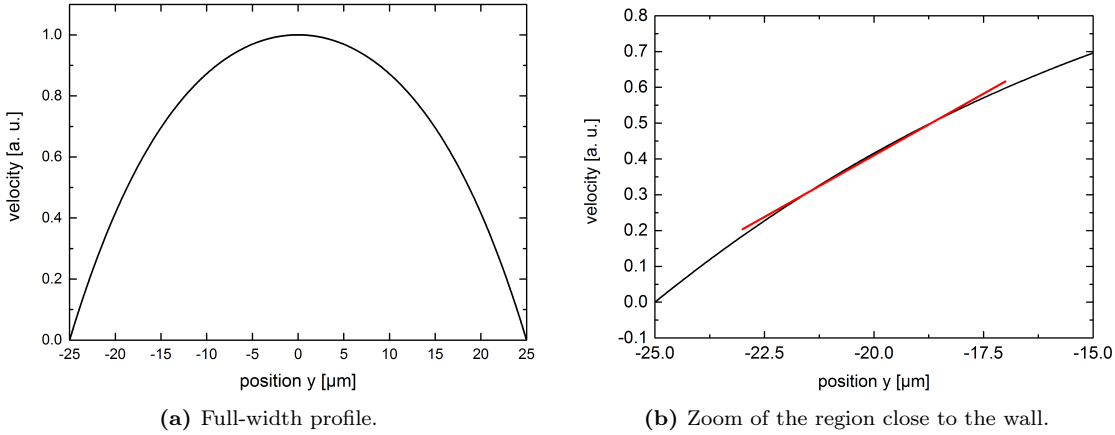


Figure I.4.2.: Plot of the normalized flow velocity v against the position y at a fixed height $z = 0 \mu m$ in the middle of the channel as indicated by the white line in Fig. I.4.1. While the computed profiles are shown in black, a linear fit to the data close to the wall is shown in red.

In this case, the origin is placed in the middle of the channel. A color-coded plot in the y - z -plane of a rectangular channel is drawn in Fig. I.4.1. Since all the experiments were performed close to the center-line in respect to the height of the channel at $z = 0 \mu m$, a two-dimensional profile along that line is displayed in Fig. I.4.2. While the full profile shows the characteristic parabolic shape (Fig. I.4.2a) typical for a Poiseuille-type pressure-driven flow, in close proximity of the wall the velocity increases nearly linearly with the distance y to the wall (Fig. I.4.2b). It appears reasonable to assume a linear shear profile for the distances used in the experiments introduced later in chapter I.6, which lie in a range of 2 to 4 times the particle radius corresponding to $4 \mu m$ to $8 \mu m$. Especially, one has to take into account that only a small region around the average position of the oscillating optical trap will be visited by the confined beads; the typical amplitude amounts to $1 \mu m$. At the same time however, the bead in the optical trap should be as close as possible to the center of the channel in z -direction, because otherwise there might exist an additional shear gradient in this direction which cannot be monitored directly. An evaluation of the height of the bead is not established in the current setup.

In context with flows through small channels, a further topic shall be discussed: the laminarity of the flow. Usually, the Reynolds number is evaluated as a means to characterize the flow in this respect. It weighs the inertial forces active in the flowing fluid against the viscous ones. It is a dimensionless number and as such gives an indication whether a flow tends to be laminar - this is the case when the viscous forces dominate over the inertial ones - or turbulent depending on its magnitude. In general, it is defined

I.4. Flows through Small Channels

as

$$Re = \frac{\rho \bar{v} d_h}{\eta}, \quad (\text{I.4.6})$$

where d_h is the hydraulic diameter of the channel and \bar{v} the average flow velocity. Since the Reynolds number was originally defined for pipes with a round cross-section, a correction has to be included, if channels with a different cross-section, i. e. rectangular ones, are utilized. It can be determined as

$$d_h = 4 \frac{A}{P} = \frac{2wh}{w+h}, \quad (\text{I.4.7})$$

where A is the area of the cross-section of the channel and P is its wetted perimeter. The right-hand side of the equation shows the corresponding result for the chosen channel, where w is its width and h its height. This gives the adapted Reynolds number for a rectangular channel

$$Re_{\text{rectangular}} = \frac{2\rho \bar{v} wh}{\eta(w+h)} \approx 0.004. \quad (\text{I.4.8})$$

The typical maximum velocity of the flows applied in this part of this doctoral research study lies at $100 \mu\text{m}/\text{s}$ and since all experiments were performed in water, the density $\rho = 1000 \text{ kg}/\text{m}^3$ and viscosity $\eta = 10^{-3} \text{ Pa s}$ of water were used. For the estimation, corresponding to the experiments detailed later a channel width of $50 \mu\text{m}$ and a height of $40 \mu\text{m}$ were assumed. As far as critical Reynolds numbers are concerned, there is no general number that is valid for all geometries and systems. If the Reynolds number is much smaller than 1, the physical system can be considered as behaving purely laminar. With $Re_{\text{rectangular}}$ in the order of magnitude between 10^{-3} to 10^{-2} , any turbulence will decay faster than the temporal resolution of the measurement and will only have a marginal influence on the flows.

One important correction has to be taken into account when handling beads very close to side walls of channels: These beads will behave as if moving in a fluid of higher viscosity the closer they approach the wall. This effect is caused by hydrodynamic interaction of the spheres with the walls. It only applies for motion along the surface normal of the wall while motion perpendicular to it is not influenced at all. Assuming that a colloid approaches a wall, the fluid in-between has to be pushed out before the colloid can move any closer. This requires more force as compared to motion in the bulk of the fluid, thus, the effective viscosity for motion towards the walls seems higher. Of course, the actual viscosity of the fluid remains unchanged, the effect is just a pretended effect through the interaction of colloid and wall. The viscosity increase can be computed by using Faxén's

law [51]

$$\eta_{eff} = \eta_0 \left(1 - \frac{9}{16} \frac{r_c}{d_{cw}} + \frac{1}{8} \left(\frac{r_c}{d_{cw}} \right)^3 - \frac{45}{256} \left(\frac{r_c}{d_{cw}} \right)^4 - \frac{1}{16} \left(\frac{r_c}{d_{cw}} \right)^5 \right)^{-1}, \quad (\text{I.4.9})$$

where η_{eff} is the effective viscosity, η_0 is the bulk viscosity of the fluid, r_c is the radius of the colloid, and d_{cw} is the distance of the center of the colloid to the wall. When only the first order correction is taken into account, this leads to a viscosity increase of roughly 25% for $d_{cw} = 3r_c$. Although a viscosity change of this order is quite significant, this is the smallest distance chosen in the experiments presented in later chapters and can thus be seen as an upper limit. Since the viscosity has to be known for the calibration of the trap stiffness as well, it will be influenced implicitly (Sect. I.6.3). To avoid these influences by the walls becoming too strong, only those measurements will be considered where the trap stiffnesses parallel and perpendicular to the walls do not differ from each other by more than 10%.

I.4.2. Design of the Microfluidic Device

The main goal of this first part of the dissertation is the visualization of the motion of particles confined in an oscillating optical trap while exposed to a linear shear flow. A means to create a flow which can be approximated locally as a shear flow is given by a microfluidic device with channels of rectangular cross-section, as discussed in the past section. If the bead is placed close to the center in z-direction and at the same time close to one of the side walls of the channel in y-direction, the conditions are close to ideal (compare Fig. I.4.2). However, the techniques necessary to build such a device have to make dimensions in the order of $10 \mu\text{m}$ possible. So-called soft lithography techniques [52] are a very convenient way of fabrication. A particular one amongst these methods is designated as replica molding. First, a mold is necessary which carries the negative structures of the desirable geometry. It is then filled with a soft material like

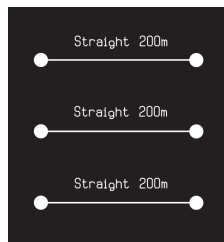


Figure I.4.3.: Example of a mask used for lithographic processing of silicon wafers in manufacturing the mold for soft lithography. The patterns shown here represent a channel width of $200 \mu\text{m}$ and a length of 2 cm . For the experiments, only channels with a width of $50 \mu\text{m}$ were used.

I.4. Flows through Small Channels

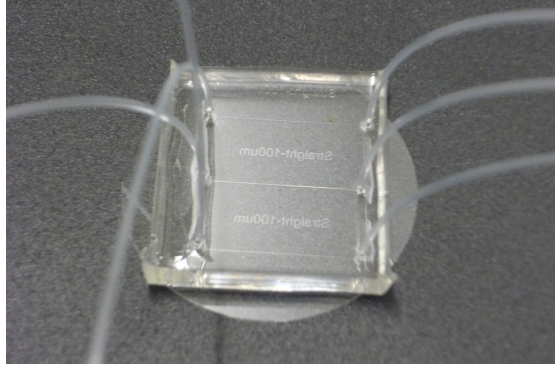


Figure I.4.4.: This photograph shows a fully prepared microfluidic device after bonding to a round coverslide and tubes having been inserted as in- and outlets for a fluid.

polydimethylsiloxane (PDMS), which gives the positive counter-structure to the mold. After curing, the PDMS hardens and can be used for example for the realization of microchannels. To avoid the evaporation of sample fluid and also dust particles in the system during an experiment, the channels should be closed off by using coverslides. Details on the production of the microfluidic devices using this method can be found in the “Methods” section of the appendix (Sect. A.2.1).

The production of the mold can also be achieved using a multitude of techniques. If the size of the structures ranges in the order of magnitude of millimeters or bigger, a mold can be manufactured using mechanical methods like the milling of metal. For smaller molds on the micrometer scale, the manufacturing can be achieved by lithography techniques on silicon. For that purpose, patterns on a mask are transferred by exposing them to light into a photo resist, followed by the removal of either the exposed or the non-exposed structures depending on the type of resist. The remainder of this procedure can finally be used as a mold.

In the scope of this thesis, the only type of pattern used for the manufacturing of microfluidic devices were straight rectangular channels (Fig. I.4.3). For a simpler handling when punching holes for the tubes leading to the channels in the PDMS, small round-shaped reservoirs were added to the design. After a full preparation of a channel according to the procedure detailed in section A.2.1, ready-for-use microfluidic devices as shown in Fig. I.4.4 result that are perfectly suited for experiments within a flowing fluid.

I.4.3. Colloids in Linear Shear Flow without Forced Oscillations

When a colloidal particle is immersed into a fluid bath, there will be many smaller molecules in a snapshot of the particle's surroundings that make up the fluid (Fig. I.1.1). However, they will not be motionless due to the fact that the bath cannot be kept at the temperature $T = 0 K$. Instead, the molecules will move rapidly back and forth in an arbitrary, undirected motion. If time would be slowed down to a crawl, we would see each single molecule move in a straight line as long as there are no other molecules in their path. As soon as two of them collide, they will exchange momentum and thus their direction of propagation as well as their kinetic energy will change. However, the visualization of this ballistic motion requires an extremely fast data acquisition system on a timescale of nano- to picoseconds [53]. With slower recording, the single impacts cannot be distinguished from one another anymore and the only possible way of a description may happen on stochastic terms.

This Brownian force can be described using stochastic properties. On the one hand, the temporal average of the force through the impacts on a non-ballistic timescale must disappear [54]

$$\langle \vec{F}_r(t) \rangle_t = 0. \quad (\text{I.4.10})$$

On the other hand, one can find by application of the fluctuation-dissipation theorem [55] that the auto-correlation function of this random force is expressed by

$$\langle \vec{F}_{r,i}(t_1) \vec{F}_{r,j}(t_2) \rangle = 2k_B T \zeta \delta(t_1 - t_2) \delta_{ij}, \quad (\text{I.4.11})$$

where k_B is Boltzmann's constant, $\zeta = 6\pi\eta r_c$ is the coefficient of friction of ideal spheres of radius r_c in a fluid of viscosity η , $\delta(t_1 - t_2)$ is Dirac's delta distribution

$$\delta(t_1 - t_2) = \frac{1}{2\pi} \int_{-\infty}^{\infty} d\omega e^{i\omega(t_1 - t_2)}, \quad (\text{I.4.12})$$

and δ_{ij} is Kronecker's delta. i and j represent arbitrary Cartesian coordinates, i. e. x , y , and z . The stochastic forces are only correlated if they act in the same direction and if the events are simultaneous. Otherwise, no correlations are found. More details about the definition of correlation functions will follow later (Eq. I.4.18).

Stochastic forces are not the only forces one needs to take into account when considering particles in a fluid. Additional forces are inertial forces $\vec{F}_{inertia}$, the force of friction \vec{F}_{fric} , and, if present, the influence of an optical trap \vec{F}_{trap} [56]. As already discussed before in case of flows of low Reynolds number, friction forces will always dominate over inertial forces (Sect. I.4.1), thus, inertial forces can be omitted. As far as friction is

I.4. Flows through Small Channels

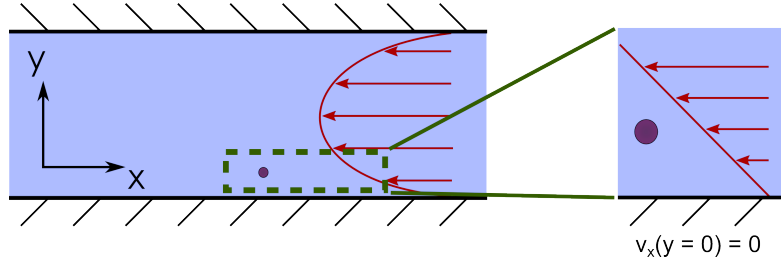


Figure I.4.5.: Sketch of a colloid in a microfluidic device with a rectangular cross-section as seen from above.

concerned, since all experiments reported later are performed using spherical particles, Stokes' friction formula for ideal spheres can be applied

$$\vec{F}_{fric} = \zeta \vec{v}. \quad (\text{I.4.13})$$

In the case of simple Newtonian fluids, i. e. fluids that show no viscoelastic behavior, ζ is given as a constant value. In part II of this thesis, in context with microrheology, more details on viscoelastic properties of complex fluids will be given. Here, however, only water was sent through the microfluidic devices, so no complex behavior of the fluid needs to be taken into account.

In chapter I.3, the interaction of a focused laser beam with spherical objects was reviewed. While the description of the electromagnetic interaction is a multifaceted topic by itself, independent of the scattering regime or in other words the particle size versus wavelength ratio, the effect of the laser can be reduced to equation I.3.8. For the sake of brevity, the index “trap” will from now on be omitted from the trap stiffness k_{trap} .

Differential equations of this kind, which include stochastic forces, are labeled Langevin equation. They were first used by Paul Langevin in 1908 for the description of Brownian motion [57]. In this case however, it is expanded by the influence of the optical trap. For the specific case of a colloid near one of the side walls of a rectangular channel (Fig. I.4.5), one further modification of the equation is necessary. While the out-of-plane gradient in flow velocity along the z-axis can be safely neglected since the colloid is placed in the middle between top and bottom wall of the channel, this is certainly not true for the gradient along the y-axis. This particular gradient was supposed to be used for the creation of the shear flow in the first place. Thus, for motion in the perpendicular direction to the flow propagation, i. e. the y-direction, the total force balance yields

$$\zeta \frac{\partial y(t)}{\partial t} + k(y(t) - y_{trap}(t)) - F_{r,y}(t) = 0. \quad (\text{I.4.14})$$

Here, it is assumed that the position of the optical trap does not vary during the conduction of the experiment, but rather remains in a constant position $\vec{r}_{trap} = (x_{trap}, y_{trap}, 0)$. Without loss of generality, the origin of the coordinate system is chosen in such a way

I.4.3. Colloids in Linear Shear Flow without Forced Oscillations

that it is identical to the center of the optical trap, i. e. $\vec{r}_{trap} = \vec{0}$. In x-direction, the equation including the shear forces reads

$$\zeta \left(\frac{\partial x}{\partial t} - \dot{\gamma} y(t) \right) + kx(t) - F_{r,x}(t) = 0, \quad (\text{I.4.15})$$

where $\dot{\gamma}$ is the shear rate. The force created by shearing has to carry a negative sign since the colloid has to move against the flow direction to keep its position, hence resulting in a negative force contribution. Both equations I.4.14 and I.4.15 are inhomogeneous differential equations of first order and can be solved by at first tackling the homogeneous equation and then determining a special solution of the inhomogeneous problem by variation of parameters. This yields for the equation in y-direction

$$y(t) = e^{-t/\tau_r} \left\{ y_0 + \int_0^t dt' \left[e^{t'/\tau_r} \frac{F_{r,y}(t')}{\zeta} \right] \right\}, \quad (\text{I.4.16})$$

where the decay constant is given by $\tau_r = \zeta/k$ and y_0 is the starting position of the colloid defined by the initial conditions. This concurs with the classical solution of the equation of motion of a colloid in a quiescent fluid. By introducing equation I.4.16 into equation I.4.15, a solution in flow direction can be found as well:

$$x(t) = e^{-t/\tau_r} \left\{ x_0 + \dot{\gamma} y_0 t + \int_0^t dt' \left[e^{t'/\tau_r} \frac{F_{r,x}(t')}{\zeta} + \dot{\gamma} \int_0^{t'} dt'' \left(e^{t''/\tau_r} \frac{F_{r,y}(t'')}{\zeta} \right) \right] \right\}, \quad (\text{I.4.17})$$

where again x_0 is defined through the initial conditions. The structure of this solution becomes identical with the shear-free solution in y-direction if the shear rate is set to zero. Due to the coupling of both equations through the shearing, the effects of Brownian motion in y-direction will also play a role for the motion in x-direction. To get a clearer insight into the type of coupling present, the auto- and cross-correlation functions of motion will be computed.

Correlation Functions in Linear Shear Flow without Forced Oscillations

In general, cross-correlation functions are applied when the relation of two signals or time-dependent mathematical functions $f(t)$ and $g(t)$ is in question. Such relations are characterized on the one hand by their strength, in other words by the absolute value of the correlation, but also by their direction as indicated by the sign of the function. They are defined as

$$C_{fg}(\tau) = \langle f(t)g(t+\tau) \rangle = \lim_{T_m \rightarrow \infty} \frac{1}{T_m} \int_{-T_m/2}^{T_m/2} dt f(t)g(t+\tau). \quad (\text{I.4.18})$$

I.4. Flows through Small Channels

If a cross-correlation function carries a positive sign, one considers the functions f and g to be correlated, in case of a negative sign they are denoted as anti-correlated. If the functions f and g are identical, this special case is denoted as auto-correlation function. The temporal limits of the integral in equation I.4.18 is given by the duration of the measurement T_m or respectively the range of definition of the signal. A very important feature of correlation functions is that they do not depend on an absolute time-frame t , but only on events on a relative timescale τ . By definition, an additional symmetry property is given by

$$C_{fg}(\tau) = C_{gf}(-\tau). \quad (\text{I.4.19})$$

If the order of the functions to be correlated is interchanged, it leads to time-inversion of the correlation function at the same time. Hence, due to symmetry reasons, auto-correlation functions are always even functions in respect to time.

As the computation of the cross-correlation functions as well as the discussion of their features is the central topic of this first part of the dissertation, their derivation will be explained in detail. Very recently, a paper which focused on the same aspects was published [58]; the argumentation will very much follow the train of thought in it. This first case of colloidal Brownian motion in a shear flow was already discussed before in literature by Ziehl and Bammert [5, 18]. However, it shall be analyzed here again because it acts as a basic case to the situation of an added forced oscillation in the next section. By inserting the solution of the equation of motion in y-direction (Eq. I.4.16) in equation I.4.18, the corresponding auto-correlation function will read

$$C_{yy}(\Delta t) = \left\langle \left(\left(y_0 e^{-t/\tau_r} + e^{-t/\tau_r} \int_0^t dt' \left[e^{t'/\tau_r} \frac{F_{r,y}(t')}{\zeta} \right] \right) \right. \right. \quad (\text{I.4.20}) \\ \left. \left. \left(y_0 e^{-\tau/\tau_r} + e^{-\tau/\tau_r} \int_0^\tau dt'' \left[e^{t''/\tau_r} \frac{F_{r,y}(t'')}{\zeta} \right] \right) \right) \right\rangle,$$

where $\tau = t + \Delta t$. The execution of the multiplication in brackets leads to four terms, one of which does not contain the Brownian random force at all, two of which contain it to the first power, and one contains the second power of it. The first term converges very fast towards zero and does not contribute to the correlation function, while the two first-power terms are eliminated by the averaging property of the correlation function (compare Eq. I.4.10). Only the term with the second power of the random force will lead to a non-zero contribution due to the property of the auto-correlation function (Eq.

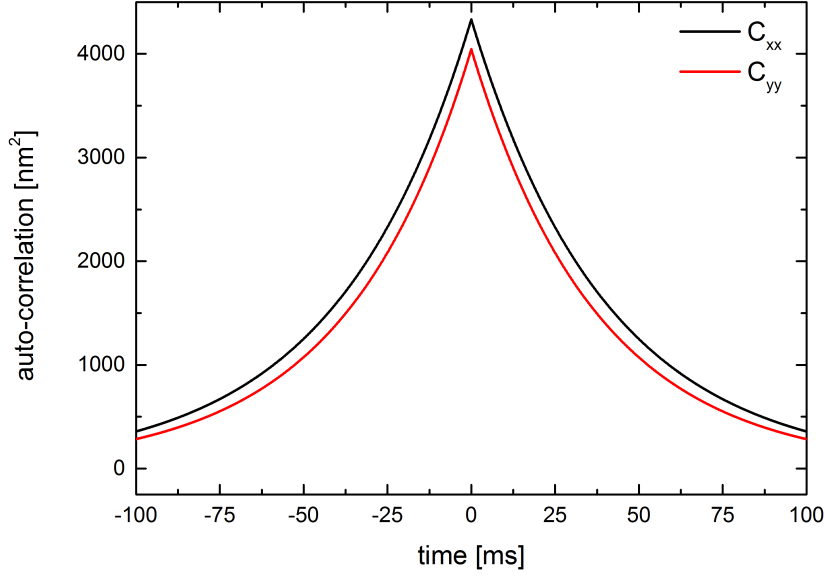


Figure I.4.6.: Plot of the analytical auto-correlation functions C_{xx} and C_{yy} of a colloid with a size of $4 \mu m$ confined in an optical trap with a stiffness of $1 \mu N/m$, according to the equations I.4.23 and I.4.24. The shear rate was chosen as $\dot{\gamma} = 10 \text{ 1/s}$. The data set corresponds to the one shown in figure I.4.7.

I.4.11)

$$C_{yy}(\Delta t) = \frac{2k_B T}{\zeta} e^{-(t+\tau)/\tau_r} \int_0^t dt' \int_0^\tau dt'' \left\{ e^{(t'+t'')/\tau_r} \delta(t' - t'') \right\}. \quad (\text{I.4.21})$$

Assuming $\tau \geq t$, the integral can be computed in the written order, resulting in

$$C_{yy}(\Delta t) = \frac{k_B T}{k} \left(e^{-(\tau-t)/\tau_r} - e^{-(\tau+t)/\tau_r} \right), \quad (\text{I.4.22})$$

which for large times ($t, \tau \gg \tau_r$) leaves only the first term

$$C_{yy}(\Delta t) = \underbrace{\frac{k_B T}{k}}_{A_{C_{yy}}} e^{-\Delta t/\tau_r}. \quad (\text{I.4.23})$$

As claimed before, this function does not depend on any absolute, but only the relative timescale Δt .

The computation of the auto-correlation function $C_{xx}(\Delta t)$ and the cross-correlation function $C_{xy}(\Delta t)$ is of higher complexity and will therefore be discussed in detail in the

I.4. Flows through Small Channels

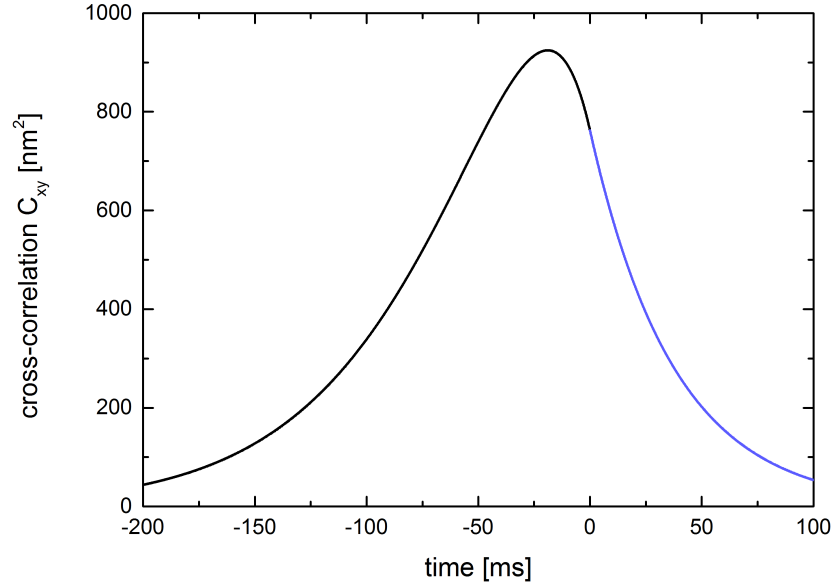


Figure I.4.7.: Plot of the analytical cross-correlation function C_{xy} of a colloid with a size of $4\ \mu\text{m}$ confined in an optical trap with a trap constant $k = 1\ \mu\text{N}/\text{m}$ according to the equations I.4.25 and I.4.26. Black and blue colors were chosen to distinguish the positive and negative half-plane. The shear rate was set to $\dot{\gamma} = 101/\text{s}$. The data set corresponds to the one shown in figure I.4.6.

appendix (Ch. B.1). They amount to

$$C_{xx}(\Delta t) = \underbrace{\frac{k_B T}{k}}_{A_{C_{xx}}} e^{-\Delta t/\tau_r} \left[1 + \frac{Wi^2}{2} \left(1 + \frac{\Delta t}{\tau_r} \right) \right], \quad (\text{I.4.24})$$

$$C_{xy}(\Delta t) = \underbrace{\frac{k_B T}{k} \frac{Wi}{2}}_{A_{C_{xy}}} e^{-\Delta t/\tau_r}, \quad (\text{I.4.25})$$

$$C_{yx}(\Delta t) = \underbrace{\frac{k_B T}{k} \frac{Wi}{2}}_{A_{C_{yx}}} e^{-\Delta t/\tau_r} \left(1 + 2 \frac{\Delta t}{\tau_r} \right). \quad (\text{I.4.26})$$

In these expressions, $Wi = \dot{\gamma}\tau_r$ is the Weissenberg number, a dimensionless parameter commonly used in the analysis of viscoelastic flows. Since in the case of an optical trap elastic properties are included by the purely elastic contribution of the trap itself, it is justified to use it as a means of description of the system here. It is also important to note that these formulas only represent the positive time axis. For C_{xx} and C_{yy} , the negative axis is gained by replacing all instances of Δt by $-\Delta t$. In case of the cross-correlation functions, C_{yx} represents C_{xy} at negative times, it is just mapped to the positive time axis as given by equation I.4.19.

I.4.3. Colloids in Linear Shear Flow without Forced Oscillations

As opposed to the quiescent case where $C_{xx}(\Delta t) = C_{yy}(\Delta t)$ and $C_{xy}(\Delta t) = C_{yx}(\Delta t) = 0$, the shear flow leads to a change in appearance of all correlation functions except for C_{yy} . The amplitude of C_{xx} is increased, albeit in a small manner, in the order of magnitude of Wi^2 and a linear contribution is added. A comparison of C_{yy} and C_{xx} is plotted in figure I.4.6. As mentioned before, C_{yy} represents the equilibrium case and only C_{xx} shows a slight increase due to the shearing. In the cross-correlation function C_{xy} , or C_{yx} respectively, as claimed by Bammert [18], a correlation peak appears close to $\tau = 0$ s (compare Fig. I.4.7), which is asymmetric since the system is constantly driven out of equilibrium. This is indicated by the color change of the curve at $\tau = 0$ s. The shear-free equilibrium case is regained when setting the shear rate or respectively Wi to zero.

I.4.4. Colloids in Linear Shear Flow Forced by an Oscillating Optical Trap

In this section, the system as presented in the past section will be expanded by adding a forced oscillation. Experimentally speaking, this will not be implemented by oscillating the position of the optical trap along the y -axis as indicated in figure I.4.8, but instead the whole microfluidic device will be moved in the opposite direction by applying an oscillation to the piezoelectric stage it rests upon (Ch. I.6.1). Still, the mathematical description of the system in equation I.4.14 will not change; the oscillation will be implemented in the former differential equation by assuming a non-constant position of the optical trap

$$y_{trap}(t) = B \sin(\omega t), \quad (\text{I.4.27})$$

where the amplitude B of the oscillation and its frequency ω can be freely chosen. In case of the experimental setup, the temporal resolution is of course limited, frequencies above $10,000 \text{ rad/s}$ or $1,500 \text{ Hz}$ cannot be sampled entirely. The structure of the solution given for the oscillation-free case in the past section as well as the solution procedure remain the same. Since the solution of the equation in oscillation direction changes, an

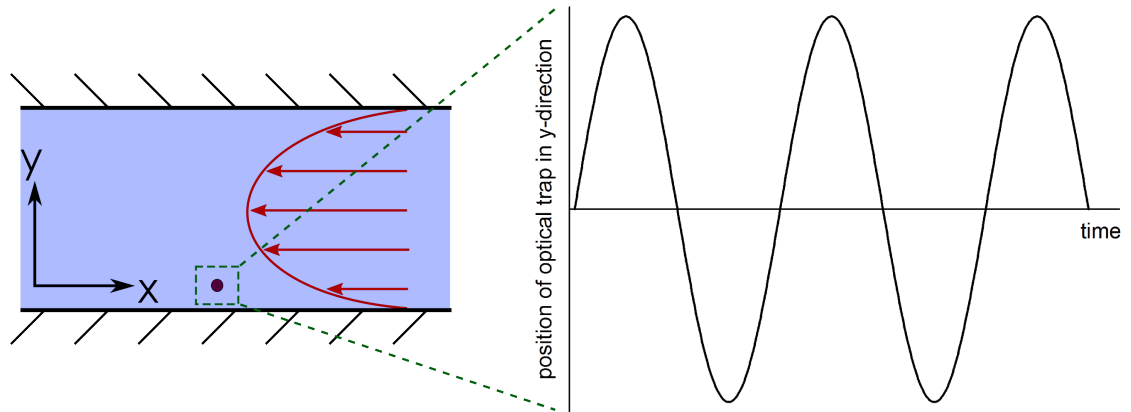


Figure I.4.8.: Sketch of a colloid which is driven to oscillations in y -direction in a microfluidic device with a rectangular cross-section as seen from above.

implicit change of the solution in x-direction will follow. They read

$$y(t) = \left(y_0 + \frac{B\alpha}{1 + \alpha^2} \right) e^{-t/\tau_r} + \frac{B}{1 + \alpha^2} (\sin(\omega t) - \alpha \cos(\omega t)) \quad (\text{I.4.28})$$

$$+ e^{-t/\tau_r} \int_0^t dt' \left[e^{t'/\tau_r} \frac{F_{r,y}(t')}{\zeta} \right],$$

$$x(t) = e^{-t/\tau_r} \left[x_0 + \dot{\gamma} y_0 t + \frac{B\alpha Wi}{1 + \alpha^2} \left(\frac{2}{1 + \alpha^2} + \frac{t}{\tau_r} \right) \right] \quad (\text{I.4.29})$$

$$+ \frac{B Wi}{(1 + \alpha^2)^2} [(1 - \alpha^2) \sin(\omega t) - 2\alpha \cos(\omega t)]$$

$$+ e^{-t/\tau_r} \left\{ \int_0^t dt' \left[e^{t'/\tau_r} \frac{F_{r,x}(t')}{\zeta} + \dot{\gamma} \int_0^{t'} dt'' \left(e^{t''/\tau_r} \frac{F_{r,y}(t'')}{\zeta} \right) \right] \right\}.$$

A new parameter is introduced here, the dimensionless frequency $\alpha = \omega\tau_r$, which will be used later for the representation of the data sets.

Correlation Functions in Linear Shear Flow Forced by an Oscillating Optical Trap

Similar to before, the focus of this section shall be set on the auto- and cross-correlation functions of motion. Major parts of the earlier computations concerning terms with integrals of stochastic functions can be kept, since they reappear here. Additional terms are caused by the oscillation functions. However, to ease the interpretation of the experimental results, which will be recorded in a reference frame centered at the position of the optical trap, the correlation-functions should be determined for this particular frame, too. While this causes no changes to the motion along the x-axis, in other words perpendicular to the oscillations, the change to the y-direction reads $\Delta y(t) = y(t) - y_{trap}(t)$. By following the same procedure leading to equation I.4.22, one reaches similar expressions as before. However, additional sine and cosine terms appear.

By expressing τ on the absolute timescale t as $\tau = t + \Delta t$, addition theorems [59] can be applied to recast these equations

$$\begin{aligned} \sin(\omega(t + \Delta t)) &= \sin(\omega t) \cos(\omega \Delta t) + \cos(\omega t) \sin(\omega \Delta t), \\ \cos(\omega(t + \Delta t)) &= \cos(\omega t) \cos(\omega \Delta t) - \sin(\omega t) \sin(\omega \Delta t). \end{aligned} \quad (\text{I.4.30})$$

In order to determine the average, the necessary integration is performed over exactly one oscillation period from 0 to $T_p = 2\pi/\omega$. In the definition of cross-correlation functions (Eq. I.4.18), each of the computed integrals has to be normalized by the length of the measurement. If only full oscillation periods are included in the integrations above, this leads to T_p canceling out. The result becomes independent of the duration of the

I.4. Flows through Small Channels

experiment. The result then reads

$$C_{yy}(\Delta t) = \underbrace{\frac{B^2 \alpha^2}{2(1 + \alpha^2)}}_{C_{yy,osc}} \cos(\omega \Delta t) + \frac{k_B T}{k} e^{-\Delta t / \tau_r}, \quad (\text{I.4.31})$$

$$C_{xx}(\Delta t) = \underbrace{\frac{B^2 Wi^2}{2(1 + \alpha^2)^2}}_{C_{xx,osc}} \cos(\omega \Delta t) + \frac{k_B T}{k} e^{-\Delta t / \tau_r} \left[1 + \frac{Wi^2}{2} \left(1 + \frac{\Delta t}{\tau_r} \right) \right], \quad (\text{I.4.32})$$

$$C_{xy}(\Delta t) = \frac{B^2 \alpha Wi}{2(1 + \alpha^2)^2} [\alpha \cos(\omega \Delta t) + \sin(\omega \Delta t)] + \frac{k_B T}{k} \frac{Wi}{2} e^{-\Delta t / \tau_r}, \quad (\text{I.4.33})$$

$$C_{yx}(\Delta t) = \frac{B^2 \alpha Wi}{2(1 + \alpha^2)^2} [\alpha \cos(\omega \Delta t) - \sin(\omega \Delta t)] + \frac{k_B T}{k} \frac{Wi}{2} e^{-\Delta t / \tau_r} \left(1 + 2 \frac{\Delta t}{\tau_r} \right). \quad (\text{I.4.34})$$

The cross-correlation functions still contain sine as well as cosine terms which can be combined to one single trigonometric function including a phase shift [59]

$$a \sin(\omega \Delta t) + b \cos(\omega \Delta t) = \begin{cases} \sqrt{a^2 + b^2} \sin(\omega \Delta t + \arctan(\frac{b}{a})), & \text{if } a > 0, \\ \sqrt{a^2 + b^2} \cos(\omega \Delta t - \arctan(\frac{a}{b})), & \text{if } b > 0. \end{cases} \quad (\text{I.4.35})$$

This yields the more compact expressions

$$C_{xy}(\Delta t) = \underbrace{\frac{B^2 \alpha Wi}{2(1 + \alpha^2)^{3/2}}}_{C_{xy,osc}} \cos \left[\omega \Delta t - \arctan \left(\frac{1}{\alpha} \right) \right] + \frac{k_B T}{k} \frac{Wi}{2} e^{-\Delta t / \tau_r}, \quad (\text{I.4.36})$$

$$C_{yx}(\Delta t) = \underbrace{\frac{B^2 \alpha Wi}{2(1 + \alpha^2)^{3/2}}}_{C_{yx,osc}} \cos \left[\omega \Delta t + \arctan \left(\frac{1}{\alpha} \right) \right] + \frac{k_B T}{k} \frac{Wi}{2} e^{-\Delta t / \tau_r} \left(1 + 2 \frac{\Delta t}{\tau_r} \right). \quad (\text{I.4.37})$$

Plots are presented in figures I.4.9 and I.4.10. The same parameters as in the past section were chosen (Fig. I.4.6 and I.4.7). While the characteristic features of all correlation functions from the oscillation-free case are still present, now there is an additional linear superposition of a continuous cosine function in each component. In case of the cross-correlation functions, this renders the correlation peak that was present before close to 0 s invisible. As far as the phase behavior is concerned, the oscillatory terms in both auto-correlation functions are identical to cosine functions, showing no additional phase shift. For the cross-correlation functions however, a frequency-dependent phase shift appears (Fig. I.4.11). It leads to the oscillatory component of C_{xy} to behave as a sine function at small frequencies, while it shifts continuously towards a cosine function with increasing frequency. These properties are mirrored by C_{yx} , which starts as a -sine function and shifts towards a cosine function. This leaves both cross-correlation functions continuous at all frequencies.

I.4.4. Colloids in Linear Shear Flow Forced by an Oscillating Optical Trap

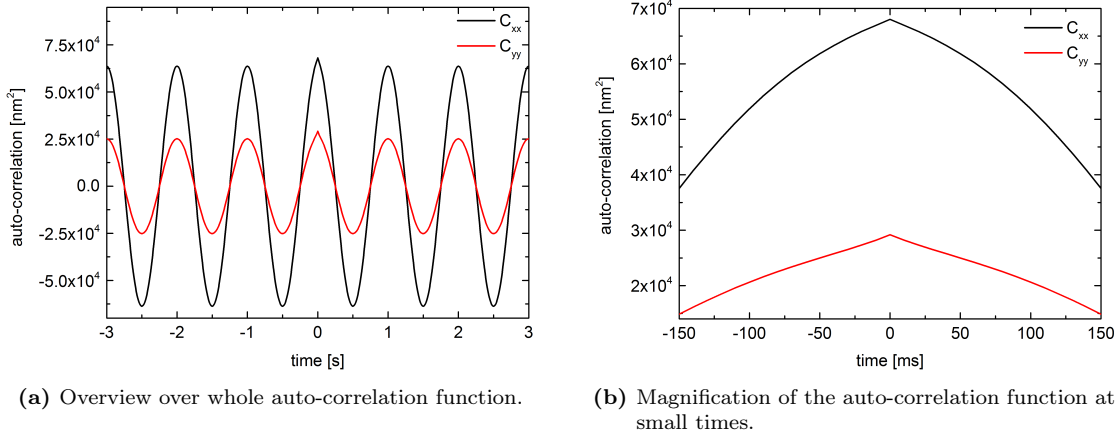


Figure I.4.9.: Sketch of the analytical auto-correlation functions C_{xx} and C_{yy} of a colloid with a size of $4\mu\text{m}$ in an optical trap of stiffness $1\mu\text{N/m}$ according to equations I.4.31 and I.4.32. The shear rate was set to $101/s$, the driving amplitude and frequency amount to $1\mu\text{m}$ and 1Hz respectively.

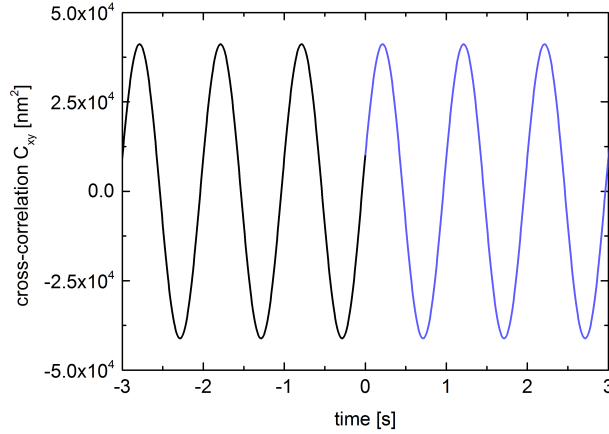


Figure I.4.10.: Sketch of the analytical cross-correlation functions C_{xy} (blue) and C_{yx} (black) of a colloid with a size of $4\mu\text{m}$ in an optical trap of stiffness $1\mu\text{N/m}$ according to equations I.4.36 and I.4.37. The shear rate was set to $101/s$, the driving amplitude and frequency amount to $1\mu\text{m}$ and 1Hz respectively. Colors are used to facilitate the distinction between times smaller and bigger than 0s .

Especially in regard to later experiments (Sect. I.6.4.2), the analytical expressions for the correlation functions will be very helpful. Besides the determination of the relaxation rate τ_r of the optical trap - hence information about the viscosity of the surrounding fluid as well as the trap stiffness - the average local Weissenberg number during the course of the experiment can be measured. This way, the local shear rate $\dot{\gamma}$ can be recovered as well. Since both C_{xx} and C_{xy} , or C_{yx} respectively, exhibit a dependence on Wi , both can be used for fitting purposes. However, due to external influences and noise, which can never be completely eliminated from the experimental data sets, and also due to the

I.4. Flows through Small Channels

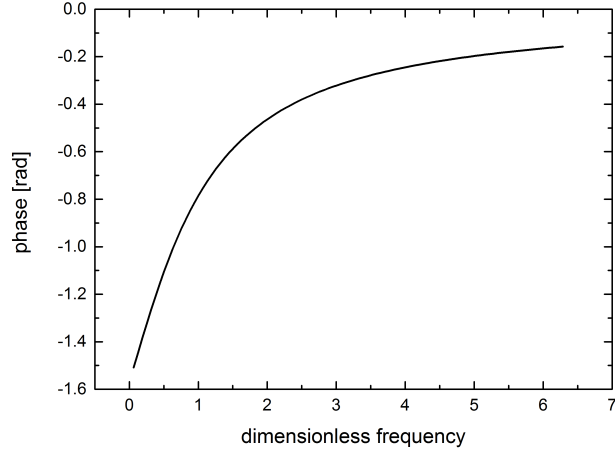


Figure I.4.11.: Dependence of the phase of the cross-correlation function C_{xy} on α . The phase $\delta = -\arctan(1/\alpha)$ taken from equation I.4.36 is plotted.

strong dependence on α , determining Wi by evaluating the amplitude of the oscillatory component of C_{xy} in equation I.4.36 will only give a very imprecise result. Instead, the correlation amplitudes of the auto-correlation functions $C_{yy,osc}$ and $C_{xx,osc}$ can be employed by computing their quotient

$$\frac{C_{xx,osc}}{C_{yy,osc}} = \frac{\dot{\gamma}^2}{\omega^2(1 + \alpha^2)}. \quad (\text{I.4.38})$$

Now, $\dot{\gamma}$ can be determined in a very easy manner, assuming that the correlation amplitudes were determined earlier and the oscillation frequency is known. Exact knowledge of α is still an experimental challenge, since besides the frequency ω also the relaxation rate τ_r has to be known. As soon as the optical trap is placed close to the walls of a microchannel, the presence of the wall may lead to an asymmetrical trap because it may deflect the laser beam on account of deviant refractive properties. This makes a reliable prediction of the trap stiffness k , and thus of τ_r , a delicate task. Hence, as mentioned earlier, only if the deviations of the experimentally determined trap stiffness k_x and k_y are weak, the experiment will be evaluated as successful.

I.4.5. Summary

In this chapter, the behavior of a fluid flowing through microchannels was discussed (Sect. I.4.1). By simplifying the Navier-Stokes to the Stokes equation which suffices for the description of the flow, an analytical expression for the flow profile could be derived (Eq. I.4.4). As can be seen in the three- and two-dimensional plots in figures I.4.1 and I.4.2, it can be described as a parabolic profile. Nonetheless, for a colloidal particle placed close to one of the side-walls, it locally shows a strong resemblance to a linear shear flow. This is of course only true if the bead size is much smaller than the width of the channel. Although a similar shear profile is present when moving along the z-axis through the channel, i. e. varying the height in the channel, its influence can be minimized by placing the particle close to the middle between the bottom and top wall of the channel. Due to the small cross-section of the microchannel, it could be shown that the flow conditions present during later experiments will always remain laminar as indicated by a Reynolds number of 0.004 (Eq. I.4.8). Additionally, techniques for the production of such microchannels were detailed (Sect. I.4.2).

The main focus of this chapter was the behavior of a colloid placed in a fluid bath. At first, the situation in the aforementioned shear flow without a forced oscillatory driving motion of the optical trap was reckoned (Sect. I.4.3). Contributions to the equation of motion were caused by friction forces, the restoring force of the optical trap, as well as the Brownian random force. Inertial forces could be neglected as already shown earlier by the means of the small Reynolds number. The Langevin equation of motion was solved (Eq.s I.4.16 and I.4.17) and the auto- and cross-correlation functions were determined (Eq.s I.4.23, I.4.24, I.4.25, and I.4.26). They were expanded in section I.4.4 by a forced oscillation applied to the position of the optical trap. We found that active driven oscillations offer the benefit of bigger bead displacements and hence a better signal-to-noise ratio. This entails an improvement of both the auto- and cross-correlation signals which eases the determination of the local shear rate. At the same time, bigger displacements of the confined bead result in the mapping of the shear gradient within a broader area. The resulting modified correlation functions (Eq.s I.4.31, I.4.32, I.4.36, and I.4.37) still contain the earlier case, but all of them additionally show the effects of the oscillatory perturbations. The shear flow present in the microchannel causes the motion in x- and y-direction to be coupled which is thus also true for their correlation functions. As a reference to later experiments in chapter I.6, these properties can be applied to determine the local shear rate $\dot{\gamma}$ experimentally (Eq. I.4.38).

I.5. Numerical Analysis

Following the analytical examination of colloids in a shear flow (Ch. I.4), a numerical inspection will complement it here. At first, the Langevin equations of motion will be recast in a form suitable for numerical treatment. This will happen in such a way that an iterative algorithm will result. A series of parameters will be utilized to determine the general behavior of the system. These parameters are: the stiffness of the optical trap k , the shear rate $\dot{\gamma}$, and in the oscillatory perturbed case also the oscillation amplitude B and frequency f . In section I.5.1, the analysis is started by considering the oscillation- and shear-free case which is then expanded by a linear shear flow in section I.5.2. The full system including the oscillating optical trap is treated in section I.5.3.

Before going into the discussion of the simulation results, the general ideas used to realize them will be sketched here. The starting point is the Langevin equations already introduced in the past chapter (Eq.s I.4.14 and I.4.15). These are the complete equations which may also contain the shear flow and forced oscillations of the trap. Before they can be used for numerical purposes, they have to be recast from their continuous form to an iterative expression. This is achieved by replacing the temporal derivative by a differential quotient $\partial x/\partial t \rightarrow \Delta x/\Delta t = (x_{i+1} - x_i)/\Delta t$ and the respective formulation for the y-direction. The simulation step is given by i . Each known position x_i is separated from the following one x_{i+1} by the time step Δt , so the absolute time can be expressed as $t_i = i \cdot \Delta t$. Special care has to be taken when treating the Brownian random force. Since it carries the properties of a Wiener-process, the following approximation can be applied [60]

$$F_{r,j}(i \cdot \Delta t) \approx \frac{F_n}{\sqrt{\Delta t}} n_{i,j}, \quad (\text{I.5.1})$$

where the normalization is given by $F_n = \sqrt{2k_B T \zeta}$ and $n_{i,j}$ is a Gaussian distributed random number which again depends on the simulation step i and the direction $j = x, y$. The full numerical equation then reads

$$x_{i+1} = x_i \left(1 - \frac{\Delta t}{\tau_r}\right) + \sqrt{\frac{2k_B T \Delta t}{\zeta}} n_{i,x} + \dot{\gamma} y_{i+1} \Delta t, \quad (\text{I.5.2})$$

$$y_{i+1} = y_i \left(1 - \frac{\Delta t}{\tau_r}\right) + \sqrt{\frac{2k_B T \Delta t}{\zeta}} n_{i,y} + \frac{B \Delta t}{\tau_r} \sin([i+1] \cdot \omega \Delta t). \quad (\text{I.5.3})$$

Since the equation of motion in x-direction is coupled to the solution in y-direction but

I.5. Numerical Analysis

not vice versa, the calculation can be easily completed by first computing simulation step i in the y -direction followed by the same step in the x -direction. The coupling of course is only present if a shear flow is assumed, otherwise it does not exist. Some position has to be assumed as a starting position which in all cases without loss of generality will be set to $(x_0, y_0) = (0, 0)$. Further fixed parameters are the temperature T , which was set to $293.2(5) K$, and the dynamical viscosity, for which the value of water will be used ($\eta = 1 \text{ mPa s}$). The size of the colloid was chosen to match the experimental value of $4 \mu\text{m}$. The simulation time step was set to coincide with the recording frequency of the high-speed camera in the experiments $\Delta t = 1/f_{rec} \approx 120 \text{ ms}$. In general, the duration of the simulated measurement was set to 32 s , which corresponds to roughly $250,000$ position values per direction. The simulation scripts as well as the fitting procedures were realized in the software Matlab (version R2011b, The MathWorks, Inc., Aachen, Germany), while the calculation of the auto- and cross-correlation functions was performed in a self-developed virtual instrument (VI) in the programming environment LabVIEW (versions 2010 to 2013, National Instruments, Austin, TX, United States of America). Details about this program are given in the appendix (Sect. C.1).

I.5.1. Colloids in a Quiescent Fluid

As a check of the algorithm, a quiescent fluid ($\dot{\gamma} = 0$) is simulated while no forced oscillations of the trap are present ($B = 0$). As mentioned in the introduction of chapter I.5, the trap remains fixed at $(0, 0)$ which is also assumed as the starting position of the confined colloid. Since its velocity is described by a Maxwell-Boltzmann distribution,

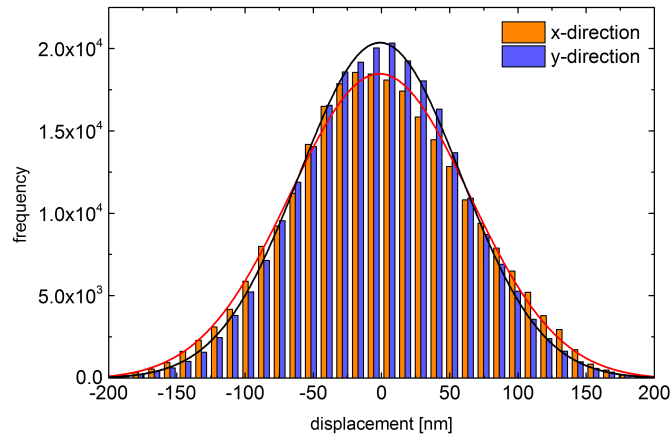


Figure I.5.1.: Histogram of the displacements of a colloid out of the center of an optical trap with a trap stiffness of $1 \mu\text{N}/\text{m}$. Data in x -/ y -direction is displayed in orange/blue with the fitting curve in red/black. The position of the center of the trap can be determined as $x_{trap} = -1, 4(7) \text{ nm}$ and $y_{trap} = -1, 1(2) \text{ nm}$ by fitting the datasets with a Gaussian distribution. Standard deviations amount to $\sigma_x = 65, 5(9) \text{ nm}$ and $\sigma_y = 59, 2(3) \text{ nm}$.

the displacements out of the center of the optical trap can be fitted with a Gaussian of which the standard deviation is given by [61]

$$\sigma = \sqrt{\frac{k_B T}{k}}. \quad (\text{I.5.4})$$

This follows from the equipartition-theorem, which claims that the energy by each degree of freedom amounts to $E_{th} = k_B T/2$. Thus, this holds also true for the potential energy $E_{pot} = k \langle x^2 \rangle / 2 = k \sigma^2 / 2$ of a colloid in an optical trap [62].

From the histogram of a simulation run with $k = 1 \mu N/m$ (Fig. I.5.1) can be seen that the deviation of the mean position of the colloid is just minor. It is caused by stochastic scattering, which can be proven by repeated simulation runs at the same parameter set. Averaging of their results can be used to reduce the effect. According to equation I.5.4, the trap stiffness can be determined as $k_x = 0,944(7) \mu N/m$ and $k_y = 1,154(3) \mu N/m$ (Fig. I.5.1). For a second simulation run with a trap that is ten times stiffer, $k_x = 10,11(1) \mu N/m$ and $k_y = 9,86(1) N/m$ result. In total, simulation results agree with theoretical predictions.

Concerning characteristic properties of the correlation functions, one would assume that the auto-correlation functions C_{xx} and C_{yy} show relaxation processes which are represented by a single-exponential decay function, while no cross-correlations are found, i. e. $C_{xy} = C_{yx} = 0$. This is directly apparent in figure I.5.2). Deviations from zero in the cross-correlation functions occur, but repeated simulation runs show that they are caused by numerical noise. Since the viscosity - and with it the coefficient of friction of

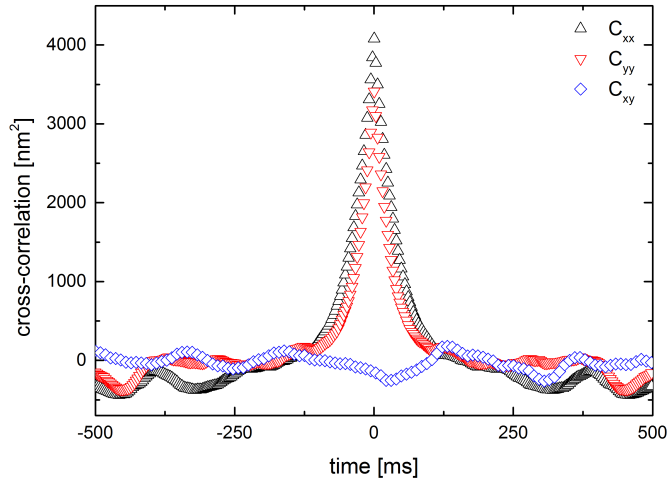


Figure I.5.2.: Auto- and cross-correlation functions of a simulated displacement of a colloid out of the center of an optical trap with a stiffness of $1 \mu N/m$. The used data sets correspond to the ones shown in the histograms in Fig. I.5.1. The relaxation rates taken from an exponential fit to the flanks (not shown) amount to $\tau_{r,x} = 45,9(2) ms$ and $\tau_{r,y} = 31,9(2) ms$.

I.5. Numerical Analysis

the system - are known, the identity $\tau_r = \zeta/k$ can be used to compute the trap stiffness. With just minor deviations as compared to the histogram method before, the fits give $k_x = 0,821(3) \mu N/m$ and $k_y = 1,180(6) \mu N/m$ in case of the first parameter set, and $k_x = 10,16(5) \mu N/m$ and $k_y = 9,82(3) \mu N/m$ in case of the second one, which is in good agreement with the chosen simulation parameters.

I.5.2. Colloids in Linear Shear Flow without Forced Oscillations

As opposed to the numerical results in the past section, a shear flow will now be added to the system. Depending on whether the colloid is placed in proximity to the upper or the lower wall, the shear rate will either have a positive or a negative sign which, thus, also has a respective effect on the correlation functions. This effect will only become visible in those correlation components, though, which are linked to the motion parallel to the flow direction. The shear flow leads to a small increase of the amplitude of C_{xx} (Eq. I.4.24), which cannot be extracted by fits to numerical or experimental data. Additionally, contributions by noise typically hide that effect.

The main point of interest in the context of shear flows is the arising non-zero cross-correlation function of perpendicular motion, in other words the functions C_{xy} and C_{yx} . This is shown for a numerical data set in figure I.5.3. As predicted by the analytical calculations in section I.4.3, a peak appears in C_{xy} at a time $\Delta t < 0$. Andreas Ziehl

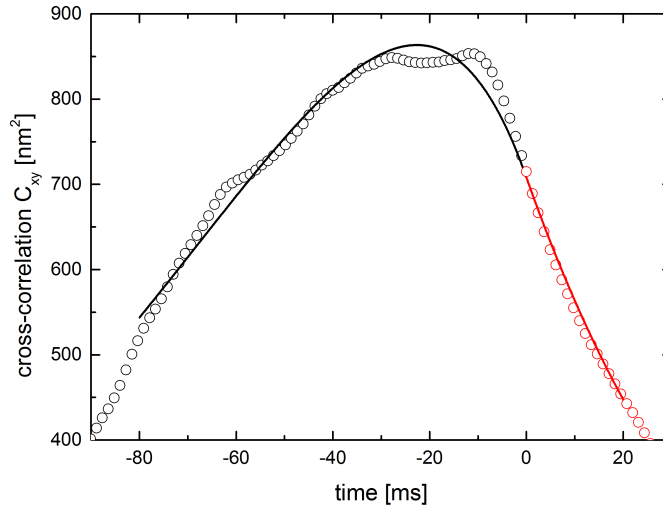


Figure I.5.3.: Cross-correlation function of a numerical dataset of the displacement of a colloid out of the center of an optical trap in a linear shear flow. The stiffness of the trap was chosen as $1 \mu N/m$, the shear rate as $101/s$. A fit with the analytical expression (Eq.s I.4.25 and I.4.26) is drawn as black and red lines.

I.5.3. Colloids in Linear Shear Flow Forced by an Oscillating Optical Trap

reported this effect in 2009 [5], however in his case the peak could be found at positive times while otherwise showing the exact same properties. This is due to the fact that the general definition of cross-correlation functions he used reads $C_{xy,Ziehl} = \langle x(t)y(0) \rangle$, while in the scope of this thesis both functions are switched by definition (Eq. I.4.18). According to the symmetry properties of correlation functions, this is identical to a time-reversal (Eq. I.4.19). Thus, the results found here can be considered in agreement with the results of Ziehl et al.

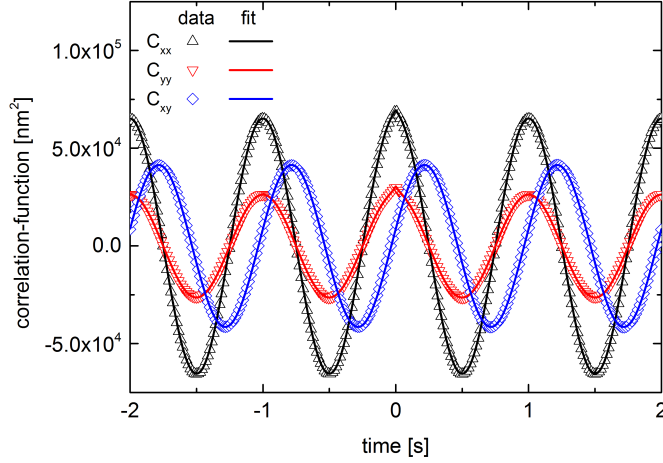
If for the example in figure I.5.3 the fitted correlation amplitude is compared to the analytical predictions (Eq.s I.4.25 and I.4.26), one finds a fitted value of $729(7) \text{ nm}^2$ as opposed to an analytical one of 762 nm^2 . Within the limits of numerical errors and statistical noise due to the Brownian processes, such deviations are to be expected. Errors from the fitting procedure have to be taken into account as well. The relaxation rate from the fit of $4.5(3) \text{ ms}$ matches the analytical prediction of 3.8 ms well, too.

I.5.3. Colloids in Linear Shear Flow Forced by an Oscillating Optical Trap

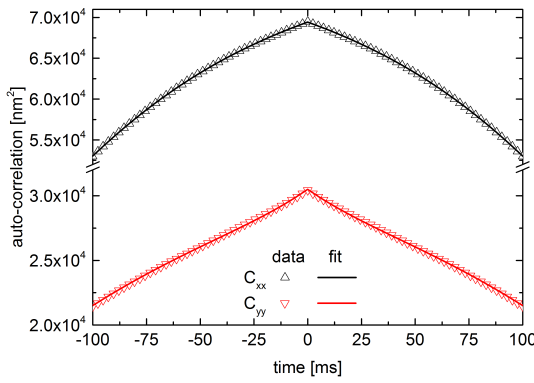
In this section, the full expressions for the influence of an oscillating optical trap derived in section I.4.4 shall be probed in terms of their validity. The main focus will be centered around the oscillatory contributions since, according to the analytical calculations, the terms from the stochastic integrals remain unchanged. Said oscillatory contributions depend on the driving amplitude B , the driving frequency ω or respectively the dimensionless frequency α , and also the applied shear rate $\dot{\gamma}$ or respectively the Weissenberg number Wi (Eq.s I.4.31, I.4.32, I.4.36, and I.4.37). A series of simulation runs was performed to check the dependence of the numerical results on these parameters.

As an exemplary result, the correlation functions of one of the simulation runs are displayed in figure I.5.4. As mentioned before, each of the auto- and cross-correlation functions contains oscillatory contributions (Fig. I.5.4a). This is due to the shear coupling. Still, the previously discussed exponential relaxation processes (Sect.s I.4.3 and I.5.2) are present and can be detected in close proximity to $\Delta t = 0$ (Fig. I.5.4b). The same is true for the cross-correlation function, however, the asymmetric correlation peak is so small as compared to the oscillations, that it becomes a difficult task to identify it. By subtracting the oscillatory contributions, it can be made visible again as shown in figure I.5.4c. An additional property of shear flows in rectangular channels is that a bead placed close to the channel walls will experience a non-zero flow velocity which leads to a shift of its equilibrium position away from the center of the optical trap. This becomes apparent in figure I.5.4c as well, since the correlation peak does not relax back to zero but towards a smaller value. One must also take into account that, due to the influence of Brownian noise, the oscillations can never be eliminated completely by the subtraction

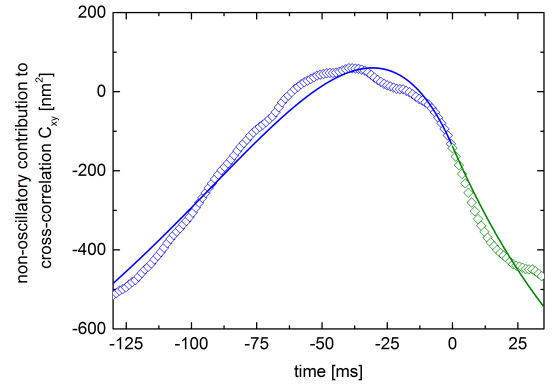
I.5. Numerical Analysis



(a) Overview of C_{xx} , C_{yy} , and C_{xy} . Fits with the analytical expressions are displayed as well.



(b) Zoom of the auto-correlation functions close to $\Delta t = 0$. The contribution of the exponential terms becomes apparent.



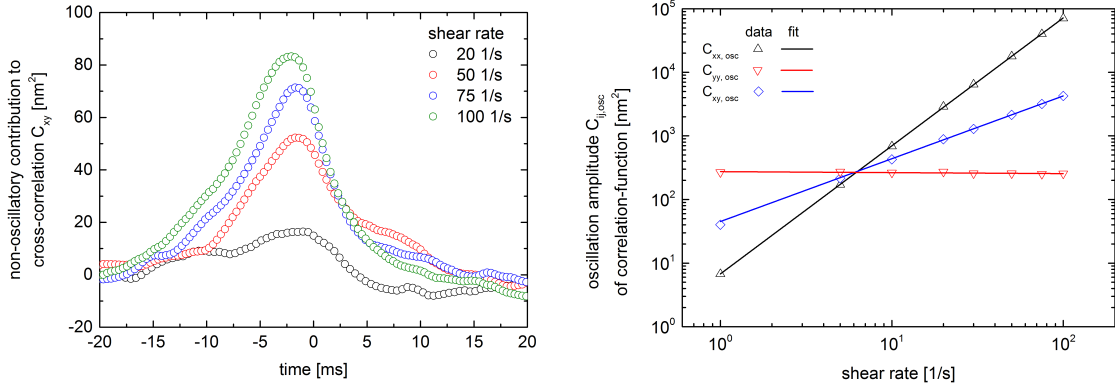
(c) Zoom of C_{xy} close to $\Delta t = 0$ after subtraction of the fitted oscillatory contribution. The subtraction also enables an accurate fit of the remaining shear-coupled terms in equation I.4.36. Symbol and line colors were chosen to point out C_{xy} at negative and positive times.

Figure I.5.4.: Correlation functions C_{xx} , C_{yy} , and C_{xy} for a colloid simulated in linear shear flow forced by an oscillating optical trap. The functions are dominated by the contributions of the oscillating terms. The trap stiffness amounts to $1 \mu\text{N}/\text{m}$ while a shear rate of $10 \text{ 1}/\text{s}$ was chosen. The trap oscillates at an amplitude of $1 \mu\text{m}$ and a frequency of 1 Hz .

since it is almost impossible to compute or fit their exact amplitudes. A good agreement is found in comparing the analytically predicted values with the correlation functions from simulations.

A whole series of simulations at different shear rates with an optical trap that is ten times stiffer is drawn in figure I.5.5a to visualize the development of the cross-correlation function C_{xy} after subtraction of the contributions through oscillations. The baseline of the functions was shifted to 0 nm^2 to facilitate a comparison. As indicated by equation

I.5.3. Colloids in Linear Shear Flow Forced by an Oscillating Optical Trap



(a) Zoom of C_{xy} close to $\Delta t = 0$ after the removal of the oscillatory contribution. A continuous increase of the height of the peak with increasing shear rate becomes apparent, scaling linearly with the Weissenberg number.

(b) Dependence of the oscillation amplitudes of the auto- and cross-correlation functions on the shear rate. The results from fits show that $C_{xx,osc} \propto \dot{\gamma}^{2.03(1)}$, $C_{yy,osc} \propto -0.02(1)\dot{\gamma}$, and $C_{xy,osc} \propto 0.99(1)\dot{\gamma}$.

Figure I.5.5.: Dependence of the height of the correlation peak in C_{xy} and of the oscillation amplitudes of the correlation functions on the shear rate. Simulation runs for shear rates between 11/s and 100 1/s were performed while all other parameters remained unmodified ($B = 1 \mu\text{m}$, $f = 1 \text{ Hz}$, $k = 10 \mu\text{N/m}$). The corresponding data sets can be found in table D.1.

I.4.36, the correlation peak increases in height linearly with the shear rate or respectively the Weissenberg number, while its width does not change. This effect is clearly visible at shear rates higher than 50 1/s, while at lower values the peak nearly disappears in the background noise. Assuming that a similar effect might appear when evaluating experimental results, it hints towards high shear rates, i. e. $\dot{\gamma} \geq 20 \text{ 1/s}$, being necessary at a trap stiffness of $10 \mu\text{N/m}$. The quality of the peaks at low shear rates can be improved by choosing an increased number of simulated data points or in other words a longer measurement length (i. e. 64 s) at the same recording frequency. In this context, the convergence of the algorithm was checked as well by an increased measurement length and an increased recording frequency. In both cases, the algorithm produced stable results with a comparable functional form and height of the peaks in C_{xy} .

When looking at the oscillatory amplitudes of the auto- and cross-correlation functions instead (Eq.s I.4.31, I.4.32, and I.4.36), one would assume that $C_{yy,osc}$ is independent of the shear rate, $C_{xx,osc}$ is proportional to its squared value, and $C_{xy,osc}$ increases linearly with it. Fits to the oscillatory contributions to correlation functions from the same data sets as above give parameter values as displayed in figure I.5.5b (compare also Tab. D.1), and prove that the expected behavior occurs indeed.

As mentioned in the introduction to this section, not only the shear rate but also the frequency as well as the amplitude of the driving oscillation shall be varied. A change in frequency will automatically cause a change of α , which will have its repercussions on

I.5. Numerical Analysis

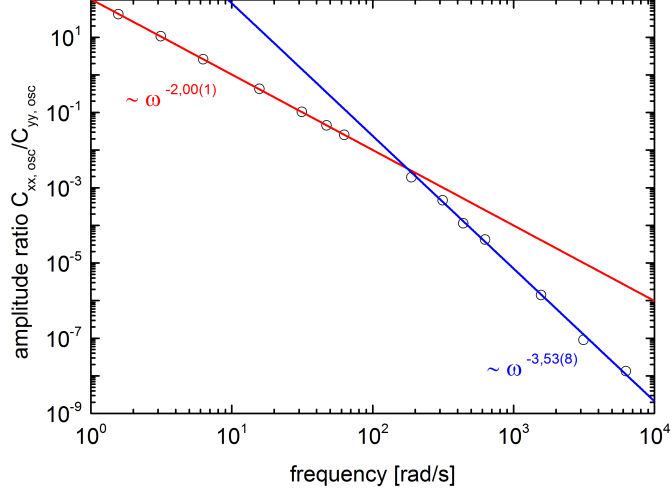


Figure I.5.6.: Dependence of the relative correlation amplitude $C_{xx,osc}/C_{yy,osc}$ on the oscillation frequency of the optical trap. A parameter set $B = 1 \mu m$, $k = 10 \mu N/m$, and $\dot{\gamma} = 101/s$ was chosen for all simulations. A fit of the values up to $60 rad/s$ to a power law gives $C_{xx,osc}/C_{yy,osc} \propto \omega^{2.00(1)}$, for frequencies higher than $300 rad/s$ the fit gives $C_{xx,osc}/C_{yy,osc} \propto \omega^{3.53(8)}$. The crossover of both fits happens at about $185 rad/s$. The corresponding data sets are provided in table D.2 in the appendix.

all of the correlation functions. These changes encompass not only the amplitude of the oscillatory terms $C_{ij,osc}$, but also the phase behavior of C_{xy} . To visualize this, a series of simulations under variation of the driving frequency were performed. With regard to later experiments, it must be remarked that the trap stiffness for frequencies higher than $60 rad/s$ is simply not high enough to successfully confine a particle in the experimental setup in a shear flow with $\dot{\gamma} \geq 101/s$. In that case, the stiffness needs to be further increased, which will lead to a disappearing of all special features of the correlation functions, since their amplitudes decrease under these conditions. Experimentally speaking, only a frequency range up to $\approx 60 rad/s$ is accessible in this respect.

The dependence of the correlation amplitudes on the driving frequency is presented in the form of the auto-correlation amplitude ratio $C_{xx,osc}/C_{yy,osc}$ (Fig. I.5.6). According to equation I.4.38, for small frequencies $\omega \ll 1/\tau_r$, or in other words $\alpha \ll 1$, the amplitude ratio decreases proportionally to ω^{-2} , while for the opposite case $\omega \gg 1/\tau_r$ it will decrease proportionally to ω^{-4} . If the results from simulations are compared to this prediction, the behavior for small frequencies (up to $60 rad/s$) is recovered with a very high precision ($C_{xx,osc}/C_{yy,osc} \propto \omega^{-2.00(1)}$), while at higher frequencies (above $300 rad/s$), there are deviations from the predicted power law ($C_{xx,osc}/C_{yy,osc} \propto \omega^{-3.53(8)}$). The change in power occurs at about $185 rad/s$, which is given by the cross-over frequency of the red and blue curve corresponding to the low and high frequency power law fits (Fig. I.5.6).

I.5.3. Colloids in Linear Shear Flow Forced by an Oscillating Optical Trap

The critical transition frequency can also be computed by

$$\omega_{crit} = \frac{1}{\tau_r} = 265 \frac{rad}{s}. \quad (I.5.5)$$

The deviation between the analytic value and the value from the crossover is due to the imprecision when graphically determining the frequency value in the log-log-plot. The value in equation I.5.5 can be considered as exact. The relaxation rate τ_r needs to be determined by the quotient of the coefficient of friction and the trap stiffness present in the system. In the experimental context, the assumption of moving in the low-frequency range is justified, which enables the application of a simplified calculation of the shear rate following from equation I.4.38

$$\lim_{\alpha \ll 1} \frac{C_{xx,osc}}{C_{yy,osc}} \approx \frac{\dot{\gamma}^2}{\omega^2}. \quad (I.5.6)$$

A further reflection will concern the development of the phase of the oscillatory term in C_{xy} in respect to the driving frequency. For the remainder of this part, only the phase of C_{xy} will be discussed since the oscillatory part of C_{yx} is just given as the time-reversed function and thus, the relationship of both phases can be expressed as (compare Eq.s I.4.36 and I.4.37)

$$\delta(C_{xy,osc}) = -\delta(C_{yx,osc}) = -\arctan\left(\frac{1}{\alpha}\right). \quad (I.5.7)$$

The phase behavior is exclusively determined by the dimensionless frequency, composed of the product of the driving frequency ω with the relaxation rate τ_r . Since for all later experiments, water is always chosen as the fluid in which the colloids are immersed and since the colloid size was always the same at $4\mu m$, the relaxation rate is solely determined by the strength of the optical trap. The phase is completely uninfluenced by flow parameters like the shear rate. Figure I.5.7 shows that the phase behavior from numerical simulations agrees indeed with theoretical predictions as displayed earlier in figure I.4.11. For the relaxation rate determined by fits, the analytical curve can be calculated. It is also displayed in figure I.5.7 as a red line. Analytical predictions and fitting results from numerical data agree to a very high degree.

I.5. Numerical Analysis

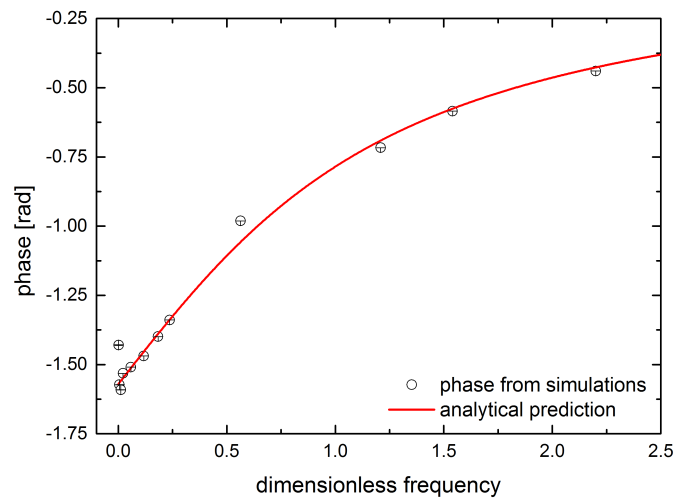


Figure I.5.7.: Phase behavior of C_{xy} as a function of the dimensionless frequency. The relaxation rate τ_r remains fixed by choosing a constant trap stiffness $10 \mu N/m$ for all simulation runs. The corresponding data sets are displayed in table D.2 in the appendix.

I.5.4. Summary

In this chapter, the system of a colloid confined in the focal region of an optical trap was exposed to a variety of flow situations in numerical simulations. For this purpose, the analytical framework developed in chapter I.4 was recast into a form suitable for an iterative numerical algorithm (Eq.s I.5.2 and I.5.3). In section I.5.1, as a trial run, a quiescent flow situation was assumed, meaning that there existed no shear flow and also no driving force was applied. Out of this, symmetrical Gaussian-like position distributions resulted. These could be used as a means to calibrate the strength of the optical trap or in other words the trap stiffness k . An almost symmetric trap could be recovered by this procedure, where deviations from the ideal case were caused by the noise-like nature of Brownian motion. From the same data sets, the equilibrium auto- and cross-correlation functions could be determined (Fig. I.5.2). A further check was performed in section I.5.2 by applying a shear flow to the bead and comparing the arising situation with the equilibrium case from before. While there was no directly apparent change as far as the auto-correlation functions C_{xx} and C_{yy} are concerned, there was a very clear alteration of the cross-correlation function (Fig. I.5.3). As already found by A. Ziehl [5] and J. Bammert [18], a correlation peak appears in C_{xy} close to, but not exactly centered at, time zero. It is caused by the short delay the fluctuating bead needs to adapt to the faster or slower flow slightly above or below the position of the optical trap in y-direction in the assumed shear flow. The algorithm seems well-suited for the task of simulating colloids in shear flows.

In section I.5.3, a forced oscillatory motion of the center of the optical trap was added to the system as already done before during the analytical calculations in section I.4.4. All the properties of the sheared case without forced oscillations were still present, however, each correlation function showed an additive oscillatory term just as predicted by the analytical framework. By analyzing the dependence of the oscillatory correlation amplitudes $C_{xx,osc}$, $C_{yy,osc}$, and $C_{xy,osc}$ on the shear rate as well as the amplitude ratio $C_{xx,osc}/C_{yy,osc}$ and the phase behavior $\delta(C_{xy,osc})$ on the driving frequency, a good agreement with the analytical predictions could be found.

The analytical expressions found in chapter I.4 and the numerical simulations discussed in this chapter will be of help in understanding and interpreting the experiments conducted in a setup of optical tweezers (Ch. I.6). Not only a qualitative, but also a quantitative agreement between the three will be checked in order to confirm certain parameters system-internal like the local shear rate.

I.6. Experimental Study

The current chapter is related to all the information linked to the conduction of experiments with the setup of optical tweezers present in the Wagner group in the physical department of Saarland University in Saarbrücken, Germany. Before the performed experiments will be discussed, in the first section of this chapter (Sect. I.6.1) the composition of the setup is described. This includes an in-depth discussion of the changes the setup underwent since its construction by Andreas Ziehl [4, 5]. In the second section (Sect. I.6.3), a number of steps necessary for the calibration of the experimental setup are detailed. A description of the types of measurements conducted in the scope of this part of the thesis, as well as their results are presented in section I.6.4. Their discussion in context with analytical and numerical results from earlier chapters (Ch.s I.4 and I.5) will follow in chapter I.7.

I.6.1. Experimental Setup

The setup of optical tweezers that was utilized in this thesis to perform experiments with colloids in a linear shear flow (pt. I) as well as microrheology on mucus (pt. II) will be described in this section.

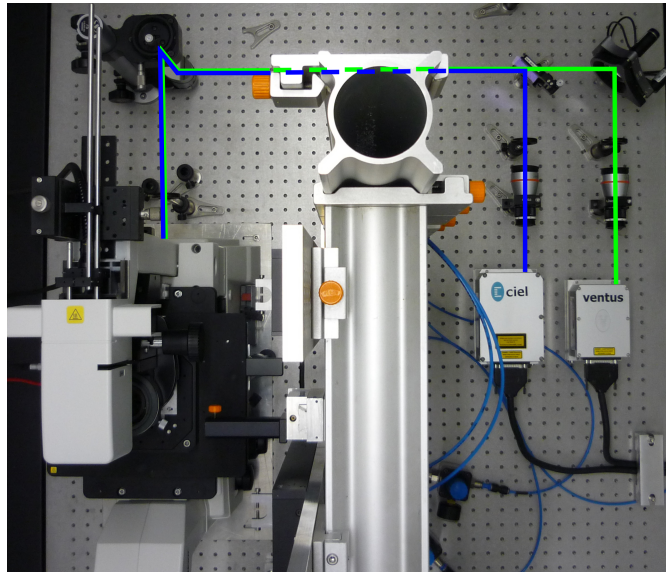
It can be roughly divided into three constituents: the guidance system of the laser beam(s), the microscope including the visualization technology, and the flow control for the microchannels. While the flow control only plays a role in the first part and not for microrheology, the other two components of the setup are important for any experiment performed in it. Respectively, this section will be divided into three subsections giving details about each of these parts, and also pointing out differences as compared to the setup used before by Andreas Ziehl.

I.6.1.1. Guidance System of the Laser Beams

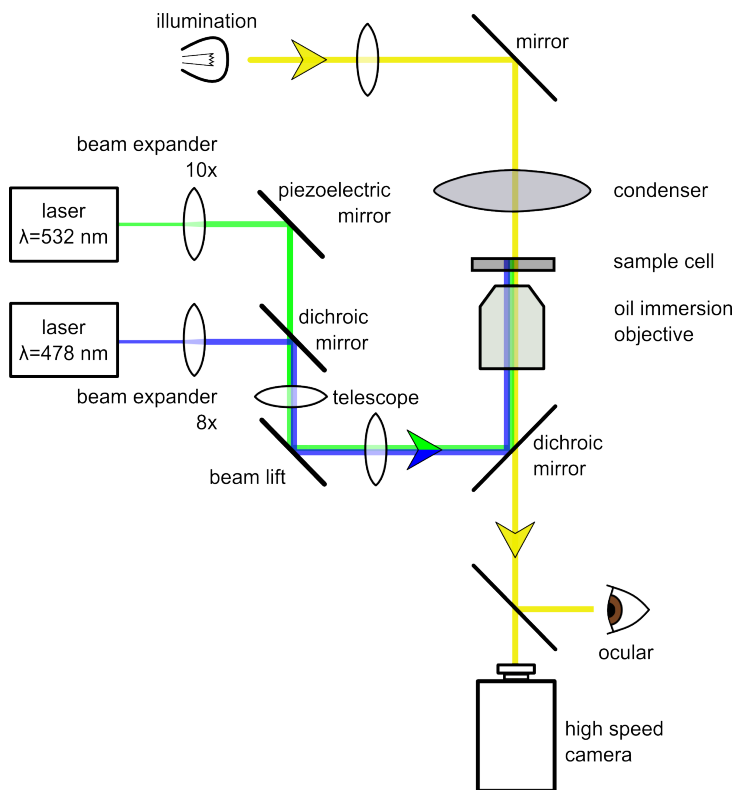
Hereinafter, the beam path of both available laser beams in the setup will be described starting at the laser sources until the beams arrive in the sample cell of the microscope. This path is also indicated in figure I.6.1 in the shape of a photograph as well as a sketch.

As already mentioned in chapter I.3, the central element of such a setup is a strongly focused laser beam. The force balance of the scattering and the gradient force exerted on a small object, i. e. a colloid, determines if a stable optical trap can be formed or not. Since the gradient force gains the most strength relative to the scattering force if the laser beam has the smallest intensity at its center while having a high intensity near its outer radius, a transverse electromagnetic TEM_{01^*} mode beam would be ideal. Its profile reminds of the cross-section of a doughnut - hence its name doughnut mode - but it also comes with a share of disadvantages. The biggest of these is the construction of the laser necessary to emit it. This is the reason why in most setups of optical tweezers Gaussian-shaped beams of the TEM_{00} mode are used. On the first glance, their beam profile is disadvantageous for efficient trapping since the maximum intensity can be found in the center of the beam. By overfilling the back aperture of the microscope objective in the setup [63], the outer rays of the beam gain more intensity in comparison to the center beams which makes strong traps possible without increasing price and complexity of the setup. Thus, in case of the setup used in scope of this thesis, two lasers are available, both of which are diode-pumped solid-state lasers. The first one operates at 532 nm (Ventus LP, Laser Quantum Ltd., Stockport, Cheshire, United Kingdom), the second one at 473 nm (Ciel, Laser Quantum Ltd., Stockport, Cheshire, United Kingdom). In both cases, the emitted spatial mode is a transversal electromagnetic mode of the TEM_{00} type, which shows a two-dimensional Gaussian intensity distribution in the plane perpendicular to the propagation direction of the beam. Both lasers produce beams of high stability of less than $2\% rms$ for the Ventus model and, respectively, less than $3\% rms$ for the Ciel model. The beam divergences are small with values of 0.8 mrad and 0.6 mrad . These properties ensure the generation of stable optical traps of high homogeneity. However, since the diameters of both beams are not equal (Ventus: $d_b = 1\text{ mm}$, Ciel: $d_b = 1.4\text{ mm}$), beam expanders with different expansion factors have to be used to ensure equally sized traps. Additionally, they take care of the required overfilling of the back aperture of the microscope objective.

Since the knowledge of the laser power is important when determining the strength of an optical trap, the stability of the emission and also the dependence of the emitted power on the applied current was measured using a power-meter (Fig. I.6.2). Within the precision limits of the sensor, which were given by the manufacturer as $\pm 100\ \mu W$, none of the lasers showed significant fluctuations. As the figure shows, the power against current dependence is not a linear one, making a calibration of the trap stiffnesses necessary before each experiment. Details about the calibration options and procedures are given



(a) Photograph of the setup of optical tweezers as seen from above.



(b) Schematic sketch of the full beam path of the lasers as well as the illumination source.

Figure I.6.1.: Illustration of the setup of optical tweezers.

I.6. Experimental Study

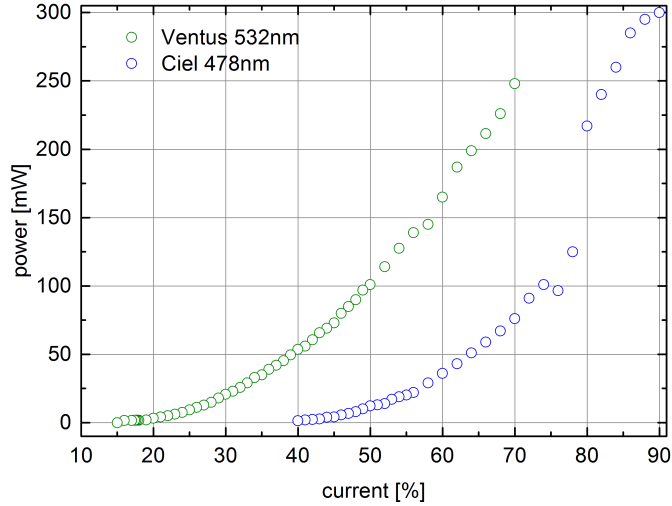


Figure I.6.2.: Power of each of the laser beams measured by a power meter. The sensor was placed in the beam path just behind the source. The corresponding data sets are presented in tables D.3 and D.4 in the appendix. Due to thermal noise in the surroundings of the sensor, the data has a precision of $\pm 100 \mu W$.

later in this chapter (Sect. I.6.3). Additionally, as a means to check the quality of the beam profiles, they were visualized on the chip of a CCD camera after a reduction of their intensities using both an OD2 and an OD4 filter¹.

Due to the different beam diameters, as mentioned, two beam expanders with corresponding optical properties had to be set up in the beam paths. As indicated in figure I.6.1, they were placed about 10 cm behind the aperture of the laser. For the 532 nm beam a 10x-expander (art.-no. G038-670-000, Linos Photonics GmbH & Co. KG, Göttingen, Germany) was used, while for the 473 nm beam a 8x-expander (art.-no. G038-678-000, Linos Photonics GmbH & Co. KG, Göttingen, Germany) was chosen.

Although this possibility was not used in the experiments presented here, the setup is designed in a way that allows both optical traps to be used simultaneously. This leads to the necessity of superimposing both beams into one. For this purpose, the 532 nm beam is first redirected by an angle of 90° using a piezoelectric mirror and then combined with the 473 nm beam using a dichroic mirror. The piezoelectric mirror can be pitched and yawed by two ultra-high resolution rotational actuators (PZA12, Newport Corporation, Irvine, CA, United States of America), which when combined with a mirror mount (U200-G, Newport Corporation, Irvine, CA, United States of America) allow angular steps in the order of magnitude of μ -radians (sensitivity according to manufacturer: 30 nm). This enables a very exact control of the relative trap positioning. The dichroic mirror on the

¹“OD” is an abbreviation for optical density and gives an indication of the intensity reduction expressed on a logarithmic scale. An optical density of 2 represents an intensity reduction by a factor of 10^2 , an optical density of 4 represents a reduction by a factor of 10^4 .

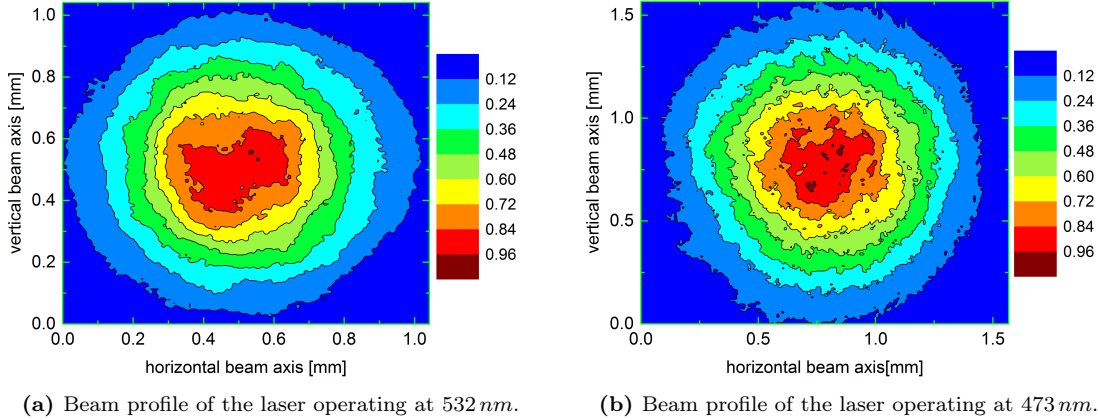


Figure I.6.3.: Beam profiles of the two lasers utilized in the setup of optical tweezers. The slight asymmetry of both profiles originates from the surface normal of the camera chip being tilted against the propagation direction of the beams. The intensities are expressed relative to the highest occurring intensity in each profile.

other hand is chosen in such a way, that a near-perfect reflection of the 473 nm beam is possible while the 532 nm beam transmits to a high degree ($\approx 94\%$). The characteristic line of this filter (505DCXR, AHF analysentechnik AG, Tübingen, Germany) is drawn in figure I.6.4 with black circle symbols.

In the earlier realization of the setup as built by Andreas Ziehl, the lasers passed a beam lift at this point in order to allow for a coupling of the combined beam into the back port of the microscope. In addition, a telescope is added to the beam path. Its first lens is positioned in front of the beam lift, the second one is placed behind it. Both lenses share identical optical properties (LA1832-A, Thorlabs GmbH, Dachau/Munich, Germany) and are covered with an anti-reflection coating to prevent power loss of the laser beams. The setup is augmented with the telescope in order to decrease divergence effects of the beams and to fine-tune the positioning of the focal plane of the lasers after passing the microscope objective or, in other words, the distance of the optical traps themselves.

At this point, the laser beams enter the back port of the inverted microscope (Eclipse TE2000-S, Nikon GmbH, Düsseldorf, Germany). Besides the lasers, this microscope is the second central device of the setup. Here, an inverted microscope is chosen since it allows the manipulation of confined objects in the traps while at the same time enabling their visualization using light directed inversely to the lasers. More information about it will follow in the next section. However, a few more elements involving the guidance of the laser beams have not been mentioned so far and shall be discussed first. After entering the microscope, the beams have to be redirected upwards in order to enter the objective from below and finally reach the sample cell. A second dichroic filter (565DCXR, AHF analysentechnik AG, Tübingen, Germany) is installed inside a filter block to fulfill that

I.6. Experimental Study

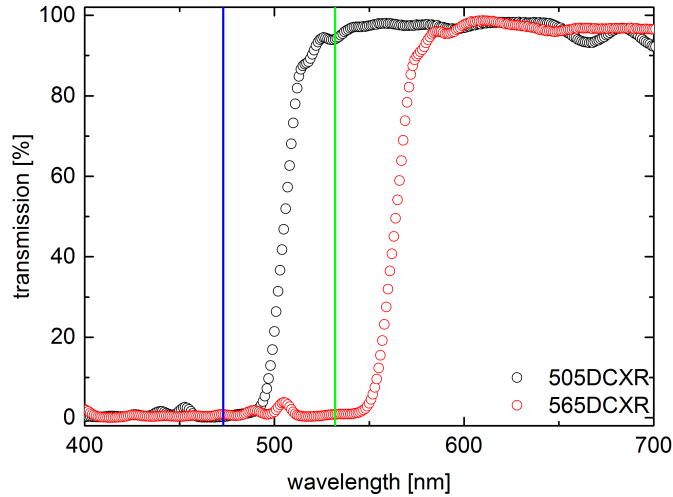


Figure I.6.4.: Characteristic transmission line for both of the dichroic mirrors utilized in the setup of optical tweezers. In addition to the filter lines, the two characteristic wavelengths of the utilized lasers are drawn as accordingly colored lines at 532 nm and 473 nm . The data sets were provided by courtesy of the manufacturer AHF analysentechnik AG.

role. Its properties are chosen in such a way, that contrary to the properties of the dichroite mentioned before, both laser wavelengths are reflected to a high degree ($> 99\%$, compare the red open circles in Fig. I.6.4). This filter enables the beams to reach the sample cell after passing the objective while, at the same time, allowing the illumination light to reach the camera.

I.6.1.2. Microscope, Visualization, & Signal-Synchronization System

In this section, the focus will be laid on the microscope and its directly related systems. As already mentioned before, an inverted microscope by Nikon is chosen for the setup of optical tweezers in Saarbrücken (Eclipse TE2000-S, Nikon GmbH, Düsseldorf, Germany). Especially in context with such a setup, inverted microscopes have huge advantages. They allow to send laser beams associated with optical tweezers into a sample cell and thus to confine and manipulate colloids. At the same time, the traps are not fixed and can be moved within the sample, giving a high degree of mobility. This is realized by realigning the positions of the optical traps, however, a much easier method is the relative displacement through a mechanical translation of the microscope stage. Since the visualization of the displacements of colloids is of crucial importance in this thesis, this is a necessary prerequisite to the setup as well. Due to its alignment, it is possible to orient the beam path of illumination light in reverse to the laser beam path, and thus record the motion of colloids with a suitable recording device. Details will be mentioned later in this section.

Vibrations, particularly the avoidance of external vibrations, play a very important

role in any setup of optical tweezers. Since these setups aim at recording Brownian motion, which is a noise-based process, any additional external noise makes the interpretation of measurement hard or even close to impossible. Thus, a vibration dampening table by Halcyonics named Active Workstation 1100 (Halcyonics GmbH, Göttingen, Germany) is used. Only those devices and elements which are needed close by for the conduction of experiments are placed on top of that table. All elements that cause additional vibrations like the illumination source, which is actively cooled by a fan, are removed from the table and situated below or next to the table on stands instead. Also, a laboratory in the cellar of the building is chosen to prevent strong influences by low-frequency building vibrations, which cannot be efficiently removed by the dampening table.

As noted above, displacements of the field of view and, linked to that, of the positions of the traps can be performed by mechanically moving the microscope stage. However, the resolution of such displacements is limited. An improvement can be administered by mounting a piezoelectric stage on top of the mechanical one. For this purpose, a stage by PI is chosen (P-517.2CD, Physik Instrumente (PI) GmbH & Co. KG, Karlsruhe, Germany) in combination with two controllers (E-665.CR, Physik Instrumente (PI) GmbH & Co. KG, Karlsruhe, Germany), one for each translation direction. With a travel path of up to $200\ \mu\text{m}$ at a spatial resolution of $2\ \text{nm}$, a very precise positioning of the traps can be achieved. Since in this part of the dissertation, oscillatory motion will play an important role, the linearity error of 0.03% and the repeat accuracy of $\pm 10\ \text{nm}$ are noteworthy as well. According to the voltage calibration of the manufacturer, displacements Δx_i are linked to applied input voltages U by

$$\Delta x_i \approx 10.0012 \frac{\mu\text{m}}{\text{V}} \cdot U, \quad (\text{I.6.1})$$

where i represents the respective direction of the displacement, i. e. x or y . The voltage amplification of the controller of $10\times$ is already taken into account with this calibration. The controllers also enable the coupling of an external electric signal into the stage. The signals necessary to steer the piezoelectric stages are typically created by a signal generator. Here, a device by Thurlby Thandar (TG230, Thurlby Thandar Instruments Limited, Huntingdon, Cambridgeshire, United Kingdom) is used which allows output amplitudes of sinewaves between $20\ \text{mV}$ and $20\ \text{V}$ and frequencies between $2\ \text{mHz}$ and $2\ \text{MHz}$.

Some additional optical elements and filters are involved in the construction of the microscope. One of them is the objective, which is an oil-immersion objective with a $60\times$ magnification and a numerical aperture of $NA = 1.4$ (mat.-no. MRD01602, Nikon GmbH, Düsseldorf, Germany). As already discussed in context with the scattering regimes in optical tweezers (Ch. I.3), a high numerical aperture is crucial for an efficient trapping since it increases the gradient force as compared to the scattering force and hence stabilizes the optical trap. The objective utilized in this study is designed for the use with

I.6. Experimental Study

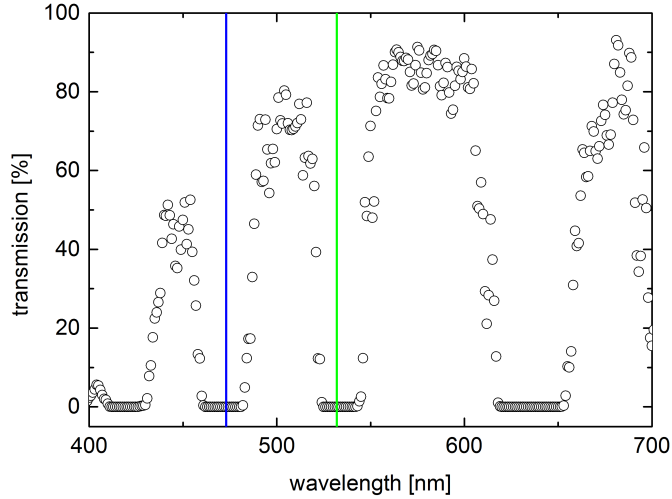


Figure I.6.5.: Characteristic transmission line for the two rejection band filters utilized in the setup of optical tweezers. Additionally to the filter lines, the two characteristic wavelengths of the utilized lasers are drawn as accordingly colored lines at 532 nm and 473 nm . The data sets were provided by courtesy of the manufacturer AHF analysentechnik AG.

coverslips and has a focal length of $170\ \mu\text{m}$.

Below the filter block which carries the dichroic filter for redirecting the laser beams through the objective, an additional filter is placed. It prevents any misguided laser radiation to reach the eyes of the user or the chip of the high-speed camera (art.-no. F62-456, AHF analysentechnik AG, Tübingen, Germany). A second filter of this type is inserted into the ocular of the microscope to shelter the eyes even more. At the wavelengths of the utilized lasers, each of the filters offers an optical density of more than 6 as indicated by the characteristic line in figure I.6.5. While blocking the laser radiation, however, the radiation of the illumination source still needs to pass these filters since otherwise a visualization of the surroundings of the optical traps would be impossible. Thus, this type of filter is ideally suited for this purpose.

This section is also intended for the description of the visualization system of the setup. It consists mainly of an illumination source, a condenser, the microscope objective described earlier in this section, and a high-speed camera. The dichroic filter 565DCXR and the aforementioned rejection band filters are also part of it, but since they have already been discussed, they will be omitted here. The illumination source used in the setup in Saarbrücken is LED-based (light emitting diode) and consists of a single high-power white-light LED source. Since there is no diode that emits at multiple wavelengths at the same time, such LEDs are realized by mixing the contributions of different optical transitions of multiple semi-conducting materials². This is also the case for the model

²Typically, for this purpose a galliumnitride (GaN) or a indiumgalliumnitride (InGaN) transition com-

used here, which is a Zett ZLED 9000 CLS by Zett Optics (art.-no. 799000, OptoSys GmbH, Darmstadt, Germany). Since the light source has its own casing, it is set up below the laboratory bench and only an optical fiber needs to be mounted to the microscope. This contributes to reduce the amount of mechanical noise in the setup. The model Eclipse TE2000-S offers an extension arm above the condenser, which is designed specially for the purpose of aligning light sources. Before the integration of this light source, Andreas Ziehl utilized a halogen lamp by Schott. However, in combination with the high-speed camera model currently used in the setup at typical recording frequencies of 8 kHz , strong intensity fluctuations due to the AC power supply of the lamp become apparent and reduce the quality of the recorded pictures. This effect also reduces the precision of particle tracking which will be explained later (Sect. I.6.2). Replacing the lamp with an equally or even more powerful lamp on a non-alternating current basis is preferable. The Zett ZLED 9000 CLS has exactly these properties and shows almost no fluctuations, although still being supplied by an AC current. Supporting lenses, mounted to the microscope arm, optimize the beam divergence further to couple as much light as possible through the sample cell and into the camera.

Before reaching the sample cell, the light from the illumination source reaches a condenser (TI-C-CLWD 0.72, Nikon GmbH, Düsseldorf, Germany) with a numerical aperture of $NA = 0.72$ which focuses the light into the cell. After passing through it, the light crosses the objective as well as the dichroic and the rejection band filter and propagates towards either the ocular or the camera, depending on the setting of the microscope. As a camera, the model HighSpec 1 by the manufacturer Fastec Imaging³ (Fastec Imaging, San Diego, CA, United States of America) is used. It offers a camera chip with 1,280 pixels in width and 1,024 pixels in height at an 8-bit greyscale resolution. The pixel size is $14\ \mu\text{m} \times 14\ \mu\text{m}$ and it enables a temporal resolution of 506 pictures per second at full-frame resolution while allowing recording rates up to 20 kHz at a reduced resolution of $128\text{ px} \times 64\text{ px}$. When taking the 60x magnification of the objective into account, this gives a pixel size of $233.3\text{ nm} \times 233.3\text{ nm}$. The camera also offers 2 GB of internal memory, making the recording of about 250,000 pictures at reduced resolution within about 16 s possible.

In order to record oscillatory forced motion of colloids, it is necessary to couple these oscillations into the system and at the same time synchronously record the confined colloids. The synchronization is realized by a custom-built trigger box. It was manufactured by the electronics workshop of the experimental physics department in Saarbrücken. It receives a 5 V TTL-pulse as input and down-converts it to a 3.3 V low-voltage TTL-pulse, but only if a mechanical, debounced switch is activated. Now, this TTL-signal is used to start the recording of the camera while at the same time the electrical driving signal

lined with a cerbium: yttrium-aluminium-garnet (Ce:YAG) transition is used.

³The model is identical to the camera MotionBLITZ EoSens mini1 by Mikrotron, Unterschleißheim, Germany.

I.6. Experimental Study

stemming from the same frequency generator as the TTL-signal is sent to the piezoelectric stage. If both the TTL-signal and the driving signal are recorded, the pictures taken by the camera and the motion of the stage can be synchronized. The data acquisition of these signals is performed by a National Instruments analog input module (NI 9215, National Instruments, Austin, TX, United States of America) which is then recorded by a custom program written in the graphical programming environment LabVIEW (versions 2010 to 2013, National Instruments, Austin, TX, United States of America).

I.6.1.3. Flow Control in the Microfluidic Device

In the scope of this thesis, flows through small channels of microfluidic devices are used to create shearing close to their walls. There exists a variety of ways to produce such flows, the most popular among which are probably syringe pumps. In these devices, a syringe is fixed inside a mechanism which is set to empty or fill the syringe at a constant flow velocity. Other velocity profiles can typically be chosen or programmed as well. However, these systems only offer a limited accuracy when choosing slow emptying velocities and are also sensitive to irregularities in the manufacturing of the syringes. This leads to non-constant flow velocities and thus ill-defined shear gradients which vary over time. Thus, in the setup instead of syringe pumps a passive system was utilized that uses the hydrostatic pressure difference of an inlet reservoir positioned at a greater height than the outlet reservoir. The pressure difference in the system is caused exclusively by the weight of the fluid column between inlet and outlet

$$\Delta p = \rho g \Delta h, \quad (\text{I.6.2})$$

where ρ is the fluid density, g the gravitational acceleration, and Δh the height difference between in- and outlet. The flow velocity can thus be tuned by slightly changing the height difference by moving the inlet reservoir up or down. Theoretically, the flow velocity will decrease over time since the reservoir is not infinitely large. On the one hand, it takes a very long time until the reservoir is emptied completely which means that over the course of a single measurement, no variations in flow velocity need to be taken into account. After each experiment, the height can be re-adapted to reach the desired velocity. Thus, the flow velocity is assumed to remain stable.

Such a system is realized in the setup of optical tweezers in Saarbrücken. As reservoirs, syringe bodies with their pistons removed (art.-no. 4606027V, B. Braun Melsungen AG, Melsungen, Germany), equipped with needles of a diameter of 0.6 mm (art.-no. 4657667, B. Braun Melsungen AG, Melsungen, Germany) are chosen. The syringe offers an experimentation volume of more than 2 ml . Leakage can be avoided since the size of the needle tightly fits into the tubing connected to the microfluidic device. The production of the microfluidic device has already been described earlier (Sect.s I.4.2 and A.2.1). As in- and outlet tubing, polyethylene oxide (PEO) tubes with an inner diameter

of 0.5 mm and an outer diameter of 1 mm are used (art.-no. 3550501, Laborshop24, Gross-Zimmern, Germany).

For such a kind of gravitational driving of flows, a reproducible way of setting the height of the reservoirs is necessary. In the utilized setup, two linear motors of type LTM 80F-300-HiDS (art.-no. 41.084.30GJ, Owis, Staufen, Germany) with one controller of type PS10-32-DC each (art.-no. 55.11.2432, Owis, Staufen, Germany) are used. They are mounted perpendicular to the surface of the laboratory bench. The mounting aids are about 1 m long aluminium boards with threaded holes for fixing the motor to it. The boards were custom-built by the mechanical workshop of the experimental physics department in Saarbrücken. The same is true for the fixtures that were used to attach the syringe bodies to the moving slide of the device. By moving the motors back and forth, the height of the reservoir can thus be set with very high precision. Both motors offer a long travel path of 21 cm at a low positioning error of less than $25\text{ }\mu\text{m}/100\text{ mm}$ and a bidirectional repeatability within $\pm 15\text{ }\mu\text{m}$. The motors can be attached to a computer which allows the steering of the devices. As an additional driving option for the flows, a compressed air bottle can be attached to the tops of the open syringe bodies via tubing. Since such a bottle provides a pressure of $2 \cdot 10^7\text{ Pa}$, it needs to be adapted using pressure reducing regulators ($p_{max} = 7,000\text{ Pa}$). This is particularly useful when colloids or dust particles block the microchannels, since the higher pressure tends to unblock the channels and pumping the contamination out of them. They should be avoided in the first place, but even under cleanroom conditions this is not always possible; blockage through sedimentation of particles within the channels is taking place during the whole course of the experiments, independent of how clean and dust-free the channels are.

I.6.2. Utilized Software

There is a number of software applications that are used in this work to acquire datasets during the course of experiments and also to process and evaluate them later. Some of these are written in LabVIEW (versions 2010 to 2013, National Instruments, Austin, TX, United States of America), others are realized in Matlab (version R2011b, The MathWorks, Inc., Aachen, Germany). In this section, a listing of these applications with information about the environment they were developed in will be given. In some of these cases, more details will be added about the algorithms.

When performing experiments in a setup of optical tweezers, the motion of a single or multiple confined colloids needs to be recorded and, at a later stage, tracked, so a list of particle positions is created which allows further processing. In the setup in Saarbrücken, a high-speed camera by Fastec Imaging is used (see also Sect. I.6.1.2) which offers a proprietary software for recording images. A variety of image formats is offered as well. When operating the camera in high-speed mode, a huge number of pictures is created in a short amount of time. Since the operating system Microsoft Windows XP does not

I.6. Experimental Study

handle huge numbers of files with a particularly good performance, a picture container with file extension “.raw” is chosen. The images are saved within this file as a string of header-less “.tif” files. They can be transferred from the internal memory of the camera to the hard disk drive of the computer within about 3 minutes, assuming that the internal memory has been filled entirely.

During the course of the experiments, sometimes, an online realignment of the position of the optical traps is necessary. In general, this requires the realignment of the whole setup. However, if only the trap generated by the 532 nm laser beam needs to be repositioned, this can also be achieved by carefully moving it through manipulation of the orientation of the piezoelectric mirror in the beam path. It can either be controlled by using electrical switches or by a software written by Andreas Ziehl in LabVIEW [4]. When working with a microfluidic device and a change of the flow velocity is desirable, this is practicable by adapting the height of the syringe body attached to a linear motor. These settings can be chosen in a proprietary application called OwiSoft that was distributed alongside the motors. It allows not only to set a displacement, but also the driving of the motor with a certain velocity profile. However, these options are not necessary for the conduction of the experiments, so simply setting a height is already sufficient.

As mentioned before in section I.6.1.2, in order to determine the reaction of a confined colloid to a shear flow, it is necessary to record the electric sinewave signal in synchronicity with the images recorded by the camera. A custom virtual instrument in LabVIEW was designed to acquire the input sinewave together with the TTL-signal triggering the start of the recording by the camera.

After the successful transfer of pictures from the camera to the hard drive, an option is needed to extract the particle positions. This is achieved by an application developed by Achim Jung [64] in which each of the images is Fourier-transformed and then correlated with a template image (typically the first image of a measurement). By applying a two-dimensional Gaussian fit, the shift of the particle from the current image as compared to the template can be determined with sub-pixel resolution. Since the characteristic circumference of the colloid in each picture covers a multitude of pixels, the accuracy of the fitting procedure is improved immensely. As a result, the software gives a list of x- and y-displacements and the picture number, which can be used as a time axis. The original program of A. Jung was slightly modified to directly accept the “.raw” format of the high-speed camera, saving the time and effort necessary for a conversion.

Since in part I of this dissertation, auto- and cross-correlation functions play a central role, a software is needed which is able to handle very large data sets created by each measurement and to calculate these functions. It was custom-developed in LabVIEW. The specific calculation sequence is described in section C.1 of the appendix. As input, a formatted text document (”.txt” or “.dat”) with one time and two position columns in this order is accepted, whereas the results are exported as a second text document with one time and three correlation columns C_{xx} , C_{yy} , and C_{xy} .

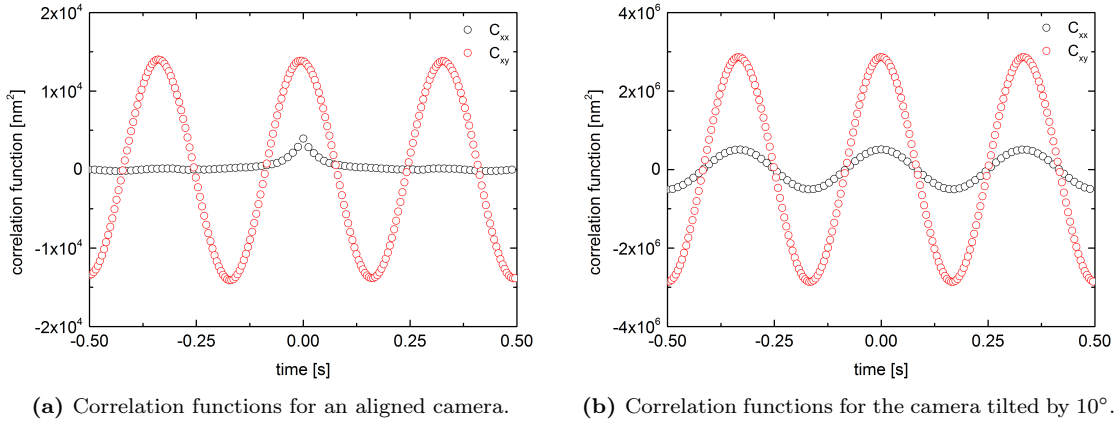


Figure I.6.6.: Influence of the camera angle alignment on the correlation functions of the displacements of a trapped bead. A data set from a numerical simulation was used, where an oscillation with a frequency of 3 Hz and an amplitude of $10 \mu\text{m}$ was applied to the optical trap in y -direction for demonstration purposes. The trap stiffness was set to $1 \mu\text{N}/\text{m}$, no shear flow was present. The auto- and cross-correlation functions of the data set were at first calculated for the unmanipulated data set, then, this step was repeated after virtually rotating the data set by 10° .

As a general tool for handling and organizing data, Origin (version 9, OriginLab Corp., Northampton, Massachusetts, United States of America) was utilized. It allows the fitting of functions to data sets and also offers additional options like performing a Fourier-analysis.

I.6.3. Calibration of the Setup

In this section, details about components of the setup of optical tweezers which need to be calibrated regularly will be given. Typically, before the setup can be used, it needs to be cleaned first using pressurized air and cleaning tissues. Afterwards, the alignment of the laser beam path is performed.

There are two additional elements whose alignment needs to be taken care of. When the high-speed camera is attached to the side-port of the microscope, it will record the focal plane of the objective. However, since the camera has a rotational degree of freedom, the tilting angle is not defined. This will play a crucial role, especially in context with the measurement of the correlation functions of bead displacements. To visualize the effect of a tilted camera on the correlation functions, a data set was created by numerical simulations where an oscillation was applied to the optical trap in y -direction while no shear flow was present. As such, due to the missing coupling effect by the shear flow, the motion of the bead in perpendicular directions should be uncorrelated. For the unmanipulated data set, this is definitely true (Fig. I.6.6a) since oscillations can only be found in the auto-correlation function C_{yy} (not displayed due to

I.6. Experimental Study

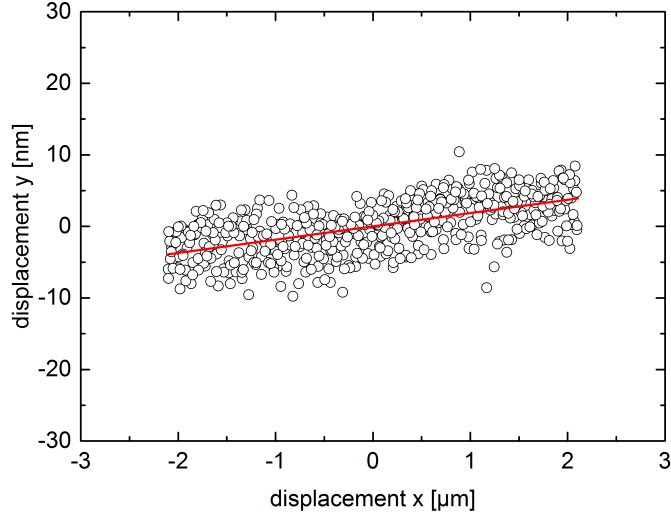


Figure I.6.7.: Typical displacement curve recorded for the tilt calibration of the camera. An oscillation was applied to the piezoelectric stage in x-direction while the camera recorded the motion of a bead that was immobilized at the surface of a coverslide. From the deviation of the trajectory from a horizontal line, the remaining tilting angle of the camera can be deduced. In this graph, the angle amounts to $0.107(1)^\circ$.

the large extent of the ordinate) and to a much smaller degree in the cross-correlation function C_{xy} . C_{xx} is still given by the pure exponential relaxation behavior from the quiescent case and shows no influence whatsoever from the oscillations. If, however, a tilt of the virtual recording device by 10° is assumed, the situation changes (Fig. I.6.6b). The tilt is performed by transforming the data set to spherical coordinates, adding the value of 10° to the angle, and transforming the data set back to the Cartesian frame. Now, the oscillatory contribution to the cross-correlation function is increased by roughly two orders of magnitude, while the auto-correlation function C_{xx} also shows an oscillatory behavior. The original exponential relaxation disappears almost completely. It is noteworthy that these spurious correlations always occur as unshifted cosine functions, since they originate from auto-correlated contributions.

Under the assumption that such an error occurs, it is of central importance to assess the consequences of it on the outcome of a measurement and shall be conducted as a simplified calculation. Consider a tilt of the recording device, i. e. the camera, versus the oscillation direction by an angle $\beta = 5^\circ$. In case of an oscillation otherwise perfectly aligned with the y-axis, this will cause it to be mixed into the motion in x-direction. The percentage change of the positions in x- and y-direction in respect to a reference position cannot be calculated since it depends on the exact positions. Expressed in a spherical coordinate system, the length $|\vec{r}|$ of the position vector remains the same, while only the angle increases by β . For the sake of presentability, let us assume nonetheless that the error can be expressed as a percentage value p . This means that motion recorded in the

frame of the camera C , from this moment on denoted by the Cartesian coordinates x' and y' , can be recast to the frame of the piezoelectric stage S , expressed in the Cartesian coordinates x and y

$$x' = x \cdot (1 - p) + y \cdot p, \quad (\text{I.6.3})$$

$$y' = x \cdot p + y \cdot (1 - p). \quad (\text{I.6.4})$$

The consequence of this for the cross-correlation function can then be written as

$$C_{x'y'}(\tau) = \langle x'(t)y'(t + \tau) \rangle \quad (\text{I.6.5})$$

$$= \langle (x(t) \cdot (1 - p) + y(t) \cdot p)(x(t + \tau) \cdot p + y(t + \tau) \cdot (1 - p)) \rangle \quad (\text{I.6.6})$$

$$= (1 - p)^2 C_{xy}(\tau) + p(1 - p)(C_{xx}(\tau) + C_{yy}(\tau)) + p^2 C_{yx}(\tau). \quad (\text{I.6.7})$$

Hence, in the expression for the measured cross-correlation function $C_{x'y'}$, there is not only a contribution of C_{xy} , but also of all auto-correlation functions C_{xx} and C_{yy} , and the time-inverted cross-correlation function C_{yx} as well. This calculation will be used later to estimate the influence of mixing of the signals in x- and y-direction.

The aim of this thesis is a measurement of the correlation functions in a manner as free from external noise as possible. Since the influence from a tilted camera can hide the true correlation signals, it is essential to have a very exact camera alignment. One of the easiest means to achieve this goal is to record the motion of a bead that is immobilized at a coverslide. It is not necessary to take additional preparation steps as compared to the standard recipe (see Sect. I.6.4) since, after a certain amount of time after sedimentation onto the coverslide, the particles become immobile automatically. When these particles are now oscillated by driving the piezoelectric stage and with it the whole sample chamber, the main axis of the oscillation can be visualized using the camera. If deviations of the main axis from a straight pixel line exist, the camera needs to be rotated respectively. This procedure must be repeated until an alignment is reached where the oscillation axis and pixel row or column are adjusted as parallel as possible. The result of such an alignment process is displayed in figure I.6.7. After fixation of the camera at the aligned rotation angle, an oscillation was applied to the coverslide with an amplitude of $2 \mu\text{m}$. The recorded trajectory is shown as an x-y-displacement plot. Over an oscillatory displacement of $4 \mu\text{m}$ in total, the perpendicular displacement of the immobilized bead is smaller than 20nm . The remaining tilting angle of the camera amounts to $0.107(1)^\circ$ which is close to the limit of a manual mechanical alignment.

Additional information is gained from figure I.6.7 about the resolution limit of the setup. When removing the effect of the camera tilt by subtracting the linear fit depicted in the figure from the data set in y-direction, it seems as if the immobilized bead was fluctuating around a center line very similar to the Brownian diffusion processes observed in the following chapters. However, in this case, the fluctuations are due to the electric

I.6. Experimental Study

noise of the camera chip. Excursions on this scale can not be resolved during later experiments since they could originate from electric noise as well as from actual Brownian fluctuations of particles. They can hence not be distinguished from one-another. By fitting a Gaussian to the histogram of particle positions in y-direction the standard deviation due to electric noise is determined to a value of approximately 3.3(2) nm. In a turbid medium like mucus additional scattering of light occurs which leads to a weaker illumination of the camera chip. Thus, the resolution limit can be estimated conservatively at approximately 5 nm. This value also includes the effects of all external noise and vibration sources that might negatively influence the conduction of an experiment. Overall it should be noted that the visualization of motion on the nanometer scale well below the typical optical resolution limit of $\lambda/2$ is only possible due to the utilization of the cross-correlation algorithm mentioned in section I.6.2. It should also be noted that during the conduction of the measurement depicted in figure I.6.7 no additional significant drift is observable. The calibration measurement was recorded within 16s which coincides with the typical length of all experiments performed with optical tweezers in part I and II. Hence, the influence of drift effects can be excluded.

A second calibration is required before quantitative measurements with a setup of optical tweezers are possible. For this purpose, however, the trap needs to be calibrated. There is a multitude of methods to achieve this goal [65]. Three of them shall be discussed here since they are the ones which are the most straight forward to apply. Two out of these are so-called passive calibration methods since they rely on Brownian motion as the driving force. They require no additional driving which would need to be applied actively to the system. This is the case for the third method, which is therefore denoted an active calibration method.

The first passive method can be found in literature under the name equipartition method [61]. As already detailed in section I.5.1, due to the equipartition theorem, a particle confined in a harmonic potential has a thermal energy of $E_{th} = k_B T/2$ by each degree of freedom. Thus, one can conclude for the kinetic energy that

$$\frac{k_B T}{2} = \frac{k_i \langle x_i \rangle^2}{2}. \quad (\text{I.6.8})$$

In other words, the mean squared distance from the center of the optical trap is determined by the thermal energy of the bead if there is no other energy source. This gives the formulation of equation I.5.4

$$\langle x_i \rangle^2 = \frac{k_B T}{k_i}. \quad (\text{I.6.9})$$

By plotting a histogram of positions for a confined bead and successive fitting of the resulting curve to a Gaussian function (compare Fig. I.5.1), its standard deviation, which

is identical to the mean distance $\langle x_i \rangle$, can be determined. By insertion into equation I.6.9 together with the temperature, the trap stiffness k_i can be directly computed. This method comes with the advantage that no knowledge about the surrounding fluid is required since no fluid parameters are necessary for this computation. However, the method relies on the knowledge of the temperature in the focal region. According to Peterman et al. [66], the temperature increase due to laser-induced heating can be determined to amount to less than 4 °C for all bead materials utilized in this thesis. This calibration method is applied to a number of measurements for a variation of laser powers (Fig. I.6.9, Tab. D.5).

The second method is based on one of the features of the auto-correlation functions of bead displacements. As already detailed in context with the derivation of the auto- and cross-correlation functions in section I.4.3, if no shear flow is applied to the system ($\dot{\gamma} = 0$), the cross-correlation function disappears at all times and the auto-correlation functions are identical to the equilibrium case of a quiescent fluid. According to equation I.4.23, C_{xx} and C_{yy} are given as

$$C_{xx}(\Delta t) = C_{yy}(\Delta t) = \frac{k_B T}{k_i} e^{-\Delta t / \tau_{r,i}}, \quad (\text{I.6.10})$$

where the relaxation rate is defined as $\tau_{r,i} = \zeta / k_i$. The height of the correlation peak as well as the relaxation of the peak depend on the trap stiffness, the most robust way to determine k_i is an exponential fit to the data to gain the relaxation rate. Only the knowledge of ζ is required for a successful calibration. In the scope of this part of the thesis, only water is used as a surrounding medium of which the viscosity and thus also the coefficient of friction is known. This method is particularly useful here since it allows an online calibration during each single measurement, so the actual trap stiffness for both directions x and y comes as a bonus. In case of the experiments presented in part II, this method is not applicable in a direct fashion since the surrounding material is a complex fluid and ζ becomes a time-dependent function. Just as for the past calibration method, this method was applied to a series of measurements at different laser powers. They are also shown in figure I.6.9 and in table D.5.

The final calibration method discussed here is an active method, meaning that an external driving force is applied to the system and its response is recorded. It uses the equality of the restoring force of the optical trap to Stokes' friction force and is thus denoted Stokes method or drag force method. Taking equation I.4.14 as the base equation, for oscillation amplitudes much bigger than the mean displacements by stochastic forces, one can assume that the stochastic force is negligible. Only the friction forces, due to the relative velocity of the confined bead to the surrounding fluid, and the restoring force of the optical trap remain, which results in

$$k_x \Delta x(t) = \zeta (v_{d,x}(t) - \dot{x}(t)). \quad (\text{I.6.11})$$

I.6. Experimental Study

As long as the friction forces do not exceed the restoring force of the trap, the latter can be described as a linear law (Eq. I.3.8). From a technical point of view, driving is achieved by applying an oscillation with a frequency f and an amplitude $x_{d,0}$ to the piezoelectric stage. This leads to a displacement of the stage $x_d(t) = x_{d,0} \sin(2\pi ft)$ and a velocity $v_{d,x}(t) = x_{d,0}\omega \cos(\omega t)$ with $\omega = 2\pi f$ and $v_{d,0} = x_{d,0}\omega$. Such kind of oscillatory driving also results in an oscillating trajectory of the bead $\Delta x(t) = x_0 \sin(\omega t + \delta)$. However, the phase behavior is of no concern for the purpose of calibrating the stiffness of the optical trap. Instead, the amplitudes of the driving and its response can be compared directly, so that

$$k_x = \zeta \omega \frac{x_{d,0}}{x_0}, \quad (\text{I.6.12})$$

where the amplitude of the bead measured from the trap center x_0 can be determined by sinusoidal fits to the measured displacement data. As becomes obvious from equation I.6.12, a further requirement for this method is the knowledge of the coefficient of friction ζ of the medium the calibration is performed in. It is required for the computation of the trap stiffness. A calibration within a complex fluid (see Pt. II for more details on complex fluids) using this method is possible [67], however, an exact knowledge of the medium and its analytical description is required. Otherwise, elastic contributions of the medium could be misjudged as to originate from the trap, thus leading to an overestimation of its stiffness. This method is better suited for a separate calibration run inside a well-known calibration fluid like water or a glycerol solution, both of which are Newtonian fluids.

In figure I.6.8, the displacement amplitudes from the trap center are plotted against the velocity amplitudes of the piezoelectric stage. For each laser power and thus for each trap stiffness, a linear dependence results when the driving force or respectively the driving velocity is increased. By determining the slope of each line, the corresponding trap stiffness can be determined according to equation I.6.12. The resulting stiffnesses are plotted together with the results from the two passive methods in figure I.6.9. In case of each of the methods, with increasing laser power a proportional increase in trap stiffness concurs. Each of them is described well by a straight line. There is a bigger variation in the offset than in the slope of the lines. Also the deviation between the stiffness in x- and y-direction is small (typically less than 10%) and in this case probably due to a small alignment error. A very common reason for such deviations is the stochastic nature of these measurements. To reduce this effect, multiple calibrations at the same power setting should be performed.

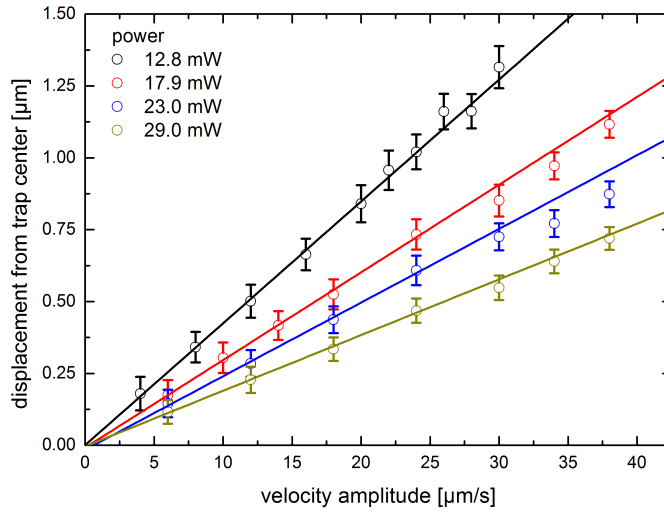


Figure I.6.8.: Results of multiple independent drag force calibrations with sinewave oscillations at different settings of the laser emission power. The displacement amplitudes are plotted against the velocity amplitude of the piezoelectric stage used for driving. Linear fits to the data sets give a good agreement, the trap strengths can be determined by applying equation I.6.12 to the slope values.

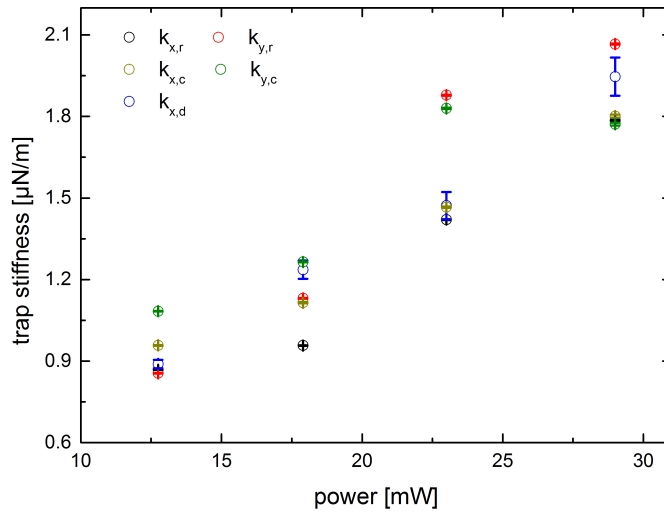
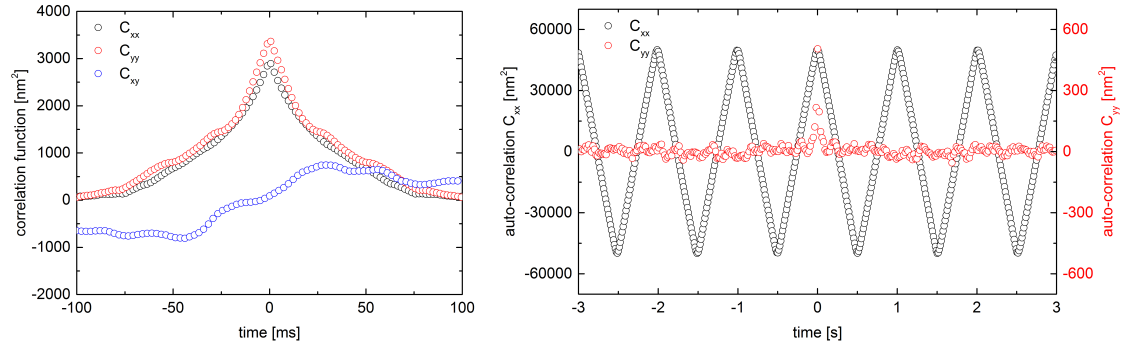


Figure I.6.9.: Trap stiffnesses resulting from different calibration methods. For the equipartition (index “r”) and the cross-correlation method (index “c”), the exact same data sets were used. The drag force calibration was performed on separate data sets where forced oscillations were applied to the piezoelectric stage (compare Fig. I.6.8). The trap stiffness from the drag force calibration is denoted with the index “d” and was only performed in x-direction due to the much bigger effort and time consumption of this method.

I.6.4. Results

In this section, experimental results will be presented and discussed. The equilibrium situation of a bead confined in a stationary optical trap with no flow present was already partially discussed in context with the calibration of the setup (Sect. I.6.3). Hence this situation will only be mentioned briefly before going into the in-depth discussion of the cases involving shear flows (Sect. I.6.4.1) and oscillations (Sect. I.6.4.2). Typically, before performing a measurement run with the setup, it was calibrated first. The gained stiffness values for the optical trap could then be compared to the online calibration results stemming from the exponential relaxation processes of the auto-correlation functions as explained in the calibration section.

A few classical experiments shall be reproduced with the setup of optical tweezers for verification purposes before moving on to the more complex experiments. They are conducted in quiescent fluids with Newtonian properties, in other words, instead of a microchannel, a closed-off air-tight sample cell is utilized and the PMMA beads (Tab. A.1) are immersed in water. This leads to the auto- and cross-correlation functions in figure I.6.10a, which show exponential relaxation processes, to appear. There is no clear cross-correlation which can be shown by a repetition of the experiment. As expected, the motion in orthogonal directions is uncorrelated as long as there is no flow or similar



(a) Oscillation-free equilibrium case at a stiffness of $1.25 \mu\text{N}/\text{m}$. (b) Effect of the application of a triangular oscillation ($B = 8 \mu\text{m}$, $f = 1 \text{ Hz}$) in x-direction on the shape of the auto-correlation functions while the trap stiffness was set to $6 \mu\text{N}/\text{m}$. The correlation amplitude in oscillation direction C_{xx} is larger by more than three orders of magnitude than the one perpendicular to it.

Figure I.6.10.: Auto- and Cross-correlation functions with no flow present in the pure quiescent case as well as under application of a forced oscillation. As expected no clear correlation can be found in C_{xy} in the oscillation-free case. Due to small tilts of the camera against the ideal angle, the oscillations do not only appear in C_{xx} but also in all other correlation functions (C_{xy} not shown). However, the amplitudes of C_{yy} are much smaller than these of C_{xx} , which indicates a good pre-alignment. Additionally, all correlation functions including C_{xy} are in phase, indicating that these are spurious correlations.

effect which drives the system out of its equilibrium.

If an oscillation of the optical trap is forced in the x-direction, assuming a perfect tilt alignment of the camera, no influence of the oscillation should show in the y-direction and its auto-correlation. In this case, no correlation should exist in C_{xy} , either. In figure I.6.10b, the auto-correlation functions C_{xx} and C_{yy} are shown for such an experiment with a triangular oscillation in x-direction. Albeit a small spurious coupling appears in the auto-correlation function C_{yy} , the oscillating contributions to this function are weak. In the depicted case, the oscillation amplitudes of C_{yy} stay well-below 50 nm^2 while those of C_{xx} reach values of approximately 46000 nm^2 . Since the driving amplitude contributes to the power of two to each correlation function, this means that less than 3% of the motion in oscillation direction was mixed into the oscillation-free direction due to a tilt of the recording device. While the exponential relaxation behavior disappears almost completely in the x-direction as compared to the oscillatory contribution, this is not true for the y-direction. Due to the mixing of the displacement signals, it is also not surprising to find an oscillating non-zero cross-correlation function. Its frequency concurs with those of the auto-correlation functions, while its amplitude shows an intermediate height between those of C_{xx} and C_{yy} (curve not shown). It is very characteristic for this case however, that the oscillations of the cross-correlation function happen in phase with those of the auto-correlation functions, meaning that all of them can be described by an unshifted cosine function. If not caused by spurious correlations, this case can only be reached for very high driving frequencies $f \gg 1/2\pi\tau_r \approx 16 \text{ Hz}$ which were not applied for the experiments presented in this thesis.

I.6.4.1. Colloids in Linear Shear Flow without Forced Oscillations

Now, the system of a colloid confined in an optical trap that is placed in a linear shear flow shall be considered. At this point, no forced oscillatory driving shall be applied. This case is identical to the one in the studies by Ziehl [5] and Bammert [18], except that the experimental realization is not conducted by designing a microfluidic device with a region of zero flow velocity and maximal gradient. Instead, by choosing a particular placement of the optical trap close to the side walls of a straight microchannel, a similar local flow profile is recovered as shown in section I.4.1. Hence, this analytical proof shall be additionally conducted in an experimental way.

For this purpose, a trap position about $2r_c$ away from the lower channel wall was chosen (compare Fig. I.4.5). Since the flow is directed from the right-hand to the left-hand side of the device, a negative shear gradient can be found in vicinity of the bead. If one compares two independent experiments under these conditions as depicted in figure I.6.11, one always finds the same features, albeit a certain measure of variation due to stochastic reasons is possible. As predicted by theory, the main feature of the auto-correlation functions are exponential relaxation processes (Fig. I.6.11a). The mean relaxation rate,

I.6. Experimental Study

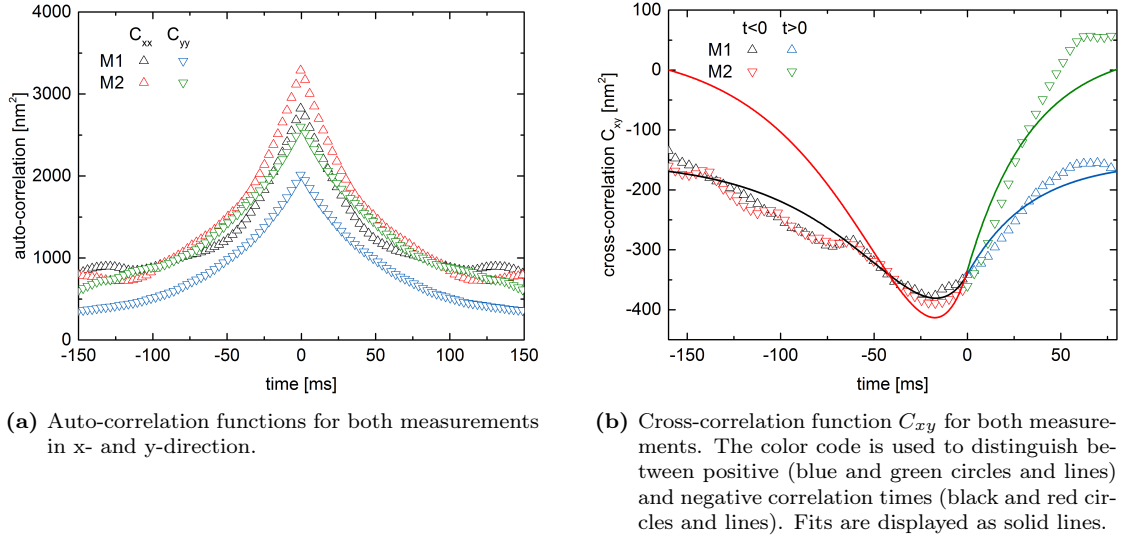


Figure I.6.11.: Auto- and cross-correlation functions of two independent measurements M1 and M2 at the same experimental settings ($k = 1.25 \mu\text{N}/\text{m}$). In both cases, the trap was placed about $2r_c$ away from the lower channel wall, while the fluid flowed from the right to the left, thus, creating a negative shear gradient.

which can be recovered by fitting, amounts to 50 ms . The corresponding trap stiffness of $0.75 \mu\text{N}/\text{m}$ is clearly smaller than the value of $1.25 \mu\text{N}/\text{m}$, gained by calibration in a separate sample cell as mentioned in the past section. This is unsurprising since a change of the sample cell is also linked with a change in optical properties (i. e. a different coverslide, etc.) and hence may lead to a different calibration. The best estimation of the stiffness is given by the online calibration method via the auto-correlation functions.

When comparing not only the shape of the auto-correlation functions but also their offset, one finds that C_{xx} for both measurements reaches a higher absolute value at $t = 0 \text{ s}$ than C_{yy} . Whether this effect is due to an offset or a different amplitude cannot be distinguished. Theory predicts (Eq. I.4.24) that the amplitudes in flow direction are enhanced through the shear flow by the colloidal motion perpendicular to the flow direction, in other words the y-direction. A similar effect would be caused if there was a slight tilt of the camera axis versus the oscillation direction of the piezoelectric stage; a mixing of the displacement signals would occur.

Theory also predicts an asymmetric minimum in respect to $t = 0 \text{ s}$ that can be found at small negative times in C_{xy} (Eq. I.4.25). Indeed, this minimum is apparent for both measurements in figure I.6.11b, their asymmetry is indicated by the color code. The minimum is in both cases located at roughly -20 ms . The shape of the curves is distinct, which becomes quite clear for $t > 0 \text{ s}$. At -150 ms , the correlation function of the measurement M1 reaches a functional value of approximately -150 nm^2 , which is identical to its value at 75 ms . While at -150 ms , the functional value of M2 agrees, this

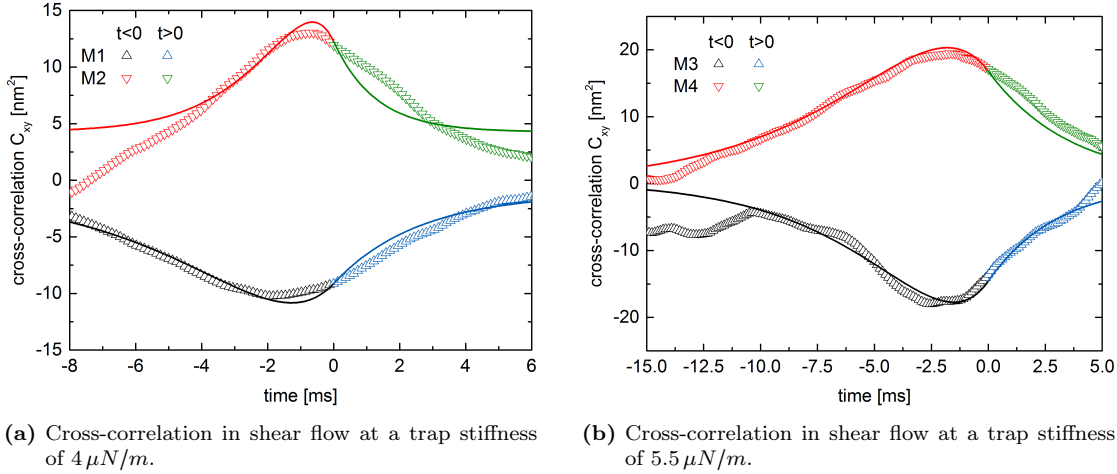


Figure I.6.12.: Influence of the sign of the shear gradient in a linear shear flow. Four independent measurements M1-M4 are shown exemplarily. While in case of M1 and M3 the colloid was placed about $4r_c$ away from the lower wall in a negative shear gradient, for M2 and M4 an equally distanced placement near the upper wall in a positive gradient was chosen.

is not true at 75 ms where it is much bigger ($\approx 50 \text{ nm}^2$). This leads to an askew looking shape of M2 which can be recovered in many experiments. The reason is a not perfectly stationary flow. Slight variations in flow velocity lead to a shift of the equilibrium position of the optical trap and thus a shifting baseline of the cross-correlation function. Still, it is possible to apply a fit with the analytical function to the data sets and to find at least a qualitative (black and blue curve in Fig. I.6.11b) and in some cases even a quantitative agreement (red and green curve).

Additional features predicted by theory can be checked, like the dependence of the depth and position of the cross-correlation peak on the sign of the shear gradient and also on a varying stiffness of the optical trap. The first experiment can be conducted by placing the trap in proximity of the lower wall (measurements M2 and M4 in Fig. I.6.12) to get a negative shear rate and afterwards performing the same type of measurement close to the upper wall with a positive shear rate (measurements M1 and M3 in Fig. I.6.12). All other settings should remain identical, i. e. the trap stiffness and the distance to the side wall. Two independent experiments of this kind are shown in figure I.6.12. In both cases, a distance between colloid and wall of $4r_c$ was chosen. The pre-calibrated stiffness values are well recovered by the online calibration, which estimates them at $4.4 \mu\text{N}/\text{m}$ and respectively at $6 \mu\text{N}/\text{m}$. The height of the correlation peak changes from 8 nm^2 for the lower stiffness to 15 nm^2 for the higher one. This is counterintuitive since, according to theory, the amplitude of the peak should behave reciprocally to the stiffness (Eq. I.4.25), while it seems to depend linearly on it here, instead. However, this amplitude additionally depends linearly on the Weissenberg number, which thus might compensate

I.6. Experimental Study

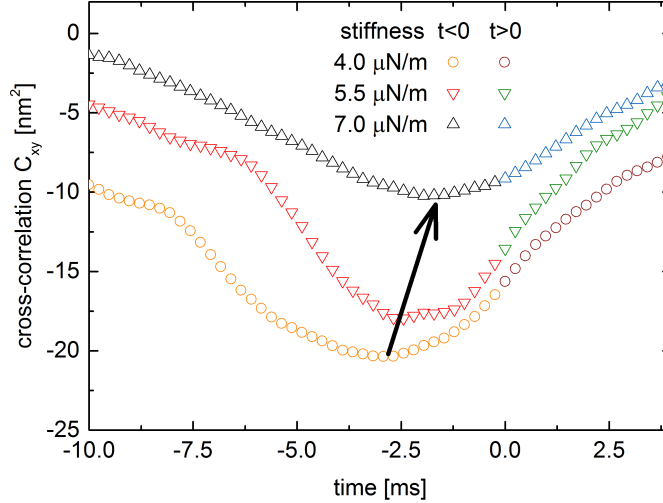


Figure I.6.13.: Dependence of the depth and position of the cross-correlation peak near $t = 0$ s on the trap stiffness. It was varied between $4 \mu\text{N}/\text{m}$ and $7 \mu\text{N}/\text{m}$ while in all cases a similar placement $4r_c$ away from the lower wall was chosen. By fitting the peaks with the corresponding analytical expression (eq. I.4.25), the relaxation rate can be determined as $6.32(2)$ ms, $3.0(1)$ ms, and $2.6(1)$ ms, sorted by increasing trap stiffness. The arrow indicates the shift of the correlation peak in relation to time.

the effect of the varying stiffness. The shear rate and thus Wi could not be measured directly, they may differ here.

Apart from these features, the main property that catches the eye is the switch in sign of the cross-correlation function, while the auto-correlation functions remain completely unaffected (curves not shown). This effect is predicted by theory as well, since the correlation amplitudes, as mentioned before, depend on the Weissenberg number (Eq. I.4.25) and are computed by the product of the shear rate and the relaxation rate. The curve progression is in all cases fitted well by theory.

A final comparison shall be drawn before moving on to oscillating traps. Assuming a very stable stationary flow, there should be a characteristic dependence of the amplitude $A_{C_{xy}}$ of the cross-correlation function on the stiffness. To be more exact, the height should decrease reciprocally proportional to the stiffness, i. e. $A_{C_{xy}} \propto 1/k$. Additionally, a shift of the peak position towards $t = 0$ s should occur. In figure I.6.13, the results of such a measurement series are presented. In all cases, the bead was placed at the same distance of $4r_c$ away from the lower wall while the stiffness was varied from $4 \mu\text{N}/\text{m}$ to $7 \mu\text{N}/\text{m}$. Indeed, one finds that the peak becomes shallower with increasing stiffness and the shift of the peak position also becomes evident as indicated by the arrow. Since no movement of the bead from the lower to the upper wall is involved here, a similar shear rate could be kept during all three experiments.

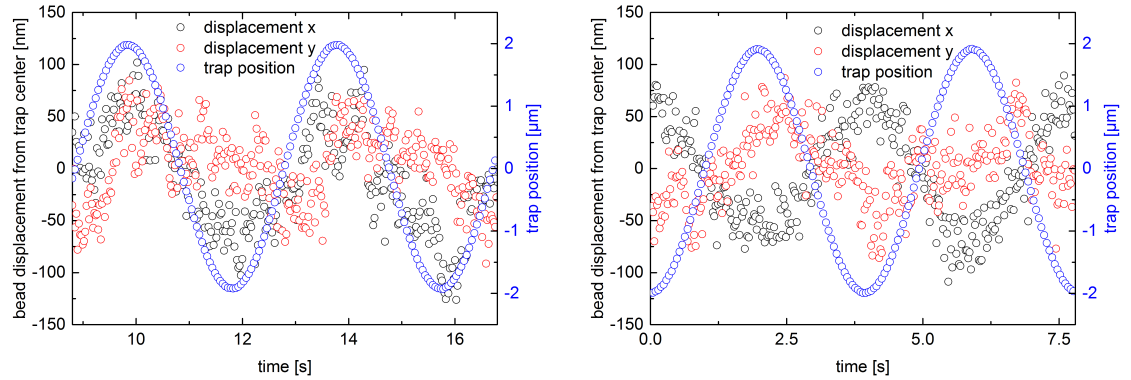
The shape of the auto- as well as the cross-correlation functions can be matched well with the analytical expressions computed earlier (Sect. I.4.3). In some cases, the

agreement is good enough to allow fitting with the analytical functions from equations I.4.24, I.4.23, and I.4.25. These results concur with those reported by Ziehl and Bammert, although the experimental realization of the shear flow is not a flawless and ideal one - keep in mind that the microchannel used here creates a parabolically shaped Poiseuille velocity profile which only comes close to a linear gradient in proximity to the side walls. This however hints that, when taking an elaborate placement of the colloid into account, the flow can reasonably be assumed as a linear shear flow and is thus well suited for later experiments including forced oscillations.

I.6.4.2. Colloids in Linear Shear Flow Forced by an Oscillating Optical Trap

This section will deal with the core of the experimental study of the first part of this thesis. An optical trap will be utilized to confine colloids, keeping them stable even though a shear flow will be present. Still, Brownian motion will occur and cause characteristic auto- and cross-correlation functions, which are the main interest here. The special feature added as compared to earlier studies will be an oscillatory driving of the piezoelectric stage of the microscope, which aims at constantly bringing the colloid out of its force equilibrium. This kind of driving can be depicted more easily as an oscillatory motion of the position of the optical trap. The oscillations will be directed perpendicularly to the flow direction in the microfluidic device and thus have a shearing effect on the colloid. Since the high-speed camera utilized for image acquisition always records the co-moving frame of the optical trap, only relative displacements in respect to the center of the trap will be shown, unless otherwise indicated.

When brought into such a situation, the colloid will constantly feel changing flow velocities and thus react to the varying forces of friction by being displaced further or less far from the center of the trap. This case is depicted in figure I.6.14, where the absolute motion of the trap is drawn in blue circles, while the relative displacement in x- and y-direction - or respectively motion in flow direction and perpendicular to it - is shown as black and red circles. However, in subfigure I.6.14a, a placement in a shear gradient of positive sign close to the upper wall was chosen, while in subfigure I.6.14b



(a) Average position of the bead about $3r_c$ away from the upper wall in a positive shear gradient.

(b) Average position of the bead about $3r_c$ away from the lower wall in a negative shear gradient.

Figure I.6.14.: Effect of the sign of the shear gradient on the confinement of a colloid. The trap stiffness was set to $5.5 \mu N/m$, an oscillation amplitude of $2 \mu m$ and a frequency of $0.25 Hz$ were chosen. While in both cases the oscillatory displacements in y-direction run roughly by $\pi/2$ ahead of the driving, the phase behavior of the displacements in x-direction depend on the sign of the shear gradient. In a positive gradient, they are approximately in phase with the driving, while being out of phase (shifted by π) with the driving in a negative gradient.

the gradient carries a negative sign at a similar absolute value. The y-displacement out of the trap center is described by a sinusoidal oscillation with identical frequency to the excitation, which follows the excitation with a phase shift of roughly $\pi/2$. Since a certain reaction time on the order of the relaxation rate is necessary for the bead to adapt to the changed flow situation, there is no exact shift by $\pi/2$.

There is a distinct difference between both shown cases regarding the displacement in x-direction. In case of the positive gradient, the bead is displaced further to the left the farther down it is dragged, and vice versa for an upwards displacement. This is just a logical reaction to the stronger friction closer to the center of the microchannel, which due to its flow direction pushes the particle to the left. This pattern changes to the contrary when switching from the upper to the lower wall, thus, the additional phase shift is precisely π . A feature that is very hard to spot is a slight additional phase shift as compared to the oscillations of the trap motion and the relative bead displacement in y-direction. It is again of the same order of magnitude as the relaxation rate. These properties will become very important in context with the correlation functions later on, which at the same time are much better tools for a visualization of this shift.

A different way of presenting the x- and y-displacements is an x-y-plot. These are shown in figure I.6.15 for the same measurements as discussed before. Here, however, not the relative displacements out of the trap center are shown but the absolute positions. This is trivial for the data set in x-direction, since relative and absolute displacements are identical. In case of the y-displacements, the plotted quantity is the sum of the red and blue symbols in figure I.6.14 in order to give $y_{abs}(t) = y_{trap}(t) + y_{rel}(t)$ (compare

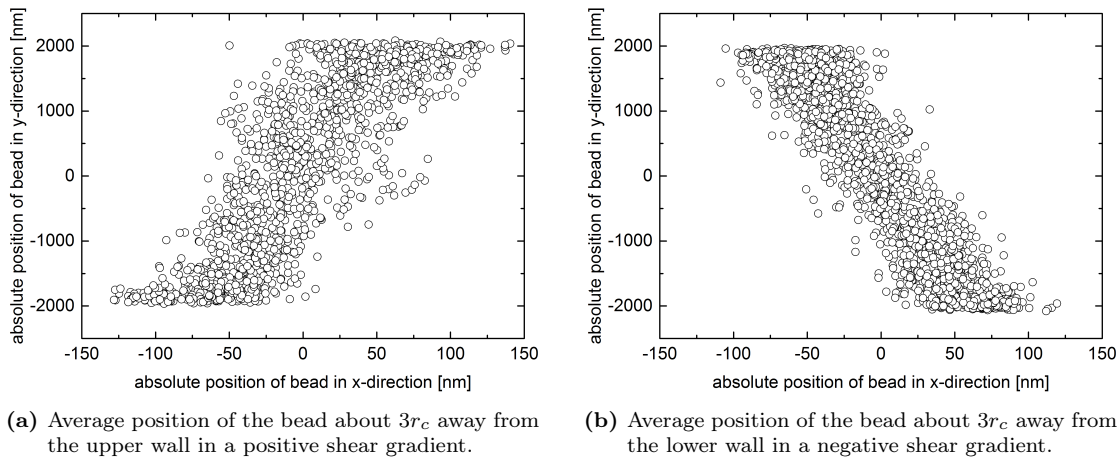


Figure I.6.15.: Effect of the sign of the shear gradient on the spatial distribution of a colloid. The trap stiffness was set to $5.5 \mu N/m$, an oscillation amplitude of $2 \mu m$ and a frequency of $0.25 Hz$ were chosen. The data sets correspond to the ones in figure I.6.14. The tilt of the distribution curve and especially the sign of the tilting angle relative to a vertical line hint at the strength of the shearing.

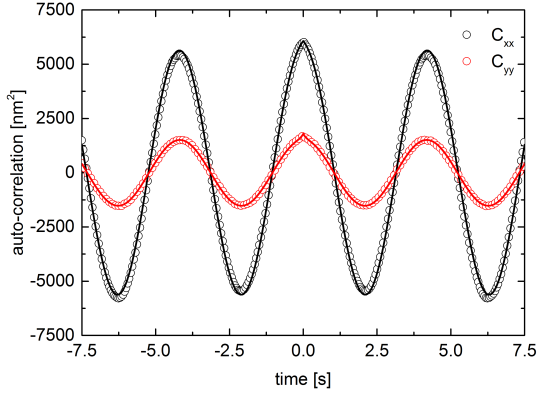
I.6. Experimental Study

Sect. I.4.4 dealing with the corresponding analytical expressions). The reaction of the bead to the changed flow conditions and friction forces becomes directly apparent in these sketches. A quite nice feature of the curves is their shape. Both plots indicate that there is practically no curvature in the data sets which would indicate a deviation from an ideal shear flow. This shows once more that the assumption of a linear flow profile close to the channel walls is justified.

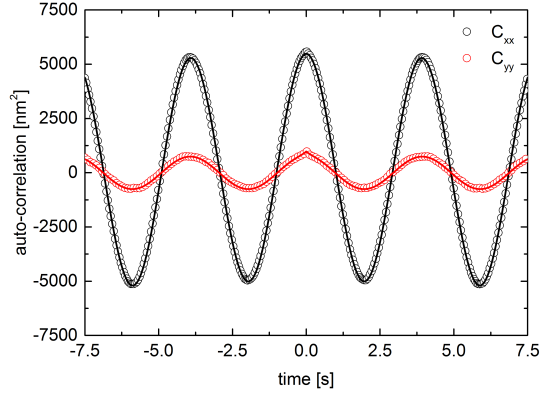
To gain some additional information about the system, the auto- and cross-correlation functions can be determined in the same way that was already applied earlier in context with the numerical data sets. A program was written in LabVIEW to take care of this. A description of its functionality is included in the appendix (Sect. C.1). As already discussed in earlier chapters, when calculating the correlation of oscillating functions, one would expect correlation functions that oscillate in a similar fashion. This is indeed the result for the functions in this chapter, as can be seen in figures I.6.16 and I.6.17. However, more interesting details can be found.

Let us consider figure I.6.16 first which shows two independent experiments at the same setting of the trap stiffness, oscillation amplitude and frequency, and distance to the wall. The difference between subfigures I.6.16a and I.6.16b or between I.6.16c and I.6.16d, respectively, however, is that in the first case the trap was positioned next to the lower wall ($\hat{=}$ negative sign of the shear gradient) while in the second case a placement close to the upper wall ($\hat{=}$ positive sign of the shear gradient) was chosen instead. The same is true for the cross-correlation function C_{xy} presented for the same data sets in figure I.6.17.

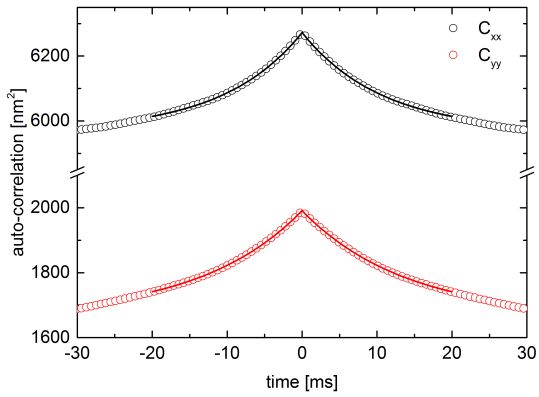
At first glance at subfigures I.6.16a and I.6.16b, for both auto-correlation functions strong oscillatory contributions become obvious. Due to the choice of parameters, these contributions are of approximately the same order of magnitude as for the exponential relaxations shown earlier in context with colloids in quiescent fluids or in a linear shear flow without any forced driving (Figs I.6.10a and I.6.11a). However, it should be kept in mind that the height of these peaks scales reciprocally proportional to the trap stiffness, which is much higher here than it was before. This choice originates in the stronger shear flow. The oscillatory contributions to the auto-correlation functions can indeed be described analytically by equations I.4.31 and I.4.32 as shown by fits to the data sets (solid black and red lines). When magnifying the region around $t = 0s$ as executed in figures I.6.16c and I.6.16d, the exponential correlation peaks already well known from oscillation-free correlations can be found. As long as fitting is restricted to rather short timescales like $20ms$ in the presented case, it is still possible to capture the relaxation process well. Since all of the curves shown in figure I.6.16 look similar and show no particular distinction besides different oscillatory and exponential relaxation amplitudes, the choice of the sign of the shear gradient seemed to have no impact at all on the auto-correlation functions.



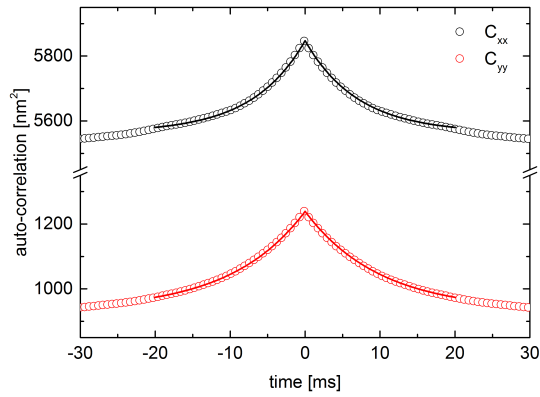
(a) Overview of the auto-correlation functions. The bead was placed close to the lower wall in a negative shear gradient.



(b) Overview of the auto-correlation functions. The bead was placed close to the upper wall in a positive shear gradient.



(c) Zoom of the auto-correlation functions in figure I.6.16a to the region of small correlation times.



(d) Zoom of the auto-correlation functions in figure I.6.16b to the region of small correlation times.

Figure I.6.16.: Auto-correlation functions C_{xx} and C_{yy} for a colloid confined in an oscillating trap ($k = 5.5 \mu\text{N}/\text{m}$) in a linear shear flow about $3r_c$ away from the channel walls. The position of the trap was oscillated at an amplitude of $2 \mu\text{m}$ and a frequency of 0.25 Hz . Fits to the data sets with the corresponding analytical functions are shown as solid lines. The data sets shown in subfigures I.6.16a and I.6.16c were taken during the same measurement. The same is true for the data sets in I.6.16b and I.6.16d. They also correspond to the data sets shown in Fig. I.6.17. By comparison of the amplitudes of the oscillating contributions $C_{xx,osc}$ and $C_{yy,osc}$ according to equation I.4.38 the shear rates can be determined as $\dot{\gamma} = 2.91/\text{s}$ for subfigures I.6.16a and I.6.16c and respectively as $\dot{\gamma} = 4.21/\text{s}$ for subfigures I.6.16b and I.6.16d.

A similar assessment can be performed with the cross-correlation functions of the same data set (Fig. I.6.17). Again, the first obvious and seemingly single property of these functions are oscillations of a frequency identical to the auto-correlations. Their amplitude can be best described as an intermediate amplitude between the ones of $C_{xx,osc}$ and $C_{yy,osc}$, however, there is an important difference: the phase behavior deviates from a cosine function. In the data sets shown, it appears more like a sine function with a

I.6. Experimental Study

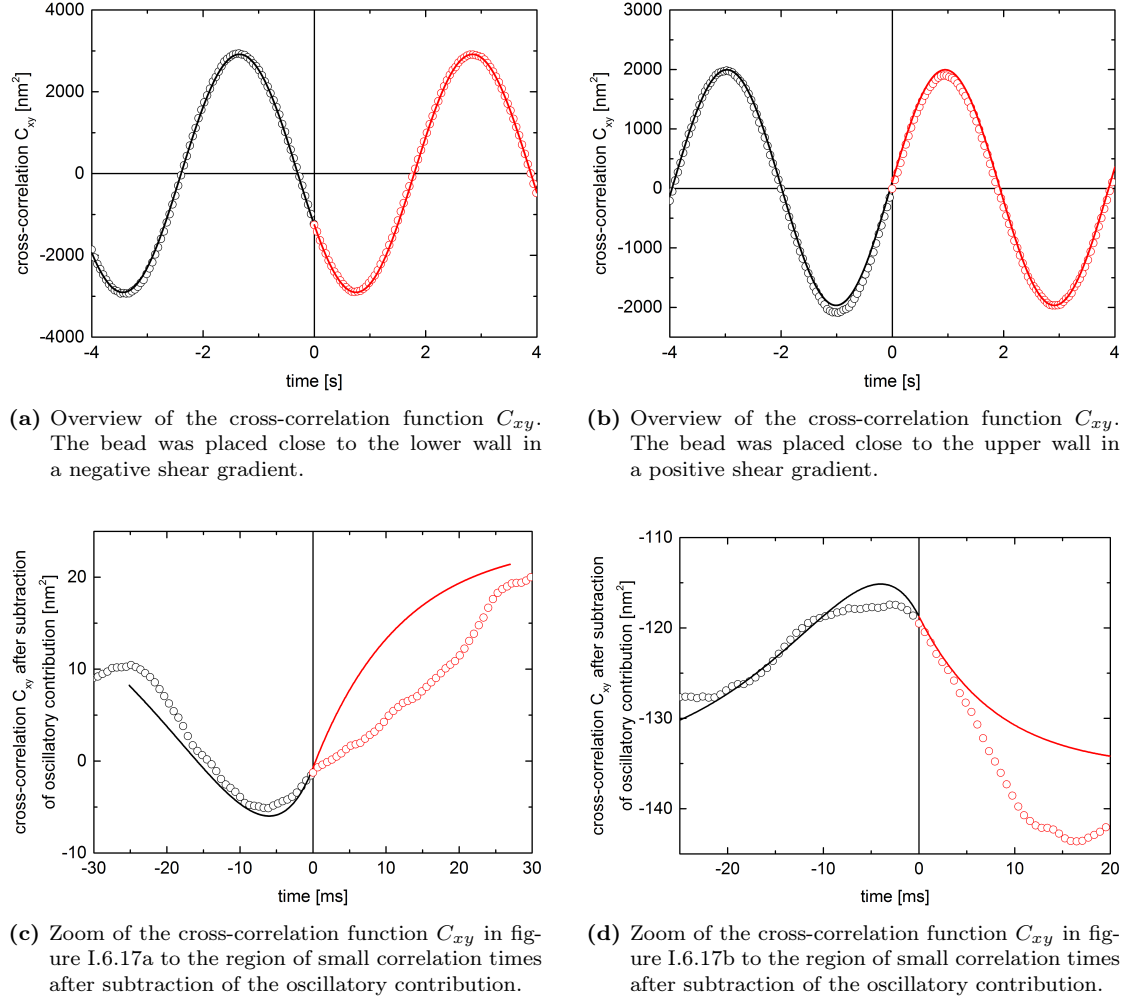


Figure I.6.17.: Cross-correlation functions C_{xy} for a colloid confined in an oscillating trap ($k = 5.5 \mu\text{N}/\text{m}$) in a linear shear flow about $3r_c$ away from the channel walls. The position of the trap was oscillated at an amplitude of $2 \mu\text{m}$ and a frequency of 0.25 Hz . Fits to the data sets with the corresponding analytical functions are shown as solid lines. Color code is used to distinguish correlation times smaller (black) and bigger than 0 s (red). The data sets shown in subfigures I.6.17a and I.6.17c were taken during the same measurement. The same is true for the data sets in I.6.17b and I.6.17d. They also correspond to the data sets shown in Fig. I.6.16.

positive or respectively a negative sign depending on the figure. In this property, two pieces of information about the cross-correlation functions are included. On the one hand, the phase behavior of C_{xy} is variable and on the other hand, it depends on which wall the bead was placed next to or, in other words, which sign the shear gradient has. The $-\sin$ case appears in the vicinity of the lower wall (the negative gradient), the $+\sin$ case is found near the upper wall (the positive gradient). Thus, the phase shift depends on $\dot{\gamma}$ or on Wi , respectively. When comparing these findings to the analytical expression (Eq. I.4.36), it

becomes clear that this is only partially correct. When placing the bead in the negative shear gradient, the fit captures the change in sign of W_i as an additional phase shift by π instead. The fact that the phase is variable within certain boundaries apart from this is also captured in the analytical expression. It claims that $\delta(C_{xy}) = -\arctan(1/\alpha)$ (compare Eq.I.5.7) and thus should only be dependent on the dimensionless frequency α . This frequency is by no means constant since it varies with the relaxation rate, which may change with the position of the optical trap in the microchannel. This is also the reason for the non-identical phase in figures I.6.17a and I.6.17b even when taking the phase shift of π due to the sign of W_i into account.

It is possible to detect a hidden feature in the cross-correlation function by removing the oscillatory contribution to the data sets. This can, for instance, be performed by fitting the correlation function with only the oscillatory contribution and afterwards extracting the fitted curve from the original data set. If done correctly, the features already known from the oscillation-free case appear as becomes obvious in figures I.6.17c and I.6.17d. Also, their properties as compared to the oscillation-free case remain unchanged. For typical settings of the trap stiffness and realizable shear rates, the height of the peaks is on the order of 10 nm^2 to about 100 nm^2 , while the amplitude of the oscillatory contributions ranges around a few thousand square nanometers. This means that the Brownian-type correlations contribute to less than 10%, in some cases even to less than 1%, to the total correlation signal, which is the reason why it is very challenging to detect and evaluate them.

Now, that the shape and the contributions to all auto- and cross-correlation functions were recovered from experimental results as well as from analytical calculations and numerical simulations, it becomes possible to apply that knowledge to test the functional dependencies of certain properties of the correlation functions. Under the assumption of an exact alignment of the laser guidance system and of the sample cell relative to the piezoelectric stage, as well as a perfectly stationary flow without fluctuations, this could be achieved. It is not possible to do a parametric analysis as done for the numerical study in chapter I.5 except for one single quantity.

When one considers the amplitude of the oscillatory contribution to C_{yy} , one finds the relation given in equation I.4.31, claiming for small dimensionless frequencies that $C_{yy,osc} \propto B^2\alpha^2$. Thus, when dividing $C_{yy,osc}$ by B^2 , one should gain a quantity which only depends on the frequency and increases proportional to its second power. This calculation was performed for a number of experiments (fitting results available in Tab. D.6) and plotted against the dimensionless frequency in a log-log plot (Fig. I.6.18). When compared to the theoretical prediction as indicated by the solid red line, the correlation amplitude scales solely depending on the frequency. Since the red line is no fit but a plot of the analytical function, the concurrence of both data sets is very good. However, due to stochastic processes a significant amount of scattering has to be dealt with, nonetheless.

I.6. Experimental Study

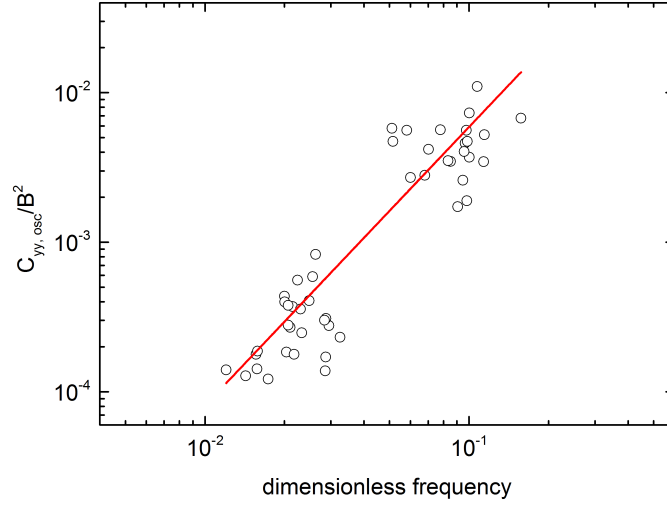
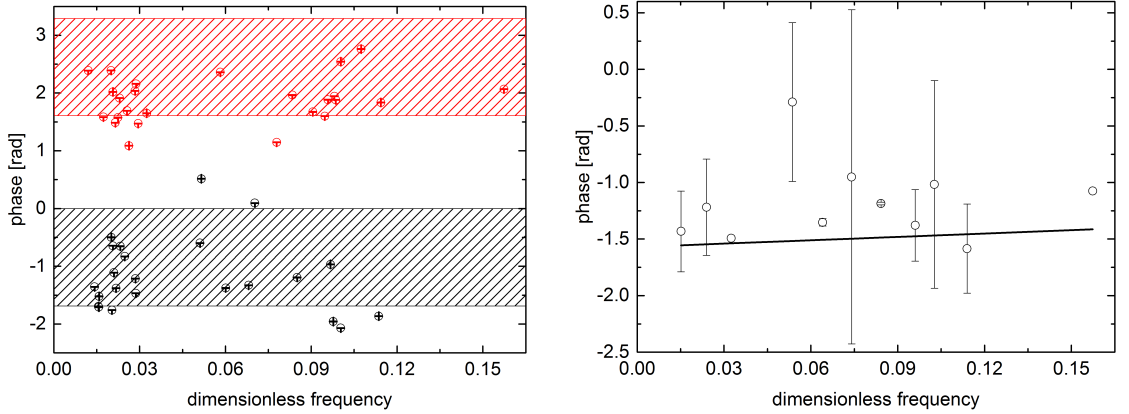


Figure I.6.18.: Dependence of the oscillatory contribution to the auto-correlation function C_{yy} on the dimensionless frequency α . For small frequencies $\alpha \ll 1$, C_{yy} increases proportional to α^2 as predicted by theory (eq. I.4.31, red line). The dependence on B^2 was removed beforehand since the shown data sets were recorded at a variety of different oscillation amplitudes. The data sets displayed are also included in table D.6.



(a) Phase behavior as recovered from sinusoidal fits to C_{xy} . The regions indicated in black and red correspond to the valid phase range for positive and negative shear gradients according to the analytical expression (eq. I.4.36). The data sets are also displayed in table D.6.

(b) Phase behavior of C_{xy} after extraction of the additional phase shift due to the shear gradient and averaging within intervals of the dimensionless frequency with a width of $\Delta\alpha = 0.01$. All data points collapse into the region between $-\pi/2 \text{ rad}$ and 0 rad as suspected, however the agreement with the analytical behavior (black line) is laden with significant errors. Values with missing error bars ($\alpha = 0.032$ and $\alpha = 0.157$) represent intervals containing only one single data point. The utilized data sets are also represented in table D.7 of the appendix.

Figure I.6.19.: Phase behavior of the oscillatory contribution to C_{xy} . The data sets were recorded at varying trap stiffnesses, average trap-wall distances, and amplitude and frequency settings of the piezo.

An additional check on the phase behavior of the oscillatory contribution to C_{xy} can be performed. In figure I.6.19, the phase $\delta(C_{xy})$ was plotted against the dimensionless frequency, which is supposedly the only parameter it depends on. However, no clear functional behavior can be found when plotting all data sets as done in subfigure I.6.19a. As mentioned earlier in this section, the sign of the Weissenberg number plays an important role in the phase behavior since if it is negative, this is equivalent to an additional phase shift by π . This is the reason why some of the data points are shown in black color (close to upper wall in positive shear gradient) and some are shown in red (close to lower wall in negative shear gradient). The two regions shaded in black and red are the “allowed” phase ranges according to theory. This criterion is met by most of the data points, however, some of them are still in the “invalid” regions between 0 rad and $\pi/2 \text{ rad}$ or between $\pi \text{ rad}$ and $3\pi/2 \text{ rad}$, respectively. When taking the sign of the shear gradient into account, the red data points can be shifted into the black region I.6.19b. Before plotting, average values were computed within intervals of the dimensionless frequency with a width of $\Delta\alpha = 0.01$. Except for a few outliers, most values seem to orient themselves close to the analytical prediction (solid black line), however, the errors remain rather significant.

I.6.5. Summary

Over the course of this chapter, all the matters involving the experimental setup of optical tweezers were discussed. It was started off by a detailed look at the setup in section I.6.1. At first, all elements involved in the guidance system of the laser beams defining the optical tweezers were presented (Sect. I.6.1.1), followed by a look at the microscope, the visualization system of the colloidal motion as well as the signal-synchronization-system (Sect. I.6.1.2), which are necessary for the active forcing of such a system with oscillations. Finally, the involvement of microfluidic devices and the control system for the flow velocities inside such a device was detailed (Sect. I.6.1.3). The kind of setup that is used as a basis for this system was already presented a few years ago by Andreas Ziehl [4, 5]. However, a few delicate changes were made to increase the sensitivity, the sample acquisition rate, and the precision of particle tracking.

For the successful conduction of an experiment in this setup, certain computer applications are required. Linear motors need to be controlled for setting the flow velocities, the synchronized acquisition of images by the high-speed camera and of electrical oscillation signals by a National Instruments acquisition card needs to be triggered. Details about the software can be found in section I.6.2.

An immensely important preparation step, the calibration of the setup, was discussed in section I.6.3. At this point, it is assumed that the whole setup is assembled and also aligned. The required calibrations were two-fold: On the one hand, the tilting of the reference frame of the camera against the axes of the piezoelectric stage needed to be reduced, and on the other hand, the experimenter had to be enabled to assess the stiffness of the trap. The tilting calibration reduces errors that would otherwise occur in the calculation of correlation functions due to mixing of the x- and y-displacements of a confined colloid out of the center of the optical trap. The calibration of the stiffness can be performed using a multitude of methods, three of which (the equipartition method, the auto-correlation method, and the drag force method) are presented, since they were applied regularly in the scope of this thesis. Especially the auto-correlation method should be mentioned here since it allows the online calibration of the stiffness during the conduction of the correlation experiments.

The central section of this chapter is section I.6.4, which gives details about the performed experiments as well as their results. After a short introduction to the case of a confined colloid in a quiescent fluid and the resulting correlation functions of motion, the trap was brought into a quasi-linear shear flow close to the side walls of a microfluidic channel (Sect. I.6.4.1). The arising auto- and cross-correlation functions were compared to earlier results by Andreas Ziehl and a qualitative agreement was found. It should be noted that a certain level of skewness of the cross-correlation function C_{xy} may occur, affected by an unideal stability of the flow and an equilibrium position of the bead that is displaced relative to the trap center. A good agreement was also found with the

analytical description from section I.4.3.

It was followed by section I.6.4.2, which included an in-depth discussion about auto- and cross-correlation functions involving a shear flow and forced oscillatory driving of the position of the optical trap. The causality of displacement-time curves was analyzed and spatial particle distributions were depicted. They prove the presence of a shear flow that very closely resembles a linear flow profile as assumed earlier. Afterwards, the shape of the arising correlation functions was discussed and described by fits with the analytical model. A good qualitative agreement could be found, however, especially in context with the cross-correlation functions, a close-to-perfect tilt alignment of the camera and the importance of a very stable flow cannot be underrated. Thus, measuring the true cross-correlation function as depicted by the model is an enormous challenge. For some of the conducted measurements, this agreement could be found nonetheless (Fig. I.6.17). Although a parametric examination is prevented as shown for the phase behavior of C_{xy} (Fig. I.6.19), the evaluation of certain systematic properties, like the shear rate for example, is possible.

1.7. Discussion

Considering the results from the past chapters about the analytical and numerical description of a confined colloid in a linear shear flow, a qualitative match to the results from experiments could be found. However, the analytical framework only considered the ideal case of a perfect spherical object in a perfect shear flow. In our experimental setup, though, the precise control of the flow rate was difficult since slight variations in channel diameter - e. g. due to particles sticking to the channel walls or due to the surface roughness of the channels which occurs during their production process - always led to flow rate fluctuations. Therefore, we assume that this should be the most significant source of error in our system.

In order to assess additional possible error sources in the experimental setup, the analytical assumptions shall be compared with experimental reality. These assumptions include a setup completely free from unwanted external vibrations, a fully stationary sample cell as well as a stationary flow through the microchannel, a perfect placement of the colloid in the channel, non-rotating beads, a perfect alignment of the whole setup, as well as many more. Although much care was taken to reach the desirable state of the system, certain deviations from it were always present.

The first mentioned assumption, a system free from external vibrations, is, in general, not easy to realize. Vibrations are always present, be it from cars passing the building that contains the setup, a construction site on the other side of the street, or simply the oscillations of the building itself. Even choosing a room in the basement of the building and mounting the setup on top of a vibration-dampened workbench were only able to remove the most significant part of these disturbances. However, this error source can indeed be considered minor as compared to other sources.

Additional error contributions stem from a non-stationary sample cell as well as a non-stationary flow. When positioning a sample cell on top of the piezoelectric microscope stage, the cell itself never stays perfectly at rest. An experiment performed with a bead fixed at the lower coverslide of such a cell showed that over the course of two minutes, the position of the bead changed by approximately 60 nm . Partially, this is due to the heating of the sample cell and bead by the illumination source, the mechanical positioning system of the microscope is accountable for the effect as well. Especially the mechanical influence is worsened when the microfluidic device is used instead of the calibration cell since tubes, which tend to touch the condenser and thus contribute to the drift as well, protrude from the top of the device. A worst-case estimation of the total drift velocity gives a value of

I.7. Discussion

approximately 10 nm/s . Compared to the flow velocities in the microchannels, however, which typically reach up to $100\text{ }\mu\text{m/s}$, the drift velocity only has a minor impact. Much more significant is the non-stationary flow, which occurs frequently in the experiments. In many cases, these irregularities are impossible to spot with the naked eye during the course of the measurements, as only an evaluation of the particle displacements is able to make them visible. They are also nearly impossible to avoid since the root of the problem are colloids piling within the tubing and the channels. When a certain area of the channel is blocked, the pressure in front of the blockage increases until it is partially removed, which allows the pressure to instantly decrease again. This leads to short pressure spikes which hence destabilize the flow significantly. Even when working with perfectly cleaned materials in a clean room, this effect cannot be avoided completely, since the colloids are a necessary element for the conduction of such an experiment. As mentioned, the appearance of such a pressure spike can be considered a huge error, thus, it may take a large number of experiments until some of those during which no spike occurs are found. Much care was taken to filter measurements containing such events and excluding them from evaluation.

When choosing a position of the optical trap and thus of the colloid within the channel, as discussed in section I.4.1 the ideal region can be found in direct vicinity of the side walls of the microchannel. Also, the particle should be placed as close as possible to the center of the channel in respect to its height, in other words in z -direction. Since the microscope in the setup allows the placement of particles with a sub-micrometer resolution in the lateral x - y -plane, this can be performed very precisely. However, the height placement cannot be resolved optically, which may cause significant deviations from the center of the channel. Also when a confined particle is subjected to a flow, this may entail a rotation of the bead in the trap and also a significant displacement from the focal plane of the trap in z -direction. Such excursions lead to a change in local flow velocity since there is a parabolic profile in z -direction as well, and thus cause an additional displacement of the bead in flow-direction, i. e. the x -direction of the channel. Since z -displacements were taken into account neither when simulating the system nor for the analytical calculations, these additional degrees of freedom result in significant deviations from the assumed state of the system.

Further important influences to the accuracy of the positioning system of particles in the x - y -plane need to be considered. Although the placement in this plane can be performed with high precision, a quite significant challenge arises in context with the visualization system of the setup: The particles need to be placed in a certain distance away from the walls. The wall itself, as well as the particles, are visible due to differences in refractive index as compared to the surrounding fluid. The contact line with the other medium shows in the pictures as a fuzzy black line. Since the channel walls were produced using a mold which again was manufactured utilizing lithography techniques, small deviations from the ideal case are natural. Thus, the walls are never flat but

slightly rough and they are also not exactly perpendicular in respect to the microscope slide. Typically, the angle shows slight deviations of up to a few degrees, which leads to the contact line showing up as a broad band with a width of multiple pixels. An exact determination of the position of the walls, and thus also of the distance of a colloid to it, becomes a highly non-trivial problem. All distance estimations need to be considered as erroneous with error bars of about $2\mu m$ which equals the radius and thus half the size of the colloids used in all experiments. The error should not lead to a strong deviation from the assumed linear velocity profile as figure I.6.15 shows, but it might lead to a misinterpretation of the influence of the wall on the bead and the effective viscosity it experiences, as given by Faxén’s law (Eq. I.4.9).

The final contribution to the total possible error is the most important one on the whole list besides the aforementioned temporal fluctuations of the flow velocity. It was already mentioned beforehand in the section detailing the calibration of the setup (Fig. I.6.6) and is probably the main reason for the strong discrepancy between analytical/numerical results for C_{xy} (Fig. I.5.7) and their experimental counterparts (for instance in Fig. I.6.17). It can be encompassed by the name “frame of reference misalignment” and is caused by a relative tilt of the main axis of the microchannel versus the oscillation direction of the piezoelectric stage or the frame of the camera, respectively. As soon as one of these three coordinate systems are not properly aligned in respect to each other, this leads to a misinterpretation of, for instance, an oscillation in y -direction as an oscillation partially in the y -direction but also partially in the x -direction. In the equations I.6.3 and I.6.4 as well as the following modified correlation functions, the tilting angle of the camera in respect to the oscillation direction of the piezoelectric stage was related to the mixing percentage p of the displacement signals in x - and y -direction. For small percentages p , the deviation from the result that one would measure in the reference frame S , are minor. However, it is never possible to achieve a perfect alignment and additionally the tilting angle changes over time (i. e. over the course of a whole session of measurements) due to small vibrations. Thus, the tilting angle is never exactly known and it is hence not possible to correct it in the data sets by hindsight. As mentioned in section I.6.3, in advance to the conduction of every measurement session, the tilting angle was calibrated to lie below 0.1° which indicates a mixing percentage $p \ll 1\%$. However, due to the continuous misalignment over time the exact estimation of p is in consequence not possible. Since the cross-correlation signal C_{xy} is strongly dependent on the exact alignment of the recording device in order to determine the local shear rate the much more robust auto-correlation quotient $C_{xx,osc}/C_{yy,osc}$ should be used instead.

I.7. Discussion

Up until now, there have not been many studies of Brownian motion in shear flows and its correlation functions. Only three publications allow the direct comparison and classification of results: In two of them, Brownian motion is studied on an analytical basis [18, 19] while the third one [5] uses a setup of optical tweezers for the examination of one single as well as two neighboring colloids in a linear shear flow. The comparison of the cross-correlation functions in shear flow with the results reported by Bammert, Holzer, and Ziehl in these earlier studies reveals the same characteristics - i. e. the asymmetry in respect to time of the correlation peak in C_{xy} - and thus proves the robustness of the setup as well as the experimental results. However, in all of these studies only passive Brownian motion without any additional external forces was studied. The addition of oscillatory motion of the optical traps is a novelty that has not been attempted before yet. Still, we have to admit that, due to the large error in the phase shift, our data does not allow a conclusive interpretation. The precise control of the flow rate remains an open issue.

Although there is quite a number of quantifiable and non-quantifiable error sources, it is still feasible to identify experimental correlation functions with their analytical counterparts and find the predicted behavior as proven in section I.6.4. Also, an estimation of the shear rate using equation I.4.38 can be performed, which at the very least gives a guess of $\dot{\gamma}$ (assuming a calibrated setup and a lot of care handling the error sources of course).

I.8. Summary

In part I of this thesis, a setup of optical tweezers was utilized to examine single colloidal particles in a stationary shear flow. This system was then driven further out of equilibrium by applying forced oscillations perpendicular to the flow direction through a microchannel. The auto- and cross-correlation functions of the colloid were used to visualize its reaction to the perturbations.

For this purpose, in chapter I.3 the theoretical description of the interaction of a colloid with a strongly focused laser beam, the central element of a setup of optical tweezers, was explained. Since it depends on the relative size of the particles as compared to the wavelength of the electromagnetic radiation, the corresponding formulations in all size regimes, the Rayleigh regime, the Mie regime, and the ray optics regime, were included. However, for small displacements from the center of the optical trap the interactions can be simplified to a harmonic potential or a linear restoring force, respectively, which then was applied in the following chapters.

In chapter I.4, a close look was taken at a pressure-driven fluid flowing through a microchannel with a rectangular cross-section. The complete Navier-Stokes equation was simplified to a Stokes equation which contains all the necessary components to characterize such a flow, assuming that it will always stay laminar, in other words no turbulence will evolve. An analytical solution to this problem was already found earlier by Pozrikidis [50] and led to the conclusion that the evolving parabolic Poiseuille profile in the vicinity of the side walls of the channel by a local linear velocity profile can be described. This profile was afterwards included in the differential equation of motion for a colloid confined in an optical trap. These differential equations are so-called Langevin equations since they include stochastic forces, and they were solved for the cases of a fixed position of the optical trap (Sect. I.4.3) as well as for harmonic oscillations perpendicular to the flow direction (Sect. I.4.4). The corresponding correlation functions were also determined. They showed that, for an oscillating trap in a linear shear flow, all correlation functions can be described by a linear superposition of the case of a colloid in a shear flow without forced oscillations and the correlation functions of pure shear-coupled oscillations without Brownian motion.

The following chapter I.5 featured a detailed numerical analysis of the system in all aforementioned configurations. The basis was given by the Langevin equations from the analytical chapter, which were then solved numerically. The resulting displacements and especially their correlation functions were analyzed and compared to the analytical re-

I.8. Summary

sults. A good agreement between both of them was found, which even made a parametric study of the system feasible.

The central chapter of this study is the experimental realization of the system presented in chapter I.6. A setup of optical tweezers was chosen for this purpose, the construction of which was explained in detail in section I.6.1. The same goes for all software necessary for data acquisition and evaluation (Sect. I.6.2). Special care was taken in the introduction of the calibration methods (Sect. I.6.3) that were applied to the setup on a very regular basis in order to ensure a correct estimation of forces in section I.6.4. There, a number of experiments were presented, including measurements in a quiescent fluid, in a linear shear flow, and the same measurements with an oscillating optical trap. Their auto- and cross-correlation functions could be compared to the corresponding analytical description of the system and to the numerical results. In the quiescent and the shear flow case without forcing, a good qualitative and quantitative agreement to theory could be found. When adding the forced oscillations to the system, though, it became increasingly difficult to match both, however, a qualitative agreement in all important features could be shown. Also, a methodology was introduced that allowed the determination of the shear rate in the system from the relation of the amplitudes of the oscillatory contributions to the auto-correlation functions. These results were critically discussed in the following chapter I.7 and possible error sources were identified. The most important among these is the tilt of the high-speed camera in the experimental setup against the frame of reference of the piezoelectric stage, which leads to a mixing of the x- and y-displacement signals. Thus, all correlation functions are given as mixtures of all other auto- and cross-correlation functions, which makes a precise evaluation of the data sets a big challenge and also requires a very exact alignment of the setup beforehand.

This work contributes to the general understanding of colloids under Brownian motion and, according to the knowledge of the author, it shows for the first time how forced oscillations perturb their behavior in a linear shear flow. A setup of optical tweezers is currently one of the few, if not even the only setup that allows measurements of Brownian fluctuations in a shear flow or other similar profiles. Thus, it is not surprising that only few studies have been published so far about this topic. Still, the presence of an active flow and the additional oscillatory forcing of particles increase the necessity of a daintily calibrated setup which does not ease its handling. Its strong susceptibility to perturbations and vibrations of any kind add immensely to the challenge of gaining clear measurements. However, when not working with active displacements of the optical trap but with a trap in rest instead, the high sensitivity of particle detection helps in making even the smallest displacement visible and thus reveals the most interesting cross-correlation behavior. In the opinion of the author, the system is best suited for measurements not involving any active displacement of the sample cell.

There is still a multitude of open questions which do not involve any active motion of the sample cell, for example experiments in different flow profiles like elongational flows. A study was already attempted by Matthias Werth [68] before, but he encountered many problems with flow stability and the detection of the stagnation point of the profile. Also, questions concerning complex fluids as well as their flow and correlation functions would be an enthralling topic. Will the cross-correlation function of a polymer in a shear flow look like the one in water or similar Newtonian fluids? Since polymers show interesting dynamics in un- and refolding and due to their length also orient in the flow, the answer is: probably not! But before actually attempting a study of these materials, nobody will know for sure.

As far as further improvements of the setup are concerned, three properties in context with the correlation studies which are so far not controlled in their entirety yet come to mind. If a control of them was possible, it would be a huge benefit to any experiment. Until now, the local temperature in direct vicinity of the bead in the optical trap has been unknown. Assumptions about it can be made due to the knowledge of the bead material and the surrounding fluid [66], however, a direct measurement of this quantity or, even better, a means to control the temperature within the sample cell would be favorable. Due to the small channel size of the typical microfluidic device, no easy way of implementing it is obvious.

Another feature that would represent a huge benefit in handling the setup is a means to do a live online measurement of the flow profile and the velocity. This would help in determining whether, during an experiment, temporal or spatial fluctuations, which may originate from a blockage in the microchannel occur. It would also help in a different context: As shown in the past chapters, the correlation measurements allow the determination of the local shear rate. However, since there is currently no other method included in the setup that would give a comparative measurement, it is so far not possible to perform tests with the method introduced here and to check on its accuracy or precision. Such comparisons should be performed before the method can be applied safely.

It would also be very handy to have a better means to determine the exact position of the trapped beads relative to the confines of the microchannel than just the visualization by the high-speed camera. As discussed in chapter I.7, one of the most influential error sources is the positioning of the beads, hence an improvement to it would be very desirable. The same goes for the technique utilized for the production of the microchannels. The manufacturing of the channels is performed by micromolding in PDMS and this technique always causes a certain surface roughness, which is not very helpful in determining the exact lateral distance.

To draw a final conclusion, one can say that a setup of optical tweezers is one of the few and best tools if one wants to evaluate correlation functions of Brownian motion.

I.8. Summary

However, the realization of these measurements becomes somewhat fiddly when active forcing of the system is involved, as presented in this part of the thesis. It is possible to find agreement between the theoretical model and experimental results, even if the agreement is not quantitative in all regards. Thus, the results from this part build a solid basis for the examination of DNA molecules in part III of the thesis. They will help to understand the shear coupling, which in that case will happen out of the optical plane, and to draw conclusions on the reaction of the DNA to it.

Part II.

Macro- & Microrheology
of Mucus

II.1. Introduction

This part focuses on mucus, a biological fluid of great importance in humans and most animals. It can be found as covering layer on top of most organs that are in physical contact with the external environment. Among others, this is the case in the gastrointestinal, respiratory, and urogenital tract, as well as the eye tissue. It is mainly composed of water (90 – 98 wt %) and mucin-type glycoproteins, also known as short mucins (2 – 5 wt %), but also contains salts, fatty acids, phospholipids, cholesterol, DNA, and other proteins [69, 70]. In healthy humans, a total daily amount of about 1 L – 1.5 L of mucus is synthesized by specialized goblet cells in the columnar epithelium. Its main function is that of a selective barrier. On the one hand, it protects cellular surfaces from mechanical influences like friction [71] and prevents the penetration of foreign molecules like pathogens, toxins, and other small particles [70]. On the other hand, it allows the passage of nutrients, antibodies, and cells of the mucosal immune system [72]. Additionally, it also maintains the water balance in the cell [73].

For pharmaceutical purposes, especially the respiratory mucus occurring in the trachea is a major concern. Many drugs that are applied through the windpipe, for example

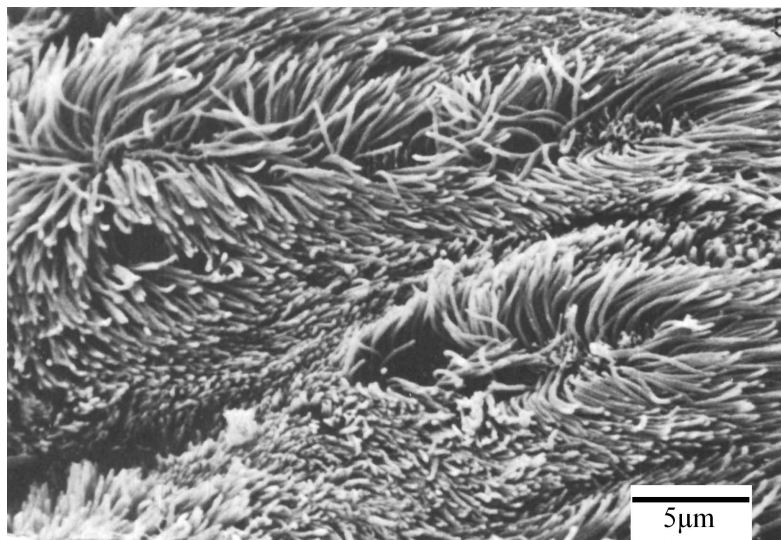


Figure II.1.1.: Scanning-electron-micrograph of the cilia found in the rabbit trachea (adapted from [74]). In our study, the cilia are not considered. We only investigate the rheological properties of mucus, the fluid the cilia are in contact with.

II.1. Introduction

a spray, have to reach the cell membrane by diffusing through this particular mucus layer. In the trachea, the epithelium is covered by the periciliary layer (PCL) followed by a mucus layer. The PCL again contains hair-like structures, the so-called cilia, which are surrounded by a low viscosity fluid containing tethered mucins. These cilia move to a particular beating pattern [74], leading to an acceleration of the upper mucus layer, which in turn causes the removal of entangled waste (Fig. II.1.1). This process is also known as clearance. The PCL is kept stable during this process in order to always keep the epithelium covered by a hydrated film. Depending on the organism (human or animal) and the body site, mucus turnover times may vary between less than an hour up to more than 24 hours [75]. In the pharmaceutical context this poses a huge challenge since drugs only have this rather limited amount of time to diffuse through the mucus layer. Optimization of drugs and their carriers is necessary to effectively transport them to their site of operation and, at the same time, allow them to dissolve and find their way through the mucus mesh.

In this part of the thesis, samples of respiratory mucus from horses are analyzed using bulk (Ch. II.4.2.1) and microrheology techniques (Ch. II.4.2.2). For objects much larger than the mean pore radius, the mucus mesh is found to behave as a viscoelastic solid with high resistance to penetration. Smaller objects in the order of magnitude below the pore radius may move through the material with only slight hindrance with mucus showing properties similar to those of water. On intermediate length scales, though, a mixture of passive and active microrheology reveals fascinating properties: While passive measurements hint at a fluid of low viscosity, displacements bigger than hundreds of nanometers in the active measurements are typically immediately hindered. Besides information about the shear modulus, a spatial mapping of pore sizes which shows that microrheological studies depend strongly on the position within a sample where they are conducted is performed. By gaining more insight into the interaction of particles with the mucus mesh, a further step can be taken towards understanding the selective filtering mechanism of mucus. This might lead to a possible way of drug optimization to make their transport through the mucus layer more efficient. This study was conducted in cooperation with several groups of the pharmaceutical department of Saarland University. Partially, the results have already been published and discussed [76]. There, mucus properties were analyzed with the combined effort of atomic force spectroscopy, capillary penetration, and microrheologic experiments, which, together with cryogenic scanning electron micrographs, were considered to draw conclusions on the diffusion behavior of colloids within the material. The study presented here expands on the rheologic considerations.

II.2. Literature Survey

For centuries, mucus has been a much studied topic. This is not much of a surprise since its role as a selective barrier in the human body is a very important one. However, the means to characterize the material using rheological methods have only become available in the late half of the 20th century. The first reported rheological study of mucus was published in 1963 by Robert Denton [77], who experimented with a rotational viscometer on human lung mucus. Many more studies followed in the following decades giving a deeper insight into the material properties [78, 79, 80, 81]. However, all results concentrated on the macrorheology of mucus since techniques that allowed a close examination of the microstructure and microscopic behavior of the material were not available yet.

As we know today, mucus is a viscoelastic gel mostly consisting of water and mucin-type glycoproteins. These mucins form the walls of porous material, while an aqueous solution fills the gaps in between. The average thickness of respiratory mucus in humans averages to $15\ \mu\text{m}$ [75]. The pore spacing ranges, according to recent studies, from $40\ \text{nm}$ up to several micrometers [76, 82]. This indicates that a material characterization on the micro- and nanometer scale might be the key to understand the barrier properties of mucus. Technology and techniques for this purpose became available in 1997 in the form of high-speed cameras and the theoretical framework for particle tracking [83]. A particle immersed in a fluid experiences impacts by the surrounding fluid molecules coming in from all directions and leading to an arbitrary, tumbling motion, the so-called Brownian motion [11] (compare also Pt. I). The particle trajectories can be related to the intrinsic rheological properties of the fluid, in other words its shear modulus. Due to the size of the used particles, this technique counts as a microrheology technique.

In the past decade, many studies which focused on the behavior of small particles or molecules in different kinds of mucus were published. The typical mesh spacing of cervical mucus was reported to range between $20\ \text{nm}$ and $200\ \text{nm}$ with an average value of $100\ \text{nm}$ [72]. More recent studies show, that depending on the particle types or molecules used in the studies, it is still possible for them to diffuse through the pores when their size is bigger ($\sim 500\ \text{nm}$) [84]. Studies for horse respiratory mucus show that pore sizes in the periciliary layer (PCL) are typically smaller than $40\ \text{nm}$ [82], while in the floating top layer pore sizes between $100\ \text{nm}$ up to several micrometers are common [76] (Fig. II.2.1). This indicates that, in the biological system, the most interesting length scale in the rheological sense lies below the micrometer range.

II.2. Literature Survey

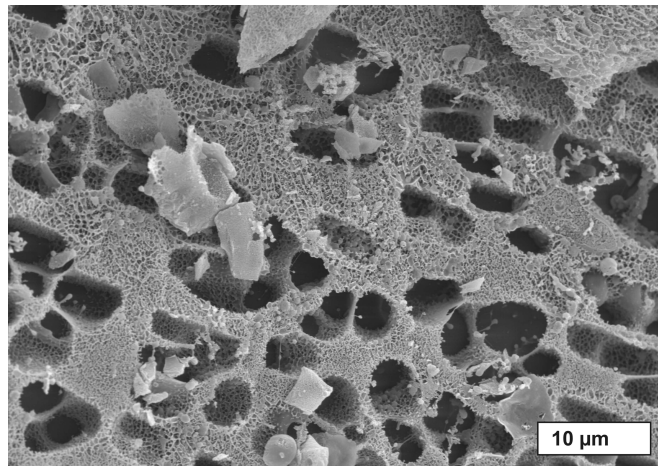


Figure II.2.1.: Cryo-scanning-electron micrograph of respiratory horse mucus (adapted from [76]).

II.3. Rheology of Fluids

Fluids and their flow have always been an important topic. When our planet was formed billions of years ago, the flow of matter crucially determined the shape it has today. But also now, in everyday examples, it remains a topic of open questions and many challenges. When opening a water tap, how will the water flow out? What will happen when it impinges on the surface of the sink?

A first, albeit simple, description of the flow of fluids was achieved by Sir Isaac Newton in 1687 [85]. He defined the viscosity η as a measure of resistance the fluid will put up against flowing. Assuming two parallel plates of area A in a distance d where one plate is fixed, while the other one is moved at a constant velocity v , the shear stress τ acting on the fluid is described by

$$\tau = \frac{F}{A}. \quad (\text{II.3.1})$$

The force F is given by

$$F = \eta v \frac{A}{d}, \quad (\text{II.3.2})$$

which through division by the area A leads to

$$\tau = \eta \dot{\gamma}. \quad (\text{II.3.3})$$

The shear rate $\dot{\gamma}$ is defined by the decrease in velocity when moving from the surface of the moving plate to the resting one. With this formula, Newton succeeded in finding the easiest way to describe a flowing fluid. It only applies to a small class of fluids, which were later denoted Newtonian fluids in his honor. Among these count water, glycerol solutions, air, and many more. There is a broad range of fluids, however, whose flow behavior is not grasped by this constitutive equation. Instead, it is necessary to take elastic properties into account.

One way of doing so was found by James Clerk Maxwell in 1867 [86] who considered the dynamical behavior of gases. Elastic properties of pure solids are given by the equation of the Hookean spring

$$\sigma = E\epsilon, \quad (\text{II.3.4})$$

where the tensile stress σ is linked to the elongation ϵ of the spring by the means of

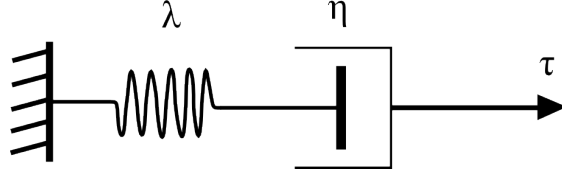


Figure II.3.1.: Equivalent circuit diagram of the Maxwell model. It is composed of a spring daisy-chained with a dashpot. A characteristic viscosity η and a relaxation rate λ suffice to describe the dynamic behavior of the system.

Young's modulus E as a constant of proportionality. Maxwell then combined both models by daisy-chaining an elastic Hookean spring with a viscous dashpot as depicted in figure II.3.1. The stress τ (or respectively σ) has an effect on both elements, so that the total strain γ (or respectively ϵ) is given as the sum of the elastic and viscous strain

$$\gamma = \gamma_e + \gamma_v. \quad (\text{II.3.5})$$

By calculating the derivative of this equation in respect to time and inserting the representations of the Newtonian fluid (Eq. II.3.3) and Hookean spring model (Eq. II.3.4), one arrives at the constitutive equation of Maxwell's fluid model, which reads

$$\dot{\gamma} = \frac{\dot{\tau}}{E} + \frac{\tau}{\eta}. \quad (\text{II.3.6})$$

Multiplication of this equation with η finally leads to the well-known notation of this model

$$\tau + \lambda \dot{\tau} = \eta \dot{\gamma}, \quad (\text{II.3.7})$$

where the relaxation rate λ is defined as the quotient of the viscosity and the elastic modulus. In terms of complexity, this model is the easiest way to include elastic as well as viscous properties into a material description. In terms of gaining a solution of this differential equation, performing a Fourier-transform is the simplest way. This gives

$$\tilde{\tau}(\omega) + i\lambda\omega\tilde{\tau}(\omega) = i\eta\omega\tilde{\gamma}(\omega) \quad (\text{II.3.8})$$

which by recasting leads to the complex shear modulus [49]

$$\tilde{G}(\omega) := \frac{\tilde{\tau}(\omega)}{\tilde{\gamma}(\omega)} = i \frac{\eta\omega}{1 + i\lambda\omega}. \quad (\text{II.3.9})$$

This expression can be expanded and subdivided into a real - or elastic - part G' and an

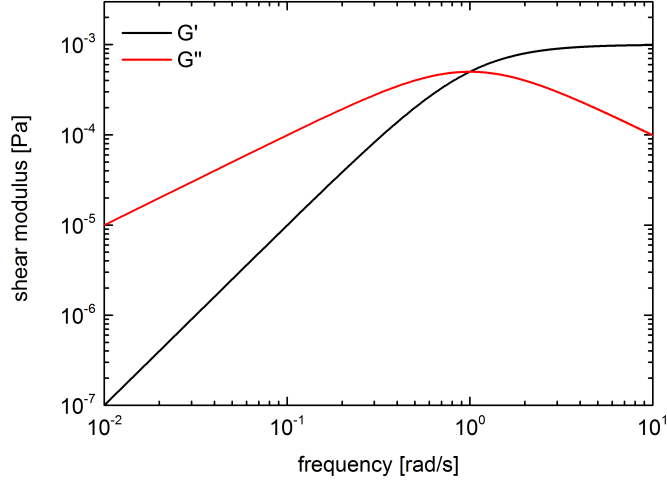


Figure II.3.2.: Typical curve progression of the shear modulus according to Maxwell's model. The elastic contribution increases proportionally with ω^2 before reaching a constant value at the characteristic frequency $1/\lambda$. The viscous contribution increases proportionally with ω at first before beginning to decrease proportional to ω^{-1} upon exceeding $1/\lambda$.

imaginary - or viscous - part G''

$$G'(\omega) := \mathcal{Re} \{ \tilde{G}(\omega) \} = \frac{\eta\lambda\omega^2}{1 + \lambda^2\omega^2}, \quad (\text{II.3.10})$$

$$G''(\omega) := \mathcal{Im} \{ \tilde{G}(\omega) \} = \frac{\eta\omega}{1 + \lambda^2\omega^2}, \quad (\text{II.3.11})$$

so that the complex shear modulus¹ is defined as $G(\omega) = G'(\omega) + iG''(\omega)$. More information on the significance of G' and G'' will follow in the next chapter. Their typical curve progression of a Maxwell fluid is depicted in figure II.3.2. Besides the complex shear modulus, a complex viscosity can be defined as $\eta^*(\omega) = -iG(\omega)/\omega$, where $\eta^*(\omega) = \eta'(\omega) - i\eta''(\omega)$.

While a basic handling of complex, viscoelastic fluids is now possible using this framework, it is still not sufficient for most polymers. Many of them do not only show a single relaxation rate but a whole relaxation spectrum. Fortunately, the versatility of this model can be expanded tremendously by shunting multiple spring-dashpot-elements, which from now on will be denoted as Maxwellian elements. Then, the total shear modulus is given as a sum over all partial Maxwell contributions

$$G(\omega) = \sum_i G_i(\omega), \quad (\text{II.3.12})$$

¹From now on, the tilde-symbol will be omitted from quantities expressed in frequency-space.

II.3. Rheology of Fluids

which leads to

$$G'(\omega) = \omega^2 \sum_i \frac{\eta_i \lambda_i}{1 + \lambda_i^2 \omega^2}, \quad (\text{II.3.13})$$

$$G''(\omega) = \omega \sum_i \frac{\eta_i}{1 + \lambda_i^2 \omega^2}. \quad (\text{II.3.14})$$

Although, under normal circumstances, it is not necessary to take a huge number of Maxwellian contributions into account, at least two of these should definitely be utilized. When considering the behavior of the viscous modulus in figure II.3.2, it becomes apparent that for large frequencies, G'' approaches a value of $0 Pa$. This, however, is equivalent to a continuously decreasing dissipation of energy. If a real fluid is examined, such a behavior cannot be found at all; rather, the dissipation increases more and more. If one Maxwellian element is shunted with a purely Newtonian one, i. e. a dashpot is added in parallel to the model presented in figure II.3.1, this leads to the desirable effect of a steadily increasing G'' . Furthermore, this has no effect on the elastic modulus. Such a two-component model is denoted Jeffrey's model [49], which will play an important role later on in context with microrheology.

II.3.1. Macrorheology

There is a number of means which allow the determination of the shear modulus of fluids. One of them, the conicylindrical viscometer, was proposed by Mooney and Ewart in 1934 [87]. First applications of the concept followed about 10 years later by Russell [88], who used it for normal stress measurements. This led to a huge increase in popularity of the instrument. Many more studies followed, for instance about the flow behavior of industry oils [89] and molten polyethylene [90]. It also caused an increased interest in the development of devices that enable rheometric experiments. Among other concepts, the cone-plate viscometer was invented in 1950 by Higginbotham [91], who intended to use it to "determine the flow curves of anomalous fluids over a wide range of rates of shear". A few years later, McKennell established the instrument for the use with Newtonian fluids under lower shear rates as well [92]. Since then, the popularity of the cone-plate rheometer has risen tremendously to a point where it is used as a standard tool for such experiments.

A cone-plate rheometer consists of a fixed bottom plate over which a rotor is aligned. It has a conic shape - however, in order to avoid damage to the bottom plate, in case of most commercially available instruments the tip of the cone is flattened. The distance between cone and plate can be controlled by a motor. The same is true for the rotation angle and velocity which can be set by a second motor. More details about the instrument utilized in this study will be presented later (Sect. II.4.1.1).

The typical experiment performed in a cone-plate rheometer is a continuous shear

experiment. For this purpose, a constant shear stress is set and the evolving shear rate can be measured after a certain amount of equilibration time. Based on their principle, these experiments are also denoted controlled stress (CS) experiments. The opposite is possible, too, by setting a shear rate and measuring the stress (controlled rate experiment, CR). Complex fluids differ from Newtonian fluids by showing shear-thickening or -thinning effects which become obvious in non-linear flow curves, i. e. the viscosity versus shear rate behavior. The extraction of elastic and viscous properties from the fluid under examination, however, is not possible. This can be achieved by performing a small amplitude oscillatory shear (SAOS) experiment [93]. In a controlled deformation (CD) experiment, the shear strain γ is oscillated by applying a forced sinusoidal rotation to the rotor. This leads to

$$\gamma(\omega, t) = \gamma_0 \sin(\omega t) \quad (\text{II.3.15})$$

with a certain strain amplitude γ_0 and frequency ω . The fluid will respond with an equally oscillating shear stress

$$\tau(\omega, t) = \tau_0 \sin(\omega t + \delta) \quad (\text{II.3.16})$$

with a certain amplitude τ_0 . Although the stress oscillations will happen at the same frequency, usually a phase shift δ becomes apparent since the fluid needs a certain amount of time to adapt to the shearing. For Newtonian fluids, this shift equals $\pi/2$ because the fluid reacts to changes in shear rate and not in shear strain. Purely elastic solids, however, react to shear deformations and thus show no phase shift. If a viscoelastic material is considered, a phase shift in between these two extrema will result.

Equation II.3.16 can be simplified using addition theorems [59] to give

$$\tau(\omega, t) = \underbrace{\tau_0 \cos(\delta)}_{\tau'} \sin(\omega t) + \underbrace{\tau_0 \sin(\delta)}_{\tau''} \cos(\omega t), \quad (\text{II.3.17})$$

which also leads to the relation

$$\tan(\delta) = \frac{\tau''}{\tau'}. \quad (\text{II.3.18})$$

If now the shear stress amplitude is divided by the shear deformation amplitude, as defined by equation II.3.9, one gains the real and imaginary part of the shear modulus

$$G'(\omega) = \frac{\tau'}{\gamma_0}, \quad (\text{II.3.19})$$

$$G''(\omega) = \frac{\tau''}{\gamma_0}. \quad (\text{II.3.20})$$

According to its definition, the real part of the shear modulus contains all information

II.3. Rheology of Fluids

about the elastic properties of the fluid. This can now be easily understood since $\tau'(\omega)$ only gives the in-phase response of the fluid. Equivalently, the imaginary part of G describes the viscous properties since it depends only on the out-of-phase response. This theoretical framework for SAOS experiments using a rheometer will be applied in section II.4.2.1 to gain insight on the flow properties of mucus.

II.3.2. Microrheology

In 1995, Mason and Weitz published an article about how the shear modulus can be extracted from particle trajectories that are confined in an optical trap [36]. They were able to relate the Laplace-transformed trajectories to the shear modulus $\tilde{G}(s)$. However, before being able to make meaningful conclusions about the material, a fit of these data sets and an extrapolation was necessary. It was only then, that it became possible to determine the shear modulus $G(\omega)$ which is equivalent to the macrorheological data gained by SAOS experiments in a rheometer (see past section). Due to the small size of the spheres on the micro- to nanometer scale, this technique was labeled microrheology. It was used during the past 15 years to examine a broad range of fluids like polyethylene oxide [83, 94], but also biological fluids like actin solutions [95] and biomaterial hydrogelators [96], of which typically only small amounts are available. Since microrheology techniques only have small volume requirements, they are perfectly suited for this task.

Two years later, in 1997, Schnurr et al. published a method which allows to determine the frequency-dependent shear modulus by calculating the power spectral density of colloidal motion [97]. This method comes with the advantage that no fitting or extrapolating is necessary in order to identify $G(\omega)$. Like the other method, this one was also applied to a wide variety of fluids. Among the researched materials count polyacrylamide gels [98], the fd virus [99], actin networks [42], aging colloidal glasses [100], and many more. Since it is also the method of choice in this thesis, a few more details about the theoretical background of microrheology shall be added here. An in-depth calculation including a detailed discussion about the feasibility of this method can be found here [101].

As a starting point, the same Langevin equation of motion that was already introduced in part I (Eq. I.4.14) can also be used here. A generalization has to be applied to the coefficient of friction ζ since the fluids under examination will not be non-elastic Newtonian fluids but rather complex, viscoelastic ones. Thus, ζ becomes a time-dependent function instead of a constant and Stokes' friction force can be written as

$$\vec{F}_{fric}(t) = \int_0^t dt' \zeta(t-t') \vec{v}(t'). \quad (\text{II.3.21})$$

Since it takes all past deformations of the fluid into account, this type of function is also

called memory function. Inserting it into equation I.4.14 gives the modified Langevin equation for complex fluids. Since the position of the trap will not change during the conduction of a measurement, $x_{trap}(t)$ can be set to zero. Also, this equation will be valid for all directions of motion because there is no additional flow or any other effect that would have an impact on the corresponding differential equation. By Fourier-transforming and recasting the equation, the following formulation is reached:

$$\tilde{x}(\omega) = \frac{1}{\underbrace{k - i\omega\tilde{\zeta}(\omega)}_{\tilde{\alpha}(\omega)}} \tilde{F}_{r,x}(\omega). \quad (\text{II.3.22})$$

The susceptibility $\tilde{\alpha}$ can be considered as the response function of the fluid that links displacements to the stochastic force. It contains all relevant information to characterize the fluid rheology. It is related to the shear modulus by

$$G(\omega) = \frac{1}{6\pi r_c} \frac{1}{\tilde{\alpha}(\omega)}, \quad (\text{II.3.23})$$

hence

$$G'(\omega) = \frac{1}{6\pi r_c} \frac{\tilde{\alpha}'(\omega)}{|\tilde{\alpha}(\omega)|^2}, \quad (\text{II.3.24})$$

$$G''(\omega) = \frac{1}{6\pi r_c} \frac{\tilde{\alpha}''(\omega)}{|\tilde{\alpha}(\omega)|^2}. \quad (\text{II.3.25})$$

Still, the challenge remains to relate measured displacement data of the beads to $\tilde{\alpha}$. This can be achieved by calculating the power spectral density, which is in turn related to the imaginary part of the susceptibility by [97]

$$\tilde{\alpha}''(\omega) = \frac{\omega}{2k_B T} \langle |\tilde{x}(\omega)|^2 \rangle. \quad (\text{II.3.26})$$

A Kramers-Kronig relation helps to determine the real part by solving [102]

$$\tilde{\alpha}'(\omega) = \frac{2}{\pi} \mathcal{P} \int_0^{\infty} \frac{\omega' \tilde{\alpha}''(\omega') - \epsilon \tilde{\alpha}''(\epsilon)}{\epsilon^2 - \omega^2} d\epsilon. \quad (\text{II.3.27})$$

The integral given here is a so-called principal value integral, indicated by the ‘‘P’’ in the integral symbol. This means that the two occurring singularities at $\omega = \pm\epsilon$ are omitted from the integration, while the remaining interval is solved as usual. In case of the experiments presented later, the integration is performed numerically and only the poles are left out.

The framework introduced here allows to determine the complex susceptibility and thus the shear modulus of a fluid straight away. The only thing required is the displacement data of a passive tracking experiment of a particle in an optical trap, or,

II.3. Rheology of Fluids

respectively, the power spectral density of that quantity. Care has to be taken when interpreting the real part of the shear modulus since it does not only contain the elastic properties of the fluid but also those of the optical trap itself. However, the contribution of the trap can be quantified as being frequency-independent and defined by [41]

$$G'_{trap} = \frac{k}{6\pi r_c}. \quad (\text{II.3.28})$$

Hence, the true elastic modulus of the fluid can be gained by subtracting equation II.3.28 from II.3.24.

II.3.3. Summary

Part II of this thesis deals with measuring and interpreting the rheological properties of mucus which is a complex biological fluid. Hence, a framework which allows its examination needs to be established. Two different devices, the cone-plate rheometer and a setup of optical tweezers, were introduced in this chapter. While both of them enable the measurement of the shear modulus G , there is an important qualitative distinction: The rheometer determines bulk properties of a comparatively large volume of fluid, while a setup of optical tweezers accesses the local material properties in the direct vicinity of a probe particle. Hence, both methods are respectively denoted as macro- and microrheology.

At first, the model of a Maxwell fluid was introduced. Besides the properties of a purely viscous, Newtonian fluid, it also shows elastic behavior similar to that of a solid. Thus, a constitutive equation which encompasses both features can be derived. By solving the arising differential equation in frequency-space, the shear modulus is given by the quotient of shear stress and strain. In general, it is a complex quantity whose real part describes the elastic features of the fluid under examination, while its imaginary part encompasses the viscous ones. However, in order to gain a realistic model of a fluid, a second Newtonian dashpot has to be shunted with the Maxwell model, thus leading to Jeffrey's model of a fluid. Otherwise, when increasing the driving frequency ω , the imaginary part of the shear modulus will decrease towards zero, indicating a decrease in energy dissipation at the same time.

In section II.3.1, the principle of small amplitude oscillatory shear (SAOS) experiments was introduced. For this macrorheological technique, a classical shear rheometer like the cone-plate rheometer is required. The rotor is then oscillated at very small amplitudes over a wide range of frequencies to record the material response. Equivalently to the driving shear strain γ , the responding shear stress τ is also given by a sine function. However, the response may be phase-shifted to a certain degree depending on the fluid under examination. For viscoelastic fluids, the phase shift is found in between the extrema of a Newtonian fluid and an ideal solid, however, it may vary with the driving frequency.

In section II.3.2, a setup of optical tweezers with the goal to examine the microrheological properties of a fluid was considered. By immersing small spherical particles into a fluid, they will collide with a multitude of fluid molecules and thus start to tumble arbitrarily. It is possible to compose a stochastic Langevin equation which contains all forces influencing the particle motion and which can be solved in frequency-space. This finally allows to determine the local shear modulus of the fluid by analyzing the shivering of a confined bead. While for Newtonian fluids the microrheological shear modulus equals the macrorheological one, significant differences may be found when considering complex fluids with a local microstructure. This will be discussed in chapter II.5.

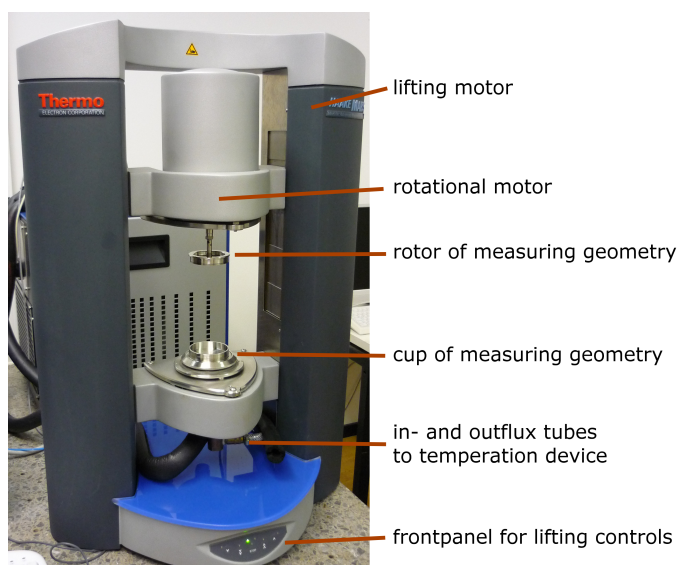
II.4. Experimental Study

In this chapter, details will be given about the experimental study. At first, the cone-plate rheometer and the setup of optical tweezers will be explained which were utilized for the conduction of all experiments in part II. Then, information about the performed experiments as well as their results will follow in section II.4.2. A part of their discussion will happen there, too. Most of it is contained in chapter II.5.

II.4.1. Experimental Setups

II.4.1.1. Rheometer

For the macrorheological examination of fluids, a rheometer can be used. This is a device that allows very precise shearing of fluids and synchronous normal force/stress measurements in a wide variety of geometries like cone-plate, plate-plate, Taylor-Couette-cylinder geometries, and many more [103]. For this study, the rotational rheometer



(a) Photograph of the HAAKE MARS II rheometer. All important components have been marked in the picture.



(b) Photograph of the cone-plate geometry C60/0.5°. It consists of a rotor (upper left part) and a cup (upper right part) as well as a plastic top cover with sponges (lower part).

Figure II.4.1.: Photograph of the utilized rheometer HAAKE MARS II as well as all of its crucial components.

II.4. Experimental Study

HAAKE MARS II (Fisher Scientific GmbH, Schwerte, Germany) was used in combination with a cone-plate geometry (C60/0.5°-Ti, Fisher Scientific GmbH, Schwerte, Germany). The geometry has a diameter of 6 cm and an angle of 0.5° of the cone mantle in respect to the bottom plate. Then, the sample volume amounts to 500 μL . In order to avoid undesirable evaporation of the sample fluid, the rotor can be additionally covered by a plastic top cover. Sponges attached to its interior can be soaked with water in advance of an experiment, so an atmosphere saturated with water around the geometry is maintained during the measurements. The rheometer and the geometry are depicted in figure II.4.1.

The rheometer itself consists of a fixture for the cup of the geometry and a rotational motor which can be adjusted in height above it. The rotor of the geometry is attached to the motor by a screw. A height adjustment motor built into the side poles of the device allows precise control of the distance between bottom plate and rotor, which due to the specifications of the C60/0.5° needs to be set to 26 μm . During the conduction of an experiment, the temperature of the fluid can be controlled by water-tempering the cup. This is achieved by a thermostat (HAAKE Phoenix II, Fisher Scientific GmbH, Schwerte, Germany) which is attached to the bottom fixture by tubes.

The HAAKE MARS II offers a wide range of measurement types with adaptable protocols. Thus, continuous shear experiments, small and large oscillatory shear experiments, creep-recovery tests, and many more are possible. However, since the viscoelastic properties of mucus are of interest, only amplitude- and frequency-sweeps were performed, which both count as small amplitude oscillatory shear experiments (SAOS). The details of the measurement protocol will follow in section II.4.2.1.

II.4.1.2. Optical Tweezers

The setup of optical tweezers utilized for the microrheological characterization of mucus is identical to the setup in the first part of this thesis (Sect. I.6.1). Since no flow control is necessary for the experiments with mucus, the corresponding part of the setup was not used here.

However, another prerequisite needed to be fulfilled to make successful measurements possible. Since the sample volumes of biological fluids are usually very small, i. e. microliters of material are available, a special sample container must be used to efficiently examine them. One such sample cell is offered by Thermo Scientific and goes by the name Gene Frame (art.-no. AB-0576, Fisher Scientific GmbH, Schwerte, Germany). It consists of a standard microscope slip on top of which an adhesive of square cross-section with a 1 cm \times 1 cm hole in the middle is attached. The preparation steps are described in the appendix (Sect. A.2.2). This type of sample cell strongly facilitates the handling of biological fluids and at the same time prevents any evaporation, so any loss of material during the conduction of an experiment can be safely neglected.

II.4.2. Measurements

This study was conducted as an expansion of the study reported in [76]. It will revisit and discuss earlier results and thus present similar findings. For this study, only native respiratory mucus obtained from the distal region of the bronchia that was gained during bronchoscopy of healthy horses was utilized. It was stored at -80°C until the experiments were conducted. The samples used for the macrorheological characterization originate from two horses, while the material for microrheology was taken from a third animal one year earlier. Although in no case the same batch of material was used to perform both experiments in parallel, studies show that the differences in macroscopic material properties do not vary in a strong manner when comparing two different healthy individuals [76]. On the contrary, the local microrheological properties within the same batch vary in a much more significant manner than the properties when comparing one sample to another. Thus, all samples utilized in this study can be assumed to be similar in respect to their shear modulus.

II.4.2.1. Macrorheology

As already mentioned in section II.4.1.1, small amplitude oscillatory shear (SAOS) experiments will be used for the macrorheologic characterization of mucus. Due to the high viscosity of mucus, it was not possible to fill the material into the measurement geometry using a pipette. Instead, the correct amount had to be estimated in advance and directly put out of an Eppendorf sample tube on top of the cup. This led to a slight underfilling of the geometry, which could not be avoided due to the lack of sufficient volumes of material. All experiments introduced here were performed on the mucus samples of each of the horses at least twice to ensure the validity of the data. The temperature was kept at $20.0(1)^{\circ}\text{C}$ at all times by tempering. To avoid evaporation of fluid, the optional plastic top cover was placed around the rotor to keep a water-saturated atmosphere inside.

Two classes of SAOS experiments were performed. The first one, an amplitude sweep, served as a preparation step for the second one, a frequency sweep. In both cases, oscillations are applied to the rotor and both the rotation angle as well as the normal stress, acting on the rotor, are recorded. Afterwards, the response is fitted automatically by the proprietary software HAAKE RheoWin (version 4.30.0017, Fisher Scientific GmbH, Schwerte, Germany) to determine the stress amplitude and its phase shift in respect to the driving oscillations. In this way, information is gained on the elastic and viscous part of the shear modulus as already detailed in section II.3.1.

Amplitude and frequency sweeps only differ in their way of parameter variation: During amplitude sweeps, the strain amplitude is varied with the frequency being constant. During frequency sweeps, the role of both parameters is reversed. As a rule of SAOS experiments, the response of the fluid should always be linear, in other words, no higher

II.4. Experimental Study

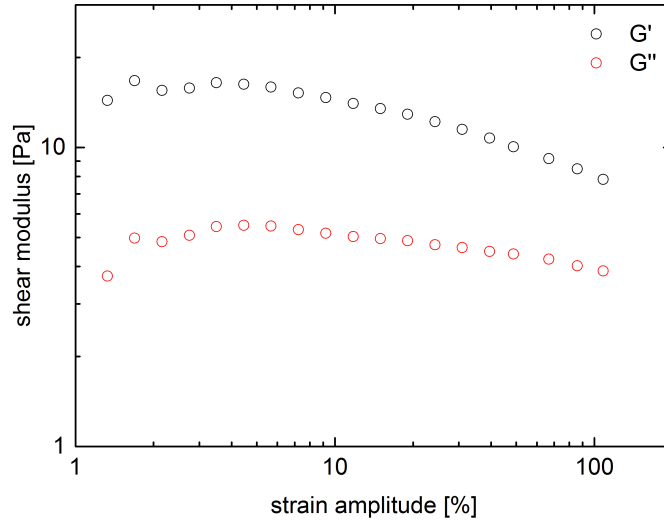


Figure II.4.2.: Evaluation of the linear response range via an amplitude sweep with a mucus sample at an oscillation frequency of 0.1 Hz.

harmonics should play a significant role. Hence, amplitude sweeps are used in advance to gauge the range of linear deformation of the fluid at fixed frequency values. For mucus, a frequency of 0.1 Hz was chosen for this purpose while the amplitudes were varied between $\gamma = 10^{-3} - 10^1$ or, respectively, between 0.1 % and 1,000 %. In shear modulus versus strain plots (Fig. II.4.2), the elastic and viscous part of G starts to show decreasing values upon exceeding $\gamma = 20\%$, hence this value marks the upper limit of the linear range. Since the signal to noise ratio during SAOS measurements is optimal when the driving signal is as strong as possible, this value will be used as strain amplitude during all later frequency sweeps.

A visualization of this transition from linear to non-linear deformations is achieved by plotting the torque wave measured by the rheometer as a response to the rotation angle of the rotor. Such a plot is equivalent to a stress versus strain plot and results in so-called Lissajous-figures (Fig. II.4.3). As can be seen in the graph, for deformations smaller than 70 % the curves are qualitatively described as ellipses. At bigger values, they transform more and more into parallelograms which additionally show wavy edges. Theory predicts that for linear responses of viscoelastic materials, ellipses can be expected. Any deviation from this shape is a strong indication for non-linear effects. In other words, these Lissajous-plots state that a linear response can only be expected well below a strain of 100 %. This result matches the choice of $\gamma = 20\%$ for the amplitude sweeps. As a comparison to the Lissajous plots of mucus, a similar plot is drawn in figure II.4.4 for a sample of 1200 ppm polyacrylamide (PAAm) with a molecular weight of 5 million u in an 80 % glycerol solution. PAAm is often used as a model polymer since it is a material that does not show significant degradation effects even over long periods

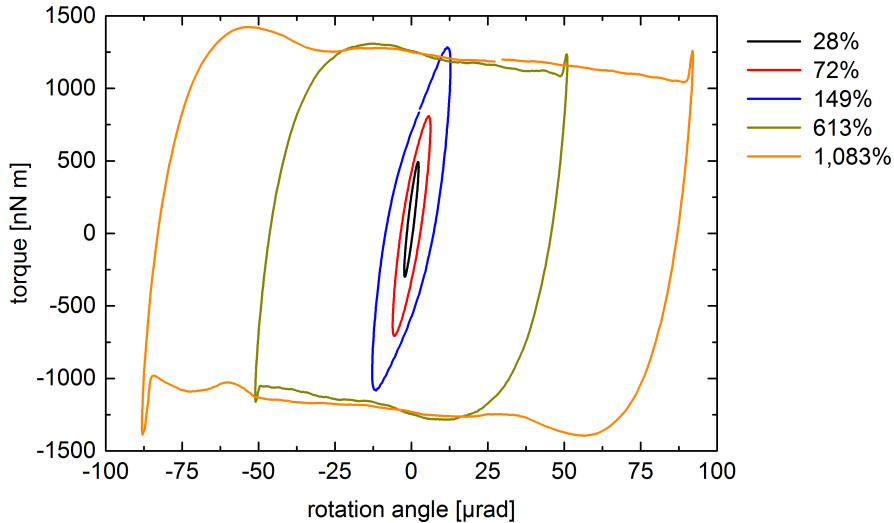


Figure II.4.3.: Lissajous-figures gained by an amplitude sweep with a mucus sample at a frequency of 0.1 Hz . The figures are drawn by plotting the measured torque wave against the shear deformation given by the rotation angle.

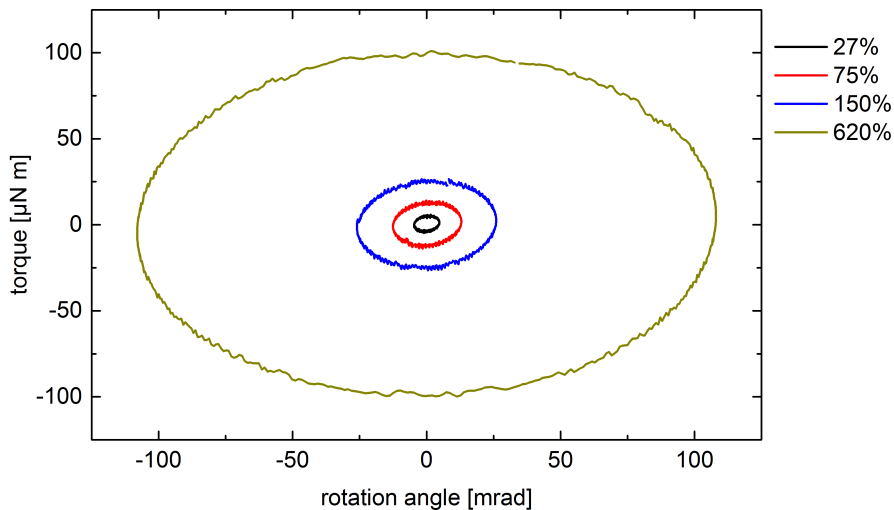


Figure II.4.4.: Lissajous-figures gained by an amplitude sweep with a sample of 1200 ppm polyacrylamide (PAAm) with a molecular weight of 5 million u in an 80% glycerol solution at a frequency of 0.1 Hz . The figures are drawn by plotting the measured torque wave against the shear deformation given by the rotation angle.

of time. Even with much higher values of the rotation angle as well as a higher torque amplitude, the Lissajous plots keep their elliptical shape. Higher harmonics do not play a significant role until much higher shear deformations are reached. For this particular material, the region of linear response ended at 50% strain which lies slightly above the value in mucus. In this respect, the Lissajous plot for mucus shown in figure II.4.3 can be

II.4. Experimental Study

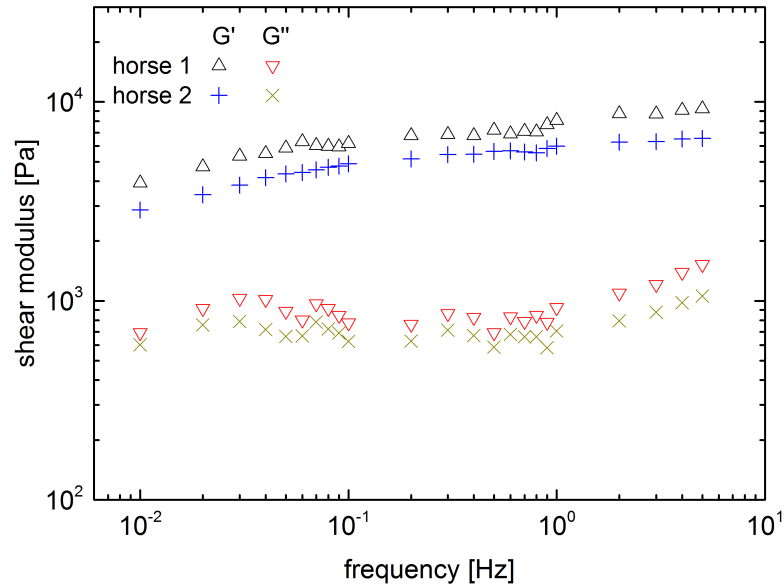


Figure II.4.5.: Results from small amplitude oscillatory shear experiments performed at two mucus samples stemming from two different horses. The elastic modulus is shown as black upwards-pointing triangles and blue plus symbols, the viscous modulus is displayed in red downwards-pointing triangles and yellow crosses. The depicted data sets can also be found in table D.8 of the appendix.

considered as a special property of the material which is not shared by many commercial polymers like PAAm.

Based on this conclusion about the linear region of native respiratory horse mucus, a series of frequency sweeps with the samples of both horses were performed. Only one of each will be discussed here (Fig. II.4.5) since there were no significant differences between successive measurements. The most notable one was that the longer the samples were exposed to the rheometer, the more both the elastic and the viscous modulus shifted towards higher values. Probably, this is due to a decrease in water saturation around the measurement geometry and thus an increased water-loss from the samples. This effect also became apparent after the conclusion of the experiments, when the geometry was cleaned. Hence, only the first measurement of each series is presented here since they reflect the physiological conditions to the highest degree.

The SAOS frequency sweep itself was set to be performed at a constant strain $\gamma = 20\%$ as discussed before. The frequency was varied between 0.01 Hz and 5 Hz . Each recorded point at each of these frequency values represents ten successive oscillations whose average oscillation was computed by RheoWin before fitting the data. Thus, the overall error could be minimized. In respect to errors, no exact value can be given since the rheometer and its software do not give an estimate. However, it appears reasonable to assume an

error margin of 10%.

A property of the examined horse mucus which can be extracted at first glance from figure II.4.5 is that it is a viscoelastic material, indeed. Both the elastic and the viscous modulus exhibit significant absolute values which are clearly above any noise level or error margin. Furthermore, in the examined frequency range, the elastic modulus always exceeds the viscous one, thus, the material behaves more like a solid than like a fluid. However, let us focus on the elastic modulus measured on the material from horse 1. If one leaves small variations out of account, the curve always increases monotonically. At low frequencies, it does so with the steepest slope which then decreases with increasing frequency until nearly reaching a slope of 0 at 5 Hz and hence a plateau value. Overall, the frequency dependence of the elastic modulus is a weak one.

The data set of the viscous modulus is significantly noisier, however, after an increase of the modulus up to $4 \cdot 10^{-2}$ Hz a decrease follows. Upon exceeding a frequency of 6 Hz, G'' starts to increase again. In total, the variation in absolute value are just minor, thus, the viscous modulus can be considered to remain constant in the probed frequency interval. For both the elastic and the viscous modulus, the frequency dependence is a weak one. Over more than two orders of magnitude in frequency, both of them roughly double. Compared to other polymer solutions like polyacrylamide where changes of the shear modulus over multiple orders of magnitude are typical, the shear modulus of mucus can be considered to be almost independent from the frequency. Thus, no matter how long or short the timescale of the excitation is chosen, the bulk response of mucus will remain almost identical.

Overall, the change in slopes of G' and G'' concur with those of a Jeffrey fluid. Since the specific power-dependencies in respect to the frequency deviate from the predictions by the model, fitting the data with it does not seem feasible. Of course, assuming more than just one Maxwellian fluid element, in other words more than just one relaxation rate, might help to gain a better agreement. However, the sheer number of fitting parameters makes a clear understanding of the mechanical properties of the fluid a very challenging task and is thus not very reasonable.

As already mentioned in the introduction to this section, additional mucus samples from other horses were examined as well. The result of a SAOS experiment on one further sample is displayed in figure II.4.5. As compared to the first sample, the real and the imaginary part of G are situated at slightly lower absolute values, however, the functional frequency dependence is duplicated in a very exact manner, indicating an identical function of the material. In other words, both curves increase and decrease at identical characteristic frequencies. Although different horses were considered and hence a certain biological variation in mucus production and composition have to be assumed, the general function of mucus is still the same. This feature is captured well in the figure since the curves do not match in their absolute value.

To the knowledge of the author, not many macrorheological studies on respiratory

II.4. Experimental Study

horse mucus were published until now. Lai and others published a study on human cystic fibrosis sputum [71], which also included SAOS experiments on the material. Although the mucus was taken from humans and, additionally, a disease condition (cystic fibrosis) was present, the function of the fluid is the same. Thus, it is not very surprising that both the elastic as well as the viscous modulus range from $10^0 Pa$ to $10^1 Pa$ for frequencies between $10^{-2} Hz$ and $5 Hz$. This means that horse mucus has a shear modulus which is higher by a factor of 10^3 . Much more interesting is that the qualitative functional behavior is similar. In case of human mucus, at frequencies smaller than $2 \cdot 10^{-1} Hz$, G' increases proportionally to $f^{0.5}$, while at higher frequencies $G' \propto f^{0.3}$. At the same time, the viscous modulus G'' remains constant. Also, the elastic modulus at all examined frequencies is bigger than the viscous one.

At this point, it is possible to draw a partial conclusion: If mucus from the same region in the body is considered, the qualitative rheologic properties may remain comparable even if it is taken from different species of mammals. This seems to hold true since the examined mucus samples had the same function in the body, and even the fact that a disease state was present in one of the subjects did not cause significant changes to the rheology of the material. However, the goal of this study consists of a comparative examination that compares macrorheologic SAOS experiments to microrheologic particle tracking experiments. Hence, in the following section, tracking experiments using optical tweezers will be introduced.

II.4.2.2. Microrheology

As mentioned in earlier chapters, the principle of determining the microrheology of a fluid is based on the Brownian motion of small particles in its bulk. It can be achieved in two ways: There is a first option to visualize a free random walk. In that case, no focused laser beam is necessary. However, in most fluids, this will lead to the sedimentation of these particles and, thus, they will move out of the focal plane. Recording their motion after they reach the cover slide is possible, but one always has to take into account that they might get immobilized by attraction to the glass. Overall, this method is not the most reliable one. Alternatively, one can trap the particles using a setup of optical tweezers. In this case, the beads will always remain in the focal plane, where they can be visualized over long periods of time without any difficulties. The influence of the confinement has been modeled earlier and is well-known (compare Ch. I.4). This technique will be applied in this section.

Each of the mucus samples is prepared as follows: Frozen samples of respiratory horse mucus in test tubes are defrosted, mixed with a small amount of melamin resin microparticles (Tab. A.1), and filled into a Gene Frame which has been made ready for use according to the manual of the appendix (Sect. A.2.2). After closure of the sample cell, it is brought into the setup and examined within the next 4 hours. Melamin resin beads were chosen for this purpose since their refractive index of 1.68 proved to be ideal to be visualized with a good contrast within mucus samples. The concentration of beads typically amounts to between 200 *ppm* and 2,000 *ppm*, which is a value that enables the experimenter to find a reasonable number of beads with which to perform all experiments, while at the same time the rheology of the fluid is not influenced in a significant manner. They also do not come in the vicinity of one another, which might otherwise cause correlations through hydrodynamic interactions. As already mentioned earlier, none of the samples which were examined in the rheometer have also been used for measurements in the setup of optical tweezers and vice versa. When the microrheologic experiments were performed only small amounts of material were available which would not have been sufficient for macrorheologic measurements. Although the samples differ, it is assumed that the material behavior will remain comparable since it was in all cases taken from healthy animals and from the same region in their bodies.

After trapping a bead, a series of four experiments is performed, two passive and two active tracking experiments. A passive tracking experiment consists of recording the motion of the bead for a certain amount of time while keeping it confined in the optical trap. No active forcing is performed. The opposite is true for the active tracking experiments, where an oscillation with a triangular oscillation profile is applied to the piezoelectric stage. While the conduction of each passive experiment is entirely identical - they are only repeated to have some measure of redundancy - during the first active experiment, the oscillation is applied in one of the two translation directions of the stage,

II.4. Experimental Study

i. e. the x-direction, while during the second one the y-direction is chosen. This is aimed at possible anisotropic material properties. All measurements are recorded at a rate of 16 kHz and a trap strength of $1.5\ \mu\text{N}/m$. The typical oscillation amplitude amounts to $1\ \mu\text{m}$, while the frequency $0.2\ \text{Hz}$ is chosen to give even a strongly confined bead much time to adapt. Afterwards, the stored picture series are evaluated using the particle tracking algorithm by Achim Jung [64], which was mentioned earlier in section I.6.2.

Passive Microrheology

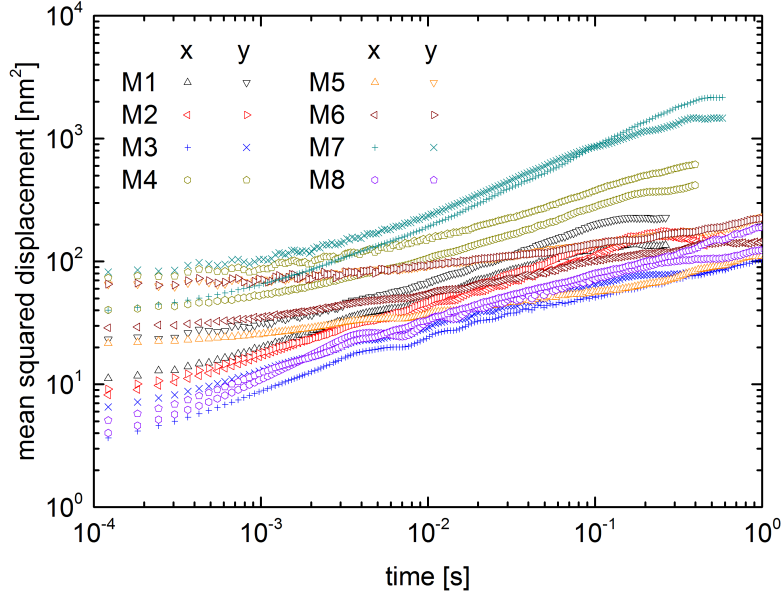
As a first part of the analysis, the mean squared displacements (MSD) of a series of eight independent measurements shall be examined. In general, the MSD is a measure very often used in statistics to describe stochastic processes like Brownian motion. It gives information about how far in average a particle can move after a certain amount of time τ . It is defined as

$$\langle \Delta r^2(\tau) \rangle = \langle (r(t+\tau) - r(t))^2 \rangle_t \quad (\text{II.4.1})$$

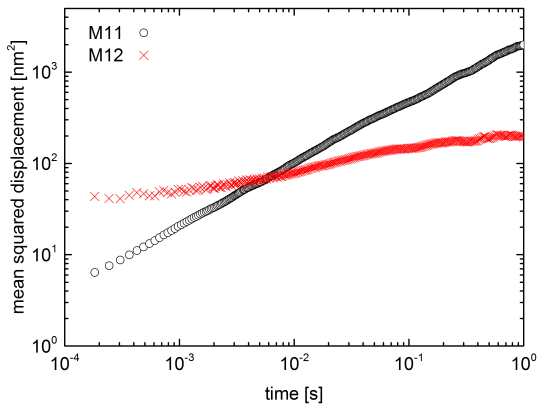
In case of purely viscous Newtonian fluids, the MSD is proportional to τ

$$\langle \Delta r^2(\tau) \rangle = 2D\tau, \quad (\text{II.4.2})$$

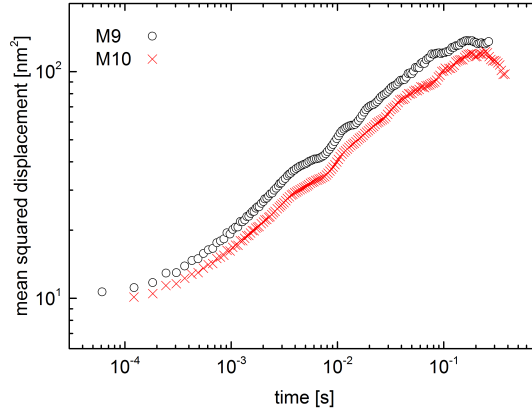
where $D = k_B T / 6\pi\eta r_c$ is Einstein's diffusion coefficient. While it is a constant in case of Newtonian fluids, for complex fluids η becomes time-dependent and differing functional dependencies of the MSD in respect to time may appear. All experiments are performed at different positions within the sample and repeated once as explained in the past paragraph. However, the repetition runs are not depicted here since the reproducibility of the measurements will be discussed later on. Each particle is tracked in two lateral dimensions, the MSD of both is displayed individually in figure II.4.6a. As opposed to mean squared displacements of homogeneous fluids like hydroxyethylcellulose (Fig. II.4.7) where curves measured at different positions within the fluid overlap neatly, mucus displays a strong degree of heterogeneity. The curves show a huge spread over nearly two orders of magnitude, i. e. from 4 nm^2 to 100 nm^2 at 10^{-4} s , and depending on the region where they were recorded, the slope and curvature of each MSD may vary significantly. As indicated by equation II.4.2, the mean squared displacement gives an indication about the diffusion behavior of beads through a particular medium. The steeper the slope in a log-log-plot of the MSD versus time is, the faster the diffusive process will occur. A logarithmic slope of 1 correlates with the Newtonian case (Eq. II.4.2), which can also be called normal-diffusive behavior, while a slope bigger than 1 means a faster diffusive or super-diffusive motion and a value smaller than 1 corresponds to a slow or sub-diffusive process. If the results for mucus in figure II.4.6a are observed, the steepest slope one can find corresponds to $\langle \Delta r^2(\tau) \rangle \propto t^{2/3}$, thus, all diffusive processes in mucus can be considered sub-diffusive. The weakest slope, on the other hand, is corresponding to



(a) Overview of the distribution of mean squared displacements within a mucus sample. The x- and y-component at each position is plotted independently (marked by different symbols of the same color) since huge variations may occur.



(b) The mobility of beads in mucus can vary drastically when considering different locations within the mucus mesh. While the first bead (black circles) shows Newtonian diffusion behavior, the second bead (red crosses) is strongly confined and can barely move at all.



(c) To check on the reproducibility of an MSD measurement, the same experiment was repeated with the same bead after about 5 minutes. While both curves are slightly shifted against each other, the curve progression does not change. Both measurements were performed in the x-direction.

Figure II.4.6.: Mean squared displacements from passive tracking experiments at different positions within the same mucus sample.

$\langle \Delta r^2(\tau) \rangle \propto t^{1/7}$. This represents such a strong confinement of the bead that nearly no motion is possible at all. These two curves are displayed separately in figure II.4.6b. A very interesting feature of some of the MSD curves is nicely visible for the blue and violet

II.4. Experimental Study

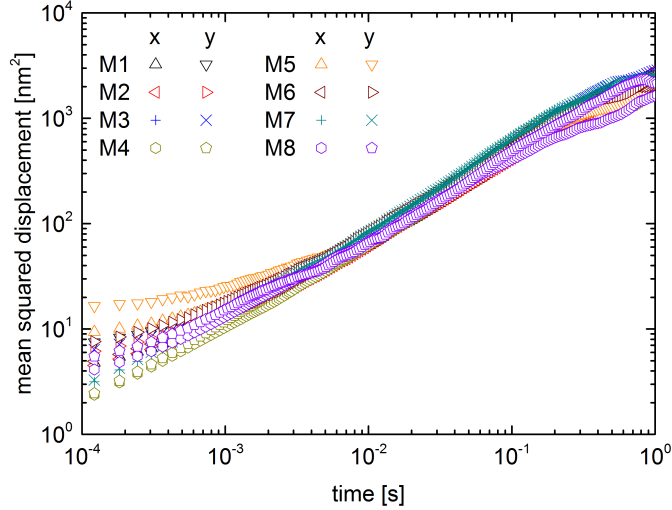


Figure II.4.7.: Overview of the distribution of mean squared displacements within a 1% hydroethoxy-cellulose (HEC) sample. The x- and y-component at each position is plotted independently (marked by different symbols of the same color). This graph was adapted from figure 4B in [76].

curves in the figure: Strong variations in curvature that sometimes even seem to cause local oscillations of the MSD and thus indicate a very complex diffusion behavior at this particular position within the sample occur.

To make sure that the displacement data and the calculated mean squared displacements are reliable, all passive tracking experiments were repeated once with the same bead at the same position within the sample. As becomes obvious in figure II.4.6c, a small shift between the curves may occur. However, the qualitative shape of the curves or, in other words, their slope and curvature remains unvaried even after waiting for about 5 minutes. Hence, the data sets shown here can be considered credible. In order to quantify the influence of the optical trap on the Brownian motion in both materials the turquoise + and × symbols in figure II.4.6a as well as all measurements shown in figure II.4.7 can be taken into account. The MSD value these curves reach after a time step of 1 s represents the physical extent of the optical trap. In case of mucus, the value lies at approximately 1000 nm^2 while in case of HEC due to a lower trap strength a slightly increased value of 3000 nm^2 is observed. Even although a colloid would diffuse further away from its starting position if it was given more time and no optical trap was present this will not happen in the presence of an optical trap. Hence, in case of all measurements presented here, for longer time steps one only observes fluctuations around this maximum value of the mean squared displacement.

In chapter II.3.2, an analytical framework that allows to determine the shear modulus of a fluid from displacement data sets of confined beads was developed. An algorithm which can be used to accomplish this task was presented in the author's diploma thesis

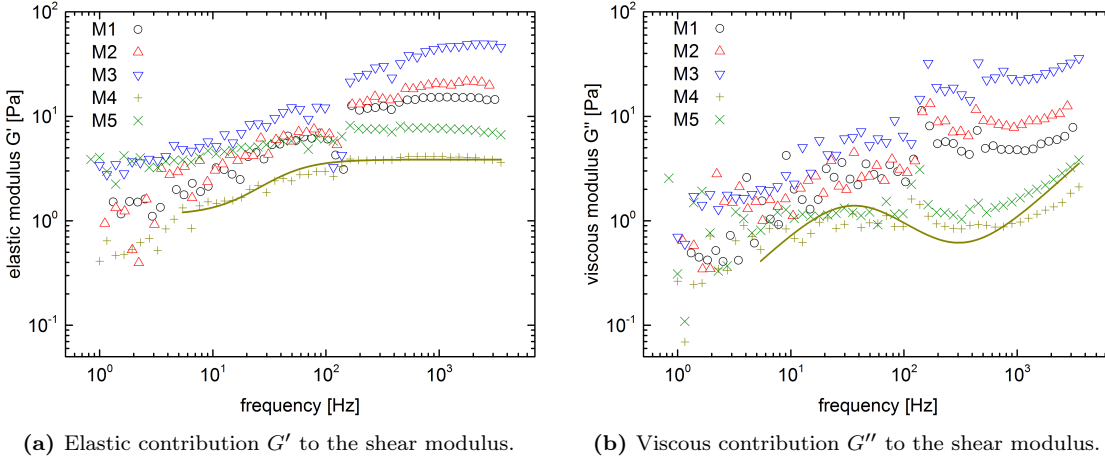


Figure II.4.8.: Results from passive particle tracking experiments at different positions within the same mucus sample. The complex shear modulus is divided into its elastic and viscous components G' and G'' and plotted in the respective subfigure. A fit of the data set M4 above 3 Hz with Jeffrey's model is included in both graphs (solid yellow line). The curves correspond to the first five data sets in x-direction displayed in figure II.4.6a.

[101] and is applied to the data sets here. The resulting shear modulus is displayed in figure II.4.8, subdivided into two separate diagrams for the elastic and the viscous part. For the sake of clarity, only the first five data sets in x-direction of those data sets in figure II.4.6a are drawn here. In general, one can say about the real part of G that, for low frequencies, an increase in modulus which reaches a plateau at high frequencies is apparent. Just as for the MSD data, a significant amount of variation from one position within the sample to the next occurs, indicating a big spectrum of relaxation rates. Still, an analysis of the functional behavior of G' yields a good agreement with Jeffrey's model although in some cases, more than just one Maxwellian fluid element (Eq. II.3.9 and Fig. II.3.1) might be necessary to capture the full curve progression. A similar conclusion can be reached for the imaginary part. An exemplary fit of data set M4 with Jeffrey's model is included in both subfigures as well to emphasize the qualitative agreement of the results with this model.

Active Microrheology

At the beginning of section II.4.2.2, an alternate kind of experiment using active displacements of the confined colloid through mucus was mentioned. Oscillations are performed with the same particle at the same position, however, the oscillation direction is switched from the x- to the y-direction in two successive measurements. The resulting displacements are depicted in figure II.4.9. Here, subfigures II.4.9a and II.4.9b were recorded at identical positions. The same is true for subfigures II.4.9c and II.4.9d. The motion of the optical trap is shown as black circles, the resulting absolute positions of the confined

II.4. Experimental Study

beads are drawn as red circles. Judging from the displacements, one can say that for the upper two figures a strong confinement by the mucus was present in both directions, while for the lower two the confinement was significantly weaker in y-direction. Thus, the motion of the bead in the first three figures was reduced to very weak quivering well below 100 nm . The motion in subfigure II.4.9d seems to have taken place along the orientation of a pore within the sample and was hence less hindered. While such anisotropies are only found in a very low percentage of cases, they still indicate a very inhomogeneous material.

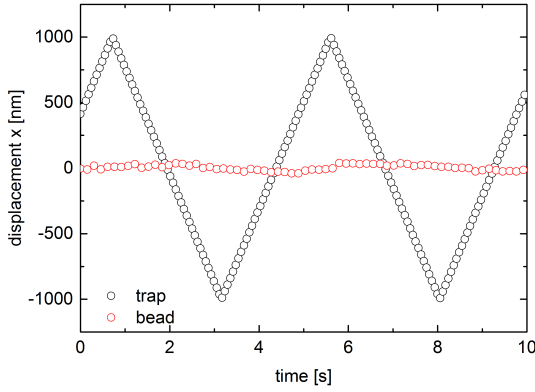
Even more information is gained from these active experiments when the mean squared displacement from a passive experiment is considered at the same position where an active experiment took place. In figure II.4.9e, the MSD in x- and y-direction is shown which corresponds to the position where the oscillations depicted in figure II.4.9a and II.4.9b were recorded. In this region, corresponding to the results from the active experiments, the mean squared displacement reveals a similar diffusion behavior of the particles when comparing the x- and y-direction between 10^{-2} s and 3 s . Both mean squared displacements vary slightly due to the different confinement by the mucus mesh. Additionally, for MSD values below 25 nm^2 the resolution limit of the setup is reached (compare Sect. I.6.3) which causes the spreading of the x- and y-curve. However, the diffusion shows similar properties in these two perpendicular directions so the influence of drift can be neglected for such a short durations of the experiments. Overall, just by considering the absolute value of the MSD the same conclusion can be drawn about the confinement situation of the colloid as in case of the oscillation measurements depicted in figures II.4.9a and II.4.9b: In both directions the confinement by the mucus mesh is quite strong and hence hinders nearly any motion of the particle.

If, on the other hand, the mean squared displacement in the region of high mobility is considered (Fig. II.4.9f) one observes quite a different picture. Again, the data points with MSD values below 25 nm^2 should be omitted since the resolution limit prevents a clear interpretation of the recorded particle displacements. Above this limit though a very specific behavior is apparent: Over all accessible time scales between 10^{-3} s and 10^1 s , there is a clear gap between the MSD in x- and the one in y-direction. As the oscillation experiment in this particular location showed earlier, the confinement in y-direction at this position is much weaker than the one in x-direction. This property is mirrored by the MSD results which show a higher mobility and thus a farther diffusion of colloids in y-direction than in x-direction.

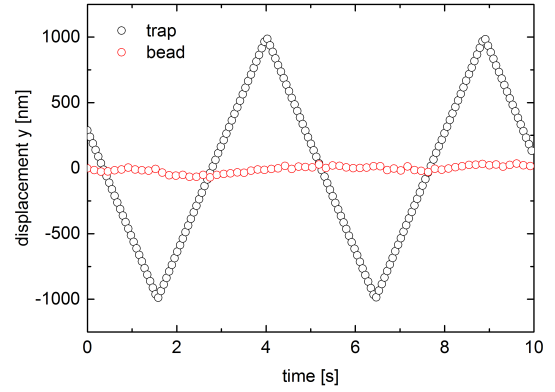
A combination of both passive fluctuation measurements and active displacements allows an in-detail mapping of the whole mucus sample. If these experiments are in turn applied to mucus samples with varying particle sizes, additionally, a very precise mapping of pore-diameters can be performed. To a certain extent, this was performed by Lai [104], however, no active measurements were attempted in this study since no setup of optical tweezers was available. Due to optical limitations of the trapping process, confining

particles smaller than 500 nm is a very challenging task. Tracking them is, until today, only possible using fluorescence visualization techniques. Also, confining just a single one of such small particles in an optical trap is a very complicated task, indeed.

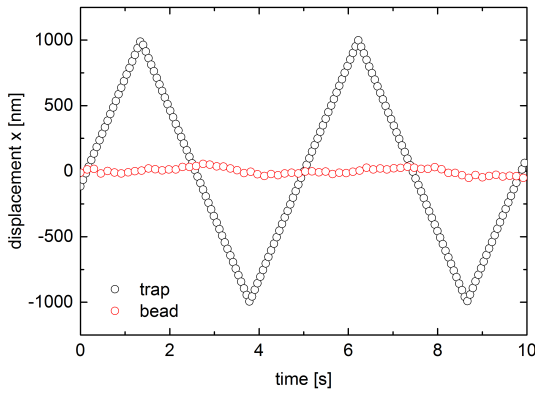
II.4. Experimental Study



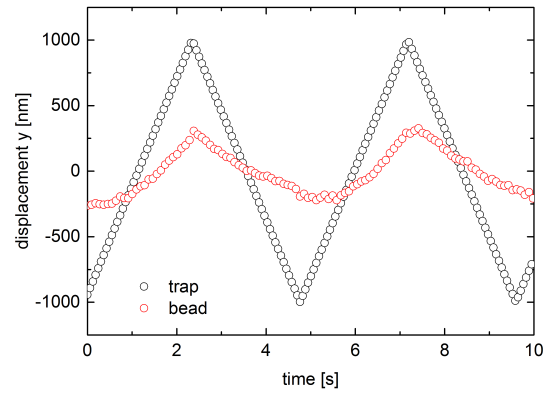
(a) Displacements in x-direction of a bead that is strongly confined by the mucus mesh.



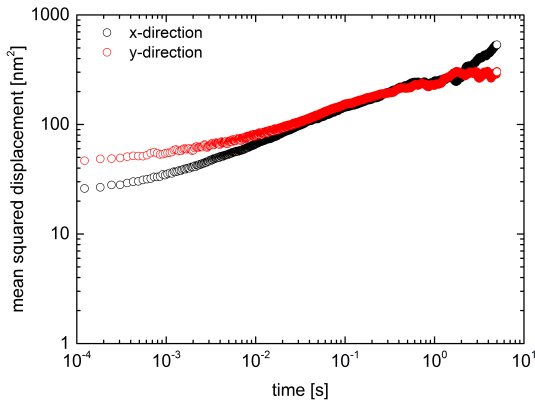
(b) Displacements in y-direction of a bead that is strongly confined by the mucus mesh.



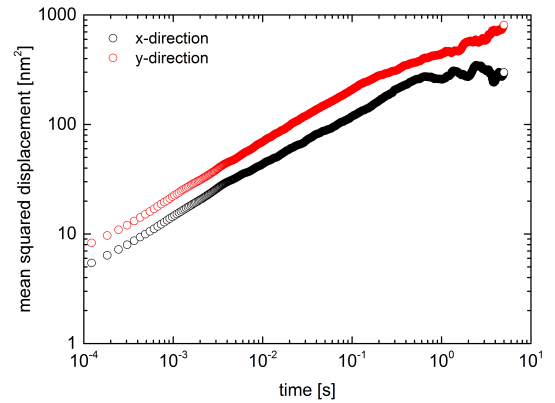
(c) Displacements in x-direction of a bead that is in a strong confinement in x-direction by the mucus mesh while being very mobile in the y-direction.



(d) Displacements in y-direction of a bead that is in a strong confinement in x-direction by the mucus mesh while being very mobile in the y-direction.



(e) Mean squared displacements from a passive experiment recorded at the same position as the curves depicted in Fig. II.4.9a and II.4.9b.



(f) Mean squared displacements from a passive experiment recorded at the same position as the curves depicted in Fig. II.4.9c and II.4.9d.

Figure II.4.9.: Oscillatory displacement experiments at two different positions within the same mucus sample. In graphs II.4.9a to II.4.9d, the motion of the optical trap is shown in black while the absolute displacement of the confined bead is drawn in red. Oscillations were performed with a triangular oscillation profile at an amplitude of $1 \mu\text{m}$ and a frequency of 0.2 Hz .

II.4.3. Summary

In the past chapter, the rheologic behavior of native respiratory horse mucus was surveyed. Two general methodologies were utilized to achieve this goal: The macrorheological properties were gained by conducting small amplitude oscillatory shear (SAOS) experiments using a rotational rheometer, microrheological information was obtained by recording the motion of colloidal particles which were confined in an optical trap.

In section II.4.1, details about both setups were given. The focus lay on the rheometer, of which all important components were described. Since all details about the setup of optical tweezers were already included in section I.6.1 in the first part of this thesis, only a few necessary specifics about the sample preparation were added here.

The main study of mucus followed in section II.4.2. It was opened by the macrorheologic SAOS experiments in section II.4.2.1. Initially, amplitude sweeps were utilized to determine the linear deformation region of native mucus, which could be visualized in Lissajous-figures of torque versus rotation angle graphs (Fig. II.4.3). With this kind of information, it was possible to move on to frequency sweeps of the material. They delivered an only weakly varying elastic and viscous modulus (Fig. II.4.5). However, the elastic material properties at all frequencies always exceeded the viscous ones.

Section II.4.2.2 was devoted to the microrheologic analysis of the material. Mean squared displacement (MSD) curves were utilized to gain an insight into the diffusion properties of colloids through the bulk of the material (Fig. II.4.6). These indicated a very inhomogeneous material with strongly varying diffusion properties. In some cases, these differences even occurred when considering perpendicular displacement directions at identical positions within a sample. Overall, respiratory horse mucus can be considered as a material with sub-diffusive properties for $5\ \mu\text{m}$ -sized beads. Additionally, the displacement data was used to calculate a microscopic, local shear modulus which gives a redundant picture to the macrorheologic information. By analysis of the curves in figure II.4.8, general agreement with Jeffrey's model was found. Furthermore, besides these passive tracking experiments also experiments involving forced active displacements of beads through mucus were performed (Fig. II.4.9). These confirmed the impression of mucus as an inhomogeneous material. Depending on the local surroundings of each bead, in most cases an almost complete confinement within mucus was found. In a small number of cases, however, the colloids were much more mobile and could follow the motion of the optical trap rather quickly (Fig. II.4.9d).

In the following chapter, these macro- and microrheologic findings will be discussed in the context of each other in order to reach a more complete understanding of mucus and its filtering function. Also, further open questions that future studies might tackle will be posed.

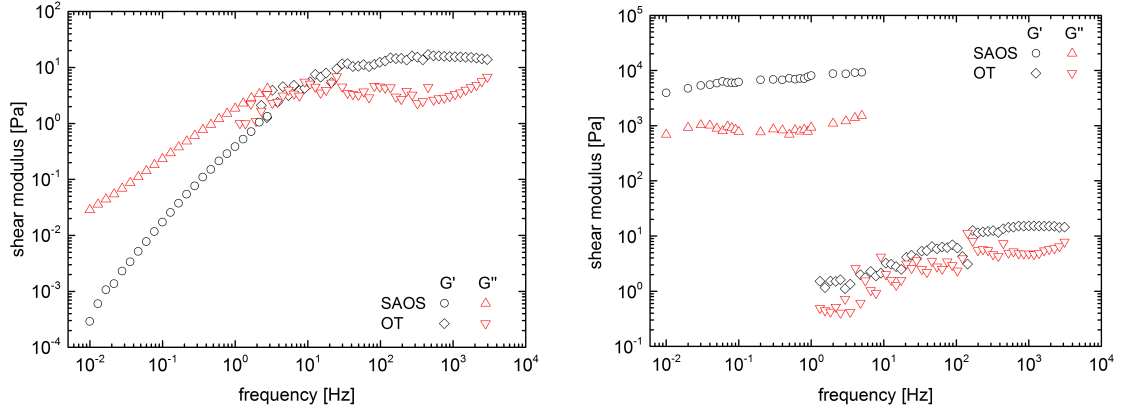
II.5. Discussion

In the recent past, the rheology of mucus has been a much discussed topic. Since it is a biological fluid, it poses a big challenge to gain sufficient amounts of material with which to perform experiments. This is particularly true when macrorheology in a rheometer is involved since typically volumes of multiple milliliters of fluid are required. Thus, it is not surprising that only a small number of macrorheological studies on mucus are available in literature. Two of the most recent and influential are the ones by Lai et al. [71] and Macierzanka et al. [105] which examined human respiratory mucus or respectively pig intestine mucus under the influence of bile salts. In some cases, the macrorheologic characterization of mucus components like sigma mucins were attempted as well [106]. More common are studies involving microparticles, usually focusing on passive tracking of beads within the bulk of the material. Most of these are quite recent as well since the required technology and tracking methods have become available during the past 10 to 20 years only. Among these studies count a number of papers by Lai and others [84, 104] and also Macierzanka et al. [105]. These mostly focus on passively tracking diffusion particles and hence gaining insight on diffusion properties of these particles. One big hope is that such studies might bring clarity to the discussion of how the barrier properties of mucus can be explained and which mechanisms they underlie [107].

So far, it seems that two possible players are involved: On the one hand, the barrier might be a purely size-based barrier which blocks the passage of particles that exceed a certain size. This, on the other hand, would mean that all particles, as soon as they are smaller than a certain critical size, could pass the mucus barrier unhindered. Of course, this critical size may vary from one mucus type to another and from one species to the next. Also, diseases may influence the material properties. A second possible mechanism is interaction filtering. If the particles have a certain composition like specific chemical surface groups or a certain charge, their passage through the mucus mesh is blocked, while others are allowed to proceed. So far, no clear winner has been found and the question about the main mechanism is still open. The results from this study may, however, help to link earlier conclusions.

In the past chapters, the results of a macro- and microrheologic study of native respiratory horse mucus were presented. This delivered a series of properties which can be concluded from the study itself. However, when put in context with earlier results reported in various studies, a bigger picture of the material is gained. But let us limit the view on the study itself, first. As reported in section II.4.2, two different kinds of

II.5. Discussion



(a) The material properties of the 1% HEC gel show a continuous transition from microrheology to macrorheology.

(b) The material properties of mucus change drastically when comparing the size scales which are probed by both methods.

Figure II.5.1.: Comparison of the shear modulus recovered from macrorheologic SAOS experiments with the results from passive microrheology.

experiments were performed: Macrorheological small amplitude oscillatory shear (SAOS) experiments deliver insight into the bulk rheological properties of mucus in shape of the frequency-dependent complex shear modulus, while a respective description of the system was gained on a microscopic level using colloidal particles confined in an optical trap. Due to the local microscopic nature of this second set of experiments, they count to the field of microrheology.

When considering both in context with each other, there is a number of common conclusions. Both methods tell us that mucus is a viscoelastic material since the real or elastic part as well as the imaginary or viscous part of the shear modulus make a significant contribution to the material behavior. Additionally, both methods agree that at all considered frequencies, $10^{-2} \text{ Hz} < f < 5 \text{ Hz}$ in case of the SAOS experiments, $1 \text{ Hz} < f < 4 \text{ kHz}$ in case of microrheology, the elastic modulus dominates over the viscous one. In other words, the material behaves more like a solid than it resembles a fluid. In terms of phase shifts, as explained in section II.3.1, mucus reacts nearly in phase with any excitation and only shows weak phase shifts. This is however the point where agreements seems to end.

When directly comparing the macro- and microrheologically gained shear modulus in the HEC gel (Fig. II.5.1a), one observes a very smooth transition between both. The elastic modulus in the frequency range between 1 Hz and 10 Hz gained by both methods matches in value, the viscous modulus in that range only differs by a factor of up to 3. When mucus is considered (Fig. II.5.1b) what at once catches the eye is a huge gap between the curves that spans roughly three orders of magnitude. This is best seen in the overlap region between 1 Hz and 10 Hz where the macrorheologic modulus is bigger than 10^3 Pa while the microrheologic one can be found around 1 Pa . This seems highly

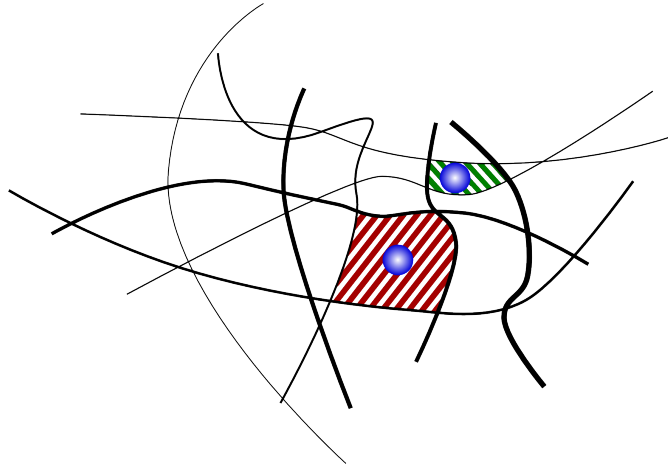


Figure II.5.2.: Sketch of the microscopic structure of mucus (adapted from [76]). Mucus is represented by black lines, small objects like beads (blue spheres) can only move within pores, indicated by red and green shaded regions (compare also the cryogenic scanning electron micrograph in Fig. II.2.1).

counterintuitive at first, however, it appears reasonable when taking the microstructure of mucus into account. In literature mucus is described as a gel with pores that consist mainly of water but also of cell components like DNA and proteins [75]. During an SAOS experiment, the whole bulk of mucus or, in other words, the pore walls as well as their contents are forced to oscillate and their total net response is measured. A continuum response which is characteristic for the material is gained. However, what a single micrometer-sized particle immersed in the bulk will experience, are very stiff and rigid walls in some directions, while others might be more easily permeable due to the presence of a pore (Fig. II.5.2). Thus, one gains a very inhomogeneous response by the material and also a much higher mobility of particles than bulk rheology would indicate. Sometimes, the particles move within larger pockets inside the material and seem to be able to move almost without hindrance over distances larger than $5\ \mu\text{m}$ or more. Mostly, a strong confinement of the beads is present nonetheless and they mostly fluctuate in unison with the pore walls. How strong the confinement actually is can only be found out by actively displacing the particles.

Now, let us put these results in context with earlier reports. One of the big questions is still how mucus performs filtering operations. Which particles are deemed harmful and are blocked from passing the mucus barrier and which ones may pass? So far, indications that seem to prove both size and interaction filtering were found. If the particles are too big in general to fit through the mucus mesh, they will get stuck. However, it seems that particles show a better penetration into the material when their surface carries a different functionalization [84]. Most surprisingly, smaller sizes ($d_c = 100\ \text{nm}$) of PEG-

II.5. Discussion

or COOH-modified particles showed an even slower diffusion through mucus than larger ones ($d_c = 200\text{ nm} - 500\text{ nm}$), which might be due to blocking of mucus pores by big aggregates of beads.

In terms of the material rheology, two scales have to be considered: On the one hand, the microscopic rheology is determined by the viscoelastic properties of the pore walls as well as the properties of the fluid filling those pores. On the other hand, if the whole bulk is probed, for example by a rheometer, a continuum response of pore walls and filling material is gained. A very superficial link between both scales can be derived by considering the whole material as a kind of rigid foam. While the pore walls show solid-like properties the filling material behaves essentially as a fluid of comparably negligible viscosity. A number of models have been suggested in the past which are able to at least roughly grasp such material properties. Among those models, the Mori-Tanaka model [108] is probably suitable the most in order to describe mucus although it is still by far not complex enough to give a realistic description. According to this model, a foam is composed of two phases, the rigid one of the walls and the fluid one of the filling material. Each of these two has its own shear modulus. Since the largest contribution to the total shear modulus is caused by the wall material the shear modulus of the fluid is negligible and the total shear modulus is given by

$$G_{total}(\omega) = G_{walls}(\omega) \left(1 - \frac{c_p}{1 - \beta(1 - c_p)} \right), \quad (\text{II.5.1})$$

where c_p is the volume fraction of the pores and β is a dimensionless number. It can be simplified under the assumption that the wall material itself without considering the pores is isotropic and homogeneous. In this case, it is given by

$$\beta = \frac{2(4 - 5\nu)}{15(1 - \nu)}, \quad (\text{II.5.2})$$

where ν is Poisson's ratio. If now a volume fraction of $c_p = 60\%$ (compare Fig. II.2.1) and also the incompressibility of the pore material and thus $\nu = 0.5$ are assumed, a value of $\beta = 0.4$ results. After inserting these values into equation II.5.1, the shear modulus of only the walls is gained by multiplying the macrorheologic results by a factor of 3.5. This means that the gap between macro- and microrheologic measurements would be even bigger if only the material of the walls would be considered. Hence, the micro- and macrorheologic characteristics of mucus gained in this work should not be understood as a mean-field description of the material but rather the rheology on completely different and for the most part independent scales.

The study presented here showed that, when not taking the surface functionalization of the beads into account, they can in some cases diffuse further through the material.

This effect mainly depends on their exact position within the sample and on whether there are any larger pores present at this particular spot. It becomes apparent that even if the particles are about as large as the average pore size, it may be possible for them to cross the mucus blanket if they try to do so in the right position. Combined with reports in literature, this hints towards both size and interaction filtering being present in mucus. Beads with certain surface groups in general show different diffusion coefficients in mucus, but their size is also important. The question about “the” critical size is not easy to answer since it depends on the type of mucus (respiratory, cervicovaginal, etc.) and the health status of the donor. Even more influences which are so far unknown might be present. However, this is a question that must be answered individually.

II.6. Summary

This second part of the thesis is focused on the study of mucus, a biological fluid that is present in the organism of most mammals. It covers the surface of most organs otherwise exposed to the physical contact with their environment and thus fulfills the purpose of sheltering them. This function is not only realized by reducing mechanical influences, but also by keeping harmful substances like pathogens away while letting nutrients pass. The study attempts to fill in a few of the blanks that still remain in our understanding of the filtering functions of the material.

To achieve a deeper understanding, macro- and microrheologic experiments were conducted. In chapter II.3, Maxwell's fluid model with a basic description of complex fluids was introduced for this purpose. Its constitutive equation contains both a purely viscous dashpot which is shunted with an elastic element, typically represented by a Hookean spring. Albeit simple, this model allows the characterization of viscoelastic fluid and is very often utilized to analyze much more complex materials. However, due to an issue with energy dissipation, the model had to be expanded to contain one additional dashpot, representing a viscous solvent. In this composition, this model, also known as Jeffrey's model, could be applied in the interpretation of the experiments following later.

The following two sections were devoted to the theory of macrorheologic small amplitude oscillatory shear experiments (Sect. II.3.1) and microrheologic passive tracking experiments (Sect. II.3.2). In the first case, the shear modulus is concluded from the quotient of shear stress and strain, in the second case, a similar conclusion can be drawn by solving a Langevin equation and gaining the response function of the fluid.

Chapter II.4 was solely dedicated to the conduction of experiments. The introductory section mostly contained information about the experimental setups of the utilized rheometer and the setup of optical tweezers. However, a more detailed explanation about the second setup can be found in the first part of this thesis (Ch. I.6) and, thus, was kept rather short, here. The central part of the experimental study followed in section II.4.2, which included an in-detail analysis of native respiratory horse mucus. In chapter II.5, the results were interpreted in context with earlier mucus studies and their findings, and the overall filtering functions of the material were reflected upon.

II.6. Summary

Although a little more clarity was brought into the interpretation of diffusion properties of mucus, there is still much room for improvement. Those concerning the setup of optical tweezers were already discussed in the past part (Ch. I.8), however, additional changes involving the rheometer are desirable as well. Direct access to the waveform data sets when performing SAOS experiments would help immensely in interpreting the measurements. So far, the rheometer records a set number of oscillation periods, calculates an average oscillation that is fitted and evaluated in terms of amplitude, frequency, and phase. If deviations by disturbances or other sources of noise occur in one of these oscillations, it is not possible for the user to exclude that particular oscillation period from evaluation. Also, the built-in force sensor, which is used for measuring the shear stress, is not the most sensitive exemplar. The precision of all measurements would benefit greatly from a more powerful replacement, especially, when measurements at very low shear rates or, respectively, strain amplitudes are concerned.

This study managed to answer a few of the open questions, but still many of them remain. There is a number of issues in direct context with this project that need to be studied. It would be very desirable to perform a sample-wide mapping of one or multiple mucus samples using a setup of optical tweezers in order to gain a more complete picture of these samples. The pore size distribution would become accessible and one would gain insight into particle mobilities in that volume. This might help in finding the perfect size for drugs that are intended to penetrate the mucus layer. Furthermore, the study could be expanded by varying the particle coating to additionally find the ideal surface groups to enable efficient and fast diffusion processes. Also, the field of observed mucus types could be expanded as there is no reason to restrict it to respiratory mucus.

With the analysis of macro- and microrheological data, this study could show that the material properties are accessible using currently available techniques. As compared to macrorheology, the use of optical tweezers comes with the huge advantage of very small sample volumes below $30 \mu\text{l}$. It also allows material characterization at a very high spatial and temporal resolution on scales of hundreds of nanometers and tens of microseconds. The combination of passive tracking and active forced oscillations give insight into the actual size of rifts and pores within the material. Nonetheless, macrorheologic properties should not be cast aside since they define what larger objects passing the mucus layer will experience. The rather elastic and viscous pore walls help in protecting the underlying cell walls from mechanical harm or even destruction without which the body of a mammal could not survive.

Part III.

Single-End-Grafted
DNA-Molecules in an Oscillatory
Linear Shear Flow

III.1. Introduction

Evolution of life and the build-up of diversity as it can be seen today would not have been possible without deoxyribonucleic acid or short DNA. Since it plays such a crucial role, it is unsurprising that so many studies over the past 100 years were published on the topic. The specific fields the studies concentrate on could not be broader. For example with the discovery of gene splicing in the 1970s, ideas were developed that included the active manipulation of plants to create more vermin and disease resistant crops [109]. If functional, the application of these techniques in the field of organ growth might be able to replace failing hearts or damaged lungs and thus save many lives.

But also in other fields like nano-engineering [110] DNA has become famous, since it exists in nature as macromolecules of a variety of lengths but otherwise very reproducible properties. It may help in developing new materials or patterning very fine structures on scales of length which can otherwise only be reached using other means like lithography under very unfavorable circumstances. In forensics, gene profiles of criminals have been administered in huge data bases for about 25 years, allowing rapid identification and tracking [111, 112]. Besides the very active communities in biology and chemistry which have published thousands of papers on the topic over the past century, this famous molecule plays an important role in physical research as well.

Among others, it is very popular as a model polymer. The duplication mechanisms of DNA are very robust and although errors happen during the transcription process, still, the copy has very close to identical properties like for example the same length, charge, etc. Thus, many different models were already applied to it in its equilibrium state and under plenty of flow conditions with the goal to find an accurate description of it. Among these count the Rouse and Zimm models [113], which model them as a long series of beads linked by elastic springs. Another representation, the Porod-Kratky model, considers them as worm-like chains with a small range of binding lengths and fixed binding angles [114]. Specialized models try to capture the loop formation behavior of DNA under melting conditions [115] or their bending stiffness [116]. But still until today, it is not completely clear which model qualifies as the best description of the physical behavior of DNA molecules.

III.1. Introduction

This third part of the thesis aims at a deeper understanding of the dynamic mechanical properties of tethered DNA molecules when subjected to an oscillating, linear shear flow. A crude model for the motion of the center of mass (*COM*) is developed based on the elastic dumbbell model. This system is observed experimentally by attaching one end of the DNA molecules to the surface of a cover slip and exposing them to said oscillating shear flow. The motion is created by harmonic motion of a piezoelectric single axis motor to which an optic lens is attached. The distance between lens and cover slip can be precisely controlled using a micrometer caliper, thus also allowing a tight manipulation of the velocity profile below it.

Not only does this kind of system give access to the properties of a model polymer, but it also becomes possible to check on the maximum loads a DNA molecule can take and to define limits in this respect for other research projects. For example in medicine, the usage of so-called microarrays has become very common in the meantime. These are small sample plates with hundreds of cavities which can be filled with a variety of chemicals. A huge advantage of this technique is that massive parallel processing of DNA with different reactants is available. They can also be filled and emptied dynamically when combined with microchannels, so even reaction dynamics can be surveyed. When the DNA molecules are attached within the cavities and an influx of fluid passes them by, they may be subjected to large forces which can detach them or rip them into pieces. Also, oscillating dynamics may occur at the moment when the flux is stopped since a certain amount of reaction time is necessary before the flow actually comes to rest. Thus, a study of tethered DNA molecules in an oscillating shear flow is helpful in understanding these basic properties. The results of the analysis of auto- and cross-correlation functions of colloids in part I are serviceable as well since the system in consideration here shares many properties like the shear flow and Brownian dynamics.

III.2. Literature Survey

The existence of DNA molecules has been known since 1869, when Friedrich Miescher, a Swiss medical scientist and physiologist, first detected and isolated it [117]. However, it took about 30 years until Albrecht Kossel discovered that it was a polymer which also contained four different nucleobases (among others in [118]). He was awarded the Nobel Prize for Physiology or Medicine for this achievement in 1910. The further components, deoxyribose and phosphate, were identified by Phoebus Levene in 1919 [119] who performed his analysis on yeast DNA. 30 years later, Erwin Chargaff contributed to the progress in deciphering the structure of DNA by detecting the presence of fixed ratios of the base molecules in different species [120]. A critical step was taken a few years later by Watson and Crick [121] who suggested the double-helix structure which is associated with DNA molecules today. They based their proposal on a single X-ray diffraction image which was recorded and published by Maurice Wilkins [122]. This groundbreaking discovery was also awarded with a Nobel Prize in 1962.

However, this just marks the beginning of a large number of studies involving DNA. Since it is not possible to give a complete overview of DNA research since the mid-1950s in the scope of this literature survey, the focus will be laid on the most relevant studies involving single DNA molecules and shear flows. As a side note, setups of optical tweezers were utilized in their passive and active examination as well. Wang used them to stretch attached molecules [35] and Mason determined their microrheologic properties [83]. When concentrating on single molecule studies, among the first breakthroughs are the following two: Steven Smith and Carlos Bustamante grafted a DNA molecule to the surface of a cover slip with one extremity, while the other was attached to a magnetic particle [123]. While an exact measurement of the acting forces was tedious, he could manipulate their stretching and thus nicely examine their mechanical properties. A study of Thomas Perkins and Steven Chu [34] can be counted as a follow-up experiment. They attached a bead to one end of a DNA molecule while the other end was floating freely. By trapping the bead using a setup of optical tweezers, they could observe the stretching of the molecule when subjected to varying velocities of the surrounding fluid. As opposed to the earlier study by Smith, they used YOYO-1 as an intercalating dye, which made the extension analysis of the molecule much easier. They were able to quantify the scaling of the relaxation rate depending on the pre-stretching defined by the flow velocity before stopping the flow. Additionally, they found much faster recoiling dynamics as soon as the extension of the molecule amounted more than 70 % of the contour length.

III.2. Literature Survey

In 2000, Patrick Doyle and Jean-Louis Viovy published a noteworthy study in which they attached a double-stranded DNA molecule to a cover slip and exposed it to a linear shear flow [124]. Similar to the experiment in part I of this thesis, they created the shear flow by pushing the fluid using a syringe pump. Although these kinds of pressure-driven flows have a parabolic velocity profile, they do not deviate significantly from a linear shear flow when considering regions in close proximity to one of the side walls. Oscillating shear flows were not taken into account by them, though. By analyzing the auto-correlation functions of the grafted molecules, they found the average of the longest relaxation rate at approximately 400 ms . Compared to the value found by Smith [123], which amounts to about 74 ms , they argued that the effective length of the DNA can be considered as doubled when it is attached to a surface and that additionally, hydrodynamic interaction with the walls needed to be included as well. Overall, this meant an increase of the relaxation rate by roughly a factor of 4 to 5. They also found different relaxation regimes as well as cyclic dynamics: When the Weissenberg number was lower than 0.88, the DNA seemed to relax more slowly than in its equilibrium state. Faster relaxations could be found for Weissenberg numbers that exceeded that value. Cyclic dynamics showed for a different reason. When the fluid surrounding the DNA flowed, sometimes fluctuations away from the cover slip occurred due to Brownian motion. This led to the molecule moving into a region with higher flow velocity, thus resulting in a stronger stretching. It then took a certain relaxation time for the DNA to come back to its earlier state. This process afterwards reappeared in a very irregular fashion.

A study by Christopher Lueth and Eric Shaqfeh goes in a similar direction. They took the same approach grafting one end of a DNA molecule to a surface and creating a shear flow in the bulk of the surrounding fluid. Complementary to their experiments, they applied simulations based on a bead-spring model including hydrodynamic interactions. They saw cyclic dynamics as reported by Doyle and could also identify the chain extensions from their experiments with simulation results by optical comparison. However, they found that extensional fluctuations are overpredicted by their model and especially at low Weissenberg numbers, the average distance of the chains to the wall differs.

Oscillatory flows are often not taken into account in context with DNA molecules. One of the few examples is a numerical study by Chen [125]. Brownian dynamics simulations in an oscillatory pressure-driven flow through a microchannel were performed to observe chain extension and migration. However, no grafting of the molecules was conducted, thus, leading to a different system. Comparable to this paper, in a publication by Lo [126] an AC electric field was applied to DNA samples experimentally to create such a flow situation. Again, however, no grafting of the molecules was conducted.

There is one study, though, that combines both oscillating and linear shear flows with grafted DNA molecules in an experimental fashion. It was performed by Maryam Khaksar in her PhD thesis [127]. By driving DNA molecules attached to a cover slip using a piezoelectric device, she could visualize their harmonic dynamics and examine their

center of mass (*COM*) motion and, from that, determine their response amplitude and phase. A model of the system consisted of a Hookean spring fixed at a defined distance away from the cover slip to which the center of mass of the DNA molecule was attached. Polymer dynamics were not assumed, instead the molecule was assumed to behave as a bead of a constant radius attached to the aforementioned spring. She found that under the assumption of a constant height of the *COM*, the relative amplitude of the DNA molecule versus the driving amplitude of the piezo device first increases linearly with the driving frequency. Upon exceeding $\omega_c = 1/\tau_{r,max}$, where $\tau_{r,max}$ is the longest relaxation rate of the DNA molecule, according to her model the maximum extension of the spring should be reached, thus, leading to a constant relative amplitude. In her experiments, she found a more resonant-like behavior indicated by a maximum in the relative amplitude at ω_c , which then quickly decreased towards zero. No clear conclusion could be drawn from this behavior, especially, no modified model was created to describe it.

Hence, the goal of the third part of this thesis is two-fold: On the one hand, the experiments of Maryam Khaksar will be repeated over a broader range of frequencies. A study at higher driving frequencies will be attempted, testing the limits of currently available fluorescence microscopy techniques. These results will then be compared to Maryam Khaksar's bead-spring model in order to check on its feasibility. Comparisons will be drawn to the conclusions by Maryam and differing results will be pointed out. In chapter III.3, interesting background information about DNA will be given. This will be combined with a revision of the flow profile in the experimental setup as well as an introduction to the utilized bead-spring model. In chapter III.4, the experimental setup used in this study will be presented, followed by a description of the performed experiments and their results. These will be discussed afterwards in chapter III.5 and considered controversially in context with earlier results by Maryam Khaksar.

III.3. Theory

Deoxyribonucleic acid or short DNA is one of the most important biological molecules as already mentioned in the introduction. As presented in figure III.3.1, it is a polymer, consisting of three building blocks: a sugar called deoxyribose (marked orange in sketch), a phosphate group (yellow), and four different nucleobases (remaining colors). The sugar bound to the phosphate group is denoted as a nucleotide. When several of these are bound to each other such that a linear polymer is formed, one considers them as the backbone of the DNA molecule. The nucleobases are adenine (A, indicated in green),

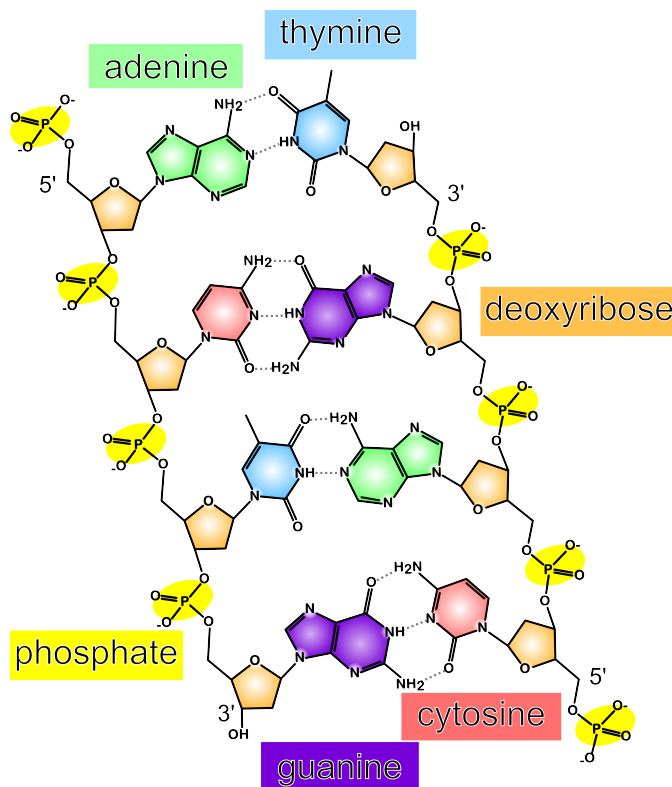


Figure III.3.1.: Planar structural binding model of a double-stranded DNA molecule (adapted from [128]). The backbone, consisting of deoxyribose and phosphate groups, is displayed together with the bases adenine, thymine, guanine, and cytosine linking both strands. At the extremities of both strands, the index of the final carbon atom of the last sugar molecule is indicated by 3' or, respectively, 5'.

III.3. Theory

cytosine (C, indicated in red), guanine (G, indicated in violet), and thymine (T, indicated in blue). These are bound to the innermost carbon atom of the sugar group and thus appear in regular intervals along the backbone. The combination of single base molecules bound to the backbone is also denoted a single-stranded DNA molecule (ssDNA). If two DNA strands are aligned to each other in such a way that the bases of one strand are able to bind to those of the other strand, then a double-stranded DNA molecule (dsDNA) is formed. However, the bases can only appear pair-wise¹ and bind to each other in the combinations $A = T$ and $C = G$, thus, a special requirement for two stably bound DNA molecules is a very specific sequence of bases. This is realized in nature by two complementary DNA strands which are aligned anti-parallel to each other for binding. The actual biological information is encoded in the sequence of bases. When talking about binding sites in context with DNA, typically, one considers the different carbon atoms of the sugar groups for this task. They carry indices of 1' ("one prime") through to 5' ("five prime"), which are counted from the innermost C-atom, bound to the nucleobase, towards the outermost one. Along the whole strand, the 3' as well as the 5' binding site are bound to phosphate groups neighboring the sugar molecules. If one considers one of the extremities of a single strand, either the 3' or the 5' C-atom is available for binding, thus, the extremities are named according to the index of the "final" C-atom. This fact is also indicated in the sketch in figure III.3.1. As displayed by the "-" sign next to each phosphate group, every single one of them carries one total negative charge, leading to a negative net charge of the DNA molecule. This enables manipulation through electric fields, as used in gel electrophoresis for example [129].

The spatial orientation of the dsDNA is another particularly interesting topic since it does not happen in a planar fashion as indicated in the sketch. Instead, the molecule is wound up to an asymmetric, helical conformation. The asymmetry causes the appearance of two spaces of different sizes, the so-called grooves. The smaller one, which is 12 Å wide, is denoted minor groove, the bigger one with 22 Å is denoted major groove. Since this helical structure is not stiff in respect to its main axis, the helix is not straight and typically experiences a stochastic quaternary structure which strongly fluctuates and shows frequent conformational changes depending on the thermal energy of the system.

Depending on which life form or species is considered, the length of DNA molecules can vary strongly. In context with the study presented in this thesis, DNA of enterobacteria phage λ , or short λ -DNA, is used. Enterobacteria phage λ is a virus that infects *Escherichia coli* for reproduction purposes. It consists of 48,502 base pairs and is thus one of the longest DNA molecules utilized for research purposes. From a physical point of view, there are a few more important properties. These include the contour length, which is the length of a polymer at maximum extension, and the radius of gyration, which represents the average effective radius of the polymer in its coiled state. For λ -DNA, a

¹This binding rule is also called Chargaff's rule, named after its discoverer.

III.3.1. Flow Profile between Two Parallel Oscillating Surfaces

contour length of $16.3 \mu m$ is referenced in literature [124]. This value increases to $21 \mu m$, however, when YOYO-1 is utilized as the intercalating dye (see Sect. III.4.1). The radius of gyration amounts to $690 nm$ and, according to earlier studies, remains uninfluenced by the dye molecules [130].

In the following, two important aspects of the system in consideration will be analyzed. On the one hand, an oscillating piezoelectric device will be used to create a linear shear flow to which DNA molecules will be subjected. The visualization of the molecules will be facilitated by attaching - also denoted as grafting - them to the surface of a cover slip after they have been functionalized with fluorescing dye molecules. So far, the question if the created flow is indeed linear has not been tackled, yet. This will happen in the next section. Afterwards, in section III.3.2, a simplified model for grafted polymers based on a dumbbell model will be developed.

III.3.1. Flow Profile between Two Parallel Oscillating Surfaces

In this section, the flow profile between an oscillating and a resting flat surface shall be analyzed. Both plates are aligned parallel to each other as indicated in figure III.3.2. The upper surface is displaced according to the time-dependent function $y_{up}(t) = y_{lens,0} \sin(\omega t)$ with the oscillation frequency ω and the amplitude² $y_{lens,0}$, while the lower surface stays in rest all the time. This can also be recast in terms of shear amplitudes in the following form

$$\gamma(t) = \gamma_0 \sin(\omega t), \quad (\text{III.3.1})$$

where the shear strain amplitude is defined by $\gamma_0 = y_{lens,0}/h_{lens}$ and h_{lens} is the distance between the upper and lower plate. Starting again from the full Navier-Stokes equation introduced in part I (Eq. I.4.1), now, a different set of boundary conditions needs to be taken into account. Since the whole flow-cell is closed off, there is no pressure gradient in the system. Instead, the fact that no stationary flow can be assumed has to be considered. All other simplifications can be applied in this case as well. The adapted equation then reads

$$\rho \frac{\partial v_y(z, t)}{\partial t} = \eta \frac{\partial^2 v_y(z, t)}{\partial z^2}. \quad (\text{III.3.2})$$

As boundary conditions, it can be assumed that the velocity of the fluid at the interface to the upper ($z = h_{lens}$) and lower plates ($z = 0$) is identical to the one of the plates

²Although two plates are considered here, the index ‘‘lens’’ is utilized, instead. The reason for this choice will become obvious when the experimental setup will be presented in chapter III.4 since as the upper surface an optical lens will be used.

III.3. Theory

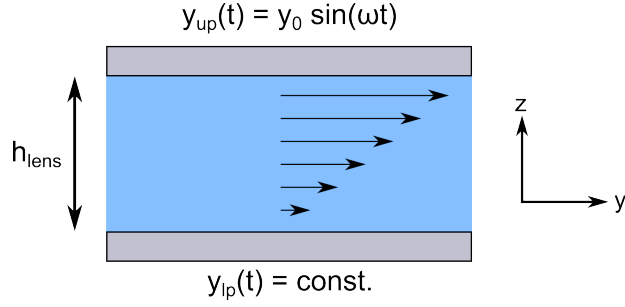


Figure III.3.2.: Sketch of the oscillating, linear flow profile between a fixed lower plate (lp) and an oscillating upper plate (up). In the experimental setup, the upper plate is replaced by an optical plano-convex lens.

themselves (no-slip boundary condition). Thus,

$$v_y(z = 0, t) = 0, \quad (\text{III.3.3})$$

$$v_y(z = h_{lens}, t) = y_{lens,0} \omega \cos(\omega t). \quad (\text{III.3.4})$$

To solve this differential equation, it is possible to use an ansatz via the separation of variables. One assumes that $v_y(z, t) = f(z)g(t)$ and that the equation can be recast as

$$\frac{\rho}{\eta} g^{-1}(t) \frac{\partial g(t)}{\partial t} = f^{-1}(z) \frac{\partial^2 f(z)}{\partial z^2} \stackrel{!}{=} k^2. \quad (\text{III.3.5})$$

By solving of the time-dependent partial equation, k is determined as

$$k = \pm(1 + i) \sqrt{\frac{\rho \omega}{2\eta}}. \quad (\text{III.3.6})$$

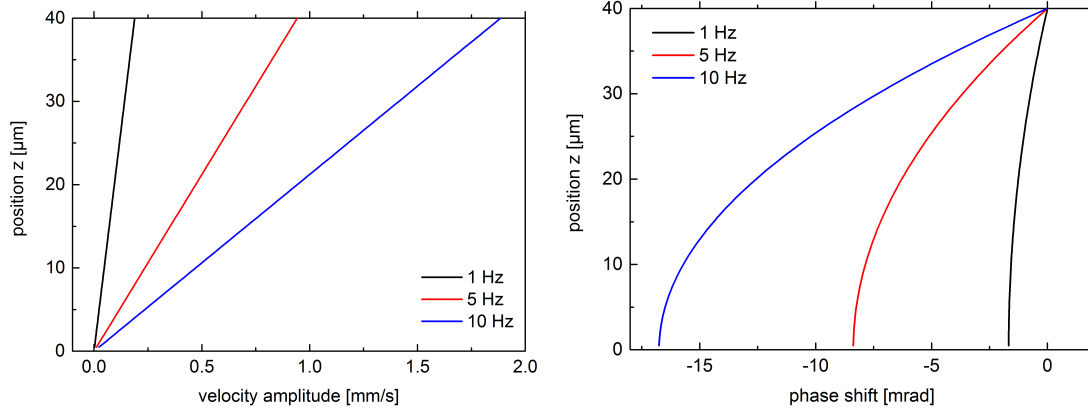
Under consideration of the boundary conditions, the spatial equation is solvable as well, so the complete solution reads

$$v_y(z, t) = y_{lens,0} \omega \cos(\omega t) \frac{\sinh \left[(1 + i) \sqrt{\frac{\rho \omega}{2\eta}} z \right]}{\sinh \left[(1 + i) \sqrt{\frac{\rho \omega}{2\eta}} h_{lens} \right]}. \quad (\text{III.3.7})$$

In context with the description of a DNA molecule within this flow profile, it is more handy to re-express the hyperbolic sine functions as an exponential expression [59]. This finally leads to

$$v_y(z, t) = \Theta(z) \cos(\omega t + \phi(z)) \quad (\text{III.3.8})$$

III.3.1. Flow Profile between Two Parallel Oscillating Surfaces



(a) Plot of the velocity amplitude $\Theta(z)$ at all positions between the two plates. (b) Plot of the phase shift $\phi(z)$ at all positions between the two plates.

Figure III.3.3.: Dependence of the velocity amplitude and the phase shift of the moving fluid on the position in z -direction between the plates. The position in z -direction is drawn on the ordinate to facilitate a comparison with the sketch in figure III.3.2. The distance of the plates was fixed at $40 \mu\text{m}$ for all calculations. The amplitude of the plate amounted to $30 \mu\text{m}$, while the frequency was set to three different values, indicated by different colors in the graphs.

with the amplitude

$$\Theta(z) = y_{lens,0}\omega \left[\frac{\cosh\left(\sqrt{\frac{2\rho\omega}{\eta}}z\right) - \cos\left(\sqrt{\frac{2\rho\omega}{\eta}}z\right)}{\cosh\left(\sqrt{\frac{2\rho\omega}{\eta}}h_{lens}\right) - \cos\left(\sqrt{\frac{2\rho\omega}{\eta}}h_{lens}\right)} \right]^{0.5} \quad (\text{III.3.9})$$

and the phase

$$\phi(z) = \arctan \left[\frac{\tan\left(\sqrt{\frac{\rho\omega}{2\eta}}z\right) \tanh\left(\sqrt{\frac{\rho\omega}{2\eta}}h_{lens}\right) - \tan\left(\sqrt{\frac{\rho\omega}{2\eta}}h_{lens}\right) \tanh\left(\sqrt{\frac{\rho\omega}{2\eta}}z\right)}{\tanh\left(\sqrt{\frac{\rho\omega}{2\eta}}z\right) \tanh\left(\sqrt{\frac{\rho\omega}{2\eta}}h_{lens}\right) + \tan\left(\sqrt{\frac{\rho\omega}{2\eta}}z\right) \tan\left(\sqrt{\frac{\rho\omega}{2\eta}}h_{lens}\right)} \right]. \quad (\text{III.3.10})$$

Thus, not only the amplitude of the flow profile depends on the position z between the plates, but also the phase shift ϕ . Since the phase shift of the DNA molecule relative to the driving oscillation will play a crucial role later, a check should be performed whether the flow profile itself can cause a significant phase shift all by itself.

In figure III.3.3, the equations III.3.9 and III.3.10 are plotted for a fixed height of the lens as well as a given amplitude of the upper surface. The driving frequency was varied between 1 Hz and 10 Hz . When considering the amplitude, it becomes apparent that the profile is completely linear if the phase is not considered. For the given distance between the plates and the given frequency range, the phase shift between the fluid motion and the driving oscillation of the upper plate does also not play a significant role.

III.3. Theory

The biggest occurring phase shift always stays below 20 mrad . Thus, for the parameter range relevant for this work, no additional phase shifts need to be taken into account. This result facilitates the description of a DNA molecule attached to the fixed plate by a dumbbell model, which will be discussed in the following section.

III.3.2. Model for a Single-End-Grafted DNA-Molecule

As already explained in the introduction, one of the goals of this study is to find a simple model to describe the dynamic behavior of grafted DNA molecules. Quite a wide variety of models has been used earlier to characterize them in certain flow situations. The Rouse and Zimm models are very popular when the extension behavior of the polymer is in focus, the Porod-Kratky model or worm-like chain model is preferred when the properties in the freely floating or flowing state are an issue. However, since these options already show quite a high level of complexity, a much simpler model will be applied here.

The basic idea is sketched in figure III.3.4. When a DNA molecule is attached by some kind of bond to a cover slip, it typically shows a “mushroom”-like shape: A rather thin stem links the polymer to the cover slip. Above it, however, a big cloud containing most of its mass floats. This has the particular consequence that the center of mass (COM) of the molecule in average is situated at a certain distance z_0 away from the cover slip. As a result, instead of describing the DNA as a base-pair-wise bead-spring model, a reduction down to two springs and a bead can be performed. A first spring attaches the COM at its average height z_0 above the cover slip (not drawn in figure III.3.4b), a second one links it to the lateral center position directly above the grafting point. The polymer itself can be modeled using the radius of gyration. In later experiments, the focal plane will be aligned parallel to the x-y-plane, thus, motion towards or away from the cover-slide will not be visualizable. Since only the motion in this plane can be evaluated, hence, just one spring is depicted in the figure. During this modeling phase, the second spring will

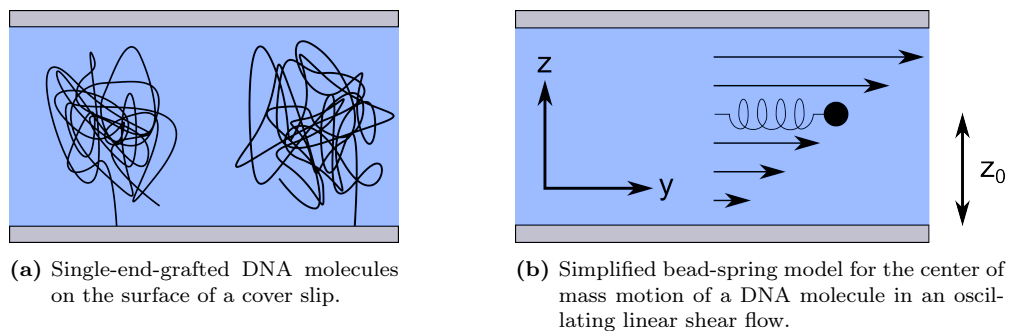


Figure III.3.4.: Model system for single-end-grafted DNA molecules on a cover slip.

III.3.2. Model for a Single-End-Grafted DNA-Molecule

be taken into account, because it determines how far away from the lower cover slip the *COM* is able to move and it will also determine how the occurring Brownian fluctuations will be dampened.

Overall, if the model in the x-y-plane is considered, it consists of a spherical bead which is attached to a spring of a stiffness κ . The other end of the spring is grafted at a distance z_0 away from the cover-slide. Although such a system cannot be realized in an experiment without any complications, it will be very helpful in developing an analytical description and a simulation of it. A flow oscillating in time created by a moving upper plate will be assumed. Due to advantages in analytic processing, the shear rate will be shifted by $\pi/2$ as compared to the past section and read $\dot{\gamma}(t) = \dot{\gamma}_0 \sin(\omega t)$. Since no noteworthy additional phase contribution will occur because of the flow profile itself, this shift will not play any further role at all. In context with optical tweezers, in section I.4.3 a Langevin equation for a confined colloid was solved. Equation I.4.14 can be adapted to be suitable for the motion of the grafted DNA molecule as well. It then reads

$$\zeta \frac{\partial z(t)}{\partial t} + \kappa(z(t) - z_0) = F_{r,z}(t), \quad (\text{III.3.11})$$

$$\zeta \left(\frac{\partial y(t)}{\partial t} - \dot{\gamma}(t)z(t) \right) + \kappa y(t) = F_{r,y}(t). \quad (\text{III.3.12})$$

Unlike the case involving optical tweezers, now, there is a shear-coupling between the z- and the y-direction, while no coupling is found to the x-direction. Just as before, this system of equations is solved by first tackling the z-direction via variation of variables and then inserting the solution into the equation of motion in y-direction. That equation is solved by the same process. The solutions are given by

$$z(t) = z_0 + e^{-t/\tau_r} \left\{ z_s - z_0 + \int_0^t dt' \frac{F_{r,z}(t')}{\zeta} e^{t'/\tau_r} \right\}, \quad (\text{III.3.13})$$

$$\begin{aligned} y(t) = & \frac{z_0 Wi}{1 + \alpha^2} \{ \sin(\omega t) - \alpha \cos(\omega t) \} \\ & + e^{-t/\tau_r} \left\{ y_s + \frac{Wi}{\alpha} (z_s - z_0) (1 - \cos(\omega t)) + \frac{z_0 \alpha Wi}{1 + \alpha^2} \right\} \\ & + e^{-t/\tau_r} \left\{ \int_0^t dt' \left[e^{t'/\tau_r} \frac{F_{r,y}(t')}{\zeta} + \dot{\gamma}_0 \sin(\omega t') \int_0^{t'} dt'' \left(e^{t''/\tau_r} \frac{F_{r,z}(t'')}{\zeta} \right) \right] \right\}, \end{aligned} \quad (\text{III.3.14})$$

where $\alpha = \omega \tau_r$ is the dimensionless frequency and $\vec{r}_s = (x_s, y_s, z_s)$ is the initial starting position of the bead. Similarly to before when a bead was confined in an optical trap, a relaxation rate is given by $\tau_r = \zeta/\kappa$. Since the solution for the y-direction depends on the Weissenberg number, the relative height z_0/h_{lens} is also included implicitly. This leads to a linear downscaling of the maximum displacement the bead can experience, depending

III.3. Theory

on the distance of the bead to the cover slip as well as the lens distance.

In later experiments, the system will be observed using a very light-sensitive CCD camera. The downside to this technique is that the recording rate is limited to 32 Hz. In context with Brownian motion and stochastic molecular processes, this means that all analytical considerations should be performed in the limit of long timescales. Hence, all terms included in the solution which depend on functions of the type $\exp(-t/\tau_r)$ will decay too quickly for visualization. Only those terms containing the Brownian force $F_{r,i}$ will be kept. The solution can be simplified to

$$z(t) \xrightarrow{t \gg \tau_r} z_0 + e^{-t/\tau_r} \int_0^t dt' \frac{F_{r,z}(t')}{\zeta} e^{t'/\tau_r}, \quad (\text{III.3.15})$$

$$y(t) \xrightarrow{t \gg \tau_r} \frac{z_0 Wi}{1 + \alpha^2} \{ \sin(\omega t) - \alpha \cos(\omega t) \} \\ + e^{-t/\tau_r} \left\{ \int_0^t dt' \left[e^{t'/\tau_r} \frac{F_{r,y}(t')}{\zeta} + \dot{\gamma}_0 \sin(\omega t') \int_0^{t'} dt'' \left(e^{t''/\tau_r} \frac{F_{r,z}(t'')}{\zeta} \right) \right] \right\}. \quad (\text{III.3.16})$$

Let us now leave the Brownian terms out of consideration as well. In this case, for the y-direction only the first term remains. Just like in part I, equation I.4.35 can be applied to it to obtain one single trigonometric function including a certain phase shift. It then reads

$$y(t) = \underbrace{\frac{z_0 Wi}{\sqrt{1 + \alpha^2}}}_{A_{DNA}(\alpha)} \sin(\omega t - \underbrace{\arctan(\alpha)}_{\delta_{DNA}(\alpha)}). \quad (\text{III.3.17})$$

When this displacement is compared to the driving by the oscillating lens, which is given by $y_{lens}(t) = \underbrace{\frac{\dot{\gamma}_0}{\omega}}_{y_{lens,0}} \sin(\omega t - \underbrace{\pi/2}_{\delta_{lens}})$, the phase shift between both of them can be defined as

$$\Delta\delta(\alpha) = \delta_{DNA}(\alpha) - \delta_{lens} = -\arctan(\alpha) + \pi/2. \quad (\text{III.3.18})$$

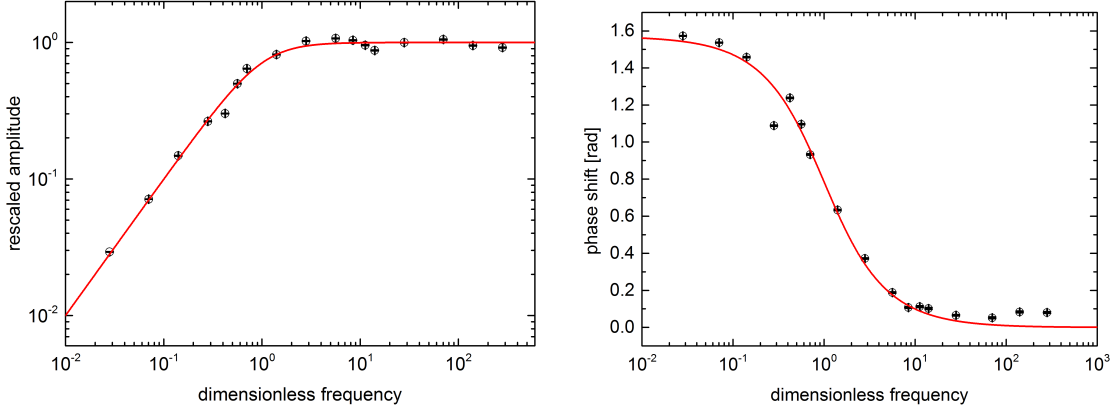
Based on the solution in equation III.3.17, two derived quantities can be defined. The first one, also denoted as the relative amplitude, is gained by dividing the amplitude A_{DNA} of the bead by the amplitude of the lens

$$A_{rel}(\alpha) = \frac{z_0}{h_{lens}} \frac{\alpha}{\sqrt{1 + \alpha^2}}. \quad (\text{III.3.19})$$

The second quantity is derived from the amplitude as well. By dividing equation III.3.19 additionally by the relative height of the bead z_0/h_{lens} , the rescaled amplitude is gained

$$A_{resc}(\alpha) = \frac{\alpha}{\sqrt{1 + \alpha^2}}, \quad (\text{III.3.20})$$

III.3.2. Model for a Single-End-Grafted DNA-Molecule



(a) Dependence of the rescaled amplitude on the dimensionless frequency.

(b) Dependence of the phase shift on the dimensionless frequency.

Figure III.3.5.: Results of the bead-spring model for DNA molecules. Analytical curves are shown in these semi-logarithmic plots as solid red lines, numerical data is presented in open black circles.

which removes any dependencies of the amplitude on other parameters than the dimensionless frequency α . Both quantities will be a great benefit when analyzing experimental data later on.

In order to grasp the functional dependency of the rescaled amplitude within equation III.3.20 as well as the phase shift within equation III.3.17 on the dimensionless frequency, both of them are plotted in figure III.3.5. Besides the analytic functions, also numerical data is included which was gained by adapting the algorithm from chapter I.5 in the first part. According to both, the expected behavior of the rescaled amplitude will increase proportionally to α for low frequencies $\alpha \ll 1$, i. e. $\omega \ll \tau_r^{-1}$. Upon exceeding $\alpha = 1$, the maximum amplitude, which cannot be surpassed, is reached. To facilitate the explanation of this effect, let us go back to the sketch in figure III.3.4b. The maximum extension of the spring, which is indicated in the figure and which leads to a perfect alignment of the bead to the velocity front of the fluid, can only be reached at high frequencies. Otherwise, the spring succeeds in partially relaxing back to its equilibrium position and thus does not experience the full stretching.

The explanation for the behavior of the phase shift is a similar one. The driving motion is coupled to the motion of the bead via the flow velocity of the surrounding fluid. Hence, when comparing the phase of the displacement of the lens with the phase of the bead displacement, at low frequencies $\alpha \ll 1$, both are shifted by $\pi/2$. This shift then decreases until $\alpha \gg 1$. Then, it becomes zero and thus the bead directly follows the motion of the displaced fluid.

III.3.3. Summary

In the past chapter, a short introduction to the chemical as well as physical structure of DNA molecules was given. In total, it can be considered as a very long-chained polymer with a negative net-charge. In the scope of this thesis, λ -DNA, which consists of roughly 50,000 base pairs and has a contour length of approximately $20\ \mu\text{m}$ when the dye-molecule YOYO-1 is intercalated, is utilized.

Since these molecules will later be attached to the surface of a cover slip and then subjected to forced driving by oscillating a second surface, the resulting velocity profile needed to be analyzed. This was performed in section III.3.1, where the corresponding Navier-Stokes equation was solved. The result, as figure III.3.3 shows, is a near-linear profile that only deviates from the ideal case by a slight phase shift which depends on the exact position between the oscillating upper and the resting lower plate. Since all occurring phase shifts are quite small ($\delta_{flow} < 20\ \text{mrad}$), it is not necessary to take them into account during further analysis.

Afterwards, the DNA molecule was modeled as a bead which was linked by a spring to the lateral position of the grafting point. The bead was identified with the center of mass (COM) of the DNA, the stiffness of the spring represents the mechanical properties of the molecule. A second spring attached it to the height z_0 within the channel. This height coincided with the typical distance of the COM of a grafted λ -DNA molecule. It was described analytically using a two-dimensional Langevin-equation, which also included the height-dependent shear coupling. Equation III.3.17 gives the simplified solution in the limit of long times under negligence of the stochastic effects of Brownian motion. Basically, it consists of a sinusoidal response oscillation whose amplitude depends on the dimensionless frequency α , the average height of the COM z_0 , as well as the distance of the lens h_{lens} causing the driving. Moreover, a characteristic phase shift between driving and response oscillation which solely depends on the dimensionless frequency according to the model is included. In the following chapter, this result will be compared to experimental data sets and its validity will be checked.

III.4. Experimental Study

This chapter will focus on all elements that are required to perform experiments with single-end-grafted DNA molecules in an oscillating shear flow. On the one hand, a cover slip as well as the DNA need to be prepared. This process will be explained in the following. On the other hand, a specific setup using fluorescence microscopy is required, which will be described in section III.4.1. After acquiring picture series of bright, fluctuating molecules, their positions and especially their center of mass need to be determined. A software built by André Schröder (Institut Charles-Sadron, Strasbourg, France) denoted “NEW Magneto” was utilized for this task (see Sect. III.4.2 for details). The performed experiments as well as their results will follow in section III.4.3.

Before any experiments can be conducted, the DNA and a cover slip have to be prepared first. The general idea of this process is to use a streptavidin-biotin bond to attach the DNA to the cover slip. This kind of bond is one of the strongest non-covalent, biological bonds. Streptavidin is a protein produced by the bacterial species *Streptomyces avidinii*, biotin is better known as vitamin B₇ or vitamin H. However, streptavidin comes with the disadvantage of an isoelectric point between pH 6.8–7.5 which may vary within these bounds. Instead, for this study NeutrAvidin (ref.-no. A2666, Life Technologies GmbH, Darmstadt, Germany), which has its isoelectric point at pH 6.3 with no variation, was used. This helped to reduce non-specific binding.

To utilize this bond, the surface of the cover slip is treated with NeutrAvidin, while each DNA molecule is functionalized with a biotin molecule, which will be attached to each other later on by bringing them in contact. This technique was introduced by Koota et al. in 2007 [132] and has found a wide application since then [127, 131, 133]. However, both processes are not straight forward. λ -DNA are typically available in their circular state as shown in figure III.4.1a. By a heat treatment, the ring has to be opened at two nicks, which leaves unbound overhangs with the sequences 5'-AGGTCGCCGCC-3' and 5'-GGGCGGCGACCT-3', one at each extremity of the molecule. Oligonucleotides with the desirable functional group appended to them can now be bound to the DNA at these positions (Fig. III.4.1b). Quite a variety of functional groups like biotin, thiol, and many others are available. For the experiments presented here, a biotin- and a thiol-group were chosen. The biotin-group, as explained earlier, will be used for the grafting of DNA, while the thiol-group shows no interaction or binding to NeutrAvidin at all and is thus ideal as a second functional group. In a final step, the backbone between DNA and oligomers

III.4. Experimental Study

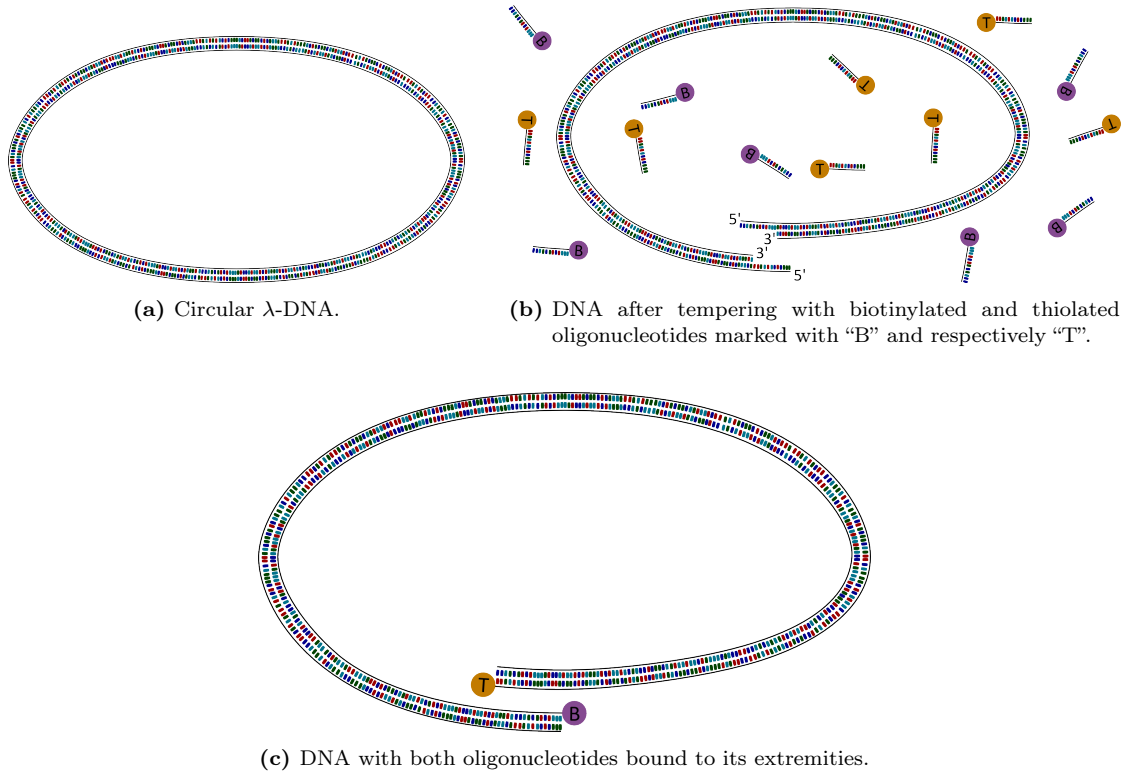


Figure III.4.1.: Ligation process of λ -DNA in preparation for single-end-grafting (drawing adapted from [131]).

has to be repaired using a ligation reaction (Fig. III.4.1c). A more detailed description of this process can be found in the appendix (Sect. A.2.3).

The second part of the preparation involves the cover slip. A NeutrAvidin layer as thin and homogeneous as possible needs to be brought on top. Again, a number of steps is necessary to successfully reach this goal. They were adapted from the procedure by Yuting Sun [131]. An step-by-step guide for the preparation is given in the appendix (Sect. A.2.4).

At this point, it is possible to attach the DNA molecules to the cover slip without risking a collapse of the molecule or multiple attachment positions of a single DNA (comparable to the comic in Fig. III.3.4). However, in their current state, it is not possible to visualize them. After all, the average radius of gyration is smaller than $1 \mu m$ with the single monomers on size scales of a few nanometers. Thus, before adding the DNA molecules on the prepared cover slips, fluorescent dye molecules need to be bound to the DNA first. Quite a wide range of dyes has become available in the past decades. By now, they are widely accepted with their photophysical properties [134], their function [135], and their mechanical properties [136] being well-researched. In this thesis, the intercalating dye YOYO-1 (ref.-no. Y3601, Life Technologies GmbH, Darmstadt,

Germany) is utilized for this purpose since it shows a strong increase in emitted intensity only if it is bound to a DNA molecule. This reduces the background noise and contributes to a clearer visualization with an improved contrast. Intercalation means that the dye is positioned in between the base pairs. The maximum amount of this particular dye, which can be inserted in each DNA, is one dye molecule for every four base pairs. Following the preparation steps in the appendix (Sect. A.2.4), the maximum amount of YOYO-1 molecules per DNA is reached, thus, ensuring the strongest fluorescence intensity.

III.4.1. Experimental Setup

In the scope of this third part of the thesis, grafted DNA molecules are recorded while they are subjected to a shear flow. Two particular techniques are required to conduct these experiments: On the one hand, the fluorescence emitted by intercalated dye molecules has to be recorded. This technique is well-known as fluorescence microscopy. Since its invention, it has been utilized in a wide variety of studies [137, 138] and is especially popular in researching biological matter. On the other hand, a well-defined shear flow whose gradient is strongly dependent on the distance between the oscillating lens and the resting surface to which the DNA molecules are attached has to be created (see Fig. III.4.2). Thus, it is essential to determine the lens distance as exactly as possible. For this purpose, a technique called reflection interference contrast microscopy (RICM) is used. It was invented by Zilker, Engelhardt, and Sackmann in 1987 [139] and has ever since been applied to many systems in order to enable the examination of dynamic processes on surfaces, high precision distance measurements, and much more. In this section, at first a short introduction to both microscopy techniques will be given, which will afterwards be followed by a description of the setup.

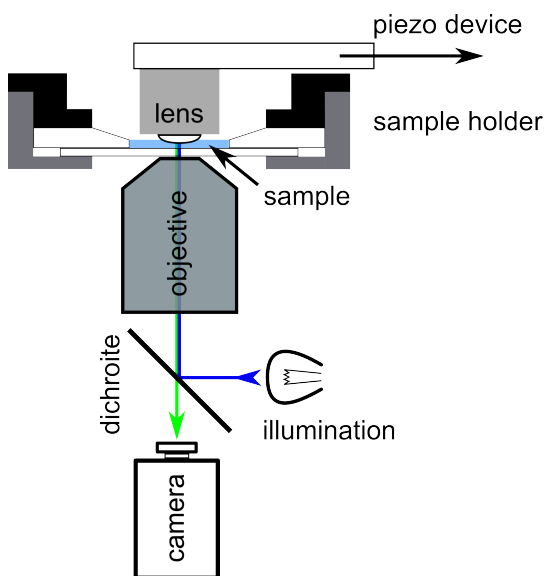
The general idea in fluorescence microscopy is that an object is supposed to be recorded although it is too small to become visible using standard objectives and optics. Since one would usually risk different kinds of optical aberrations if one tried to image the object under an even larger magnification, another approach uses active emission of light by the object itself to visualize it. Of course, most objects cannot be forced to emit light directly, thus, methods which allow fluorescent dyes to be attached to the object of interest have been developed. These methods are most frequently applied in biology. Among others DNA [140], bacteria [141], and viruses [142] were prepared with a series of dyes. In context with DNA in specific, a long list of possible dyes which all show different qualities but also disadvantages exists. For this study, a dye called YOYO-1 is used. It absorbs light with a wavelength of 489 nm and re-emits light with a wavelength of 509 nm .

The second technique that was mentioned in the introduction to this chapter, reflection interference contrast microscopy (RICM), is a handy tool to measure small distances

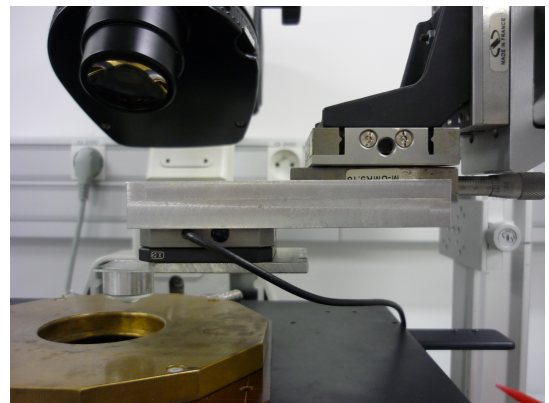
III.4. Experimental Study

between microscopic objects. The principle of this technique is, as its name suggests, interference-based [143]. Light is sent through the microscope objective and then reaches the sample cell. There it transmits through the cover slip and reaches the interface to a fluid, typically water or a buffer solution. Due to a change in refractive index, this causes a partial reflection back towards the objective. If a second object lies in the path of the transmitting beam, again, a certain amount of light is reflected. Since both reflected beams are optically retarded by a small amount in respect to each other, an interference which depends on the distance of the object and the cover slip is caused. For point-like or round objects, the interference appear in form of Newton rings, which periodically modify the intensity of the recorded light. However, for these rings to appear, the object and the cover slip have to be in very close proximity. In other words, when measuring the distance between the lens which will be used for driving the shear flow later and the cover slip carrying the DNA molecules, the appearance of these Newton rings signal the contact between both of them. A micrometer screw can now be used to tune the distance between them as required.

For the application of both techniques, the same setup is used (Fig. III.4.2), which also allows the rapid switching between them. This has the advantage of allowing a quick determination of the distance of the lens, followed by the recording of a fluorescence picture series without much loss of time. As a base, the inverted microscope Nikon



(a) Sketch of the key elements of the experimental setup.



(b) Photograph of the shear device above the microscope.

Figure III.4.2.: Representation of the experimental setup for shearing and visualizing the DNA molecules.

Eclipse TE200 (Nikon GmbH, Düsseldorf, Germany) is used in combination with an oil immersion objective HCX PL Fluotar 100x RC by Leica (ref.-no. 11506199, Leica, Wetzlar, Germany). The objective has a numerical aperture of 1.3 and thus allows to visualize a very broad field of view at a 100x magnification. As an illumination source, a mercury torch (HB-10104AF, Nikon GmbH, Düsseldorf, Germany) is attached to the back port of the microscope. The visualization for the fluorescence as well as for the RICM technique is realized using a very light sensitive 16 bit greyscale CCD camera (ImagEM C9100-13, Hamamatsu Photonics Deutschland GmbH, Herrsching am Ammersee, Germany).

The most important part for the conduction of the experiments is a system which allows to generate the necessary shear flows. This is realized by attaching an optical lens via a spacer to a piezoelectric device (ref.-no. PX400 with amplifier ENV300, piezosystem Jena GmbH, Jena, Germany). The lens (ref.-no. LA1576-A, Thorlabs GmbH, Dachau, Germany) has a low curvature radius $r_{curv} = 6.2\text{ mm}$ and is covered by an antireflex coating for visible wavelengths. It allows to move the lens along one axis parallel to the surface of the cover slip with the DNA molecules. Although an exactly parallel alignment of the piezo axis to the cover slip is a big challenge, any tilt over the very small displacement amplitudes used later is compensated by the curved surface of the lens and thus does not need to be taken into account. The assumption of flat parallel surfaces in chapter III.3.1 is thus perfectly reasonable. The control over the displacements of the piezo is conducted by a signal generator which is linked to the voltage input of the amplifier. This voltage signal is recorded synchronously to the picture series during fluorescence microscopy via a National Instruments USB signal card (ref.-no. NI USB-6008, National Instruments, Austin, TX, United States of America). In order to be able to identify the measured voltage signals with displacements, a calibration of the piezo device is performed by attaching fluorescing beads to the surface of the lens and visualizing them using the fluorescence camera (Fig. III.4.3). A linear law becomes apparent, which is described by

$$A_{lens} = 31.0(2) \frac{\mu\text{m}}{\text{V}} \cdot A_{volt} - 0.4(1) \mu\text{m}, \quad (\text{III.4.1})$$

where A_{lens} is the traveled distance in micrometers and A_{volt} is the applied voltage in Volts.

Especially in context with the analysis of oscillating signals and their relative phase, a precise timing of the recorded images is of the essence. In order to make sure that no additional temporal delays need to be taken into account, we calibrated the recording timestamps of the camera with a known signal. This was performed by attaching a colloidal sphere to the surface of the lens which is coupled to the piezoelectric device as described above. A sine signal of known amplitude and frequency was then applied to the piezo device and recorded at the same time. This signal and its timestamp was compared

III.4. Experimental Study

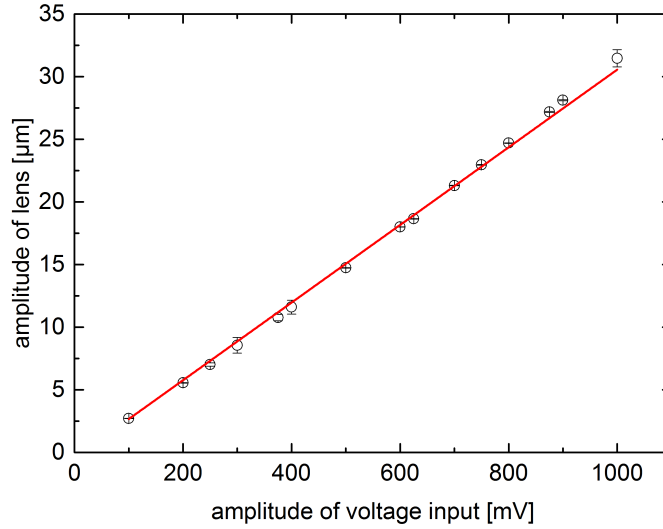


Figure III.4.3.: Calibration curve of lens amplitude versus piezo voltage. The lens amplitude was estimated by tracking attached fluorescing beads.

to the oscillations of the colloid. Overall, we found a signal delay of approximately 30 ms between driving and response signal. This delay will be considered in all following measurements by a corresponding shift of the timestamp of every image by -30 ms.

Depending on whether fluorescence excitation is used or whether an RICM measurement is of interest, a series of filters can be inserted. In RICM mode, the light is sent through a polarizer before it passes the objective, which is additionally equipped with a quarter-wave plate. An analyzer helps in enhancing the contrast before the light reflected by the sample reaches the camera. In fluorescence mode, a combination of exciter filter, dichroic mirror, and barrier filter is used (Nikon B-2A, Nikon GmbH, Düsseldorf, Germany). The exciter only allows a small band of visible light in the blue range between 450 nm and 490 nm from the mercury torch to pass, which is then reflected by the dichroic mirror towards the sample. The fluorescent light from the YOYO-1 molecules at 510 nm then moves backwards through the objective and can also transmit through the dichroic mirror due to its design. The subsequent barrier filter blocks all excitation wavelengths from passing towards the camera and only allows the fluorescence light to transmit.

Since the camera is extremely sensitive to light, the “correct” amount of light depends mainly on the recording frequency. If too much light arrives at the chip, all pixels display the brightest greyscale value and all details are lost. If, on the other hand, not enough light arrives, it is hard to make out any details since the contrast of the recorded images is too weak. An ideal compromise would be a setting that shows the brightest pixels close to maximum value while at the same time the background is as close to the darkest gray level as possible. Neutral density filters (ref.-no. ND4 and ND8, Nikon GmbH, Düsseldorf,

Germany) help in reducing the incoming amount of light from the illumination source to levels that can be visualized by the camera in a manner as optimal as possible. Another property that has to be taken into account is the fact that the fluorescence of YOYO-1 bleaches after a certain amount of time. This means that, over the course of time, less and less light is emitted, thus, there is a tight time limit to the measurements. If the recording should be performed over a longer amount of time, the intensity of the incident light can be reduced, which at the same time will reduce bleaching.

III.4.2. Utilized Programs

Nearly all necessary software for data evaluation was already mentioned in part I of this thesis. Data handling and fitting was mostly conducted using Matlab and Origin. Before these tasks could be performed, the data sets had to be extracted from extensive picture series first. In general, they consisted of $512\text{ px} \times 512\text{ px}$ wide areas containing bright spots, where the DNAs were attached to the cover slip. The *COM* of each molecule was gained from each picture using the batch processing function of the software “NEW Magneto”. It had been written by André Schröder (Institut Charles-Sadron, Strasbourg, France) and provided all required options.

Typically, at first a region of interest (ROI) containing exactly one single DNA molecule was selected. Additionally, a second ROI showing just the intensity background recorded by the camera was chosen. It was also possible to perform nearest-neighbor-filtering to reduce local intensity fluctuations and thus smoothen the evaluation of the

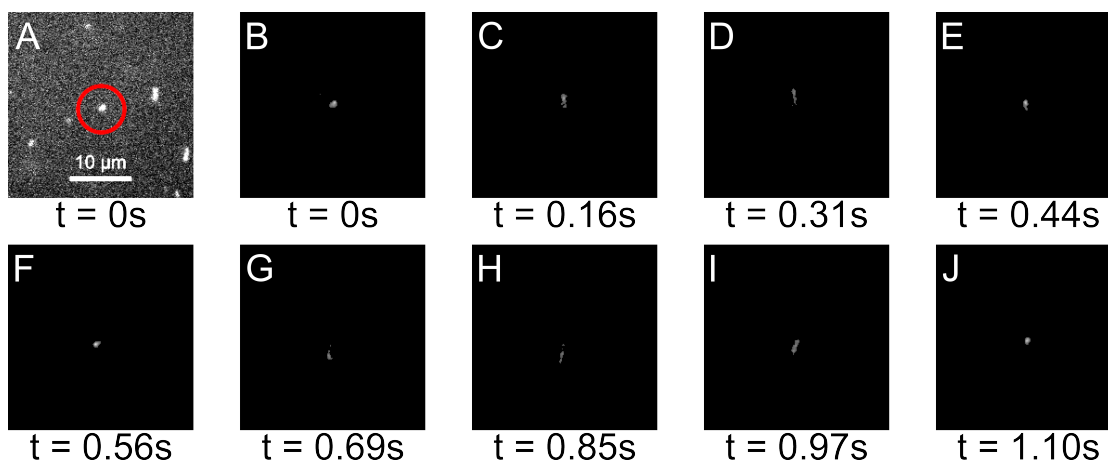


Figure III.4.4.: Comparison of originally recorded picture of grafted DNA molecules (Fig. A) and post-processed picture after filtering (Fig. B). Oscillatory driving was applied to the sample cell ($h_{lens} = 40\ \mu\text{m}$, $A_{lens} = 93\ \mu\text{m}$, $f = 1\ \text{Hz}$) whose resulting effect is presented in figures C to J. They contain snapshots of the following pictures with the filtering applied to them. The region of interest (red circle) and a scale bar, both valid for all pictures, are marked in the first picture.

III.4. Experimental Study

picture. For all following data evaluations, the first neighboring pixels were taken into account. As the next step, the software subtracted the average background intensity from all pixels and used a threshold value to determine which pixels actually contributed to the DNA molecule and which ones did not. The remaining pixels of interest were then used to determine the *COM* of the DNA by weighting their position by the intensity

$$r_{i,COM} = \frac{\sum_j r_{i,j} I_j}{\sum_j I_j}, \quad (\text{III.4.2})$$

where *i* denotes the direction, i. e. *x* or *y*, and *j* is the index of a pixel. The result of this image processing is depicted in figure III.4.4. For each picture, the *COM* coordinates were saved together with the time at which the picture had been recorded in a “*.txt” file.

In other situations, the analysis of the average image of a picture series was of interest. In this case, the software allowed to add all intensities over the whole series and to save the resulting average image. This, for example, allowed the analysis of the density distribution of the polymer.

III.4.3. Measurements

After the preparation of the samples has been finished, they are brought into the microscope. Typically, at first the desirable distance between lens and cover slip is set. This is achieved by bringing them into contact, which in RICM shows as Newton rings, and then increasing the distance via a micrometer screw. Then, the actual oscillation experiments are performed, however, the lens distance is checked every few experiments in order to avoid too strong variations. The y-direction is always chosen as the oscillation direction. Three parameters have to be taken into account: the height of the lens, as well as the amplitude and frequency of the driving oscillation. The phase space of the experiments is given by lens distances in the range between $40 \mu\text{m}$ and $80 \mu\text{m}$, amplitudes between $15 \mu\text{m}$ and $140 \mu\text{m}$, and frequencies between 0.1 Hz and 5 Hz . However, not all combinations of parameters can be used since for smaller lens distances the amplitudes have to be reduced to avoid damage to the DNA molecules like, for example, ripping.

After the evaluation of the *COM* of individual DNA as explained in the past section, displacement-time-curves as in figure III.4.5 result. There, the motion of the lens is depicted as black symbols and the reaction of the *COM* is shown as blue symbols. In this case, it seems as if the DNA runs ahead of the lens motion. This is due to the coupling of the *COM* motion to the velocity of the lens, which causes the additional shift by $\pi/2$ (compare Sect. III.3.2). Both data sets can be approximated by a sinusoidal function with variable amplitude and phase shift, which then allows a comparison of both

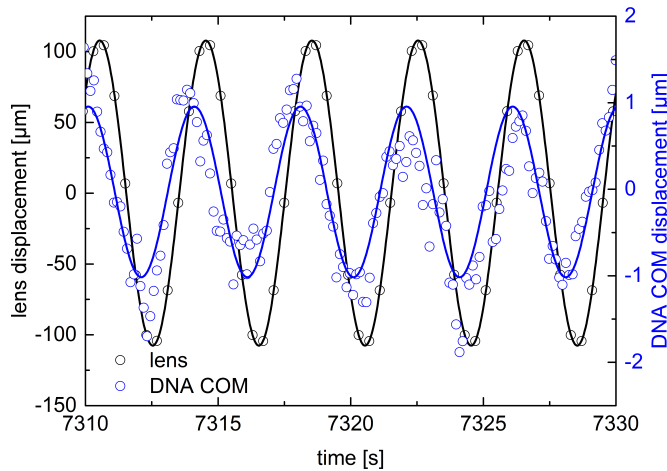


Figure III.4.5.: Displacement-time-diagram of the lens (black circles) and the center-of-mass of a DNA molecule (blue circles), as well as sinusoidal fits to both data sets (respectively colored, solid lines). The left axis corresponds to the data set of the lens, the right axis corresponds to the DNA data. Driving at a lens distance of $60 \mu\text{m}$, an amplitude of $107.7 \mu\text{m}$, and a frequency of 0.25 Hz was applied to the system. The DNA *COM* is running ahead of the driving oscillation with a phase shift of approximately $\pi/2$ as expected according to theory.

III.4. Experimental Study

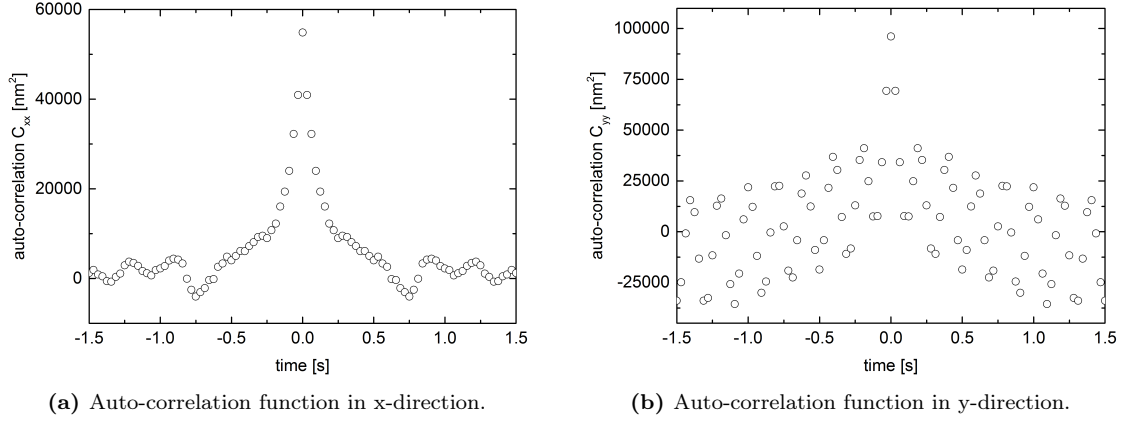


Figure III.4.6.: Auto-correlation functions of the motion of a DNA molecule under sinusoidal driving at an amplitude of $30.9 \mu\text{m}$ and a frequency of 5 Hz . The lens distance is set to $60 \mu\text{m}$.

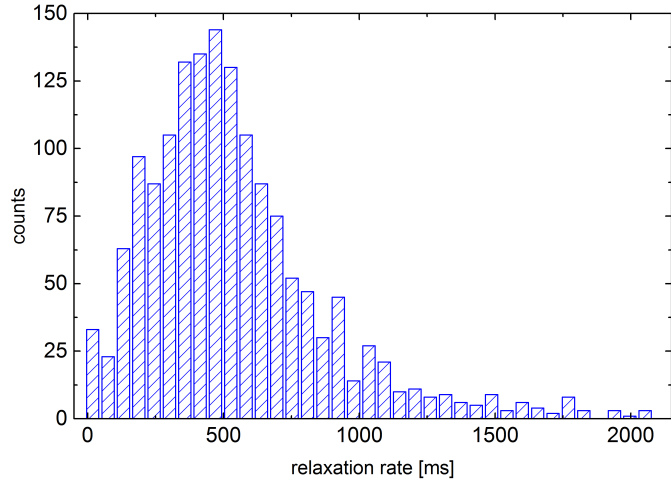


Figure III.4.7.: Histogram of the longest relaxation rates of the DNA molecules with a class width of 56.5 ms . Data was obtained by exponential fits to the auto-correlation function perpendicular to the oscillation direction, i. e. the x-direction. The maximum of the distribution is found at $442(8) \text{ ms}$, its average lies at $540 \text{ ms} \pm 350 \text{ ms}$.

oscillations.

One further quantity in context with the analytical model in section III.3.2 is gained by analyzing the auto-correlation functions of the *COM* motion: it is the longest relaxation rate τ_r . Just as in part I, the LabVIEW VI presented in the appendix (Sect. C.1) is used for this purpose. As an example, in figure III.4.6 the auto-correlation functions in x- and y-direction are shown. In the x-direction, after a quick relaxation process, which is well-described using a single exponential function, no characteristic correlation signal is found besides noise and a weak oscillatory contribution due to an imperfect alignment. Since there is no shear- or similar coupling to the x-direction present in the

system, this corresponds to the theoretical prediction. In oscillation direction, however, the exponential relaxation is superimposed by a strong oscillatory signal, which again corresponds well to the theoretical assumptions. The desirable relaxation rate can now be determined by fitting an exponential function to the auto-correlation function C_{xx} . Due to the stochastic properties of the system, in this fashion not only one single rate but a whole relaxation spectrum is determined by analyzing a series of DNA molecules (Fig. III.4.7). The histogram is described well by a Gaussian distribution whose left flank is cut-off towards negative relaxation rates. The most frequently appearing rate can be identified with the peak value at $442(8) \text{ ms}$. The average relaxation rate, though, constitutes $540 \text{ ms} \pm 350 \text{ ms}$. This average value will be used from now on throughout this chapter to determine the dimensionless frequency α . The relaxation rate determined in this study exceeds the value of 400 ms which was reported earlier by Doyle and others [124] by 35 %.

In the following, the experimental results from sinusoidal fits to the displacement data will be compared to analytic results to check on the validity of the bead-spring model. According to equation III.3.17, the amplitude A_{DNA} of the *COM* of the DNA depends on the dimensionless frequency α , the average height z_0 of the *COM*, as well as the lens distance h_{lens} and driving amplitude A_{lens} . If all parameters are kept constant except for the lens amplitude, as illustrated in figure III.4.8 for four different frequencies, the *COM* amplitude is supposed to depend linearly on A_{lens} . This is indeed proven by the experimental data since linear fits describe the curve progression well in all cases. Existing

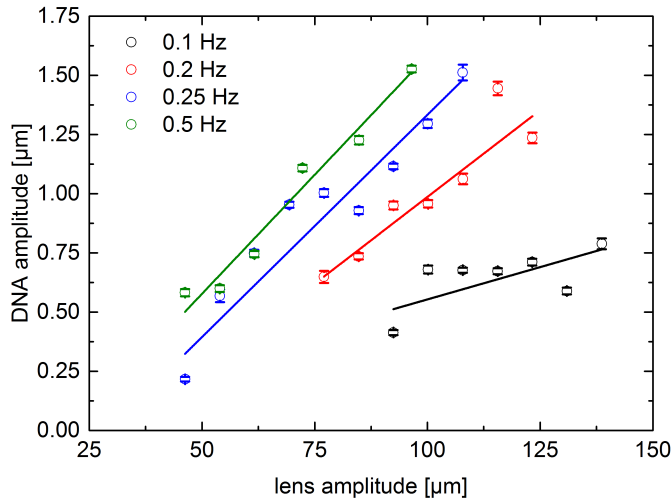


Figure III.4.8.: Graph of the DNA *COM* versus the lens amplitude. The lens distance was set to $40 \mu\text{m}$ for all experiments, the frequency was varied from 0.1 Hz to 0.5 Hz as indicated by color code. The dependence can be fitted using linear functions as illustrated by solid lines.

III.4. Experimental Study

deviations are mostly due to Brownian fluctuations, additional background noise in the picture series, and the misinterpretation of the contributions of certain pixels which do or do not belong to the examined DNA molecule. No dependence of the phase shift on the driving amplitude can be found, which is why no corresponding graph is shown in this chapter.

Furthermore, the functional behavior of both the relative amplitude (Eq. III.3.19) and the phase shift (Eq. III.3.18) can be checked in context with the lens distance. The model assumes that the average *COM* height z_0 does not change under any circumstances when shear is applied to the system. When solving the differential equation (Eq. III.3.12) this has the side effect, that the phase shift between driving and response oscillations does not depend on z_0 at all, while the response amplitude A_{DNA} shows such a dependence. When considering the relative amplitude in figure III.4.9a, a general decrease at each frequency is found for increasing distances. All of the curves can be fit with the analytically predicted behavior $A_{DNA} \propto 1/h_{lens}$. To get a more robust estimation of the average height of the *COM*, one should consider the highest driving frequencies. In this case, according to the model, the *COM* completely follows the motion of the fluid and A_{DNA} reaches a plateau value which is not influenced by an increase of the frequency. This was done in figure III.4.9a by adding the upper limiting envelope. It predicts the average *COM* height z_0 to amount to 630 nm . In case of the phase shift (Fig. III.4.9b), no clear dependence on the lens distance becomes apparent, although for frequencies higher than 2 Hz or respectively dimensionless frequencies higher than $\alpha = 6.8$ there might be a weak effect. It seems that for these higher frequencies, the phase shift decreases additionally in

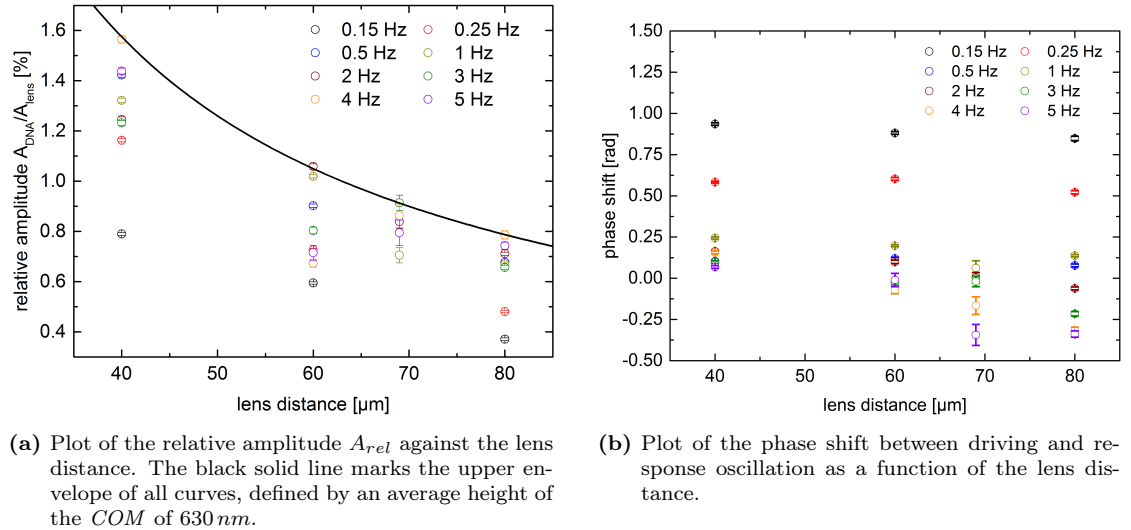


Figure III.4.9.: Dependencies of the relative amplitude and the phase shift on the distance between oscillation lens and cover slip. The relations are shown in different colors for each examined driving frequency.

a weak fashion when the lens distance is increased. However, the sinusoidal fits at higher frequencies are more prone to errors and the effect might be due to a misinterpretation of DNA motion.

The most interesting functional dependencies are those of the relative amplitude and phase shift on the dimensionless frequency. The experimentally gained values for the relative amplitude are illustrated in figure III.4.10a. At each available distance, indicated by different colors, A_{rel} increases proportionally to α for $\alpha < 1$. Upon exceeding $\alpha \approx 1$, a constant plateau value is reached. This is equivalent to the maximum extension of the DNA molecule away from its equilibrium position which the linear velocity profile allows (compare Fig. III.3.4b). However, as fits with the analytical function (Eq. III.3.19) to the data sets show, a good agreement with the experimental data sets is only found if a modification is applied to the fitting function. This modification allows small changes to the critical frequency which marks the transition from the linear increase to the constant plateau. The fitting function reads

$$A_{rel}(\alpha) = \frac{z_0}{h_{lens}} \frac{m\alpha}{\sqrt{1 + (m\alpha)^2}}, \quad (\text{III.4.3})$$

where the lens distance is always fixed at the value in the corresponding experiment and m is the fudge factor for the frequency. For the fits in figure III.4.10a, this factor varies between 1.4 and 1.8 and thus indicates a small variation of the critical frequency. This

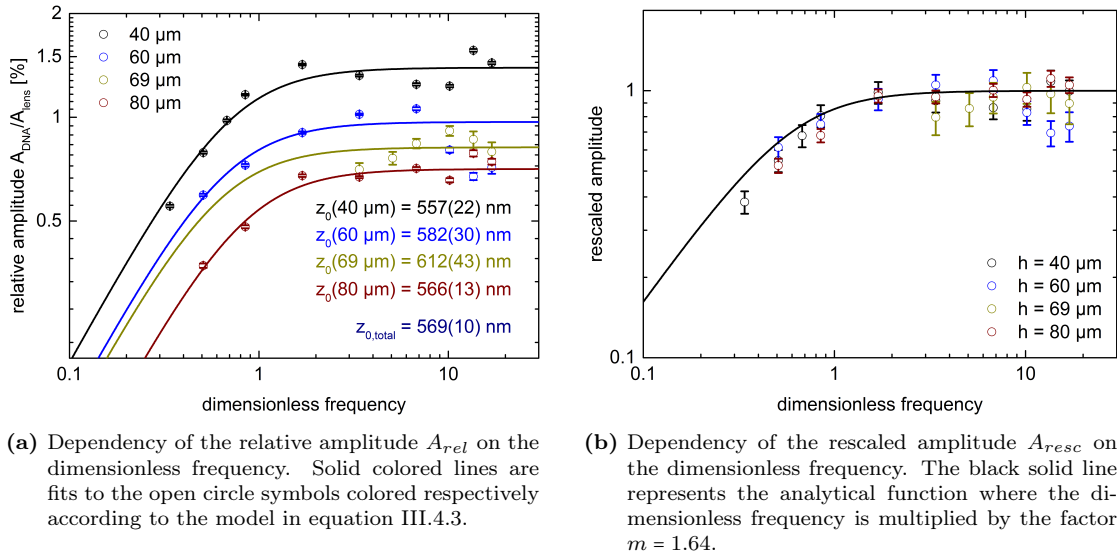


Figure III.4.10.: Amplitude dependency on the dimensionless frequency. Relative amplitudes in subfigure III.4.10a are shown in subfigure III.4.10b after rescaling by the quotient z_0/h_{lens} . Both are drawn as log-log-plots.

III.4. Experimental Study

might be due to an underestimation of the average longest relaxation rate and would lead to a correction of the rate to a range between 620 ms and 800 ms . Overall, a good total agreement of the amplitude behavior of the COM of the DNA molecules with the model description is found. The average of all modifiers is found at the value $m = 1.64$ which will be used from this point on for rescaling the dimensionless frequency.

If the relative amplitude in all curves is now rescaled by the corresponding relative height of the center of mass z_0/h_{lens} , all curves shift on top of each other and can be described by one master curve as given in equation III.3.20. It solely depends on the dimensionless frequency, which is mirrored by the results in figure III.4.10b. Again, a very good agreement to the analytical predictions (compare Fig. III.3.5a) is found.

The phase shift between the DNA COM and the displacement of the lens is plotted in figure III.4.11 as a function of the dimensionless frequency. According to theory, at low frequencies a phase shift of $\pi/2$ which decreases with increasing frequency towards 0 rad is to be expected. When this theoretical model (Eq. III.3.18) is compared to the results from the measurements the predicted behavior is indeed found. However, just as in case for the amplitude behavior, the dimensionless frequency needs to be rescaled by the factor $m = 1.64$ in order to give a more precise description of the functional behavior

$$\Delta\delta_{exp}(\alpha) = -\arctan(1.64\alpha) + \pi/2. \quad (\text{III.4.4})$$

In case of the values at a lens distance of $80\ \mu\text{m}$ a slight overshoot towards negative

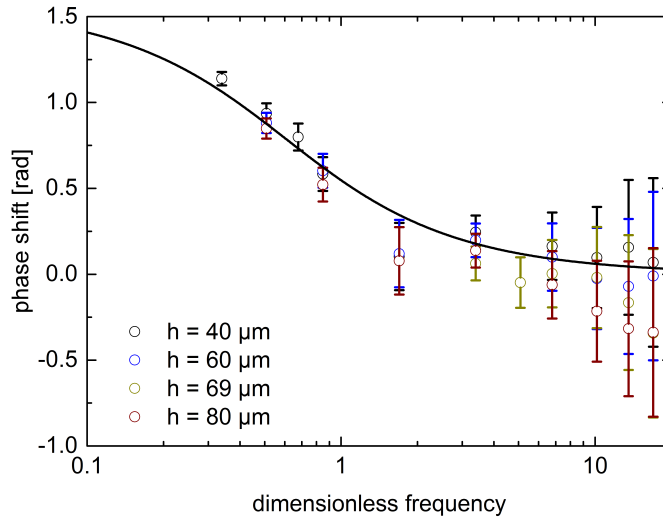


Figure III.4.11.: Dependency of the phase shift between driving and response oscillation on the dimensionless frequency. The black solid line represents a fit with the theoretical model (Eq. III.3.18) where the dimensionless frequency was rescaled by the factor $m = 1.64$. A semi-logarithmic scale was chosen.

phase shifts is observable. In this case the large error bars should be considered as well, though, which still indicate agreement with the model. Over the whole observable frequency spectrum, the assumed bead-spring model seems to capture the amplitude as well as the phase behavior of the center of mass in a perfect manner under the assumption of an effective dimensionless frequency $\alpha_{\text{eff}} = 1.64\alpha$. It is, hence, suited very well as a description of single-end-grafted molecules in a linear, oscillating shear flow.

There is an alternate way to evaluate the displacement of the DNA molecule. However, dynamic changes to the system cannot be captured by it. Instead of tracking the *COM* of each molecule, it is possible to measure the length of each DNA in an average image over a whole picture series. The calculation of these averages is also a feature of “NEW Magneto” and can be performed with ease. By choosing a region of interest parallel to the oscillation axis along the molecule, for small amplitudes, the intensity profile will be identical with a Gaussian distribution. For bigger amplitudes, this curve will broaden and finally form two separate maxima at the reversal points of the oscillation. Since the overall amplitudes are quite small, a Gaussian fit to the intensity distributions is reasonable in all cases. The standard deviation of the curves can be used as a comparative value to the amplitudes of the oscillations of the center of mass. The result for a lens distance of $40\ \mu\text{m}$ is displayed in figure III.4.12. There, the amplitudes deduced from the sine fits are shown (black circles) together with the results from the length evaluation of the intensity profiles (red circles). Additionally, three data points at even higher frequencies ($f = 10/20/32\ \text{Hz}$), which were recorded at a picture acquisition rate identical to the oscillation frequency at a lens distance of $60\ \mu\text{m}$, are displayed. Thus, it is not possible, in case of these measurements, to make out any details about their amplitude or phase behavior. In other words, the sine fit evaluation is not possible. However, the length evaluation can be conducted and the respective oscillation amplitudes can be estimated.

A property that can be deduced from figure III.4.12 straight away is that, for low dimensionless frequencies below $\alpha = 10$, the sine fit and length evaluations both give the same qualitative behavior, although there is a deviation in absolute value. This is probably due to the fact that the standard deviation of the Gaussian curves cannot be directly identified with the amplitude of the *COM*. However, this only causes an offset of both curves relative to each other and can be corrected by a calibration. The qualitative agreement between both methods is lost, though, when the frequencies are increased above $\alpha = 10$. There, the length evaluation shows much bigger relative amplitudes than the sine fits do. The fact that the high frequency oscillations were performed at a bigger lens distance should in fact not cause an increase in relative amplitude, but rather the opposite. This is of course only true if the bead-spring model is trusted as a suitable description. This will also be open for discussion in the following chapter.

Much care has to be taken when considering the robustness of those data sets. To illustrate this, the absolute length of the intensity profiles from the averages is compared

III.4. Experimental Study

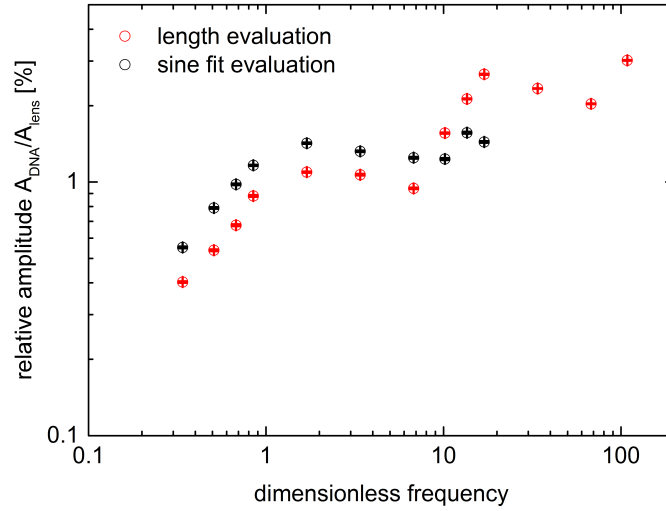


Figure III.4.12.: Plot of the results of the length evaluation of the DNA intensity profile (black symbols) versus the evaluation using sine fits to the *COM* motion (red symbols). Values below $\alpha = 17$ were recorded at a lens distance of $40 \mu m$, higher frequencies were recorded at a distance of $60 \mu m$. The plot is drawn in log-log-scaling.

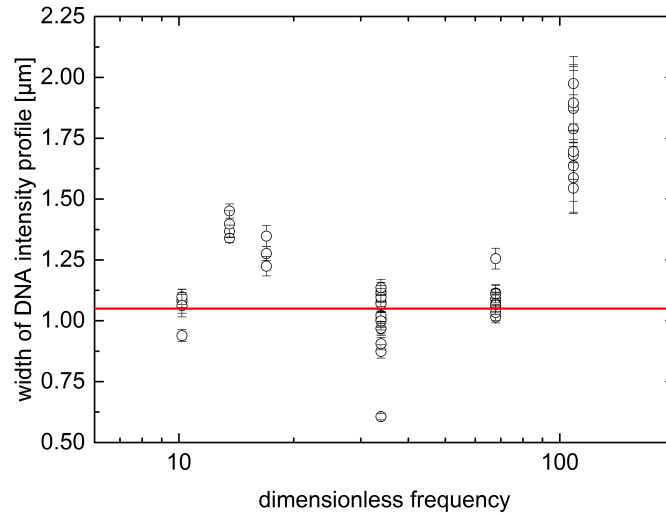


Figure III.4.13.: Plot of the results of the length evaluation of the DNA intensity profile (black symbols) as compared to the width of the equilibrium intensity distribution of such a molecule which amounts to approximately 1050 nm (red line). Driving was performed at an amplitude $A_{lens} = 31 \mu m$. Values below $\alpha = 17$ were recorded at a lens distance of $40 \mu m$, higher frequencies were recorded at a distance of $60 \mu m$.

in figure III.4.13 to the width of the equilibrium intensity distribution of the molecules. The equilibrium value was determined by measuring the width of the intensity profiles of grafted DNA molecules which were not subjected to shear and amounts approximately 1050 nm . All data points depicted in figure III.4.13 were recorded at a driving amplitude

of $31 \mu m$ in order to allow a quantitative comparison among them. At $\alpha = 10$, the width of only one of the sheared DNA molecules lies below the equilibrium value. All other values for $\alpha < 17$ are situated above this threshold. The same is true for all values that were recorded at $\alpha = 109$. However, a significant amount of values at $\alpha = 34$ and $\alpha = 68$ show a smaller width of the intensity profile under shear compared to the equilibrium threshold. Thus, the significance of these data sets must be questioned in terms of their validity. Overall, the presented data sets in figures III.4.12 and III.4.13 can be considered to be robust up to $\alpha = 17$ or respectively $f = 5 Hz$.

III.4.4. Summary

The past chapter contained a detailed description of all elements that are related to experiments with single-end-grafted DNA molecules. At first, the general idea of attaching one extremity of DNA molecules in a reproducible manner to a cover slip was explained. A detailed preparation recipe is given in the appendix (Sect. A.2.3 and A.2.4).

Although λ -DNA is a fairly long-chained molecule with a total length of about $20\ \mu\text{m}$ in its fully stretched state, its structures are still much too small to visualize them by standard optical microscopy. Instead, a setup using fluorescent excitation of dye molecules was necessary. During the shear experiments, a means was also required to determine the distance between the moving and the resting surface. This could be achieved using reflection interference contrast microscopy (RICM). Both techniques were explained in section III.4.1, as well as the experimental setup necessary to conduct them. There, the realization of the shear device was explained as well.

After the conduction of a shear experiment, picture sequences which showed many fluctuating bright spots resulted. The position of the center of mass (COM) of each of the molecules had to be extracted from the pictures before a further analysis was possible. A custom-built piece of software which was very helpful in that regard was described in section III.4.2.

In section III.4.3, the performed shear experiments on grafted DNA molecules were presented and partially discussed. A comparative analysis with the analytical bead-spring model showed very good agreement for both the relative amplitude (Fig. III.4.10) and the phase shift between driving lens oscillation and COM response oscillation becomes apparent (Fig. III.4.11). However, in both cases, the dimensionless frequency α needed to be replaced by an effective dimensionless frequency which was shifted in respect to α by a factor of 1.64. By performing an alternate evaluation of the amplitude behavior which took the length of the average intensity profiles into account instead of the dynamics of the COM , at low frequencies, the same qualitative development was found. At higher frequencies, strong deviations began to occur, though. A discussion of the possible reasons for these discrepancies will follow in the next chapter.

III.5. Discussion

The third part of this thesis deals with single-end-grafted DNA molecules that are subjected to an oscillating shear flow. In chapter III.3, a strongly simplified model which described each DNA via its center of mass was developed. It was then modeled as a bead with the same total mass as the molecule and with a radius that is identical to the radius of gyration of the polymer. In order to take the attachment point at the cover slip into account, the motion of the center of mass (*COM*) was restricted by linking it to an equilibrium position placed above the grafting point with a spring. In chapter III.4, the analytical predictions by the model were compared to results from experiments which were gained by fluorescence microscopy. Two central features were analyzed: On the one hand, the frequency dependence of the amplitude of the *COM* is an interesting topic, on the other hand, the phase shift between driving and response oscillations is important as well. Thus, in this chapter, the amplitude and phase behavior of the model shall be discussed.

Let us begin by considering the relative or, respectively, the rescaled amplitude. Figure III.4.10b shows that for all lens distances, the dependency of the relative amplitude on the dimensionless frequency is described well by the bead-spring model. However, it was mentioned before that, in order to achieve this agreement, the frequency needs to be rescaled by a pre-factor as presented in equation III.4.3. Before the addition of this pre-factor, the position of the transition value of the frequency at $\alpha = 1$ seemed to have slightly too small a value. The pre-factor m , which in all experiments amounted between 1.4 to 1.8, allows the shift of this transition frequency, such that a better agreement becomes possible. In average, it amounts to the value $m = 1.64$. A probable reason for the false estimation of the transition frequency lies in the misinterpretation of pixel values. Either pixels which do not belong to the DNA molecule were included in the calculation of the *COM* or pixels which should have been included were left out. This is a general problem of the evaluation of a picture series relying on a threshold value, be it a dynamically adapted threshold or a static one. Under any circumstance, the bead-spring model and the experimental values agree to a very high degree as far as the relative amplitude is concerned, thus, the model can be trusted to reflect the actual behavior of the DNA.

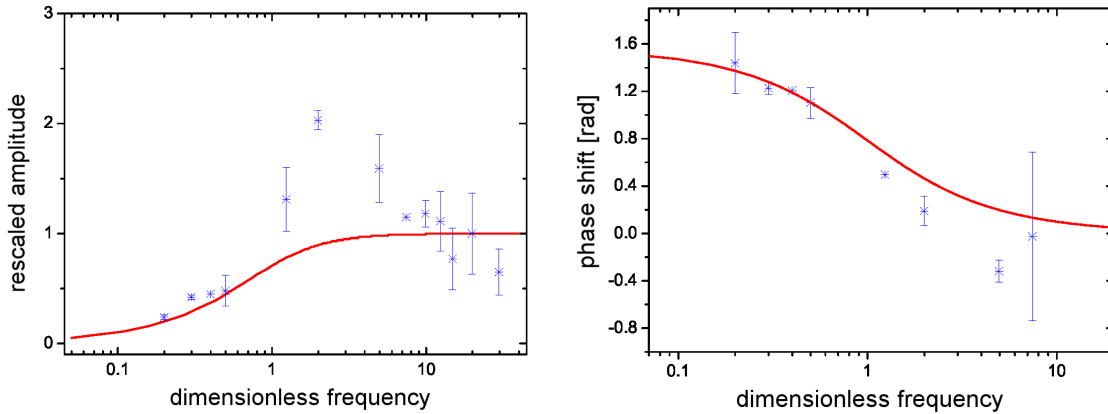
An alternate evaluation method was applied to the data sets, in which the length of a DNA molecule was considered by analyzing the average image over all pictures recorded

III.5. Discussion

in a measurement and thus over multiple oscillation periods of the DNA. For dimensionless frequencies $\alpha < 10$ a reasonable agreement to the relative amplitude values from the sine fits is found (Fig. III.4.12). For higher frequencies, a clear overshoot results from the length evaluation. The reasons for this effect are so far unclear, especially since the three highest frequencies at $\alpha = 34/68/109$ were recorded at lens distances of $60 \mu\text{m}$ and not at $40 \mu\text{m}$ like all other data points shown. Bigger lens distances result in smaller relative amplitudes at the same frequency value as figure III.4.10a depicts, which is exactly the contrary of what is the case for the alternate evaluation. One additional aspect that has not been discussed yet needs to be considered. For many picture series among these high frequency measurements, it seems that the DNA molecules are not only attached at their functionalized extremity, but they also temporarily adsorb to the cover slip at some point along their backbone. This can be seen as a kind of unspecific interaction, which in total leads to a shorter segment of the DNA molecule following the oscillatory driving, while the rest of it remains stuck to the cover slip in a stretched state. This again leads to what looks like a more elongated molecule and thus to an overestimation of its length. These adsorption processes, however, only start to play a role if the driving happens at dimensionless frequencies larger than $\alpha = 17$.

If the phase shift is considered, the bead-spring model predicts a decrease starting at $\pi/2$ for low frequencies, which then drops towards 0rad at high frequencies. This specific behavior is indeed found over the whole accessible frequency spectrum for $0.1 \text{ Hz} \leq f \leq 5 \text{ Hz}$ or respectively $0.3 \leq \alpha \leq 17$ (Fig. III.4.11). However, as mentioned above, the functional behavior is captured in a more precise manner when using the effective dimensionless frequency $\alpha_{\text{eff}} = 1.64\alpha$ instead of α for the description of the phase behavior.

When examining the phase shifts at different lens distances, it seems as if $\Delta\delta$ gets smaller the bigger the lens distance is. In other words, the smallest value of approximately -0.34rad is reached for a lens distance of $80 \mu\text{m}$, while it amounts to 0.07rad at the same frequency in case of a lens distance of $40 \mu\text{m}$. Since all oscillation processes happen very fast and due to the small amount of light depicted by each image in each picture series, it is a very challenging task to grasp the oscillatory behavior. However, as already mentioned, it is not an easy task to distinguish between those bright pixels belonging and those not belonging to a certain DNA molecule. Additionally, the small number of pictures and thus also *COM* displacement values in each oscillation period at high driving frequencies makes the exact determination of the correct amplitude and phase values of the DNA oscillations a challenge as well. This is also a possible reason for the phase shift overshoot in the data set for $h = 80 \mu\text{m}$. This is also the reason why the size of the error bars in the fits increases with increasing frequency. Overall, there might be a hidden dependency of the phase shift on the lens distance which only seems to play a role at high driving frequencies. At the current state of technology, an in-detail mapping of the high frequency range above $\alpha = 17$ is hindered by a wide number of experimental



(a) Behavior of the relative amplitude of the DNA *COM* (Fig. 2.44 in [127]).

(b) Behavior of the phase shift (Fig. 2.46 in [127]).

Figure III.5.1.: Results of the experimental study of M. Khaksar with single-end-grafted DNA [127]. Blue crosses indicate measured data points, while the solid red line represents the corresponding prediction by the analytical model.

issues. In the following chapter, a series of improvements and other changes which might help in enabling high frequency measurements will be mentioned.

As a final topic of discussion, the results which were gained in scope of this thesis shall be compared to those results reported earlier by Maryam Khaksar [127]. Two of her central graphs, which show the dependency of the rescaled amplitude and the phase shift on the dimensionless frequency, are depicted in figure III.5.1. In case of the amplitude, a distinct peak at $\alpha = 2$ is apparent. She identified this feature as the strongest deviation from the assumed bead-spring model, which is identical to the model used in this thesis. Furthermore, she assumed that it was either related to the internal energy landscape of the DNA or a specific dynamic response function. If, indeed, a peak is present at this position, even a resonant response of the DNA molecule would be a possible explanation. When compared to the rescaled amplitude from this study depicted in figure III.4.10b, no such peak appears, though. The rescaled amplitude follows the analytical model over the whole examined part of the frequency spectrum. Even multiple repetitions of her measurements did not show any similar feature. Thus, one might argue that the peak in her results originated from a different source like for example external noise or a misinterpretation of the picture series.

Let us consider her results of the phase shift between the driving and response oscillation of the DNA *COM* in figure III.5.1b. Here, it becomes apparent that for frequencies $\alpha < 1$ she found a good agreement between her measurements and the predictions by the model of the damped harmonic oscillator. However, for higher frequencies, she reported significant deviations from the model which are characterized by an overshoot

III.5. Discussion

towards negative phase shifts and large error bars. In other words, her phase analysis results in a nearly identical curve progression of the phase shift that was also found in this study (Fig. III.4.11). It has to be kept in mind that her analysis of the frequency spectrum above $\alpha = 1$ only consists of four values, the last of which shows a significant error ($> \pm 0.5 \text{ rad}$). If the negative phase overshoot is considered as significant it may mean that in case of both experiments similar difficulties in performing the measurements were met and that improvements are required in order to be able to reliably resolve the motion of DNA at higher frequencies. Both setups contain the identical shear device, both of them are mounted on top of an inverted microscope. Also, the major part of the sample preparation and the lab environment were similar, hence, a similar effect on the conduction of the experiments can be assumed.

Since the plot of the phase shift in Maryam Khaksar's thesis does not allow a distinction of the phase shifts at different lens distances, a more detailed comparison of the results is not possible. However, the partial agreement of both studies casts an interesting light on the mechanical properties of single-end-grafted DNA molecules.

III.6. Summary

In this part of the thesis, the mechanical properties of single-end-grafted DNA molecules were under examination. More specifically, by attaching single DNA molecules to the surface of a cover slip, their motion could be restricted to a small region of interest. At the same time, their mechanical properties were mostly uninfluenced and even their dynamical behavior could be visualized.

The challenge was two-fold: From an experimental point of view, the DNA molecules needed to be grafted to the cover slips and a series of shear experiments were to be performed with them. From a theoretical point of view, a model which allowed the interpretation of the behavior of the molecules and enabled predicting the response to certain excitations had to be developed. The results of the analytical considerations were presented in chapter III.3, where at first the flow profile between an upper oscillating and a lower resting plate was calculated by solving the corresponding Navier-Stokes equation of motion. The results predicted that for typical oscillation frequencies and amplitudes of the shear device, a linear velocity profile which only showed a very weak phase shift of fluid motion when comparing the fluid motion at the surface of both plates could be expected. Thus, the phase shift can safely be ignored and a perfectly linear velocity profile can be assumed in all cases. This result then led to the development of a bead-spring model for grafted DNA molecules (Sect. III.3.2), which could be described by a two-dimensional Langevin equation. After a series of simplifications, the motion of the center of mass of a grafted polymer driven by an oscillating top plate was given by a phase-shifted sine-function (Eq. III.3.17). Both the phase shift and the amplitude of the response were dependent on the driving frequency, however, the amplitude additionally depended on the average distance between the center of mass and the lower plate, the distance to the upper plate, as well as the amplitude of the driving oscillation. This analytical result could also be verified by numerical simulations (Fig. III.3.5).

For the experimental observation of λ -DNA (Ch. III.4), an existing preparation protocol by Yuting Sun [131] which enabled the functionalization of the cover slip with NeutrAvidin, a streptavidin derivate with a different isoelectric point, and of the DNA molecules with biotin was adapted. When brought into contact, the DNA tended to attach itself with its biotinylated extremity to the cover slip, while the rest of the molecule remained unconfined and could react to changed flow conditions. A whole series of experiments was performed with the polymers in section III.4.3 involving different distances between oscillating and resting surface, as well as a variation of driving amplitudes and

III.6. Summary

frequencies. When taking the behavior of the response amplitude of the DNA into account (Fig. III.4.10), the predicted curve progression was recovered to a very exact degree. The same is true for the phase shift between driving and response oscillation (Fig. III.4.11). In some cases though, at frequencies above $\alpha = 6$, an overshoot towards negative phase shifts became apparent. Probably, this is due to imprecision during the image analysis and insufficient lengths of the recorded data sets which hence cause significant fitting errors. A similar behavior was already recovered two years ago by Maryam Khaksar [127], a detailed comparison and discussion of the results was conducted in chapter III.5.

There are a few changes and improvements which are desirable for future studies in this field. If possible, the setup should be modified in such a way that noise can be reduced further and image series can be recorded with an improved contrast. This would help immensely in evaluating the contribution of certain more or less bright pixels to the center of mass calculation and thus give a clearer result especially at high driving frequencies. This directly leads to another improvement: A camera which supports an even higher recording frequency at a similar or even better sensitivity would help in expanding the experimentally accessible frequency spectrum. This would give insight into the behavior of DNA molecules at even higher driving frequencies and thus maybe contribute to answering the question whether the currently utilized bead-spring model is sufficient in describing the dynamic properties of the system. If, afterwards, it should still be necessary, a more complex model for the system could be developed. So far, it is largely unsettled what such a model might look like since no clear picture of the reaction of the DNA molecules to a faster driving can be drawn yet. A first step might be the expansion of the model of the dampened harmonic oscillator to include additional relaxation rates of the polymer.

In total, although still many open questions exist in context with single-end-grafted DNA molecules, insight was gained into their mechanical behavior. So far, most studies focused on properties of non-attached molecules [125] or they examined the static elongation under a steady instead of an oscillating shear flow [124]. Experimental observation of DNA molecules in flows is a very challenging task since many preparation steps are required before such studies become feasible in the first place. Although much more sophisticated models for DNA molecules already exist and were applied successfully in the past, their modeling as beads linked to a spring was attempted. And even though the model is as simple as it can be, for the most part, the response of the molecule can be described fairly well. However, some open questions remain like for example the question of the significance of negative phase shifts at high frequencies. Finding the solution to these will be the quest for future studies.

Summary

In this study, Brownian motion of colloids or colloid-like systems in oscillatory fields was examined. Three different systems were investigated: In part I, a colloid was confined by an optical trap within a shear flow and then subjected to oscillations by moving the optical trap. In part II, the identical setup of optical tweezers was utilized in order to probe respiratory mucus of horses with colloidal particles. This was conducted by analyzing both passive Brownian motion as well as active oscillations of the colloid in the mesh of the material. Part III gave details about the study of DNA molecules which were attached to the surface of a coverslip while being subjected to an oscillating shear flow.

The idea behind the study in part I was to find out how the shear-induced coupling of Brownian motion in a shear flow would be influenced if external oscillations were added to the system. This was achieved experimentally by combining the use of a setup of optical tweezers with a gravitationally driven microfluidic device. In case of stochastic systems involving Brownian motion, such coupling effects are accessible well by considering auto- and cross-correlation functions of the motion in flow direction and perpendicular to it, i. e. in direction of the shear gradient. Thus, we decided to approach the analysis of our system by the help of correlation functions as well. This approach included the analytic solution of the Langevin equation of motion for the colloid and the determination of the analytic auto- and cross-correlation functions. These were afterwards compared with the results of a numerical study basing on the same differential equation as well as experimental results gained in our setup of optical tweezers.

Overall, we found an analytic solution to the Langevin equation including the respective correlation functions. These solutions were reproduced by the numeric study and also displayed the characteristics found in the experimental study. However, we experienced significant perturbations which hinder the successful conduction of such experiments. There were two perturbations which were considered the most important ones: The frame of reference misalignment of the recording device, i. e. the high-speed camera, used to visualize the motion of the confined colloids led to an undesirable coupling of the motion in flow- and gradient-direction and hence caused spurious correlations. Even more important were temporal fluctuations of the flow velocity which contradict the assumption of a stationary flow in the theoretical part of this study. Thus, although the examined system was built as simple as possible the results can be considered inconclusive. However, suggestions were made which may help in improving the setup for further studies and hence lead to more conclusive results.

In part II, the setup of optical tweezers and a cone-and-plate rheometer were utilized to study the rheological behavior of mucus. This did not only lead to the discovery of rich viscoelastic response properties of this material but also revealed a clear gap between the microscopic and the macroscopic response. As a comparison the Mori-Tanaka model

was applied which is typically used to describe rigid foams. These are characterized by two separate phases, a solid-like phase which forms the walls of the foam and a viscous phase which fills the pores between these walls. While in microrheologic experiments with optical tweezers the colloid for the most part only “feels” the viscous phase, in case of the macrorheologic experiments with the rheometer the whole continuum including both phases is probed. Thus, in that case, the elastic material properties play a much more significant role. Partially, the results of this study were already published earlier [76].

In part III of this study, DNA molecules were studied in a similar flow situation as the colloids in part I. One extremity of these molecules was attached to a surface while the remainder of them stayed afloat in a buffer medium. By driving the surrounding medium with external oscillations originating from a second surface attached to a piezoelectric device, the response behavior of the DNA was examined. As free parameters, the distance between both surfaces, the amplitude of the driving oscillations and their frequency were varied. We analyzed the displacements of the DNA center of mass and observed the dependence of its amplitude and phase behavior on the driving frequency. A surprisingly good agreement with the model of a dampened harmonic oscillator was found. However, we observed a shift of the characteristic relaxation rate intrinsic to the model as compared to the one determined during our experiments. We assume that this effect might be caused by the complexity of a DNA molecule and hence the fact that one single relaxation rate probably does not suffice in order to describe the full dynamic behavior of such a molecule.

Part IV.
Appendix

A. Materials & Methods

A.1. Materials

| name | manufacturer | vendor | art.-no. |
|--|--------------------------|------------------------|------------|
| 3-aminopropyltriethoxysilane (APTES) | The Dow Chemical Company | Sigma-Aldrich | 440140 |
| Gene Frame 25 μ l | ABgene Ltd. | Fisher Scientific GmbH | AB-0576 |
| glutaraldehyde, EM Grade, 8% | Polysciences, Inc. | | 00216 |
| λ -DNA | Fermentas | Fisher Scientific GmbH | SD0011 |
| melamin resin beads size: 5 μ m | Fluka | Sigma-Aldrich | 90641 |
| Microcon DNA Fast Flow Centrifugal Filter Unit | Merck Millipore | | MRCF0 R100 |
| NeutrAvidin | Molecular Probes | Life Technologies GmbH | A2666 |
| oligonucleotides | MWG Biotech | | n/a |
| phosphate buffered saline (PBS) | Sigma-Aldrich | | P4417 |
| polyacrylamide (PAAm) | Sigma-Aldrich | | 92560 |
| polydimethylsiloxane (PDMS) Sylgard 184 | The Dow Chemical Company | Sigma-Aldrich | 761036 |
| polymethylmethacrylate (PMMA) beads, size: 4 μ m | Fluka | Sigma-Aldrich | 73371 |
| T4 DNA ligase | New England Biolabs | | M0202S |
| YOYO-1 iodide (491/509) | Molecular Probes | Life Technologies GmbH | Y3601 |

Table A.1.: Chemical products and microparticles utilized to conduct the experiments in all parts of this thesis.

A.2. Methods

A.2.1. Production of Microfluidic Devices

In chapter I.4.2, the design aspects of a microfluidic device with channels of rectangular cross-section were described. Before the conduction of each experiment, one of these devices had to be produced. The protocol is as follows:

1. As polydimethylsiloxane (PDMS) material Sylgard 184 (ref.-no. 761036, Sigma-Aldrich, Germany) containing elastomer base and a curing agent is used. Both of them are mixed in a 10:1 base to curing agent volume ratio inside a small mixing glass bottle. The total volume may vary depending on the surface area of the microfluidic device. It should be chosen so that the height of the poured PDMS-layer will be about 5 mm high. The mixture is stirred by hand for half a minute using a disposable plastic stirrer.
2. The bottle is brought into a vacuum reactor and degassed until no air bubbles are left.
3. The mixture is poured onto the silicon wafer with the negative structures of the microfluidic device which rests inside a plastic dish. Afterwards, the dish is closed with a lid in order to avoid the inclusion of dust.
4. The dish is brought into a pre-heated oven at a temperature of 65°C and left inside for one hour. It is taken out afterwards and passively cooled down to room-temperature.
5. The device is generously cut out of the mold using a scalpel and carefully peeled out of the plastic dish. Special care has to be taken not to bring the device in contact with dust. This is best performed inside a flow-box.
6. Holes for the in- and outlet tubes are punched into the PDMS using a syringe with a blunted tip and the device is put upside-down with the channel structures pointing upwards in an O_2 -plasma-cleaner together with a microscope coverslip big enough to cover the whole area of the PDMS device. It is exposed to the plasma for about one minute.
7. The side of the PDMS with the structures of the microfluidic channels and the activated side of the coverslip are oriented pointing towards each other and then carefully brought into contact.
8. The in- and outlet tubes are inserted into the holes of the device.

At this point, the microfluidic device is ready for use. Tubes made from polyethylene (LDPE) with an inner diameter of 0.5 mm and an outer diameter of 1 mm were used (art.-no. 3550501, Laborshop24, Gross-Zimmern, Germany).

A.2.2. Preparation of Gene Frames for Microrheology Experiments

In context with the microrheological examination of mucus or biological fluids in general, in section II.4.1.2 a special low-volume sample cell denoted Gene Frame was mentioned. Here, the specific preparation steps of the cell will be detailed. A package of Gene Frames contains two items: the adhesive frame and a plastic cover slip. The adhesive has the shape of a square with a $1\text{ cm} \times 1\text{ cm}$ hole in the middle, its thickness amounts to $250\text{ }\mu\text{m}$, thus defining a volume of $25\text{ }\mu\text{l}$. The preparation steps are as follows:

1. A standard cover slip is cleaned using two rinsing steps with acetone and ethanol. The ethanol is afterwards removed using compressed air.
2. The adhesive frame is aligned over the surface and attached to it by pressing it down gently. To improve the adhesion, the cover slip is heated for about 5 minutes to $94\text{ }^\circ\text{C}$.
3. The back cover of the adhesive frame is now removed to expose the inner volume. The respective amount of sample fluid is pipetted into it.
4. The plastic cover slip from the Gene Frame package is now carefully aligned over the adhesive. It should be attached at one side of the frame first, then bent and slowly rolled over the whole adhesive surface. In this way, air inclusions in the sample volume can be avoided. Also, excess fluid is pushed out of the frame.

The sample cell is now ready for use.

A.2.3. DNA preparation

λ -DNA molecules have to be prepared before they can be attached to cover slips. In their delivery state, they are available in circular form. This form needs to be linearized and functionalized using oligonucleotides with certain molecules like biotin, thiol, or other groups appended to them. To achieve this, the following recipe originally suggested by Yuting Sun [131] was used:

1. $66\text{ }\mu\text{L}$ λ -DNA at $0.5\text{ }\mu\text{g}/\mu\text{L}$ is pipetted into an Eppendorf tube and heated to $75\text{ }^\circ\text{C}$ for 10 to 15 minutes to open the circular DNA. This step is followed by a quick cooling process down to room temperature for about 5 minutes using ice.
2. $10\text{ }\mu\text{L}$ ligase buffer, $3.4\text{ }\mu\text{L}$ oligomer 1, $3.4\text{ }\mu\text{L}$ oligomer 2, and $17.2\text{ }\mu\text{L}$ Milli-Q water are added to the tube to give a total volume of $100\text{ }\mu\text{L}$. Oligomer 1 and 2 can be chosen as necessary for the experiments, they have to be complementary to each of the two base sequences finalizing the DNA molecules. For the experiments in part III, a biotin and a thiol group were chosen as the corresponding functional groups.
3. The hybridization of the DNA is performed by heating the sample to $50\text{ }^\circ\text{C}$ and keeping the temperature constant for about 1 hour.
4. A slow tempering process down to room temperature is performed over night by switching off the heating unit.

A. Materials & Methods

5. $3.4\ \mu\text{L}$ T4 ligase are added to the sample to close the gap in the backbone between the DNA molecule and the oligonucleotides. For this purpose, the sample is heated to $25\ ^\circ\text{C}$ for approximately 30 minutes.
6. The sample is then purified by filtering it five times through special filters (ref.-no. MRCF0R100, Microcon DNA Fast Flow Centrifugal Filter Unit, Merck Milipore, Darmstadt, Germany) using a centrifuge at very low rotation velocities ($150\ \text{rcf}$).

All materials are listed in table A.1. After these preparation steps, the DNA solution is split into multiple aliquots of $\approx 20\ \mu\text{L}$ within Eppendorf tubes and afterwards frozen at $-80\ ^\circ\text{C}$ until they are needed.

A.2.4. Preparation of a cover slip and DNA for shear experiments

The preparation of a cover slip and the λ -DNA for their use in the shear device in part III consists of a separate preparation process for both of them. The cover slip is prepared by the following steps:

1. 3-aminopropyltriethoxysilane (ref.-no. 440140, Sigma-Aldrich, Germany) is purified by a distillation process.
2. Up to 10 cover slips can be stored in a ceramic slip holder. It is then immersed into a piranha solution (50% H_2SO_4 , 50% H_2O_2) for 30 minutes.
3. The slip holder with the slips is rinsed multiple times using Milli-Q water to remove the acid.
4. The slips are rinsed once using ethanol and directly afterwards immersed into a silane mixture for 5 to 10 minutes. It contains 2% silane in ethanol as the solvent.
5. The slip holder is dipped into ethanol to remove any excess silane and afterwards into Milli-Q water to remove the ethanol. Since the presence of water can cause the formation of agglomerates, the slips are dried at $110\ ^\circ\text{C}$ for 5 to 10 minutes.

In this state, the slips can be stored for about 10 days in a closed box without risking any major contamination. When needed for usage, the following additional steps need to be taken:

1. The cover slip is immersed into a 4% glutaraldehyde solution (ref.-no. 00216, Polysciences, Inc., Warrington, Pennsylvania, United States of America) for one hour.
2. The slip is rinsed in Milli-Q water, excess fluid is afterwards removed by blowing the slip dry with nitrogen.
3. The slip is built into a custom sample holder which leaves a circular area with a diameter of approximately $1.5\ \text{cm}$ accessible for experimentation. To prevent leakage, the outer area of the slip is covered with a small amount of vacuum grease using a syringe before a teflon ring is placed on top of it. The accessible circular region is then covered with NeutrAvidin (ref.-no. A2666, Life Technologies GmbH, Darmstadt, Germany) at a concentration of $0.02\ \text{mg/mL}$. The amount should be

chosen in such a way that the complete surface is fully covered with fluid.

4. The slip is rinsed multiple times by adding phosphate buffered saline (PBS) and removing fluid from the slip with a pipette in successive steps. A certain layer of fluid should be kept at all times!

Now, the cover slip is ready for usage. However, there is a series of preparation steps for the DNA molecules that need to be taken as well. This preparation can be performed at the same time as the preparation of the cover slip.

1. YOYO-1 iodide (Y3601, Life Technologies GmbH, Darmstadt, Germany) is diluted from the stock concentration of 1 mM to 0.02 mM using PBS.
2. 100 ng DNA is mixed with $1.5\text{ }\mu\text{L}$ of the diluted YOYO solution and incubated at room temperature for about 1 hour. Since YOYO bleaches under irradiation of light at a wavelength of 491 nm , it must be kept in a dark environment at all times!
3. The solution is diluted using PBS to a concentration of $1\text{ ng}/\mu\text{L}$.

If it is stored in a dark environment, the diluted YOYO solution can be kept in a frozen state ($T = -20^\circ\text{C}$) for a few months without a significant loss of fluorescence intensity. However, care has to be taken to avoid contamination. At this point, both the cover slip as well as the DNA solution are ready for usage. By pipetting about $100\text{ }\mu\text{L}$ of the DNA solution onto the cover slip and waiting for a few minutes, a DNA brush can be attached to the slip and be used for experiments afterwards. The density of the brush can be controlled, on the one hand, by tuning the concentration of the DNA solution. On the other hand, the incubation time on the surface can be changed as well. Typically, at the given concentration in the recipe above, the incubation time necessary ranged at about 10 minutes to receive a large amount of single DNA molecules, which were attached far enough from each other to prevent them from making contact and from entangling. After this waiting time, the DNA remaining unattached within the solution on the slip is removed by rinsing with PBS.

B. Calculations

B.1. Auto- and Cross-Correlation Functions of Brownian Motion in a Shear Flow

In chapter I.4.3, the differential equation for the motion of a colloid undergoing Brownian motion in an optical trap while at the same time being exposed to a shear flow was discussed. However, the auto-correlation function $C_{xx}(\Delta t)$ (eq. I.4.24) and the cross-correlation functions $C_{xy}(\Delta t)$ (eq. I.4.25) and $C_{yx}(\Delta t)$ (eq. I.4.26) were just given and not derived. Details will follow here.

The calculation of the auto-correlation in x-direction is performed in the same way as for the y-direction by inserting the solution of the Langevin equation (Eq. I.4.17) into the definition of the correlation function (Eq. I.4.18)

$$C_{xx}(\Delta t) = \langle x(t)x(\tau) \rangle \quad (\text{B.1})$$

$$= \left\langle \left(x_0 e^{-t/\tau_r} + e^{-t/\tau_r} \int_0^t dt' \left[e^{t'/\tau_r} \left(\dot{\gamma} y(t') + \frac{F_{r,x}(t')}{\zeta} \right) \right] \right) \right. \\ \left. \left(x_0 e^{-\tau/\tau_r} + e^{-\tau/\tau_r} \int_0^\tau dt'' \left[e^{t''/\tau_r} \left(\dot{\gamma} y(t'') + \frac{F_{r,x}(t'')}{\zeta} \right) \right] \right) \right\rangle. \quad (\text{B.2})$$

With a similar reasoning as for the calculation of $C_{yy}(\Delta t)$, none of these terms but the double integral contribute to the correlation function due to the specific properties of the Brownian random force (eq. I.4.10 and I.4.11). Somehow, in this case, there is an additional contribution due to $y(t)$

$$C_{xx}(\Delta t) = \left\langle e^{-(t+\tau)/\tau_r} \int_0^t dt' \int_0^\tau dt'' \left[e^{(t'+t'')/\tau_r} \left(\dot{\gamma} y(t') + \frac{F_{r,x}(t')}{\zeta} \right) \right. \right. \\ \left. \left. \left(\dot{\gamma} y(t'') + \frac{F_{r,x}(t'')}{\zeta} \right) \right] \right\rangle \\ = e^{-(t+\tau)/\tau_r} \int_0^t dt' \int_0^\tau dt'' \left[e^{(t'+t'')/\tau_r} \left(\dot{\gamma}^2 \langle y(t')y(t'') \rangle \right. \right. \\ \left. \left. + \frac{1}{\zeta^2} \langle F_{r,x}(t')F_{r,x}(t'') \rangle \right) \right]. \quad (\text{B.3})$$

B. Calculations

This representation can be used since the random force in orthogonal directions is uncorrelated. The integration of the second term containing the second power of the random force in x-direction leads to a result identical with equation I.4.22. By directly inserting $C_{yy}(\Delta t) = \langle y(t')y(t'') \rangle$, the contribution of the first term in equation B.3 can also be determined. However, care has to be taken since $C_{yy}(\Delta t)$ is not only defined for $\Delta t \geq 0$, but is also an even function. The negative half-plane can be included by

$$C_{xx}(\Delta t) = \frac{k_B T}{k} \dot{\gamma}^2 e^{-(t+\tau)/\tau_r} \int_0^t dt' \int_0^\tau dt'' \left[e^{(t'+t'')/\tau_r} \left(e^{-|t'-t''|/\tau_r} - e^{-(t'+t'')/\tau_r} \right) \right] \quad (\text{B.4})$$

$$+ \frac{k_B T}{k} \left(e^{-(\tau-t)/\tau_r} - e^{-(\tau+t)/\tau_r} \right),$$

which after tackling the integrals leads to the complete solution

$$C_{xx}(\Delta t) = \frac{k_B T}{k} \frac{W_i^2}{2} \left[e^{-(\tau-t)/\tau_r} \left(1 + \frac{\tau-t}{\tau_r} \right) - e^{-(\tau+t)/\tau_r} \left(1 + \frac{\tau+t}{\tau_r} + \frac{2\tau t}{\tau_r^2} \right) \right] \quad (\text{B.5})$$

$$+ \frac{k_B T}{k} \left(e^{-(\tau-t)/\tau_r} - e^{-(\tau+t)/\tau_r} \right).$$

For large times $t, \tau \gg \tau_r$, this gives

$$C_{xx}(\Delta t) = \frac{k_B T}{k} e^{-\Delta t/\tau_r} \left[1 + \frac{W_i^2}{2} \left(1 + \frac{\Delta t}{\tau_r} \right) \right] \quad (\text{B.6})$$

which is identical with the result in section I.4.3 (eq. I.4.24).

The cross-correlation function

$$C_{xy}(\Delta t) = \dot{\gamma} e^{-t/\tau_r} \int_0^t dt' \left[e^{t'/\tau_r} \langle y(t')y(\tau) \rangle \right] \quad (\text{B.7})$$

can be computed in the same fashion by first inserting equation I.4.22 and again taking the symmetry properties into account, leading to

$$C_{xy}(\Delta t) = \frac{k_B T}{k} \dot{\gamma} e^{-t/\tau_r} \int_0^t dt' \left[e^{t'/\tau_r} \left(e^{-|\tau-t'|/\tau_r} - e^{-(\tau+t')/\tau_r} \right) \right]. \quad (\text{B.8})$$

The integral then gives

$$C_{xy}(\Delta t) = \frac{k_B T}{k} \frac{W_i}{2} \left[e^{-(\tau-t)/\tau_r} - e^{-(\tau+t)/\tau_r} \left(1 + 2 \frac{t}{\tau_r} \right) \right] \quad (\text{B.9})$$

or for large times $t, \tau \gg \tau_r$

$$C_{xy}(\Delta t) = \frac{k_B T}{k} \frac{W_i}{2} e^{-\Delta t/\tau_r} \quad (\text{B.10})$$

B.1. Auto- and Cross-Correlation Functions of Brownian Motion in a Shear Flow

which corresponds to equation I.4.25. Analogously, $C_{yx}(\Delta t)$ can be determined

$$\begin{aligned}
 C_{yx}(\Delta t) &= \dot{\gamma} e^{-\tau/\tau_r} \int_0^\tau dt' \left[e^{t'/\tau_r} \langle y(t') y(t) \rangle \right] \\
 &= \frac{k_B T}{k} \frac{Wi}{2} \left[e^{-(\tau-t)/\tau_r} \left(1 + 2 \frac{\tau-t}{\tau_r} \right) - e^{-(\tau+t)/\tau_r} \left(1 + 2 \frac{\tau}{\tau_r} \right) \right]
 \end{aligned} \tag{B.11}$$

or, respectively, for large times $t, \tau \gg \tau_R$ (eq. I.4.26)

$$C_{yx}(\Delta t) = \frac{k_B T}{k} \frac{Wi}{2} e^{-\Delta t/\tau_r} \left(1 + 2 \frac{\Delta t}{\tau_r} \right). \tag{B.12}$$

C. Custom written Software

C.1. Calculation of Auto- and Cross-Correlation Functions

The program used to calculate the auto- and cross-correlation functions of the experimental as well as the numerical datasets was developed as a LabVIEW virtual instrument. Since LabVIEW is a graphical programming language and there is no feasible way to export the program code, in the following the program flow will be described.

1. Import of a text file with three columns containing one time and two position columns for x- and y-displacements respectively.
2. Subtraction of the average position of each position dataset to remove offsets of the correlation functions.
3. Computation of all auto- and cross-correlations of the input signals using an FFT-based algorithm offered by LabVIEW. It is performed based on the definition given in equation I.4.18 and reads

$$C_{fg}((i - N + 1)\Delta t) = \frac{1}{Z_i} \sum_{k=0}^{N-1} f_k \cdot g_{i+k-N+1}, \quad (\text{C.1})$$

where $j = -(N - 1), -(N - 2), \dots, (M - 2), (M - 1)$, $i = 0, 1, \dots, N + M - 2$, N is the dimension of dataset f , and M is the dimension of dataset g . The normalization Z_i of the dataset is performed by dividing each element $C_{fg}(i\Delta t)$ by the number of terms contributing to this element

$$Z_i = \begin{cases} i + 1, & \text{for } i \leq \min(M, N) - 1, \\ \min(M, N), & \text{for } \min(M, N) - 1 < i < \max(M, N) - 1, \\ \min(M, N) + \max(M, N) - i - 1, & \text{for } i \geq \max(M, N) - 1. \end{cases} \quad (\text{C.2})$$

Since the dimension of both datasets is always the same in the context of this thesis, $N = M$ can be assumed here.

4. Export of the datasets as a formatted text file.

D. Supplementary Tables

| $\dot{\gamma}$ [1/s] | $C_{xx,osc}$ [nm ²] | $C_{yy,osc}$ [nm ²] | $C_{xy,osc}$ [nm ²] | $\dot{\gamma}_{fit}$ [1/s] |
|----------------------|---------------------------------|---------------------------------|---------------------------------|----------------------------|
| 1 | 6.74(7) | 268.22(7) | 40.23(4) | 1.00(1) |
| 5 | 171.62(7) | 273.4(7) | 216.21(4) | 4.980(3) |
| 10 | 689.70(7) | 263.88(7) | 426.13(4) | 10.161(4) |
| 20 | 2,887.35(8) | 272.42(7) | 885.78(4) | 20.461(6) |
| 30 | 6,441.17(7) | 257.23(7) | 1,286.56(6) | 31.450(9) |
| 50 | 17,830.23(7) | 257.02(6) | 2,138.51(6) | 52.35(1) |
| 75 | 39,960.68(7) | 252.06(6) | 3,176.9(2) | 79.13(2) |
| 100 | 71,018.8(1) | 255.24(6) | 4,254.10(7) | 104.84(2) |

Table D.1.: Data sets shown in figures I.5.5b.

| ω [rad/s] | $C_{xx,osc}$ [nm ²] | $C_{yy,osc}$ [nm ²] | $C_{xx,osc}/C_{yy,osc}$ | $\tau_r(C_{xx})$ [ms] | $\delta(C_{xy})$ [rad] |
|------------------|---------------------------------|---------------------------------|-------------------------|-----------------------|------------------------|
| 0.63 | 628(3) | 0.54(7) | $1.16(16) \cdot 10^3$ | 3.2(2) | -1.43(1) |
| 1.57 | 724.87(8) | 17.6(1) | $4.12(2) \cdot 10^1$ | 3.58(3) | -1.57(1) |
| 3.14 | 715.65(7) | 67.8(1) | $1.06(1) \cdot 10^1$ | 3.78(3) | -1.59(1) |
| 6.28 | 691.58(7) | 264.7(1) | $2.61(1) \cdot 10^0$ | 3.53(3) | -1.53(1) |
| 15.71 | 689.07(7) | 1,620(1) | $4.25(1) \cdot 10^{-1}$ | 3.70(3) | -1.51(1) |
| 31.42 | 678.15(7) | 6,505(1) | $1.04(1) \cdot 10^{-1}$ | 3.74(3) | -1.47(1) |
| 47.12 | 651.94(7) | 14,344(1) | $4.55(1) \cdot 10^{-2}$ | 3.90(3) | -1.40(1) |
| 62.83 | 626.00(6) | 24,816(1) | $2.52(1) \cdot 10^{-2}$ | 3.77(3) | -1.34(1) |
| 188.50 | 301.30(9) | 158,896(1) | $1.90(1) \cdot 10^{-3}$ | 3.0(1) | -0.98(1) |
| 314.16 | 128.3(1) | 278,265(1) | $4.61(1) \cdot 10^{-4}$ | 3.85(3) | -0.72(1) |
| 439.82 | 41.50(9) | 364,205(1) | $1.14(1) \cdot 10^{-4}$ | 3.50(3) | -0.58(1) |
| 628.32 | 17.0(1) | 408,591(1) | $4.16(3) \cdot 10^{-5}$ | 3.50(3) | -0.44(1) |
| 1,570.80 | 0.7(1) | 470,034(3) | $1.4(2) \cdot 10^{-6}$ | 3.82(3) | -0.37(1) |
| 3,141.59 | 0.04(14) | 480,232(9) | $9(29) \cdot 10^{-8}$ | 3.65(3) | -1.31(1) |
| 6,283.19 | 0.01(14) | 482,838(190) | $1(29) \cdot 10^{-8}$ | 3.53(3) | -0.68(1) |

Table D.2.: Data sets shown in figures I.5.6 and I.5.7.

D. Supplementary Tables

| current [%] | power Ventus 532 nm [mW] | current [%] | power Ventus 532 nm [mW] |
|-------------|-----------------------------|-------------|-----------------------------|
| 70 | 248 | 35 | 35 |
| 68 | 226 | 34 | 33 |
| 66 | 211.5 | 33 | 29 |
| 64 | 199 | 32 | 25.8 |
| 62 | 187 | 31 | 23 |
| 60 | 165 | 30 | 20.8 |
| 58 | 145 | 29 | 17.9 |
| 56 | 139 | 28 | 14.8 |
| 54 | 127.5 | 27 | 12.75 |
| 52 | 114 | 26 | 11.2 |
| 50 | 101 | 25 | 9.25 |
| 49 | 97 | 24 | 7.47 |
| 48 | 90 | 23 | 6.25 |
| 47 | 85 | 22 | 5.1 |
| 46 | 80 | 21 | 4.09 |
| 45 | 73 | 20 | 3.15 |
| 44 | 69 | 19 | 2 |
| 43 | 65.8 | 18 | 1.8 |
| 42 | 60.5 | 17.8 | 1.75 |
| 41 | 56 | 17.6 | 1.7 |
| 40 | 53.5 | 17.4 | 1.7 |
| 39 | 49.5 | 17 | 1.6 |
| 38 | 45.3 | 16 | 1.5 |
| 37 | 42 | 15 | 0 |
| 36 | 39 | | |

Table D.3.: Data set of the emitted laser power of the Ventus laser utilized in the setup of optical tweezers in Saarbrücken. It is shown as a graph in figure I.6.2. Due to thermal noise in the surroundings of the sensor, the data has a precision of $\pm 100 \mu W$.

| current [%] | power Ciel 473 nm [mW] | current [%] | power Ciel 473 nm [mW] |
|-------------|---------------------------|-------------|---------------------------|
| 90 | 300 | 56 | 22 |
| 88 | 295 | 55 | 20.2 |
| 86 | 285 | 54 | 19 |
| 84 | 260 | 53 | 17 |
| 82 | 240 | 52 | 13.9 |
| 80 | 217 | 51 | 13 |
| 78 | 125 | 50 | 12.2 |
| 76 | 96.5 | 49 | 10.1 |
| 74 | 101 | 48 | 8.1 |
| 72 | 91 | 47 | 6.7 |
| 70 | 76 | 46 | 5.7 |
| 68 | 67 | 45 | 4.2 |
| 66 | 59 | 44 | 3.9 |
| 64 | 51 | 43 | 2.7 |
| 62 | 43 | 42 | 2.3 |
| 60 | 36 | 41 | 1.9 |
| 58 | 29 | 40 | 1.3 |

Table D.4.: Data set of the emitted laser power of the Ciel laser utilized in the setup of optical tweezers in Saarbrücken. It is shown as a graph in figure I.6.2. Due to thermal noise in the surroundings of the sensor, the data has a precision of $\pm 100 \mu W$.

| power [mW] | $k_{x,r}$ [$\mu N/m$] | $k_{y,r}$ [$\mu N/m$] | $k_{x,c}$ [$\mu N/m$] | $k_{y,c}$ [$\mu N/m$] | $k_{x,d}$ [$\mu N/m$] |
|------------|-------------------------|-------------------------|-------------------------|-------------------------|-------------------------|
| 12.8 | 0.87(1) | 0.86(1) | 0.96(1) | 1.08(1) | 0.89(2) |
| 17.9 | 0.96(1) | 1.13(1) | 1.11(2) | 1.26(1) | 1.24(3) |
| 23.0 | 1.42(1) | 1.88(1) | 1.47(1) | 1.83(1) | 1.47(5) |
| 29.0 | 1.79(1) | 2.07(1) | 1.80(1) | 1.77(1) | 1.95(7) |

Table D.5.: Results of all calibration methods detailed in section I.6.3. The trap stiffness according to the equipartition method is denoted with the index “r”, the correlation method with the index “c”, and the drag force method with “d”. The direction of the calibration is denoted with the indices “x” and “y”. The drag force calibration method was only performed in x-direction.

D. Supplementary Tables

| α | $C_{xx,osc} [nm^2]$ | $C_{yy,osc} [nm^2]$ | $\delta(C_{xy}) [rad]$ | $\frac{C_{yy,osc}}{B^2} [10^{-4}]$ |
|----------|---------------------|---------------------|------------------------|------------------------------------|
| 0.012 | 1,925.1(1) | 560.6(3) | 2.388(1) | 1.40 |
| 0.014 | 1,919.1(6) | 511(1) | -1.357(1) | 1.28 |
| 0.016 | 3,044.6(7) | 711.7(2) | -1.697(1) | 1.78 |
| 0.016 | 4,134.8(9) | 568.7(1) | -1.708(1) | 1.42 |
| 0.016 | 5,196(1) | 748.7(3) | -1.521(1) | 1.87 |
| 0.017 | 2,676.2(6) | 121.9(2) | 1.583(1) | 1.22 |
| 0.020 | 4,586.8(7) | 435.5(3) | 2.390(1) | 4.36 |
| 0.020 | 2,356.4(8) | 398.7(9) | -0.499(1) | 3.99 |
| 0.020 | 7,766(3) | 737.5(2) | -1.759(1) | 1.84 |
| 0.021 | 4,296(1) | 1,487.1(3) | -0.645(1) | 2.79 |
| 0.021 | 3,884(1) | 1,080(1) | 2.018(1) | 3.79 |
| 0.021 | 6,268(3) | 1,116.4(8) | -1.110(1) | 2.7 |
| 0.021 | 5,628(1) | 1,516(1) | 1.485(1) | 3.72 |
| 0.022 | 359(3) | 558(1) | -1.380(1) | 1.78 |
| 0.022 | 10,980(2) | 713.3(2) | 1.574(1) | 5.58 |
| 0.023 | 5,804(1) | 990.4(4) | 1.912(1) | 3.57 |
| 0.023 | 3,931.2(4) | 1,429(1) | -0.653(1) | 2.48 |
| 0.025 | 5,959(2) | 1,629(1) | -0.830(1) | 4.07 |
| 0.026 | 2,163.9(8) | 828.4(2) | 1.692(1) | 5.88 |
| 0.026 | 606(1) | 587.8(2) | 1.088(1) | 8.28 |
| 0.028 | 9,838.7(6) | 1,205.7(3) | 2.035(1) | 3.01 |
| 0.029 | 5,286.9(6) | 1,106.8(7) | -1.214(1) | 1.38 |
| 0.029 | 7,138(1) | 1,239.2(3) | -1.467(1) | 1.71 |
| 0.029 | 12,557(5) | 682.4(5) | 2.158(1) | 3.10 |
| 0.029 | 16,359(3) | 551.8(3) | 1.471(1) | 2.77 |
| 0.032 | 484.8(2) | 231.4(3) | 1.649(1) | 2.31 |
| 0.051 | 908.3(9) | 5,772.4(5) | -0.598(1) | 57.72 |
| 0.052 | 813.6(7) | 4,727.9(5) | 0.515(1) | 47.28 |
| 0.058 | 8,721(6) | 5,602(4) | 2.360(1) | 56.02 |
| 0.060 | 1,887(2) | 2,711.6(8) | -1.376(1) | 27.12 |
| 0.068 | 2,337(5) | 2,805(2) | -1.329(1) | 28.05 |
| 0.070 | 155(1) | 4,182.8(5) | 0.094(1) | 41.83 |
| 0.078 | 5,807(1) | 5,649.8(6) | 1.147(1) | 56.50 |
| 0.083 | 2,926.2(9) | 3,515.4(5) | 1.964(1) | 35.15 |
| 0.085 | 3,586(4) | 3,464(2) | -1.194(1) | 34.64 |
| 0.091 | 6,956(3) | 6,915(2) | 1.673(1) | 17.29 |

This table continues on the following page.

| α | $C_{xx,osc} [nm^2]$ | $C_{yy,osc} [nm^2]$ | $\delta(C_{xy}) [rad]$ | $\frac{C_{yy,osc}}{B^2} [10^{-4}]$ |
|----------|---------------------|---------------------|------------------------|------------------------------------|
| 0.095 | 5,704(2) | 2,602(2) | 1.600(1) | 26.02 |
| 0.096 | 2,846.6(7) | 4,046(1) | 1.884(1) | 40.46 |
| 0.097 | 3,333(3) | 4,597(3) | -0.968(1) | 45.97 |
| 0.098 | 6,486(8) | 5,614(4) | -1.957(1) | 56.14 |
| 0.098 | 4,568(3) | 7,564(3) | 1.944(1) | 18.91 |
| 0.099 | 2,835(1) | 4,714(1) | 1.880(1) | 47.14 |
| 0.100 | 2,407(1) | 3,707(2) | 2.541(1) | 73.12 |
| 0.100 | 6,534(11) | 7,312(7) | -2.070(1) | 37.07 |
| 0.107 | 2,949(2) | 10,982(5) | 2.761(1) | 109.82 |
| 0.114 | 2,983(3) | 3,462(2) | -1.864(1) | 34.62 |
| 0.114 | 1,994(1) | 5,228(2) | 1.835(1) | 52.28 |
| 0.157 | 5,019(6) | 6,745(2) | 2.067(1) | 67.45 |

Table D.6.: Fitting results to the experimental data sets as utilized in figures I.6.18 and I.6.19a.

D. Supplementary Tables

| α | $\delta(C_{xy}) [rad]$ |
|----------|------------------------|
| 0.015 | -1.4(4) |
| 0.024 | -1.2(4) |
| 0.032 | -1.5(-) |
| 0.054 | -0.3(7) |
| 0.064 | -1.35(3) |
| 0.074 | -1(1) |
| 0.084 | -1.19(1) |
| 0.096 | -1.4(3) |
| 0.103 | -1.0(9) |
| 0.114 | -1.6(4) |
| 0.157 | -1.1(-) |

Table D.7.: Phase shifts of the cross-correlation function C_{xy} after removal of the influence of the sign of the shear gradient and after averaging of the data within frequency intervals of a width $\Delta\alpha = 0.01$. These data sets were also plotted in figure I.6.19. No errors are given for $\alpha = 0.032$ and $\alpha = 0.157$ since only one single value was contained in the corresponding averaging interval.

| f [Hz] | G'_1 [Pa] | G''_1 [Pa] | δ_1 [rad] | G'_2 [Pa] | G''_2 [Pa] | δ_2 [rad] |
|-------------------|-------------|--------------|------------------|-------------|--------------|------------------|
| $1 \cdot 10^{-2}$ | 3,921 | 692 | 10.01 | 2,863 | 602 | 11.88 |
| $2 \cdot 10^{-2}$ | 4,715 | 917 | 11.01 | 3,414 | 757 | 12.50 |
| $3 \cdot 10^{-2}$ | 5,337 | 1028 | 10.91 | 3,812 | 788 | 11.69 |
| $4 \cdot 10^{-2}$ | 5,513 | 1015 | 10.44 | 4,152 | 718 | 9.81 |
| $5 \cdot 10^{-2}$ | 5,874 | 887 | 8.59 | 4,343 | 663 | 8.68 |
| $6 \cdot 10^{-2}$ | 6,309 | 802 | 7.25 | 4,420 | 667 | 8.59 |
| $7 \cdot 10^{-2}$ | 6,052 | 965 | 9.06 | 4,557 | 784 | 9.76 |
| $8 \cdot 10^{-2}$ | 5,986 | 915 | 8.69 | 4,684 | 723 | 8.77 |
| $9 \cdot 10^{-2}$ | 5,946 | 845 | 8.09 | 4,753 | 691 | 8.27 |
| $1 \cdot 10^{-1}$ | 6,186 | 774 | 7.14 | 4,873 | 627 | 7.33 |
| $2 \cdot 10^{-1}$ | 6,777 | 763 | 6.42 | 5,169 | 627 | 6.92 |
| $3 \cdot 10^{-1}$ | 6,865 | 862 | 7.16 | 5,433 | 714 | 7.48 |
| $4 \cdot 10^{-1}$ | 6,770 | 826 | 6.96 | 5,457 | 669 | 6.99 |
| $5 \cdot 10^{-1}$ | 7,219 | 692 | 5.47 | 5,628 | 586 | 5.94 |
| $6 \cdot 10^{-1}$ | 6,900 | 832 | 6.87 | 5,676 | 679 | 6.82 |
| $7 \cdot 10^{-1}$ | 7,118 | 789 | 6.32 | 5,593 | 661 | 6.74 |
| $8 \cdot 10^{-1}$ | 7,062 | 844 | 6.82 | 5,536 | 660 | 6.80 |
| $9 \cdot 10^{-1}$ | 7,688 | 781 | 5.80 | 5,820 | 581 | 5.70 |
| $1 \cdot 10^0$ | 8,076 | 926 | 6.54 | 5,987 | 705 | 6.72 |
| $2 \cdot 10^0$ | 8,716 | 1,094 | 7.15 | 6,271 | 793 | 7.20 |
| $3 \cdot 10^0$ | 8,704 | 1,208 | 7.90 | 6,310 | 878 | 7.93 |
| $4 \cdot 10^0$ | 9,076 | 1,390 | 8.71 | 6,497 | 978 | 8.56 |
| $5 \cdot 10^0$ | 9,237 | 1,520 | 9.35 | 6,542 | 1056 | 9.17 |
| $6 \cdot 10^0$ | 9,053 | 1,121 | 7.06 | 6,322 | 751 | 6.77 |
| $7 \cdot 10^0$ | 9,207 | 1,161 | 7.19 | 6,374 | 781 | 6.99 |
| $8 \cdot 10^0$ | 9,340 | 1,205 | 7.35 | 6,473 | 805 | 7.09 |
| $9 \cdot 10^0$ | 9,425 | 1,225 | 7.40 | 6,457 | 826 | 7.29 |
| $1 \cdot 10^1$ | 9,502 | 1,270 | 7.61 | 6,422 | 866 | 7.68 |

Table D.8.: Results from macrorheological SAOS results as plotted in figure II.4.5. Data recorded at the mucus sample from the first horse carries the index 1, data from the second horse is indicated by the index 2.

Acknowledgements

First and foremost, I would like to thank Prof. Dr. Christian Wagner for giving me the opportunity to work on topics like cross-correlations of Brownian motion and complex fluids in his group. Also, I would like to thank him for the chance to work on the DNA project in Strasbourg.

I would like to thank Prof. Dr. Carlos Marques for his support when planning the DNA project and for his supervision during its course. Many fruitful discussions together with André Schröder, Pierre Muller, and Tatiana Schmatko brought fresh ideas and helped in the advancement of the experiments.

Many thanks go to the complete Wagner and Huber groups in Saarbrücken as well as the Marques group in Strasbourg for their great atmosphere and collegueship. Whenever chemical mixtures were necessary, Karin Kretsch was there to advise and help out, if there was any bureaucratic issue, Elke Huschens knew the answer. Thus, additional thanks are reserved for them.

A further thank you goes to the mechanical as well as the electronics workshop of the experimental physics department in Saarbrücken.

I would like to thank Devin Townsend and many more excellent heavy metal bands for the best soundtrack to a dissertation. Also, big thanks go to the many indie game developers out there for really great games like “Papers, please!”, “The Stanley Parable”, and all the others which helped in gaining the necessary distance from my own work.

I would also like to thank my two proofreaders, Elke and Dominik, for their patience in hunting spelling and other errors as well as the mapping of labyrinthine sentences.

An immensely big thank you goes to my parents and my whole family. Without their support while growing up and during my studies later I would never have come this far!

The biggest acknowledgement goes to my fiancée Elke. Thank you for always bearing with me, especially during hard times, and for always supporting me! I couldn't have done this without you!

Eidesstattliche Versicherung

Hiermit versichere ich an Eides statt, dass ich die vorliegende Arbeit selbstständig und ohne Benutzung anderer als der angegebenen Hilfsmittel angefertigt habe. Die aus anderen Quellen oder indirekt übernommenen Daten und Konzepte sind unter Angabe der Quelle gekennzeichnet.

Die Arbeit wurde bisher weder im In- noch im Ausland in gleicher oder ähnlicher Form in einem Verfahren zur Erlangung eines akademischen Grades vorgelegt.

Saarbrücken, 10. September 2014

Andreas Gross

List of Variables

| symbol | unit | meaning |
|------------------|--------------------------|---|
| $A_{C_{ij}}$ | m^2 | amplitude of non-oscillating contribution to cross-correlation function C_{ij} |
| A_{DNA} | m | amplitude of DNA center of mass |
| A_{rel} | m | relative amplitude of DNA center of mass in respect to driving lens |
| A_{resc} | m | rescaled amplitude of DNA center of mass in respect to driving lens amplitude and relative height |
| B | m | amplitude of driving oscillation |
| c | $\frac{m}{s}$ | speed of light in vacuum |
| C_{ii} | m^2 | auto-correlation function of direction i |
| C_{ij} | m^2 | cross-correlation function of direction i and direction j |
| $C_{ij,osc}$ | m^2 | amplitude of oscillating contribution to cross-correlation function |
| d_c | m | diameter of colloid |
| d_{cw} | m | distance of wall and center of a colloid |
| D | $\frac{m^2}{s}$ | diffusion coefficient |
| \vec{E} | $\frac{A^2 s^4}{kg m^3}$ | electric field |
| f | $\frac{1}{s}$ | frequency |
| \vec{F}_{grad} | $\frac{kg m}{s^2}$ | gradient force |
| \vec{F}_r | $\frac{kg m}{s^2}$ | Brownian random force |
| \vec{F}_{scat} | $\frac{kg m}{s^2}$ | scattering force |
| \vec{F}_{trap} | $\frac{kg m}{s^2}$ | restoring force of the optical trap |
| \vec{g} | $\frac{m}{s^2}$ | gravitational acceleration |
| G, \tilde{G} | $\frac{kg}{m s^2}$ | shear modulus |
| G' | $\frac{kg}{m s^2}$ | elastic contribution to shear modulus |
| G'' | $\frac{kg}{m s^2}$ | viscous contribution to shear modulus |
| h_{lens} | m | distance between coverslide and lens |
| k_B | $\frac{kg m^2}{s^2 K}$ | Boltzmann's constant |
| k, k_{trap} | $\frac{kg}{s^2}$ | trap stiffness |
| m | kg | mass |
| m_r | – | relative refractive index |

This table continues on the following page.

D. Supplementary Tables

| symbol | unit | meaning |
|------------------|----------------------------|--|
| n_c | – | refractive index of colloid material |
| n_m | – | refractive index of surrounding medium |
| p | $\frac{kg}{m \cdot s^2}$ | pressure |
| P | $\frac{kg \cdot m^2}{s^3}$ | power of a laser beam |
| Q | $\frac{m^3}{s}$ | flow rate |
| Q_{grad} | – | quality factor of gradient force |
| Q_{scat} | – | quality factor of scattering force |
| r_c | m | radius of colloid |
| Re | – | Reynolds number |
| R_F | – | Fresnel's coefficient of reflection |
| \vec{r}_{trap} | m | position vector of trap |
| \vec{S} | $\frac{kg}{s^3}$ | Poynting vector |
| T | K | temperature |
| T_F | – | Fresnel's coefficient of transmission |
| Wi | – | Weissenberg number |
| z_0 | m | average distance of grafted DNA center of mass from coverslide |
| α | – | dimensionless frequency |
| $\tilde{\alpha}$ | $\frac{s^2}{kg}$ | fluid susceptibility |
| α_p | $\frac{A^2 \cdot s^4}{kg}$ | electromagnetic polarizability |
| γ | – | shear strain |
| $\dot{\gamma}$ | $\frac{1}{s}$ | shear rate |
| δ | rad | phase |
| δ_{DNA} | rad | phase of DNA center of mass |
| δ_{lens} | rad | phase of lens |
| ζ | $\frac{kg}{s}$ | coefficient of friction |
| η | $\frac{kg}{m \cdot s}$ | dynamic viscosity |
| θ_i | rad | angle of incidence |
| θ_e | rad | angle of emergence |
| κ | $\frac{kg}{s^2}$ | spring constant |
| λ | m | wavelength |
| ρ | $\frac{kg}{m^3}$ | density |
| σ_s | m^2 | scattering cross-section |
| τ | $\frac{kg}{m \cdot s^2}$ | shear stress |
| τ_r | $\frac{1}{s}$ | relaxation rate |
| ω | $\frac{rad}{s}$ | angular frequency |

List of Figures

| | | |
|---------|--|----|
| I.1.1. | Arbitrary path of a colloidal particle in the bulk of a fluid | 7 |
| I.2.1. | Contributions of correlated and anti-correlated modes of motion of two beads along the same coordinate axis | 10 |
| I.3.1. | Quality factors for scattering (Eq. I.3.6) and gradient force (Eq. I.3.7) | 15 |
| I.3.2. | Total force balance of scattering and gradient force for the interaction of a focused laser beam with a sphere | 17 |
| I.4.1. | Color-coded plot of the flow velocity in the x-direction of a rectangular channel in the y-z-plane | 20 |
| I.4.2. | Plot of the normalized flow velocity v against the position y | 21 |
| I.4.3. | Mask used for lithographic processing of the mold | 23 |
| I.4.4. | Photograph of a fully prepared microfluidic device | 24 |
| I.4.5. | Sketch of a colloid in a microfluidic device with a rectangular cross-section | 26 |
| I.4.6. | Analytical auto-correlation functions of a colloid confined in an optical trap | 29 |
| I.4.7. | Analytical cross-correlation functions of a colloid confined in an optical trap | 30 |
| I.4.8. | Sketch of a colloid which is driven to oscillations in y-direction in a microfluidic device with a rectangular cross-section | 32 |
| I.4.9. | Analytical auto-correlation functions of a colloid forced by an oscillating optical trap | 35 |
| I.4.10. | Analytical cross-correlation functions of a colloid forced by an oscillating optical trap | 35 |
| I.4.11. | Dependence of the phase of the cross-correlation function C_{xy} on α . | 36 |
| I.5.1. | Histogram of displacements of a numerical data set of a colloid in an optical trap | 40 |
| I.5.2. | Auto- and cross-correlation functions of a simulated displacement of a colloid out of the center of an optical trap | 41 |
| I.5.3. | Cross-correlation function of a numerical dataset of the displacement of a colloid out of the center of an optical trap in a linear shear flow . | 42 |

List of Figures

| | | |
|---------|--|----|
| I.5.4. | Correlation functions C_{xx} , C_{yy} , and C_{xy} for a colloid in linear shear flow forced by an oscillating optical trap | 44 |
| I.5.5. | Dependence of the oscillation amplitudes of the auto- and cross-correlation functions on the shear rate | 45 |
| I.5.6. | Dependence of the relative correlation amplitude $C_{xx,osc}/C_{yy,osc}$ on the oscillation frequency of the optical trap | 46 |
| I.5.7. | Phase behavior of C_{xy} as a function of the dimensionless frequency at a fixed relaxation rate τ_r | 48 |
| I.6.1. | Illustration of the setup of optical tweezers | 53 |
| I.6.2. | Power of each of the laser beams measured by a power meter | 54 |
| I.6.3. | Beam profiles of the two lasers utilized in the setup of optical tweezers | 55 |
| I.6.4. | Characteristic transmission line for both of the dichroic mirrors utilized in the setup of optical tweezers. | 56 |
| I.6.5. | Characteristic transmission line for the two rejection band filters utilized in the setup of optical tweezers. | 58 |
| I.6.6. | Influence of the camera angle alignment on the correlation functions of the displacements of a trapped bead | 63 |
| I.6.7. | Typical displacement curve recorded for the tilt calibration of the camera | 64 |
| I.6.8. | Results of multiple independent drag force calibrations with sinewave oscillations at different laser emission power settings | 69 |
| I.6.9. | Trap stiffnesses resulting from different calibration methods | 69 |
| I.6.10. | Auto- and Cross-correlation functions with no flow present. | 70 |
| I.6.11. | Auto- and cross-correlation functions of two independent measurements M1 and M2 at the same experimental settings | 72 |
| I.6.12. | Influence of the sign of the shear gradient in a linear shear flow | 73 |
| I.6.13. | Dependence of the depth and position of the cross-correlation peak near $t = 0$ s on the trap stiffness | 74 |
| I.6.14. | Effect of the sign of the shear gradient on the confinement of a colloid | 76 |
| I.6.15. | Effect of the sign of the shear gradient on the spatial distribution of a colloid | 77 |
| I.6.16. | Auto-correlation functions C_{xx} and C_{yy} for a colloid confined in an oscillating trap ($k = 5.5 \mu N/m$) in a linear shear flow about $3r_c$ away from the channel walls | 79 |
| I.6.17. | Cross-correlation functions C_{xy} for a colloid confined in an oscillating trap ($k = 5.5 \mu N/m$) in a linear shear flow about $3r_c$ away from the channel walls | 80 |
| I.6.18. | Dependence of the oscillatory contribution to the auto-correlation function C_{yy} on the dimensionless frequency α | 82 |

| | | |
|----------|--|-----|
| I.6.19. | Phase behavior of the oscillatory contribution to C_{xy} | 82 |
| II.1.1. | Scanning-electron-micrograph of the cilia found in the rabbit trachea | 97 |
| II.2.1. | Cryo-scanning-electron micrograph of respiratory horse mucus | 100 |
| II.3.1. | Equivalent circuit diagram of the Maxwell model | 102 |
| II.3.2. | Typical curve progression of the shear modulus according to Maxwell's model | 103 |
| II.4.1. | Photograph of the utilized rheometer HAAKE MARS II as well as all of its crucial components. | 111 |
| II.4.2. | Evaluation of the linear response range via an amplitude sweep with a mucus sample | 114 |
| II.4.3. | Lissajous-figures gained by an amplitude sweep with a mucus sample | 115 |
| II.4.4. | Lissajous-figures gained by an amplitude sweep with a polyacrylamide (PAAm) sample | 115 |
| II.4.5. | Results from small amplitude oscillatory shear experiments performed at two mucus samples stemming from two different horses | 116 |
| II.4.6. | Mean squared displacements from passive tracking experiments at different positions within the same mucus sample | 121 |
| II.4.7. | Overview of the distribution of mean squared displacements within a 1% hydroethoxycellulose (HEC) sample. The x- and y-component at each position is plotted independently (marked by different symbols of the same color). This graph was adapted from figure 4B in [76]. | 122 |
| II.4.8. | Results from passive particle tracking experiments at different positions within the same mucus sample | 123 |
| II.4.9. | Oscillatory displacement experiments at two different positions within the same mucus sample | 126 |
| II.5.1. | Comparison of the shear modulus recovered from macrorheologic SAOS experiments with the results from passive microrheology | 130 |
| II.5.2. | Sketch of the microscopic structure of mucus | 131 |
| III.3.1. | Planar structural binding model of a DNA molecule | 145 |
| III.3.2. | Sketch of the oscillating, linear flow profile between a fixed lower plate and an oscillating upper plate | 148 |
| III.3.3. | Dependence of the velocity amplitude and the phase shift of the moving fluid on the position in z-direction between the plates | 149 |
| III.3.4. | Model system for single-end-grafted DNA molecules on a cover slip. . | 150 |
| III.3.5. | Results of the bead-spring model for DNA molecules | 153 |

List of Figures

| | | |
|-----------|---|-----|
| III.4.1. | Ligation process of λ -DNA in preparation for single-end-grafting . . . | 156 |
| III.4.2. | Representation of the experimental setup for shearing and visualizing the DNA molecules | 158 |
| III.4.3. | Calibration curve of lens amplitude versus piezo voltage | 160 |
| III.4.4. | Comparison of originally recorded picture of grafted DNA molecules and post-processed picture after filtering | 161 |
| III.4.5. | Displacement-time-diagram of the lens and the center-of-mass of a DNA molecule as well as sinusoidal fits to both data sets | 163 |
| III.4.6. | Auto-correlation functions of the motion of a DNA molecule under sinusoidal driving | 164 |
| III.4.7. | Histogram of the longest relaxation rates of the DNA molecules . . . | 164 |
| III.4.8. | Graph of the DNA <i>COM</i> versus the lens amplitude | 165 |
| III.4.9. | Dependencies of the relative amplitude and the phase shift on the distance between oscillation lens and cover slip | 166 |
| III.4.10. | Amplitude dependency on the dimensionless frequency | 167 |
| III.4.11. | Dependency of the phase shift between driving and response oscillation on the dimensionless frequency | 168 |
| III.4.12. | Plot of the results of the length evaluation of the DNA intensity profile versus the evaluation using sine fits to the <i>COM</i> motion | 170 |
| III.4.13. | Plot of the results of the length evaluation of the DNA intensity profile as compared to the width of the equilibrium intensity distribution of such a molecule | 170 |
| III.5.1. | Results of the experimental study of M. Khaksar with single-end-grafted DNA | 175 |

List of Tables

| | |
|--|-----|
| A.1. Chemical products and microparticles utilized to conduct the experiments in all parts of this thesis. | 185 |
| D.1. Data sets shown in figures I.5.5b. | 197 |
| D.2. Data sets shown in figures I.5.6 and I.5.7. | 197 |
| D.3. Data set of the emitted laser power of the Ventus laser utilized in the setup of optical tweezers in Saarbrücken | 198 |
| D.4. Data set of the emitted laser power of the Ciel laser utilized in the setup of optical tweezers in Saarbrücken | 199 |
| D.5. Results of all calibration methods detailed in section I.6.3 | 199 |
| D.6. Fitting results to the experimental data sets | 201 |
| D.7. Phase shifts of the cross-correlation function C_{xy} after removal of the influence of the sign of the shear gradient and after averaging of the data within frequency intervals of a width $\Delta\alpha = 0.01$. These data sets were also plotted in figure I.6.19. No errors are given for $\alpha = 0.032$ and $\alpha = 0.157$ since only one single value was contained in the corresponding averaging interval. | 202 |
| D.8. Macrorheological SAOS results | 203 |

Bibliography

- [1] Anderson, V. J. and Lekkerkerker, H. N. W.; “Insight into Phase Transition Kinetics from Colloid Science”; *Nature* **416** (2002) 811
- [2] Radu, M. and Schilling, T.; “Hydrodynamic Interactions of Colloidal Spheres under Shear Flow”; arXiv **cond-mat.soft:1203** (2012) 1203.3441v1
- [3] Ashkin, A., Dziedzic, J. M., Bjorkholm, J. E., and Chu, S.; “Observation of a Single-Beam Gradient Force Optical Trap for Dielectric Particles”; *Optics Letters* **11** (1986) 288
- [4] Ziehl, A.; Untersuchung Brownscher Partikel im Scherfluss durch Korrelationsanalysen unter Verwendung optischer Pinzetten; Ph.D. thesis; Universität des Saarlandes (2009)
- [5] Ziehl, A., Bammert, J., Holzer, L., Wagner, C., and Zimmermann, W.; “Direct Measurement of Shear-Induced Cross-Correlation of Brownian Motion”; *Physical Review Letters* **103** (2009) 230602
- [6] Ingenhousz, J. and Molitor, N. C.; *Vermischte Schriften physisch-medicinischen Inhalts*; Wappler (1784)
- [7] Brown, R.; “A Brief Account of Microscopic Observation Made in the Months of June, July, and August, 1827, on the Particles Contained in the Pollen of Plants and on the General Existence of Active Molecules in Organic and Inorganic Bodies”; *Philosophical Magazine* **4** (1828) 161
- [8] Wiener, C.; “Erklärung des atomistischen Wesens des tropfbar-flüssigen Körperzustandes, und Bestätigung desselben durch die sogenannten Molecularbewegungen”; *Annalen der Physik und Chemie* **194** (1863) 79
- [9] Exner, S.; “Untersuchung über Brown’s molecularbewegung”; *Sitzungsberichte der Kaiserlichen Academie der Wissenschaften* **56** (1867) 116
- [10] Delsaulx, J.; “Thermo-dynamic Origin of the Brownian Motions”; *The Monthly Microscopical Journal* **18** (1877) 1
- [11] Einstein, A.; “Über die von der molekularkinetischen Theorie der Wärme geforderte Bewegung von in ruhenden Flüssigkeiten suspendierten Teilchen”; *Annalen der Physik* **322** (1905) 549
- [12] Smoluchowski, M.; “Zur kinetischen Theorie der Brownschen Molekularbewegung und der Suspensionen”; *Annalen der Physik* **326** (1906) 756
- [13] Perrin, J. and Dabrowski, M.; “Mouvement Brownien et Constantes Moléculaires”; *Comptes Rendus de l’Académie des Sciences de Paris* **149** (1909) 477
- [14] Maret, G. and Wolf, P. E.; “Multiple Light Scattering from Disordered Media. The Effect of Brownian Motion of Scatterers”; *Zeitschrift fuer Physik B - Condensed Matter* **65** (1987) 409

Bibliography

- [15] Ehrenberg, M. and Rigler, R.; “Rotational Brownian Motion and Fluorescence Intensity Fluctuations”; *Chemical Physics* **4** (1974) 390
- [16] Meiners, J.-C. and Quake, S. R.; “Direct Measurement of Hydrodynamic Cross Correlations between Two Particles in an External Potential”; *Physical Review Letters* **82** (1999) 2211
- [17] Skryabina, M. N., Lyubin, E. V., Khokhlova, M. D., and Fedyanin, A. A.; “Probing of Pair Interaction of Magnetic Microparticles with Optical Tweezers”; *JETP Letters* **95** (2012) 560
- [18] Bammert, J., Holzer, L., and Zimmermann, W.; “Dynamics of Two Trapped Brownian Particles: Shear-Induced Cross-Correlations”; *European Physical Journal E: Soft Matter* **33** (2010) 313
- [19] Holzer, L., Bammert, J., Rzehak, R., and Zimmermann, W.; “Dynamics of a Trapped Brownian Particle in Shear Flows”; *Physical Review E* **81** (2010) 041124
- [20] Santiago, J. G., Wereley, S. T., Meinhart, C. D., Beebe, D. J., and Adrian, R. J.; “A Particle Image Velocimetry System for Microfluidics”; *Experiments in Fluids* **25** (1998) 316
- [21] Meinhart, C. D., Wereley, S. T., and Santiago, J. G.; “PIV Measurements of a Microchannel Flow”; *Experiments in Fluids* (1999)
- [22] Olsen, M. G. and Adrian, R. J.; “Brownian Motion and Correlation in Particle Image Velocimetry”; *Optics & Laser Technology* **32** (2000) 621
- [23] Hohreiter, V., Wereley, S. T., Olsen, M. G., and Chung, J. N.; “Cross-Correlation Analysis for Temperature Measurement”; *Measurement Science and Technology* (2002)
- [24] Volpe, G. and Petrov, D.; “Torque Detection Using Brownian Fluctuations”; *Physical Review Letters* **97** (2006) 210603
- [25] Einstein, A.; “Über einen die Erzeugung und Verwandlung des Lichtes Betreffenden Heuristischen Gesichtspunkt”; *Annalen der Physik* **14** (1905) 164
- [26] Ashkin, A.; “Acceleration and Trapping of Particles by Radiation Pressure”; *Physical Review Letters* **24** (1970) 156
- [27] Ashkin, A. and Dziedzic, J. M.; “Optical Levitation by Radiation Pressure”; *Applied Physics Letters* **19** (1971) 283
- [28] Ashkin, A.; “Trapping of Atoms by Resonance Radiation Pressure”; *Physical Review Letters* **40** (1978) 729
- [29] Gordon, J. P. and Ashkin, A.; “Motion of Atoms in a Radiation Trap”; *Physical Review A* **21** (1980) 1606
- [30] Ashkin, A.; “Forces of a Single-Beam Gradient Laser Trap on a Dielectric Sphere in the Ray Optics Regime”; *Biophysical Journal* **61** (1992) 569
- [31] Simmons, R. M., Finer, J. T., Warrick, H. M., Kralik, B., Chu, S., and Spudich, J. A.; “Force on Single Actin Filaments in a Motility Assay Measured with an Optical Trap”; *Advances in Experimental Medicine and Biology* **332** (1993) 331
- [32] Khan, S. and Sheetz, M. P.; “Force Effects on Biochemical Kinetics”; *Annual Review of Biochemistry* **66** (1997) 785
- [33] Mehta, A. D., Finer, J. T., and Spudich, J. A.; “Use of Optical Traps in Single-Molecule

- Study of Nonprocessive Biological Motors”; *Methods in Enzymology* **298** (1998) 436
- [34] Perkins, T. T., Quake, S. R., Smith, D. E., and Chu, S.; “Relaxation of a Single DNA Molecule Observed by Optical Microscopy”; *Science* **264** (1994) 822
- [35] Wang, M. D., Yin, H., Landick, R., Gelles, J., and Block, S. M.; “Stretching DNA with Optical Tweezers”; *Biophysical Journal* **72** (1997) 1335
- [36] Mason, T. G. and Weitz, D. A.; “Optical Measurements of Frequency-Dependent Linear Viscoelastic Moduli of Complex Fluids”; *Physical Review Letters* **74** (1995) 1250
- [37] Valentine, M. T., Dewalt, L. E., and Ou-Yang, H. D.; “Forces on a Colloidal Particle in a Polymer Solution: a Study Using Optical Tweezers”; *Journal of Physics: Condensed Matter* **8** (1996) 9477
- [38] van Zanten, J. H., Amin, S., and Abdala, A. A.; “Brownian Motion of Colloidal Spheres in Aqueous PEO Solutions”; *Macromolecules* **37** (2004) 3874
- [39] Valentine, M. T., Kaplan, P. D., Thota, D., Crocker, J. C., Gisler, T., Prud’homme, R. K., Beck, M., and Weitz, D. A.; “Investigating the Microenvironments of Inhomogenous Soft Materials with Multiple Particle Tracking”; *Physical Review E* **64** (2001) 061506
- [40] Williams, M. A. K., Vincent, R. R., Pinder, D. N., and Hemar, Y.; “Microrheological Studies offer Insights into Polysaccharide Gels”; *Journal of Non-Newtonian Fluid Mechanics* **49** (2008) 63
- [41] Addas, K. M., Schmidt, C. F., and Tang, J. X.; “Microrheology of Solutions of Semiflexible Biopolymer Filaments Using Laser Tweezers Interferometry”; *Physical Review E* **70** (2004) 021503
- [42] Brau, R. R., Ferrer, J. M., Lee, H., Castro, C. E., Tam, B. K., Tarsa, P. B., Matsudaira, P., Boyce, M. C., Kamm, R. D., and Lang, M. J.; “Passive and Active Microrheology with Optical Tweezers”; *Journal of Optics A: Pure and Applied Optics* **9** (2007) S103
- [43] Weihs, D., Mason, T. G., and Teitell, M. A.; “Bio-Microrheology: A Frontier in Microrheology”; *Biophysical Journal* **91** (2006) 4296
- [44] Bohren, C. F. and Huffman, D. R.; *Absorption and Scattering of Light by Small Particles*; Wiley-VCH; 1st edition (2004)
- [45] Chaumet, P. C. and Nieto-Vesperinas, M.; “Coupled Dipole Method Determination of the Electromagnetic Force on a Particle over a Flat Dielectric Substrate”; *Physical Review B* **61** (2000) 14119
- [46] Maheu, B., Gouesbet, G., and Grehan, G.; “A Concise Presentation of the Generalized Lorenz-Mie Theory for Arbitrary Location of the Scatterer in an Arbitrary Incident Profile”; *Journal of Optics* **19** (1988) 59
- [47] Ren, K. F., Grehan, G., and Gouesbet, G.; “Prediction of Reverse Radiation Pressure by Generalized Lorenz-Mie Theory”; *Applied Optics* **35** (1996) 2702
- [48] Wohland, T., Rosin, A., and Stelzer, E. H. K.; “Theoretical Determination of the Influence of the Polarization on Forces Exerted by Optical Tweezers”; *Optik* **102** (1996) 181
- [49] Bird, R. B., Armstrong, R. C., and Hassager, O.; *Dynamics of Polymeric Liquids: Volume 1 Fluid Mechanics*; volume 1; Wiley-Interscience (1987)
- [50] Pozrikidis, C.; *Introduction to Theoretical and Computational Fluid Dynamics*; Oxford

Bibliography

- University Press (1997)
- [51] Happel, J. and Brenner, H.; *Low Reynolds Number Hydrodynamics with Special Applications to Particulate Media*; Springer Verlag; 2nd edition (2009)
 - [52] Xia, Y. and Whitesides, G. M.; “Soft Lithography”; *Angewandte Chemie, International Edition* **37** (1998) 550
 - [53] Huang, R., Chavez, I., Taute, K. M., Lukić, B., Jeney, S., Raizen, M. G., and Florin, E.-L.; “Direct Observation of the Full Transition from Ballistic to Diffusive Brownian Motion in a Liquid”; *Nature Physics* **7** (2011) 576
 - [54] Uhlenbeck, G. E. and Ornstein, L. S.; “On the Theory of the Brownian Motion”; *Physical Review* **36** (1930) 823
 - [55] Callen, H. B. and Welton, T. A.; “Irreversibility and Generalized Noise”; *Physical Review* **83** (1951) 34
 - [56] Mason, T. G., Gang, H., and Weitz, D. A.; “Rheology of Complex Fluids Measured by Dynamic Light Scattering”; *Journal of Molecular Structure* **383** (1996) 81
 - [57] Langevin, P.; “Sur la Théorie du Mouvement Brownien”; *Comptes Rendus de l’Académie des Sciences (Paris)* **146** (1908) 530
 - [58] Chakraborty, D.; “Time Correlations and Persistence Probability of a Brownian Particle in a Shear Flow”; *European Physical Journal B: Condensed Matter Physics* **85** (2012) 281
 - [59] Zeidler, E.; *Springer-Taschenbuch der Mathematik*; Springer Spektrum (2013)
 - [60] Protter, P. E.; *Stochastic Integration and Differential Equations*; Springer Berlin Heidelberg; 2nd edition (2005)
 - [61] Neuman, K. C. and Block, S. M.; “Optical Trapping”; *Review of Scientific Instruments* **75** (2004) 2787
 - [62] Schwabl, F.; *Statistische Mechanik*; chapter Brownsche Bewegung, Stochastische Bewegungsgleichungen und Fokker-Planck-Gleichungen, 417–444; Springer Berlin Heidelberg; 3rd edition (2006)
 - [63] Fällman, E. and Axner, O.; “Influence of a Glass-Water Interface on the On-Axis Trapping of Micrometer-Sized Spherical Objects by Optical Tweezers”; *Applied Optics* **42** (2003) 3915
 - [64] Jung, A.; *Untersuchung einer Ca^{2+} -induzierten Erythrozytenadhäsion mittels holographischer optischer Pinzetten*; Ph.D. thesis; Universität des Saarlandes (2008)
 - [65] Capitanio, M., Romano, G., Ballerini, R., Giuntini, M., Pavone, F. S., Dunlap, D., and Finzi, L.; “Calibration of Optical Tweezers with Differential Interference Contrast Signals”; *Review of Scientific Instruments* **73** (2002) 1687
 - [66] Peterman, E. J. G., Gittes, F., and Schmidt, C. F.; “Laser-Induced Heating in Optical Traps”; *Biophysical Journal* **84** (2003) 1308
 - [67] Fischer, M. and Berg-Sørensen, K.; “Calibration of Trapping Force and Response Function of Optical Tweezers in Viscoelastic Media”; *Journal of Optics A: Pure and Applied Optics* **9** (2007) S239
 - [68] Werth, M.; *Verhalten komplexer Fluide am Stagnationspunkt einer Elongationsströmung*; Diploma thesis; Universität des Saarlandes (2012)

- [69] Dekker, J., Rossen, J. W. A., Büller, H. A., and Einerhand, A. W. C.; “The MUC Family: an Obituary”; *Trends in Biochemical Sciences* **27** (2002) 126
- [70] Bansil, R. and Turner, B. S.; “Mucin Structure, Aggregation, Physiological Functions and Biomedical Applications”; *Current Opinion in Colloid & Interface Science* **11** (2006) 164
- [71] Lai, S. K., Wang, Y.-Y., Wirtz, D., and Hanes, J.; “Micro- and Macrorheology of Mucus”; *Advanced Drug Delivery Reviews* **61** (2009) 86
- [72] Olmsted, S. S., Padgett, J. L., Yudin, A. I., Whaley, K. J., Moench, T. R., and Cone, R. A.; “Diffusion of Macromolecules and Virus-Like Particles in Human Cervical Mucus”; *Biophysical Journal* **81** (2001) 1930
- [73] Cone, R. A.; “Barrier Properties of Mucus”; *Advanced Drug Delivery Reviews* **61** (2009) 75
- [74] Sanderson, M. J. and Sleight, M. A.; “Ciliary Activity of Cultured Rabbit Tracheal Epithelium: Beat Pattern and Metachrony”; *J. Cell Sci.* **47** (1981) 331
- [75] Sigurdsson, H. H., Kirch, J., and Lehr, C.-M.; “Mucus as a Barrier to Lipophilic Drugs”; *International Journal of Pharmaceutics* **453** (2013) 56
- [76] Kirch, J., Schneider, A., Abou, B., Hopf, A., Schäfer, U. F., Schneider, M., Schall, C., Wagner, C., and Lehr, C.-M.; “Optical Tweezers Reveal Relationship between Microstructure and Nanoparticle Penetration of Pulmonary Mucus”; *Proceedings of the National Academy of Sciences of the United States of America* **109** (2012) 18355
- [77] Denton, R.; “Rheology of Human Lung Mucus”; *Annals of the New York Academy of Sciences* **106** (1963) 746
- [78] Odeblad, E.; “The Functional Structure of Human Cervical Mucus”; *Acta Obstetricia et Gynecologica Scandinavica* **47** (1968) 57
- [79] Denton, R., Forsman, W., Hwang, S. H., Litt, M., and Miller, C. E.; “Viscoelasticity of Mucus - Its Role in Ciliary Transport of Pulmonary Secretions”; *American Review of Respiratory Disease* **98** (1968) 380
- [80] Litt, M.; “Mucus Rheology - Relevance to Muciliary Clearance”; *Archives of Internal Medicine* **126** (1970) 417
- [81] Eliezer, N.; “Viscoelastic Properties of Mucus”; *Biorheology* **11** (1974) 61
- [82] Button, B., Cai, L.-H., Ehre, C., Kesimer, C., Hill, D. B., Sheehan, J. K., Boucher, R. C., and Rubinstein, M.; “A Periciliary Brush Promotes the Lung Health by Separating the Mucus Layer from Airway Epithelia”; *Science* **337** (2012) 937
- [83] Mason, T. G., Ganesan, K., van Zanten, J. H., Wirtz, D., and Kuo, S. C.; “Particle Tracking Microrheology of Complex Fluids”; *Physical Review Letters* **79** (1997) 3282
- [84] Lai, S. K., O’Hanlon, D. E., Harrold, S., Man, S. T., Wang, Y.-Y., and Cone, R.; “Rapid Transport of Large Polymeric Nanoparticles in Fresh Undiluted Human Mucus”; *Proceedings of the National Academy of Sciences of the United States of America* **104** (2007) 1482
- [85] Doraiswamy, D.; “The Origins of Rheology: a Short Historical Excursion”; *Rheology Bulletin* **71** (2002); URL http://www.rheology.org/SoR/publications/Rheology%5FBF/Jan02/Origin_of_Rheology.pdf

Bibliography

- [86] Maxwell, J. C.; “On the Dynamical Theory of Gases”; Philosophical Transactions of the Royal Society of London **157** (1867) 49
- [87] Mooney, M. and Ewart, R. H.; “The Conicylindrical Viscometer”; R. H. Physics **5** (1934) 350
- [88] Russell, R. J.; The Determination of the Basic Rheological Constants Governing the Flow of Pseudoplastic Substances; Ph.D. thesis; University of London (1946)
- [89] Gill, F. and Russell, R. J.; “Pumpability of Residual Fuel Oils”; Industrial & Engineering Chemistry Research **46** (1954) 1264
- [90] Philippoff, W. and Gaskins, F. H.; “Viscosity Measurements on Molten Polyethylene”; Journal of Polymer Science, Part A: Polymer Chemistry **21** (1956) 205
- [91] Higginbotham, R. S.; “A Cone and Plate Viscometer”; Journal of Scientific Instruments **27** (1950) 139
- [92] McKennell, R.; “Cone-Plate Viscometer”; Analytical Chemistry **28** (1956) 1710
- [93] Walters, K. and Kemp, R. A.; “On the Use of a Rheogoniometer”; Rheologica Acta **7** (1968) 1
- [94] Dasgupta, B. R., Tee, S.-Y., Crocker, J. C., Frisken, B. J., and Weitz, D. A.; “Microrheology of Polyethylene Oxide Using Diffusing Wave Spectroscopy and Single Scattering”; Physical Review E **65** (2002) 051505
- [95] Crocker, J. C., Valentine, M. T., Weeks, E. R., Gisler, T., Kaplan, P. D., Yodh, A. G., and Weitz, D. A.; “Two-Point Microrheology of Inhomogeneous Soft Materials”; Physical Review Letters **85** (2000) 888
- [96] Schultz, K. M. and Furst, E. M.; “Microrheology of Biomaterial Hydrogelators”; Soft Matter **8** (2012) 6198
- [97] Schnurr, B., Gittes, F., MacKintosh, F. C., and Schmidt, C. F.; “Determining Microscopic Viscoelasticity in Flexible and Semiflexible Polymer Networks from Thermal Fluctuations”; Macromolecules **30** (1997) 7781
- [98] Gittes, F., Schnurr, B., Olmsted, P. D., MacKintosh, F. C., and Schmidt, C. F.; “Microscopic Viscoelasticity: Shear Moduli of Soft Materials Determined from Thermal Fluctuations”; Physical Review Letters **79** (1997) 3286
- [99] Atakhorrami, M., Sulkowska, J. I., Addas, K. M., Koenderink, G. H., Tang, J. X., Levine, A. J., MacKintosh, F. C., and Schmidt, C. F.; “Correlated Fluctuations of Microparticles in Viscoelastic Solutions: Quantitative Measurement of Material Properties by Microrheology in the Presence of Optical Traps”; Physical Review E **73** (2006) 061501
- [100] Jabbari-Farouji, S., Mizuno, D., Atakhorrami, M., MacKintosh, F. C., Schmidt, C. F., Eiser, E., Wegdam, G. H., and Bonn, D.; “Fluctuation-Dissipation Theorem in an Aging Colloidal Glass”; Physical Review Letters **98** (2007) 108302
- [101] Schneider, A.; Bestimmung der Viskosität komplexer Fluide mittels einer Optischen Pinzette sowie eines Rheometers; Diploma thesis; Universität des Saarlandes (2010)
- [102] Booij, H. C. and Thoone, G. P. J. M.; “Generalisation of Kramers-Kronig Transforms and some Approximations of Relations between Viscoelastic Quantities”; Rheologica Acta **21** (1982) 15

- [103] Macosko, C. W.; *Rheology: Principles, Measurements, and Applications*; Wiley-VCH; 1st edition (1994)
- [104] Lai, S. K., Wang, Y.-Y., Cone, R., Wirtz, D., and Hanes, J.; "Altering Mucus Rheology to "Solidify" Human Mucus at the Nanoscale"; *Public Library Of Science ONE* **4** (2009) e4294
- [105] Macierzanka, A., Rigby, N. M., Corfield, A. P., Wellner, N., Böttger, F., Mills, E. N. C., and Mackie, A. R.; "Adsorption of Bile Salts to Particles Allows Penetration of Intestinal Mucus"; *Soft Matter* **7** (2011) 8077
- [106] Kočevár-Nared, J., Kristl, J., and Šmid Korbar, J.; "Comparative Rheological Investigation of Crude Gastric Mucin and Natural Gastric Mucus"; *Biomaterials* **18** (1997) 677
- [107] Lieleg, O. and Ribbeck, K.; "Biological Hydrogels as Selective Diffusion Barriers"; *Trends Cell Biol.* **21** (2011) 543
- [108] Mori, T. and Tanaka, K.; "Average Stress in Matrix and Average Elastic Energy of Materials with Misfitting Inclusions"; *Acta Metallurgica* **21** (1973) 571
- [109] Daniell, H. and Dhingra, A.; "Multigene Engineering: Dawn of an Exciting New Era in Biotechnology"; *Current Opinion in Biotechnology* **13** (2002) 136
- [110] Rothmund, P. W. K.; "Folding DNA to Create Nanoscale Shape and Patterns"; *Nature* **440** (2006) 297
- [111] Jeffreys, A. J., Wilson, V., and Thein, S. L.; "Individual-Specific 'Fingerprints' of Human DNA"; *Nature* **316** (1985) 76
- [112] Collins, A. and Morton, N. E.; "Likelihood Ratios for DNA Identification"; *Proceedings of the National Academy of Sciences of the United States of America* **21** (1994) 6007
- [113] Quake, S. R.; "The Zimm Model Applied to Extended Single Polymers"; *Journal of Chemical Physics* **101** (1994) 4307
- [114] Porod, G.; "Zusammenhang zwischen mittlerem Endpunktabstand und Kettenlänge bei Fadenmolekülen"; *Monatshefte für Chemie und verwandte Teile anderer Wissenschaften* **80** (1949) 251
- [115] Kuznetsov, S. V., Shen, Y., Benight, A. S., and Ansari, A.; "A Semiflexible Polymer Model Applied to Loop Formation in DNA Hairpins"; *Biophysical Journal* **81** (2001) 2864
- [116] Peters, J. P., Yelgaonkar, S. P., Srivatsan, S. G., Tor, Y., and Ill, L. J. M.; "Mechanical Properties of DNA-Like Polymers"; *Nucleic Acids Research* **Advance Online Publication** (2013) 1
- [117] Dahm, R.; "Discovering DNA: Friedrich Miescher and the Early Years of Nucleic Acid Research"; *Human Genetics* **122** (2008) 565
- [118] Kossel, A.; "Ueber eine neue Base aus dem Thierkörper"; *Berichte der Deutschen Chemischen Gesellschaft* **18** (1885) 79
- [119] Levene, P. A.; "The Structure of Yeast Nucleic Acid: IV. Ammonia Hydrolysis"; *The Journal of Biological Chemistry* **40** (1919) 415
- [120] Chargaff, E., Vischer, E., Doniger, R., Green, C., and Misani, F.; "The Composition of the Desoxyribose Nucleic Acids of Thymus and Spleen"; *The Journal of Biological Chemistry* **177** (1949) 405

Bibliography

- [121] Watson, J. D. and Crick, F. H. C.; “Molecular Structure of Nucleic Acids: A Structure for Deoxyribose Nucleic Acid”; *Nature* **171** (1953) 737
- [122] Wilkins, M. H. F., Stokes, A. R., and Wilson, H. R.; “Molecular Structure of Nucleic Acids: Molecular Structure of Deoxypentose Nucleic Acids”; *Nature* **171** (1953) 738
- [123] Smith, S. B., Finzi, L., and Bustamante, C.; “Direct Mechanical Measurements of the Elasticity of Single DNA Molecules by Using Magnetic Beads”; *Science* **258** (1992) 1122
- [124] Doyle, P. S., Ladoux, B., and Viovy, J.-L.; “Dynamics of a Tethered Polymer in Shear Flow”; *Physical Review Letters* **84** (2000) 4769
- [125] Chen, Y.-L., Graham, M. D., de Pablo, J. J., Jo, K., and Schwartz, D. C.; “DNA Molecules in Microfluidic Oscillatory Flow”; *Macromolecules* **38** (2005) 6680
- [126] Lo, W.-C., Hong, H. C., Choi, H. J., Lai, P.-Y., and Chan, C. K.; “Stretching and Migration of DNA by Solvent Elasticity in an Oscillatory Flow”; *Physical Review E* **84** (2011) 021802
- [127] Khaksar, M.; DNA under Hydrodynamic and Mechanical Stretching: Structure and Dynamics; Ph.D. thesis; Universität Konstanz (2011)
- [128] URL http://en.wikipedia.org/wiki/File:DNA_chemical_structure.svg
- [129] Slater, G. W., Rousseau, J., Noolandi, J., Turmel, C., and Lalande, M.; “Quantitative Analysis of the Three Regimes of DNA Electrophoresis in Agarose Gels”; *Biopolymers* **27** (1988) 509
- [130] Balducci, A., Mao, P., Han, J., and Doyle, P. S.; “Double-Stranded DNA Diffusion in Slitlike Nanochannels”; *Macromolecules* **39** (2006) 6273
- [131] Sun, Y.; Confinement and Adsorption of End-Grafted λ -phage DNAs under Bio-Adhesive Membranes; Ph.D. thesis; Universität de Strasbourg (2010)
- [132] Koota, J., Seuffert, I., Li, H., Lehner, R., and Gisler, T.; “Reversible, Meniscus-Free Molecular Combing of Long-Chain DNA”; *Langmuir* **23** (2007) 9365
- [133] Hissette, M.-L., Haddad, P., Gisler, T., Marques, C. M., and Schröder, A. P.; “Spreading of Bio-Adhesive Vesicles on DNA Carpets”; *Soft Matter* **4** (2008) 828
- [134] Cosa, G., Focsaneanu, K.-S., McLean, J. R. N., McNamee, J. P., and Scaiano, J. C.; “Photophysical Properties of Fluorescent DNA-Dyes Bound to Single- and Double-Stranded DNA in Aqueous Buffered Solution”; *Photochemistry and Photobiology* **73** (2001) 585
- [135] Richards, A. D. and Rodger, A.; “Synthetic Metallomolecules as Agents for the Control of DNA Structure”; *Chemical Society Reviews* **36** (2007) 471
- [136] Guenther, K., Mertig, M., and Seidel, R.; “Mechanical and Structural Properties of YOYO-1 Complexed DNA”; *Nucleic Acids Research* **38** (2010) 6526
- [137] Johnson, L. V., Walsh, M. L., Bockus, B. J., and Chen, L. B.; “Monitoring of Relative Mitochondrial Membrane Potential in Living Cells by Fluorescence Microscopy”; *The Journal of Cell Biology* **88** (1981) 526
- [138] Reymann, J., Baddeley, D., Gunkel, M., Lemmer, P., Stadter, W., Jegou, T., Rippe, K., Cremer, C., and Birk, U.; “High-Precision Structural Analysis of Subnuclear Complexes in Fixed and Live Cells via Spatially Modulated Illumination (SMI) Microscopy”; *Chromosome Research* **16** (2008) 367
- [139] Zilker, A., Engelhardt, H., and Sackmann, E.; “Dynamic Reflection Interference Contrast

- (RIC-) Microscopy: a New Method to Study Surface Excitations of Cells and to Measure Membrane Bending Elastic Moduli”; *Journal de Physique France* **48** (1987) 2139
- [140] Nygren, J., Svanvik, N., and Kubista, M.; “The Interaction Between the Fluorescent Dye Thiazole Orange and DNA”; *Biopolymers* **46** (1998) 39
- [141] Hobbie, J. E., Daley, R. J., and Jasper, S.; “Use of Nuclepore Filters for Counting Bacteria by Fluorescence Microscopy”; *Applied and Environmental Microbiology* **33** (1977) 1225
- [142] Soto, C. M., Blum, A. S., Vora, G. J., Lebedev, N., Meador, C. E., Won, A. P., Chatterji, A., Johnson, J. E., and Ratna, B. R.; “Fluorescent Signal Amplification of Carbocyanine Dyes Using Engineer Viral Nanoparticles”; *Journal of the American Chemical Society* **128** (2006) 5184
- [143] Rädler, J. and Sackmann, E.; “On the Measurement of Weak Repulsive and Frictional Colloidal Forces by Reflection Interference Contrast Microscopy”; *Langmuir* **8** (1992) 848